UNIVERSITAT POLITÈCNICA DE VALÈNCIA

ESTUDIO DE NANOCOMPUESTOS DE ESPUMAS DE POLIURETANO REFORZADAS CON NANOCARGAS EN BASE CARBONO

María del Mar Bernal Ortega

Dirigida por

Dra. Raquel Verdejo Márquez

Dr. Miguel Ángel López Manchado

PROGRAMA DE DOCTORADO INGENIERÍA Y PRODUCCIÓN INDUSTRIAL

TESIS DOCTORAL INTERNACIONAL

Valencia – Mayo 2012

STUDY OF POLYURETHANE NANOCOMPOSITE FOAMS REINFORCED WITH CARBON-BASED NANOFILLERS

By

María del Mar Bernal Ortega

Supervised by

Dr. Raquel Verdejo Márquez

Dr. Miguel Ángel López Manchado

INSTITUTO DE CIENCIA Y TECNOLOGÍA DE POLÍMEROS

Valencia – May 2012

A la meua familia

AGRADECIMIENTOS

Quisiera agradecer, en primer lugar, al Ministerio de Ciencia e Investigación por la financiación para la realización de esta Tesis, mediante la concesión de la Beca FPI.

A mis directores de Tesis, Dra. Raquel Verdejo y Dr. Miguel Ángel López Manchado por darme la oportunidad de trabajar con vosotros. A Raquel, por todo lo que me has enseñado durante estos años y por todo el tiempo que me has dedicado. A Miguel Ángel por tus comentarios constructivos, tus consejos y tu paciencia.

A mi tutor en la UPV, Prof. Vicente Amigò por toda la ayuda que me has brindado sin apenas conocerme.

Al Prof. Miguel Ángel Rodríguez Pérez de la Universidad de Valladolid por darme la posibilidad de trabajar en tu grupo y aprender más sobre espumas.

I would like to thank Prof. Anthony J. Ryan, from The University of Sheffield, and Prof. Isabelle Huynen, from Université Catholique de Louvain, for your support and interest on my work.

A todos mis compañeros del grupo por todos los ánimos y las risas. A Mario, Lean, Laura Peponi, Nicoletta, Iván y Sami. A mis chicas, Nella, Nat y Lauris, por todos los buenos momentos juntas entre recetas de cocina, clases de punto y bailes Bollywood! Quiero agradecer especialmente a Nella por ser mi profesora de la vida durante estos años y por las largas tardes-noches compartidas en la oficina. Y a Mario, nuestro “chico guapo” por todo el apoyo y por esas “características limitantes” que nos unen.

A todo el grupo de Cauchos, en especial a Juan, Irene, Marta y Pilar, por ser como sois y por todas esas celebraciones en el laboratorio con vino, callos, migas y pasteles. Y a Miguel Arroyo, por esas paellas “madrileñas” que me hacen sentir como en casa.

A Rodri, Jose e Isabel Quijada por haberme dejado participar en vuestros trabajos, por todo lo que he aprendido con vosotros y por haber confiado en mí.

Al grupo del CellMat de la Universidad de Valladolid por haberme acogido tan bien durante las semanas que he estado con vosotros. En especial a Samu, Sergio y a Eusebio por vuestra colaboración en mis experimentos de radioscopia y DMA.

I would like to thank my dear friends Masa, AC and Susi, for our great times in Sheffield.

A special thanks to Isabel and Margherita for taking care of me during those hard months in Louvain-la-Neuve and for your friendship. Grazie Margheri per le nostre pause caffè e tutti gli scherzi!

A todos mis amigos que me habéis apoyado durante este tiempo y, aunque en "la terreta" siempre os he tenido cerca. Y gracias a todas las personas que me han ayudado durante estos años.

A la meua familia per ser el meu tresor. Als meus papis, Enrique i Amparo per tot el carinyo i per estar sempre quan vos he necessitat. A les meues germanes, Pilar i Amparo, per totes les hores de telèfon, les rises i els nostres viatges per Europa. Als meus germans, Pedro i Quique, per tots els ànims i per cuidar tant de mi. Gràcies family!

“I Still Haven't Found What I'm Looking For”

U2, 1987

ABSTRACT

Polymer nanocomposite foams have drawn a great deal of interest in scientific and technological areas. The reason is the combination of the excellent properties of nanoparticles with the foam technology, leading to the development of multifunctional and lightweight materials. These nanocomposite systems can find high performance applications as diverse as scaffolds for tissue engineering, electromagnetic interference shields, multifunctional structural panels and packages, among others.

This Thesis aims to develop flexible and rigid polyurethane nanocomposite foams filled with carbon-based nanofillers with interesting physical properties. The initial part of the work is focused on the synthesis and functionalisation of carbon nanoparticles (multi-walled carbon nanotubes (MWCNTs), functionalised MWCNTs and functionalised graphene sheets (FGS)) to establish the best possible filler to attain the desired properties on the nanocomposite foams. However, the work not only focuses on the effect of nanofillers on the physical properties but also on the process of polymerisation and foaming, since they strongly influence the final characteristics of polyurethane foams. Finally, thermal, mechanical and electrical characterisations were performed in order to confirm the effect of carbon nanoparticles on the properties of polyurethane foams.

RESUMEN

Las espumas de nanocompuestos poliméricos tienen un gran interés tanto en áreas tecnológicas como científicas. Esto es debido a la combinación de las excelentes propiedades de las nanopartículas y la tecnología de espumado, dando lugar al desarrollo de materiales ligeros y multifuncionales. Este tipo de sistemas se utilizan en aplicaciones de alto rendimiento tan diversas como biomedicina, electrónica, paneles estructurales y embalajes, entre otras.

Esta Tesis está basada en el desarrollo de espumas de nanocompuestos de poliuretano flexibles y rígidas con interesantes propiedades físicas. La parte inicial de este trabajo está enfocada en la síntesis y funcionalización de nanopartículas de carbono (nanotubos de carbono de pared múltiple (MWCNTs), MWCNTs funcionalizados y láminas de grafeno funcionalizadas (FGS)) para poder determinar cuál es la mejor carga para obtener las propiedades deseadas en las espumas de nanocompuestos. Sin embargo, este trabajo no se centra únicamente en el efecto de las nanocargas en las propiedades físicas, sino también en el proceso de polimerización y espumado, debido a que este tipo de nanopartículas tienen una fuerte influencia en las características finales de las espumas de poliuretano. Finalmente, los materiales desarrollados se caracterizaron térmica, mecánica y eléctricamente con el fin de confirmar el efecto de las nanopartículas de carbono en las espumas de poliuretano.

RESUM

Les escumes de nanocompostos polimèrics tenen un gran interés tant en àrees tecnològiques com científiques. Aquest fet es degut a la combinació de les excel·lents propietats de les nanopartícules i la tecnologia del escumat, el que dóna lloc al desenvolupament de materials lleugers i multifuncionals. Aquest tipus de sistemes s'utilitzen en aplicacions de alt rendiment tan diverses com biomedicina, electrònica, panells estructurals i embalatge, entre altres.

Aquesta Tesis es basa en el desenvolupament de les escumes de nanocompostos de poliuretà flexibles i rígides amb interesants propietats físiques. La part inicial d'aquest treball està centrada en la síntesis i funcionalització de les nanopartícules de carboni (MWCNTs, MWCNTs funcionalitzats i làmines de grafè funcionalitzades) per poder determinar quina és la millor càrrega per a obtindre les propietats desitjades en les escumes de nanocompostos. No obstant això, el treball no està concentrat únicament en l'efecte de les nanocàrregues en les propietats físiques, si no també en el procés de polimerització i escumat, ja que tenen una gran influència en les característiques finals de les escumes de poliuretà. Finalment, les caracteritzacions tèrmiques, mecàniques i elèctriques es van portar a terme amb el fi de confirmar l'efecte de les nanopartícules de carboni en les propietats de les escumes de poliuretà.

Table of Contents

LIST OF FIGURES

LIST OF TABLES

1. INTRODUCTION

Nanoscience has been widely described as the study of nanoscale materials that finds applications in the real world. Nowadays, this science has received increasing attention because it encloses the production and application of new systems, devices and materials at nanometer scale. In general, nanomaterials can be classified into nanostructured materials and nanophase/nanoparticle materials. Nanoscale materials present unique properties producing novel systems with excellent characteristics by themselves or in combination with macroscopic systems. In the area of nanoscience, nanocomposites have aroused great interest due to its potential in a broad range of applications. Nanocomposites are materials where at least one of the constituent phases falls into the nanometer scale. The study of nanocomposites, at a scientific and technological level, opens up the challenge of developing exceptional materials that could find applications in areas as diverse as material science, medicine, biotechnology and nanoelectronic. [1, 2]

Polymer science and technology play an important role in our daily life due to their advantages over conventional materials (wood, ceramics or metals). The main properties of polymeric materials are related to their lightness, flexibility, transparency, corrosion resistance, low cost of production and ease processing. Despite of these good properties, polymer materials do not achieve the strength and high modulus of metals and ceramics. Traditionally, the inclusion of fillers has been used to improve the properties of polymeric systems maintaining the characteristics mentioned above. However, the use of microsized particles required large quantities reducing the weight and processability characteristics of the matrix. Thus, over recent years a number of attempts have been made to produce nanoparticle-based composites stimulated by the potential achievable

properties without sacrificing the polymer processability or adding excessive weight. Nonetheless, this work is still ongoing and the interactions nanoparticle-polymer matrix and their resultant effects are still unclear. [3-7]

On the field of polymer nanocomposite materials, the reinforcement of delicate systems, such as polymer films, fibres or foams, where conventional fillers cannot be physically accommodated offers unique opportunities. [8, 9] In particular, polymer nanocomposite foams have initially shown some promising results. [8-10] Nevertheless, fundamental questions remain to be answered concerning the influence of nanoparticles on the foaming process, the resulting cellular structure and final properties of polymeric foams.

Polyurethane (PU) foams are one of the most versatile polymeric materials because they can be formulated to meet specific requirements and, hence, are used in diverse applications. [11] PU foams are essentially produced by two exothermic reactions between the isocyanate with the hydrogen-active groups of polyol and water. The reaction between the isocyanate and the polyol is called the *gelling reaction* and forms urethane linkages leading to an increase in the molecular weight. The *blowing reaction*, produced between the isocyanate and water, forms urea hard segments (HS) and carbon dioxide gas. [12] A segmented block copoly(urethane-urea) is then the result of these two reactions, where the urea hard segment groups are covalently bonded to the polyol soft segments (SS) through urethane linkages. The phase-separated morphology of PU foams and the ratio of HS/SS have a profound effect on the final properties of the system. Although PU foams have successfully been employed in a number of markets, their expansion within existing markets or into new markets often has been impeded by certain limiting characteristics, such as their electrical conductivity. Hence, the introduction of nanoparticles in PU foams promises added value properties through the formation of a reinforced cellular structure.

Among the different nanoparticles, carbon nanotubes (CNTs) and graphene have attracted particular interest because of their remarkable mechanical and electrical properties and low density setting them as ideal candidates for high performance polymer composites. [4, 13]

Carbon nanotubes are cylindrical shells of one or more co-axial graphitic sheets, with diameters in the range 1-100 nm, and lengths typically on the order of tens of microns. Individual carbon nanotubes have been predicted and observed to have unique properties: axial stiffness and strength are of the order of 1 TPa and 50 GPa, respectively, and densities are low (less than 2 $g \cdot cm^{-3}$). A variety of synthesis methods exists to produce carbon nanotubes that lead to a wide range of structural differences, such as their aspect ratio, crystallinity, purity, and entanglement, among others. [14, 15]

Graphene is a one-atom-thick planar sheet of sp^2-bonded carbon atoms arranged in a honeycomb structure. In 2004, Andre Geim and Konstantin Novoselov, Nobel Prize in Physics 2010, synthesised graphene from graphite by the so-called "scotch tape" or peel off method or micromechanical cleavage. [16, 17] Current strategies use traditional chemical processes [18-20] to produce graphene sheets, eventually functionalised, and have opened new opportunities for this carbon allotrope.

1.1. OVERVIEW OF THE THESIS

1.1.1. Motivation

Research on nanocomposite materials has been pursued with the aim of exploiting the inherent properties of nanoscaled materials to produce both structural and multifunctional systems with improved performance. The challenge and interest in this research area are to find ways to transfer efficiently the unique physical and mechanical properties of very small objects to the macroscopic components. Research on polymer nanocomposites has recently resulted in the development of multifunctional, high performance systems. [1, 4, 5] Meanwhile, research on carbon nanoparticles (CNPs), in particular, CNTs and graphene, in the last decades, has focused on their exceptional mechanical, thermal and mainly electrical properties. The mechanisms used to synthesise CNTs and graphene play a key role on the structure of these CNPs and hence on their characteristics and later applications. [15, 21]

Polymeric foams, in particular PU foams, have widespread applications in diverse areas because they can be formulated to meet specific requirements depending on their nature, flexible or rigid. [11, 22] Nowadays, polymer nanocomposite foams are receiving increasing attention due to the combination of the foam technology and the properties of the nanoparticles, generating multifunctional and lightweight materials that can find interesting appliances. [8, 9]

1.1.2. Challenges

The problems normally encountered on the development of polymer nanocomposites are related to three aspects:

- The synthesis of the CNPs with the required characteristics.
- The optimum dispersion of the CNPs in the polymer matrix.
- The effective properties transfer between the nanoparticles and the matrix.

1.2. OBJECTIVES

The aim of this thesis is to develop polyurethane foams filled with carbon-based nanoparticles with improved properties. Therefore, the specific objectives are:

- Synthesis and characterisation of different multi-walled carbon nanotubes (MWCNTs) adjusting the parameters of the growth method in order to select the best synthesis to be used in the study.
- Functionalisation and characterisation of the selected MWCNTs.
- Synthesis and characterisation of functionalised graphene sheets (FGS).

- Preparation of water-blown flexible PU foams filled with the CNPs following the next steps:
  - Study of the dispersion of the CNPs on the polyol
  - Study of the copolymer matrix morphology on the kinetics of polymerisation and foaming and the effect of the inclusion of CNPs
  - Characterisation of the physical properties of the nanocomposites
- Preparation of water-blown rigid PU foams with the CNPs:
  - Study of the dispersion of the CNPs on the polyol
  - Study of the inclusion of CNPs on the foaming process
  - Characterisation of the physical properties of the foam nanocomposites

1.3. STRUCTURE OF THE THESIS

This thesis is organised into six chapters in order to clearly lay out the research developed on CNPs and PU nanocomposite foams. It is worth noting that graphene is used for the first time in water-blown PU foams.

Chapter 2 presents the state of the art on polyurethane foams, CNPs and polyurethane nanocomposite foams.

The method employed to obtain CNPs has an important impact on the properties of these nanoparticles. *Chapter 3* describes the synthesis and characterisation of different MWCNTs by changing some parameters on the growth method. The MWCNTs with the best characteristics are then selected to be added to the polymer nanocomposite. The as-synthesised MWCNTs are functionalised, using an oxidative method, to facilitate the later dispersion on the polymer. A comparison between the pristine MWCNTs and functionalised MWCNTs (f-MWCNTs) is carried out by characterising the nanofillers. In addition, the

synthesis and characterisation of functionalised graphene sheets (FGS) are presented.

Chapter 4 details the preparation and characterisation of water-blown flexible polyurethane nanocomposite foams with two different segmented matrix morphologies and filled with the CNPs synthesised in Chapter 3. Two sets of flexible polyurethane foams varying the content of hard segment on the formulation are investigated to understand the changes of the polymer morphology on the kinetics of polymerisation and foaming and hence on the final properties of these systems. First, the rheological behaviour of the dispersions of polyol/CNPs is studied to control the quality of the dispersion that can affect the later process of foaming. Then, the polymerisation and foaming evolution of flexible PU nanocomposite foams are studied by spectroscopy techniques. The chapter ends with the measurement of the final properties of the two sets of flexible nanocomposite foams.

Chapter 5 investigates the effects of CNPs in rigid polyurethane foams. The CNPs are dispersed in the polyol of rigid PU foams and the rheological behaviour of these dispersions is analysed. After that, the kinetics of polymerisation of rigid PU nanocomposite foams are followed by adiabatic temperature rise and the mechanical, thermal and electrical properties are measured for the synthesised nanocomposites.

In *Chapter 6* general conclusions and suggestions for continuation of this research are given.

1. INTRODUCCIÓN

La nanociencia ha sido ampliamente descrita como el estudio de materiales a escala nanométrica que presentan aplicaciones en el mundo real. En la actualidad, esta ciencia está recibiendo una mayor atención porque engloba la producción y aplicación de nuevos sistemas, equipos y materiales a escala nanométrica. Generalmente, los nanomateriales se pueden clasificar en materiales nanoestructurados y materiales nanofase/nanopartícula. Dichos materiales presentan propiedades únicas produciendo sistemas novedosos con excelentes características propias o en combinación con sistemas macroscópicos. En el área de la nanociencia, los nanocompuestos han suscitado un gran interés debido a su potencial en un amplio rango de aplicaciones. Los nanocompuestos son materiales donde al menos una de las fases constituyentes pertenece a la escala nanométrica. El estudio de los nanocompuestos, a nivel científico y tecnológico, abriría el desarrollo de materiales excepcionales con aplicaciones en áreas tan diversas como medicina, biotecnología y nanoelectrónica. [1, 2]

La ciencia y tecnología de polímeros juegan un papel importante en nuestra vida diaria debido a sus ventajas frente a los materiales convencionales (madera, cerámicos o metales). Las principales propiedades de los materiales poliméricos están relacionadas con su ligereza, flexibilidad, trasparencia, resistencia a la corrosión, bajo coste de producción y fácil procesado. A pesar de estas buenas propiedades, los materiales poliméricos no alcanzan los esfuerzos y altos módulos de los metales y cerámicos. Tradicionalmente, se han empleado cargas para mejorar ciertas propiedades de los sistemas poliméricos manteniendo las mencionadas características. Sin embargo, la adición de partículas micrométricas como refuerzo en materiales poliméricos requiere el uso de grandes cantidades, reduciendo así la ligereza y procesabilidad características de la matriz polimérica.

Por tanto, en los últimos años se ha realizado un gran número de tentativas para producir materiales compuestos basados en nanopartículas, debido a las potenciales propiedades que pueden conseguirse incluso a bajas concentraciones de carga, sin por ello, sacrificar la procesabilidad del polímero. No obstante, este trabajo está todavía en curso y las interacciones nanopartícula-polímero y sus efectos aún no están claros. [3-7]

En el campo de los materiales nanocompuestos, el reforzamiento de sistemas finos, como películas delgadas, fibras o espumas poliméricas, donde las cargas convencionales no pueden acomodarse físicamente, ofrece grandes posibilidades. [8, 9] En particular, las espumas de nanocompuestos poliméricos han mostrado unos resultados iniciales prometedores. [8-10] A pesar de ello, cuestiones fundamentales relacionadas con la influencia de las nanopartículas en el proceso de espumado, la estructura celular resultante y las propiedades de las espumas poliméricas, permanecen todavía sin responder.

Las espumas de poliuretano (PU) son uno de los materiales poliméricos más versátiles debido a que se pueden formular para alcanzar unos requerimientos específicos y, por tanto, ser usadas en distintas aplicaciones. [11, 22] Las espumas de PU se producen fundamentalmente mediante dos reacciones exotérmicas entre el grupo isocianato con los grupos activos de hidrógeno del poliol y del agua. La reacción entre el isocianato y el poliol, llamada *reacción de gelificación*, forma enlaces uretano dando lugar a un incremento en el peso molecular. La *reacción de espumado*, se produce entre el isocianato y el agua, formando segmentos duros de urea y dióxido de carbono. [12] Como resultado de estas reacciones se forma un copolímero de bloque segmentado uretano-urea, donde los segmentos duros de urea están covalentemente unidos a los segmentos blandos de poliol mediante enlaces uretano. La morfología de fases separadas de las espumas de PU y la relación entre segmentos duros y blandos tienen un efecto significativo en las propiedades finales del sistema. A pesar de que las espumas de PU se han empleado con éxito en un gran número de mercados, su expansión se ve dificultada dentro de los mercados existentes o en nuevos, por ciertas características limitantes, como por ejemplo su conductividad eléctrica. Por tanto, la adición de nanopartículas en las espumas de PU proporciona un valor añadido a

las propiedades de la espuma mediante la formación de estructuras celulares reforzadas.

Entre las diferentes nanopartículas existentes, los nanotubos de carbono (CNTs) y los grafenos han atraído un particular interés debido a sus peculiares características, tales como excelentes propiedades mecánicas, térmicas y eléctricas así como una relativa baja densidad, lo que les convierten en candidatos ideales para la producción de materiales compuestos poliméricos de altas prestaciones. [4, 13]

Los nanotubos de carbono son estructuras cilíndricas de una o más láminas grafíticas coaxiales, con diámetros en el rango de 1-100 nm, y longitudes normalmente en el orden de decenas de micras. Los nanotubos de carbono individuales poseen excelentes propiedades. Su esfuerzo y rigidez axial están en el orden de 50 GPa y 1 TPa respectivamente, y presentan bajas densidades (menores de 2 $g \cdot cm^{-3}$). Existe una gran variedad de métodos de síntesis para producir nanotubos de carbono, dando lugar, por tanto a diferencias estructurales en cuanto: relación de aspecto, cristalinidad, pureza y enmarañamiento, entre otras. [14, 15]

El grafeno es una monocapa de átomos de carbono de un átomo de espesor empaquetados en una estructura hexagonal compacta a partir de la superposición de los hibridos sp^2 de los carbonos enlazados. Este material, se sintetizó por primera vez en el año 2004 mediante la denominada *"técnica de la cinta adhesiva"*, también llamada exfoliación o rotura micromecánica del grafito, por los investigadores Andre Geim y Konstantin Novoselov, quiénes recibieron el Premio Nobel de Física en el 2010. [16, 17] Las estrategias de síntesis actuales usan procesos químicos tradicionales [18-20] para producir láminas de grafeno, eventualmente funcionalizadas, y han abierto nuevas oportunidades para estos alótropos del carbono.

1.1. VISIÓN GENERAL DE LA TESIS

1.1.1. Motivación

La investigación en materiales nanocompuestos ha sido emprendida con el objetivo de explotar las propiedades inherentes de los materiales a escala nanométrica para producir tanto sistemas estructurales como multifuncionales con características optimizadas. El reto e interés en este área de investigación es encontrar el modo de transferir eficientemente las excelentes propiedades físicas y mecánicas de objetos a escala nanométrica a componentes macroscópicos. La investigación en nanocompuestos poliméricos ha llevado recientemente al desarrollo de sistemas multifuncionales de altas prestaciones. [1, 4, 5] Mientras tanto, la investigación en nanopartículas de carbono, en particular, nanotubos de carbono y grafeno, en los últimos años, se ha centrado en sus excepcionales propiedades mecánicas, térmicas y principalmente eléctricas. Los mecanismos usados para sintetizar CNTs y grafenos juegan un papel importante en la estructura de estas CNPs y por tanto, en sus características y posteriores aplicaciones. [15, 21]

Las espumas poliméricas, en particular las espumas de PU, presentan una gran variedad de aplicaciones en diversas áreas debido a que se pueden formular *"a medida"* para satisfacer necesidades específicas en función de su naturaleza, flexible o rígida. [11, 22] Actualmente, las espumas de nanocompuestos poliméricos están recibiendo una creciente atención ya que combinan la tecnología de las espumas con las propiedades de las nanopartículas, generando materiales ligeros y multifuncionales con interesantes aplicaciones. [8, 9]

1.1.2. Retos

Los problemas encontrados normalmente en el desarrollo de nanocompuestos poliméricos están relacionados en tres aspectos:

- Síntesis de las CNPs con las características requeridas.
- Optimización de la dispersión de las CNPs en la matriz polimérica.
- Transferencia efectiva de propiedades entre las nanopartículas y la matriz.

1.2. OBJETIVOS

El objetivo global de esta tesis es el desarrollo de espumas de poliuretano cargadas con nanopartículas de carbono con propiedades mejoradas. Para ello se hace necesario profundizar en los siguientes objetivos específicos:

- Síntesis y caracterización de diferentes nanotubos de carbono de pared múltiple (MWCNTs) ajustando los parámetros del método de crecimiento para seleccionar la síntesis más idónea que se usará posteriormente.
- Funcionalización y caracterización de los MWCNTs producidos mediante el método de síntesis seleccionado previamente.
- Síntesis y caracterización de láminas de grafeno funcionalizadas (FGS).
- Desarrollo de espumas flexibles de PU mediante espumado con agua, cargadas con CNPs mediante los siguientes pasos:
  - Estudio de la dispersión de las CNPs en el poliol.
  - Estudio de la morfología de la matriz copolimérica durante la cinética de polimerización y el espumado y el efecto de la adición de las CNPs.
  - Caracterización de las propiedades físicas y mecánicas de los nanocompuestos.

- Preparación de las espumas rígidas de PU con las CNPs:
  - Estudio de la dispersión de las CNPs en el poliol.
  - Estudio de la adición de CNPs en la morfología y en el proceso de espumado.
  - Caracterización de las propiedades físicas y mecánicas de las espumas de nanocompuestos.

1.3. ESTRUCTURA DE LA TESIS

Esta tesis está organizada en seis capítulos para poder clarificar la investigación desarrollada en CNPs y espumas de nanocompuestos de PU. Cabe destacar que este es el primer estudio donde se emplea el grafeno como carga en espumas de PU.

El *Capítulo 2* presenta el estado del arte en espumas de poliuretano, CNPs y espumas de nanocompuestos de poliuretano.

El método empleado para obtener CNPs tiene un impacto importante en las propiedades de estas nanopartículas. El *Capítulo 3* describe la síntesis y caracterización de las CNPs empleadas a lo largo del estudio. Se analiza el método más idóneo para la síntesis de nanotubos de carbono de pared múltiple (MWCNTs) por deposición química en fase de vapor variando algunos parámetros del proceso. Los MWCNTs seleccionados se funcionalizan usando un método oxidativo, para mejorar la compatibilidad y facilitar su dispersión en el polímero. Se lleva a cabo una exhaustiva caracterización de los MWCNTs crudos y funcionalizados (f-MWCNTs) por diferentes técnicas microscópicas, espectroscópicas y térmicas. Además, se presenta la síntesis y caracterización de las láminas de grafeno funcionalizadas (FGS).

El *Capítulo 4* detalla la preparación y caracterización de las espumas flexibles de nanocompuestos de poliuretano mediante espumado con agua con dos morfologías de matriz segmentada diferentes y con las CNPs sintetizadas en el Capítulo 3. Se estudian dos series de espumas de poliuretano flexibles, variando el contenido de segmento duro (25 y 32.5 %), para entender los cambios en la morfología del polímero, en las cinéticas de polimerización y espumado y por

tanto, en las propiedades finales de estos sistemas. Dado que la calidad de la dispersión de las CNPs puede afectar al posterior proceso de espumado, resulta necesario realizar un estudio previo del comportamiento reológico de las dispersiones poliol/CNP. Seguidamente, se estudia la polimerización y evolución del espumado *in-situ* de las espumas flexibles de PU reforzadas con CNPs mediante técnicas de espectroscopia para relacionar la microestructura de estos materiales con sus propiedades macroscópicas. Por último, se analizan las propiedades mecánicas, térmicas y eléctricas de las dos series de espumas flexibles y sus nanocompuestos.

El *Capítulo 5* investiga los efectos de las CNPs en las espumas rígidas de poliuretano. Las CNPs se dispersan en el poliol de las espumas rígidas de PU y se analiza el comportamiento reológico de estas dispersiones. A continuación, se efectúa un seguimiento de la cinética de polimerización de las espumas rígidas de PU mediante el aumento de la temperatura adiabática durante la reacción y se analiza el efecto de las CNPs en la morfología y en las propiedades mecánicas, térmicas y eléctricas de las espumas rígidas de PU.

En el *Capítulo 6* se presentan las conclusiones generales y las sugerencias para continuar con la línea de investigación.

2. LITERATURE REVIEW

Polymeric foams are used in applications such as cushioning for furniture and automobiles, thermal insulation for construction and packaging, shock- and sound absorbing applications, and scaffolds for cell attachment and growth. [11, 22, 23] These systems are formed by gas bubbles, derived from a blowing agent, which are trapped in a solid polymer matrix. There may be more than one solid present, as in the case of a blend of polymers or fillers, which may be of inorganic origin, i.e. glass, ceramic and metal, or organic nature such as carbon based fillers. However, not all polymers can be foamed and some factors have to be considered: compatibility with gas, processing window, stability during gas replacement by air and capability to hold dynamic foaming. [11, 22] In general, polymeric foams can be viewed from different practical points of view that are summarised in Table 2.1.

Table 2.1. Foaming aspects. [22]

Aspects	Technology
Material	Thermoplastic and thermoset
Mechanism	Physical foaming and chemical foaming
Nature	Flexible and rigid
Structure	Closed-cell and open-cell
Cell size	Microcellular and cellular
Density	High density and low density
Dimension	Board and thin sheet

The formation of the cellular structure in polymeric foams can be obtained by foaming a polymer system using blowing agents (BAs), by introducing gas-filled microspheres into a system or by extracting dissolved filler by means of a post-treatment. Nevertheless, the foaming method is the most employed in the polymeric foam industry and depending on the mechanism by which gas is liberated, it can be classified in: physical and chemical processes (Figure 2.1). [11, 24]

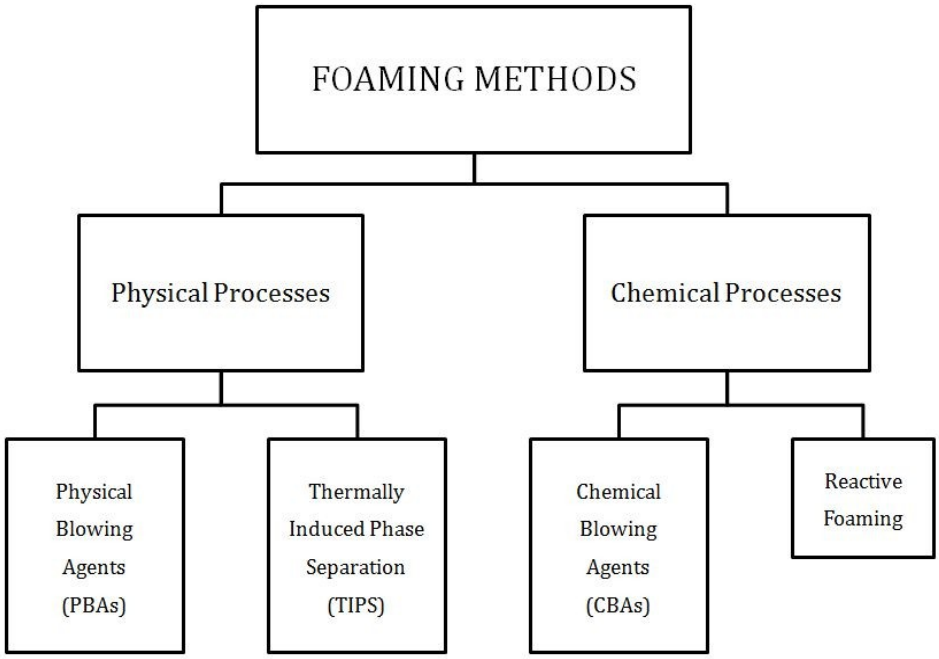

Figure 2.1. Schematic overview of foaming methods.

Physical Process

This foaming method consist on the use of physical blowing agents (PBAs) which are compounds that liberate gases as a result of physical processes (evaporation, desorption) at elevated temperatures or reduced pressures. Blowing agents of this type are supercritical gases; low-boiling volatile liquids, such as aliphatic and halogenated hydrocarbons; low-boiling alcohols such as ethers, ketones, aromatic hydrocarbons; and solid adsorbents saturated with gases or low-boiling liquids.

In the foaming mechanism of PBAs, the blowing agent (such as nitrogen, CO_2 and halogenated hydrocarbons) is introduced in the polymer system, usually by pressurisation, to form a homogeneous dispersion. When a pressure reduction or a temperature increase is applied for enough supersaturation, gas starts to form nuclei and expands due to heat or pressure reduction, or by the combination (coalescence) of two or more bubbles. [11, 22]

Another physical foam method is the thermally induced phase separation (TIPS) which is based on the thermodynamic and kinetic behaviour of a polymer solution. In this technique, the solvent can induce phase separation due to the variation of temperature of the polymer solution, which goes through a solid-liquid phase separation. Once the solvent is extracted and depending on the phase separation conditions, the foams obtained present different morphologies and characteristics. [25, 26]

Chemical Process

This foaming method is based on the use of chemical blowing agents (CBAs) which are individual or mixtures of compounds that liberate gas as a result of chemical reactions, including thermal decomposition and interactions between CBAs with other components of the formulation. The vast majority of CBAs are solids (inorganic or organic compounds) but some liquids are also employed. [11] These CBAs present the advantage of being easily introduced into the system to be foamed and can be processed with common equipment.

A second chemical process is the so called reactive foaming and it is typical for systems such as polyurethane (PU), silicone and polyisocyanurate; being PU foams the largest market among polymeric foams. Reactive foaming is a complex process which involves the formation of gas bubbles in a fluid or nucleation and the evolution of both liquid and gas until stabilisation occurs. This process involves the simultaneous foaming and polymerisation of liquid reactants, presenting a liquid-solid phase transition. The foaming is driven by a gas generated as a by-product of the polymerisation reaction. This reaction has to be well controlled in order to balance the rates of both the evolution of the gas and the increase in viscosity if not, the foam will collapse. [27] This spatial and temporal evolution

involves the interplay of several physical phenomena such as surface tension, diffusion and viscosity. One practical way to improve the stability of reactive foams is to increase the bulk viscosity of the reactants or the surface viscosity of the gas-liquid interface through a colloidal suspension of solid particles. [23]

2.1. WATER-BLOWN POLYURETHANE FOAMS

Polyurethanes (PUs) are one of the most versatile polymeric materials with the unique advantage of producing a wide variety of high-performance materials depending on their chemistry. The polymerisation of PUs involves several chemical reactions and the formation of different chemical bonds. Nonetheless, the most important reaction is produced between isocyanate (NCO) groups with polyol molecules, which form urethane linkages, leading to a phase-separated morphology. As it will be discussed in the next section, the two-phase morphology formed by hard and soft segments, strongly influences the final physical and mechanical properties of PUs. [28, 29]

One of the main markets of the PU industry is in the area of foams which can be manufactured in a large range of density and stiffness and hence they can be used in a broad range of appliances. [11, 22] PU foams can be classified as flexible, rigid and semi-rigid foams, depending on their degree of cross-linking and the cell structure. [22, 29, 30]

2.1.1. Basics of Chemistry

The water-blown PU foam chemistry is based on the reaction between isocyanates with active hydrogen containing compounds, in particular hydroxyl end groups of long polyether or polyester chains (*polymerisation reaction*) and water (*blowing reaction*). [11, 22, 31, 32] These two simultaneous reactions must be controlled in order to obtain the desired cellular structure and physical properties.

The polymerisation reaction between an isocyanate group and an alcohol functionality of the polyol, often termed the *gelling reaction* (Figure 2.2), forms urethane linkages, leading to an increase in the molecular weight. The nature of *R* and *R'* groups can vary depending on the isocyanate and polyol used in the formulation, resulting in a cross-linked polymer. This reaction is exothermic and it is reported a total heat release of approximately 24 kcal/mol of urethane formed. [22]

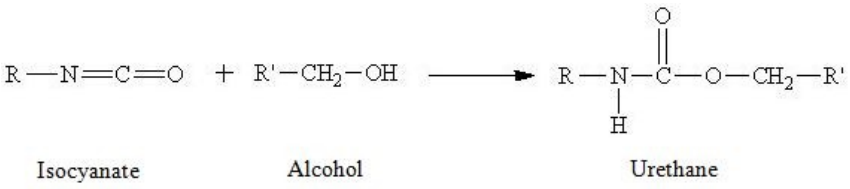

Figure 2.2. The gelling reaction.

On the other hand, the reaction of isocyanate with water is known as the *blowing reaction* (Figure 2.3), and forms urea hard segments and carbon dioxide (CO_2) gas from the decomposition of an unstable carbamic acid. [33] The overall reaction is exothermic with a reaction heat of 45-47 kcal/mol of reacted water. [22] The nature of *R* and *R'* in the isocyanate and amine compounds influences the formation of the hard segments and can produced cross-linking points if the functionality of the molecules is greater than two.

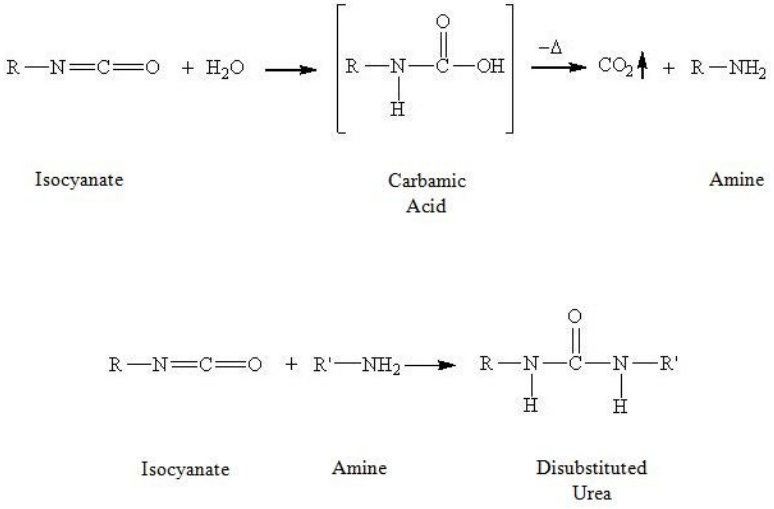

Figure 2.3. The blowing reaction.

Besides of these two primary reactions, other secondary reactions occur in water-blown PU foams with the products of the primary reactions. The main sub-products obtained are: biuret, allophanate, isocyanaurate and carbodiimide among others. [22, 31, 34]

As a result of the two main concurrent reactions a cross-linked network of a segmented block copoly(urethane-urea) is blown into a cellular structure by the evolved CO_2 and entrapped air. This reactive process provides PU foams with a structured morphology stretching over several length scales, from the macroscopic cellular structure to the microdomains of the segregated urea hard segments and the polyol soft segments joined by urethane covalent bonds (Figure 2.4), as will be explained later. [10]

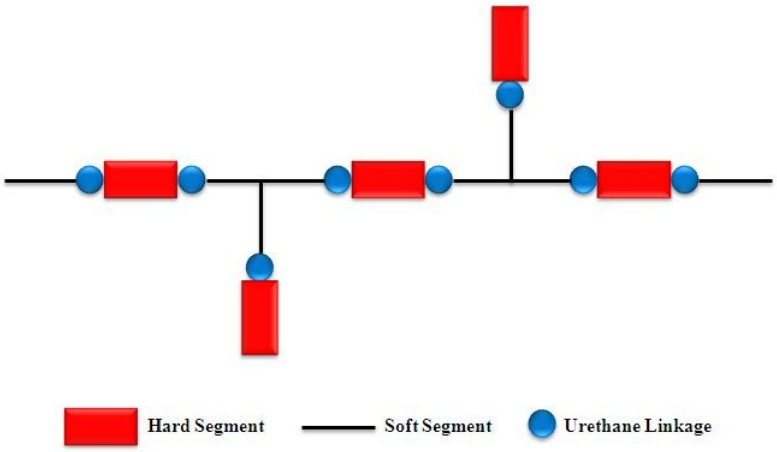

Figure 2.4. Diagram showing the segmented block poly(urethane-urea) copolymer microdomains in polyurethanes.

2.1.2. Foam Components

In general, water-blown PU foam formulations include many ingredients, depending on the desired grade of foam. Table 2.2 summarises the most common formulations for water-blown PU foams, flexible and rigid, in parts by hundred parts of polyol (phpp). The main components of the formulation will be further discussed.

Table 2.2. Formulation of water-blown flexible and rigid PU foam in phpp. [22, 35]

Component	Flexible PU foam	Rigid PU foam
Polyol	100	100
Isocyanate	25 - 85	Stoichiometric + 5 %
Water (CBAs)	1.5 - 7.5	0 - 3.0
Gelling Catalyst	0.0 - 0.5	-
Blowing Catalyst	0.1 - 1.0	0 - 0.9
Surfactant	0.5 - 2.5	0 - 2.0
Additive	Variable	Variable
Chain Extender	0 - 10	0 - 30
Cross-linker	0 - 5	-

Polyol

The polyol is a source of hydroxyl groups which mainly react with the isocyanate groups to form urethane linkages. The choice of the starting polyol structure influences the processing and properties of the final foam. Polyols used for the production of PU foams may be polyether and polyester polyols, being polyether polyols the most commonly used because they provide the largest variety of possible molecular structures as far as hydroxyl functionality. Table 2.3 lists the general characteristics of the polyols used for flexible and rigid PU foams. It is worth noting that polyols employed for rigid foams have higher functionality due to the requirement of high stiffness of the final foams which can only be achieved by means of high number of cross-links and urea precipitation. [11, 22]

Table 2.3. Characteristics of polyols used for PU foams. [36, 37]

Polyol property	Flexible Foam	Rigid Foam
OH number (mg KOH·g^{-1})	5.6 - 7.0	350 - 560
Functionality	2.0 - 3.0	3.0 - 8.0
Molecular weight	500 - 6500	70 - 800

Isocyanate

The isocyanate provides the NCO groups to react with functional groups from the polyol, water and other components on the formulation. The isocyanates used in the production of PU foams contain at least two NCO groups per molecule and are mainly aromatic isocyanates because of their higher reactivity. In flexible foams the isocyanate is based on toluene diisocyanate (TDI) while for rigid foams polymeric isocyanates of the diphenylmethanate diisocyanate (MDI) are generally employed. Nevertheless, the use of TDI is limited because of its hazardous characteristics and is substituted in flexible foams by polymeric MDI or prepolymers, which are liquid intermediates between the monomers and a final polymer. [11, 22]

In PU foams formulation, there is a parameter, called the isocyanate index, which has a pronounced effect on the hardness of the final foam. The isocyanate index is defined as the amount of isocyanate required to react with polyol and other reactive components of the formulation with respect to the theoretical amount of isocyanate and is calculated following equation (2.1):

$$Isocyanate\ Index = \frac{actual\ amount\ of\ isocyanate\ used}{theoretical\ amount\ of\ isocyanate\ required} \times 100 \qquad (2.1)$$

Flexible polyurethane foaming is usually carried out at an index from 85 to 110 while for rigid polyurethane foaming it is in the range of 105 - 120, which implies a NCO excess of 5-20 %.

Water

Water is added to the PU foam formulations to react with isocyanate to give CO_2 gas and polyurea molecules. Hence, it acts as a chemical blowing agent and contributes to the physical properties of the final foams.

Catalysts

There are two main catalysts used in formulations of flexible and rigid PU foams that catalyse the main reactions: polymerisation and blowing. [32, 34]

The polymerisation reaction between the isocyanate and the polyol is strongly promoted by organometallic compounds. These catalysts act as Lewis acids interacting with the basic sites of isocyanate and polyol. Generally, these metal catalysts are tin compounds and are usually employed in small quantities in flexible PU foams while they are not often used in rigid PU foams.

The main catalysts used for the blowing reaction are amine compounds, which also contribute in the polymerisation reaction. Their catalytic activity is related to their strength as a base and on the steric availability of the free electron pair on the nitrogen atom. Tertiary amines are the most employed in both flexible and rigid PU foams.

Other catalysts can be used in the production of PU foams: delayed action and nonfugitive catalysts. The former balances foam reactivities while the later reduces amine emissions.

Surfactants

Surfactants are substances that lower the surface tension of the foam, helping to stabilise the rising foam by reducing stress concentrations in thinning cell walls. Furthermore, they emulsify incompatible formulation ingredients, promote nucleation of bubbles during mixing and neutralise the defoaming effect of solid additives present on the formulation. The surfactants most commonly used in the PU industry are polydimethyl siloxane-polyether copolymers. [34, 37, 38]

Additives

Different additives can be incorporated into the formulation of PU foams to impart specific and required properties to these systems. The most common types of additives are: colorants, fillers, cell-openers, UV-stabilisers, plasticisers, bacteriostats, fire retardants, antistatic agents and auxiliary blowing agents. [34]

2.1.3. Morphology

The final properties of water-blown PU foams are strongly influenced by their morphology. The development of a microphase-separated morphology, similar to that of segmented copolyurethane elastomers, is very complex. [39] The simultaneous reactions of isocyanate with polyol and water form a polyurea-polyurethane multiblock copolymer of the $(H_mS)_n$ type. H_m represents the polyurea *"hard segments" (HS)* with a degree of polymerisation *m; S* is the polyurethane phase which mainly consists of polyol *"soft segment" (SS);* and *n* is the degree of polymerisation of the block copolymer (Figure 2.5). [32, 34] The process that develops the block copolymer microstructure and resultant morphology is called the reaction-induced phase separation and is influenced by the competition between kinetic and thermodynamic effects for segmented PUs. [40] The kinetic effects are related to the system viscosity, hard segment interactions and hard segment mobility, while the thermodynamic effects are associated with the incompatibility between hard and soft segments. Therefore, the morphology development of water-blown PU foams has been described by Ryan and co-workers [33, 39, 41-43] as a complex combination of kinetics of polymerisation, macro and microphase-separation and vitrification of hard segments during the foaming process. In these works, the foaming evolution has been studied by *in-situ* FT-IR spectroscopy and small angle X-ray scattering (SAXS) measurements. The combination of both techniques enables the real-time monitoring of the morphological changes of PU foams during its polymerisation, confirming that the thermodynamics of phase separation dominates the kinetics of hydrogen bonding.

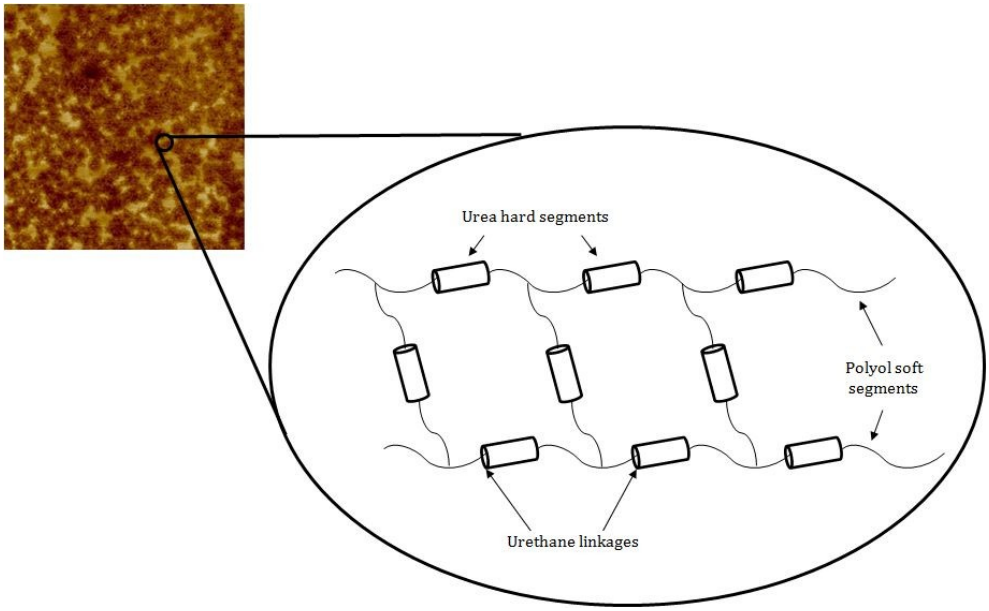

Figure 2.5. Structured morphology of polyurethane.

The final phase-separated morphology of PU foams can be analysed by other techniques. Atomic force microscopy (AFM) shows the presence of two-phases: light areas for hard domains corresponding to high modulus and dark ones for soft domains, corresponding to low modulus regions. [44-46] While, transmission electron microscopy (TEM) is only useful for conventional foams with high water content in the formulation, leading to high urea concentrations. Then, it can be observed large urea precipitated particles as dark regions in the micrographs. [47, 48] On the other hand, techniques like differential scanning calorimetry (DSC) or dynamic mechanical analysis (DMA) give values of the glass transition temperatures of the hard and soft segments. These temperature values provide information related to the HS/SS ratio or if the HS is phase-mixed in the SS. [46, 48, 49] Based on the aforementioned discussions, it is well established the presence of a two-phase morphology in PU foams.

2.1.4. Foaming Process

The final properties of foams depend on their morphology and cellular structure. Therefore, it is crucial to analyse the foaming process conditions. In

water-blown PU foams, the supramolecular architecture is formed in less than 5 min due to a liquid-solid phase transition and gas evolution. Therefore, the polymer structure must build up rapidly to support the fragile foam, i.e. to form a stable cellular structure, but not so fast as to stop bubble growth. [27] This process has been described by *in-situ* studies [12, 50, 51], establishing four stages during polyurethane foaming (Figure 2.6).

1) Bubble Nucleation

Nucleation is defined as the generation of bubbles within a liquid system. For water-blown PU foams, the gas is produced by chemical (production of CO_2) or physical (mechanical stirring) processes. Due to the exothermic nature of the chemical reactions, the temperature of the mixture raises and hence, the concentration of CO_2 in the liquid system exceeds its solubility limit and nucleation occurs. [52-54] In this phase, the initial viscosity is determined by the viscosity of the initial reactants. [41]

2) Bubble Growth

During bubble growth, reaction kinetics, diffusion and fluid flow occur simultaneously. [54] Once the bubble is formed, it grows because of gas diffusion from regions of higher pressure, the liquid phase, to regions of lower pressure, the bubble nuclei. If the liquid surface tension is low, then it favours low pressure differences between the bubbles and the liquid and hence there is better bubble stability, creating smaller average cell size. In this stage, the concurrent formation of urethane and soluble urea moieties leads to the onset of the microphase-separation of the urea hard segments, increasing the viscosity of the liquid phase and preventing the cell rupture while the expansion of the foam is going on. [22, 38]

3) Bubble Stability

During the stability of liquid foams different factors have to be considered: rate of gas evolution, surfactant effects, viscosity, pressure and presence of cell-disrupting agents. The bubbles grow until the chemical reactions achieve the gel point, when the viscosity increases to infinity due to the formation of an

interconnected physical network of hydrogen-bonded hard segments and all film movement and expansion stop.

In rigid PU foams, foam expansion and gelation occur at the same time. The partial vacuum in each cell is maintained because they are strong enough to prevent shrinkage and hence a closed-packed structure is formed. [37]

On the other hand, in flexible PU foams, as the reaction continues the microphase separation of the urea hard segments is arrested by vitrification at Berghmans point and the cell walls open. Consequently, the number of open cells in the final foam is determined by the polymer morphology development and mechanical factors. [11, 34, 36]

4) Final curing

In this step, the storage modulus continues to increase at a slow pace until it stabilises as the vitrification of the hard segments and formation of covalent cross-links are completed.

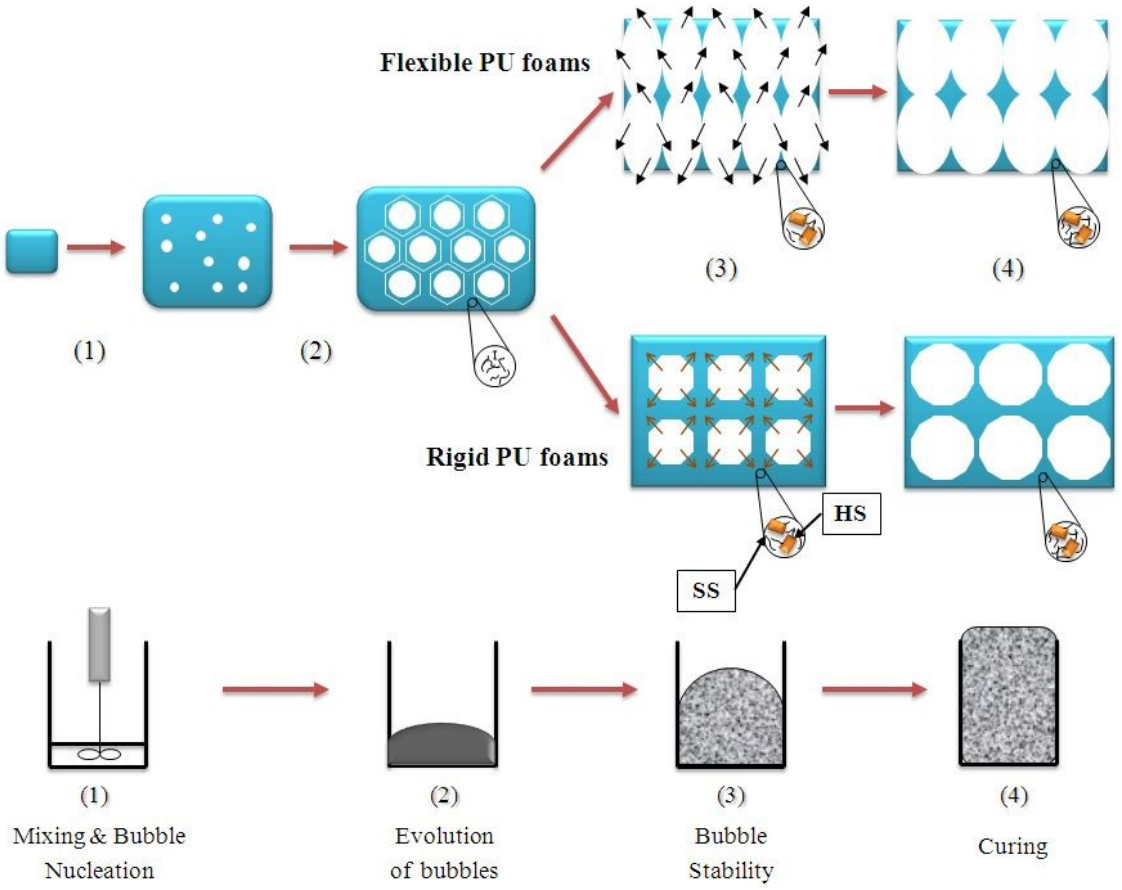

Figure 2.6. Schematic representation of the stages during polymerisation of PU foams. (*adapted with permission from Springer [12] Copyright 1996*)

2.1.5. Cellular Structure and Density

Polymeric foams exhibit two different cellular structures depending on the chemical composition of the polymer matrix and the foaming evolution, being mainly closed-cell or predominantly open-cell (Figure 2.7). The difference in the cellular structure confers different properties to the foamed polymers. Hence, flexible PU foams show an open-cell structure, being closed-cell for rigid PU foams. As a result, flexible foams have better ability to absorb and damp sound, higher absorptive capacity for water and moisture and higher permeability to gas and vapour. Meanwhile, rigid foams present better effective insulation capabilities, low thermal conductivities and high mechanical properties. [11]

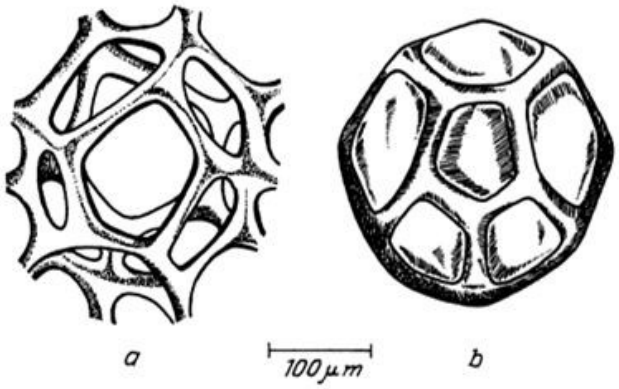

Figure 2.7. Schematic representation of: a) open gas structural element and b) closed gas structural element. [11]

On the other hand, foam density is a crucial aspect because it measures the quantity of air and polymer in the system. It can be easily calculated by the ratio between the mass and the volume and it is usually measured in $kg \cdot m^{-3}$. In water-blown PU foams, the addition of water reduces the density of the material but increases the amount of urea in the polymer making it harder. [38] Low-density flexible foams have densities in the range of 10 - 80 $kg \cdot m^{-3}$, while high-density flexible foams have values above 100 $kg \cdot m^{-3}$. Rigid foams can be made at densities from 10 - 1100 $kg \cdot m^{-3}$; however, in the industry, the most used are low-density rigid foams that show densities in the range 28 - 50 $kg \cdot m^{-3}$. [29]

On the other hand, the properties of polymeric foams are related to density (ρ) by a power function: [55, 56]

$$E = K\rho^n \tag{2.2}$$

Where E is the property, K is a constant related to the polymer and the temperature while n is a constant which normally ranges between 1 and 2 and is a function of the specific property.

2.1.6. Properties

The final applications of PU foams strongly depend on the physical properties of these systems. These properties, as above said, are function of the density of the foam, the composition and the cellular structure. Therefore, the properties of flexible and rigid PU foams are very different and are explained separately.

Flexible foams

Flexible PU foams present interesting properties making them suitable for diverse applications. They are characterised by their high flexibility, load-bearing capacity and the ability to control noise and vibrations. Nowadays, new formulations of flexible PU foams confer to these systems high resistance to moisture, odor-formation and normal cleaning scenarios, increasing their durability.

Flexible PU foams possess a high load-bearing capacity due to their flexibility. Consequently, the load-bearing properties of flexible foams are measured by compression or indentation in order to obtain the weight that the system can support. [29, 38] Hence depending on the hardness, resilience and compression properties obtained by these measurements flexible foams can be used for comfort and packaging applications. Porosity is another property in open-cell foams and is related to the air movement through the cell structure helping to transport properties such as heat and humidity from the surface of the foams. Therefore, applications such as filtering, acoustic and gasketing require the passage of air which means high porosity. Foams with high porosity present better values of resilience, mechanical properties and improve moisture and heat dissipation. Foams with high porosity have lower density. [29, 38]

Rigid Foams

Rigid PU foams act as structural materials due to their three-dimensional arrangement of the cells and struts, giving them interesting mechanical properties. These systems are more often used in compression than tension and in general tend to be more ductile than brittle. In addition, rigid PU foams possess high

mechanical strength to weight ratio, making them attractive materials in construction. Furthermore, during compression these foams effectively absorb energy without rebounding. [11]

Another important property of rigid PU foams is the thermal conductivity. Hence, the low values of this property make them useful as thermal insulators. The thermal conductivity in PU foams is mainly related to the contribution of the solid and gas conductivity and the contribution of the radiation. The gas conduction represents the 50 % of the heat transferred and it changes with time because of the thermal ageing. The radiation is function of the mean cell size; then, lower size means lower contribution. Therefore, the thermal conductivity depends on the foam density, closed cell content and composition of the blowing agent. [11, 57]

Other significant properties of rigid PU foams are their chemical and biological resistance and their durability.

2.1.7. Applications

The applications of PU foams mainly depend, as discussed above, on their properties. It is worth noting that the great advantage of these polymeric foams is that they can be formulated in order to accomplish specific requirements.

The major markets of flexible PU foams are in furnishings, transportation and some specific applications due to their load-bearing capacity and resilience that give these materials higher degrees of comfort and protection. These materials find appliances in packaging, electronics, footwear, sports mats among others. [34, 38]

On the other hand, appliances of rigid PU foams are mainly associated with their low thermal conductivity in construction, refrigeration appliances and technical insulation. Additional applications are as protective packaging, acoustic materials, energy absorbers, gaskets and electrical potting compounds. [29, 37]

The main applications of flexible, semi-rigid and rigid PU foams are summarised in Figure 2.8.

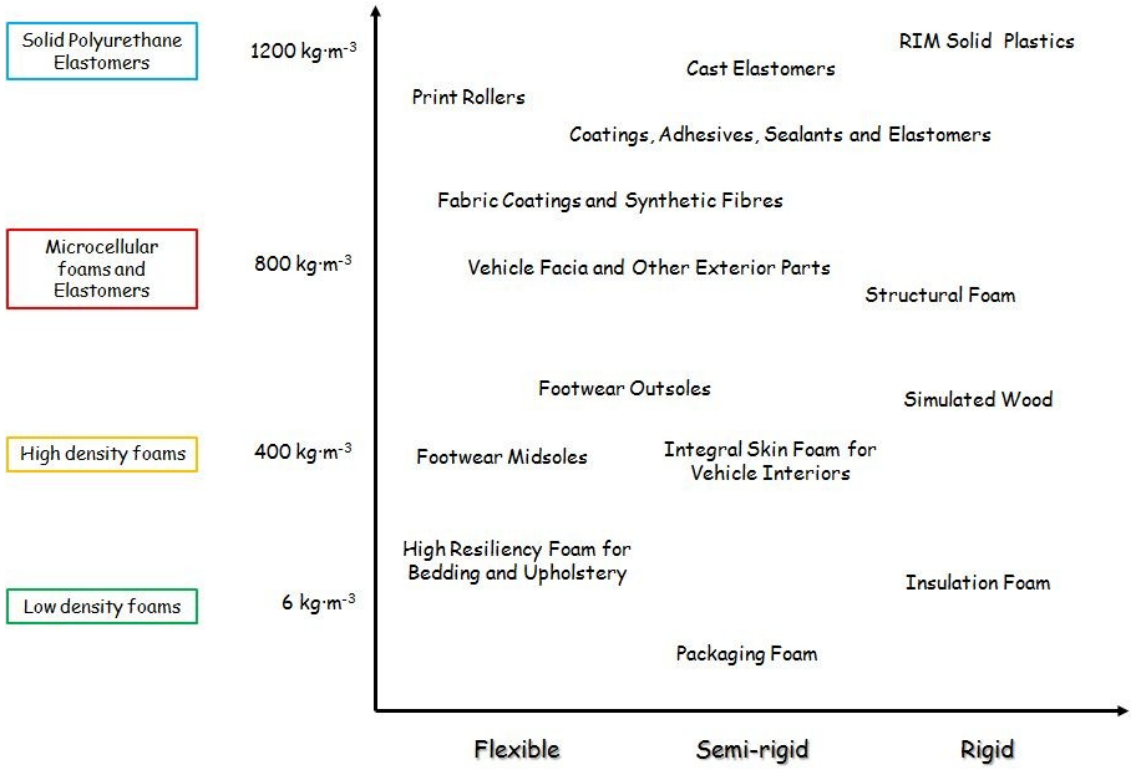

Figure 2.8. Main applications of flexible, semi-rigid and rigid PU foams as function of the density (*adapted from [29]*) .

2.2. CARBON NANOFILLERS

There are different types of nanofillers (Figure 2.9) that can be incorporated in polymeric foams. Traditionally, nanofillers are classified depending on how many dimensions are in the nanometre scale: 1) *spherical nanoparticles* have three dimensions in the nanometre range: silica, aluminium oxide, carbon black, fullerene, titanium oxide, zinc oxide, silicon carbide, polyhedral oligomeric silsesquioxane (POSS) and quantum dots; 2) *rod-like nanofillers* have at least two dimensions in the nanometer range: carbon nanotubes, carbon nanofibres, boron nitride tubes, boron carbon nitride tubes, cellulose whiskers, gold or silver nanotubes; 3) *nanoplatelet* systems where only one of their dimensions, the thickness, is on the nanometre scale while the lateral dimensions could be in the range of several hundred nanometres to microns: layered silicates (nanoclays), layered graphite flakes, graphene, and layered double hydroxides. [9, 10, 58] Next,

a description of the main carbon-based nanofillers on each group will be presented.

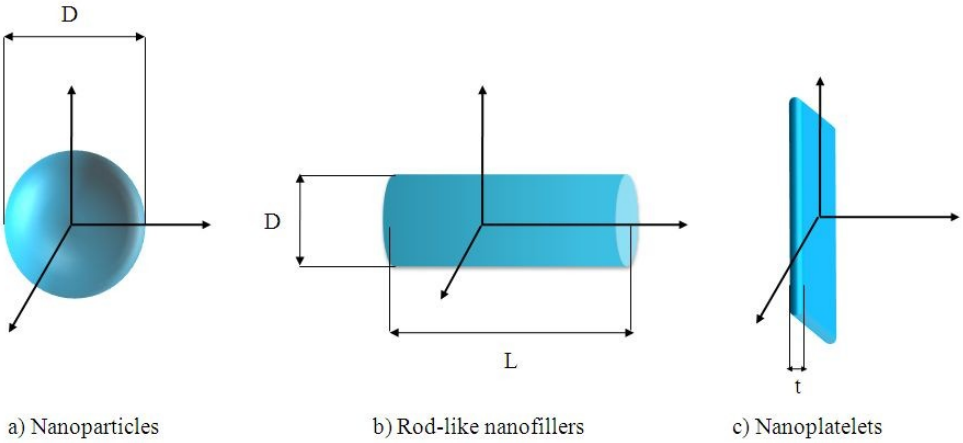

Figure 2.9. Different types of nanofillers.

2.2.1. Carbon Black (CB)

Carbon black (CB) is a zero-dimensional carbon material formed by fine particles produced due to the incomplete combustion or thermal decomposition of a hydrocarbon. These carbon particles consist of "primary" particles which are generally spherical in shape and tend to form larger aggregates (Figure 2.10). CB is composed of amorphous graphite layer planes created from the condensation of aromatic rings and the edges of these planes act as chemical reaction sites. Hence, different functional groups are present on the surface of CB which enhances its dispersibility and affinity in polymer matrices. On the other hand, the aggregates strongly influence the properties of the CB, even if their microstructure is quasi-graphitic. Therefore, CB exists in a vast number of commercial varieties in bulk with different physical and material properties. [59] CB is mainly used as reinforcing agent in automobile tires and other rubber products as well as black colouring pigment or as electric conductive agent of high–technology materials.

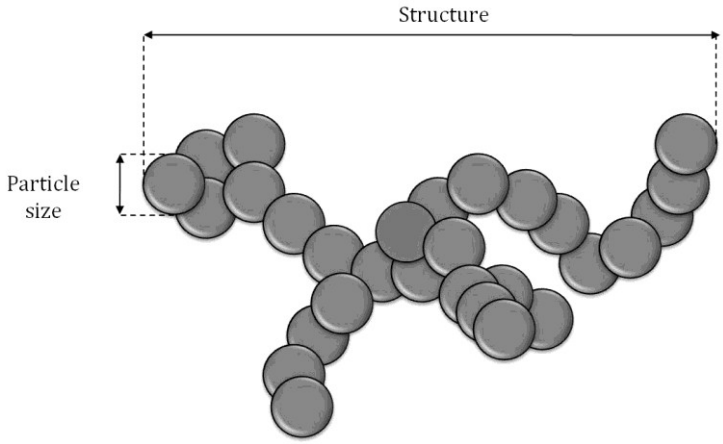

Figure 2.10. Representative structure of carbon black.

2.2.2. Carbon Nanofibres (CNFs)

Carbon nanofibres (CNFs) are cylindrical or conical with a high aspect ratio. The diameters of CNF vary from a few to hundreds of nanometres and their lengths are between microns and millimetres. The internal structure of CNFs consists on arrangements of modified graphene sheets. In general, carbon nanofibres are conformed as stacked curved graphite layers that form cones or "cups". The cone structure is usually referred as herringbone (or fishbone) while the "cup" structure is referred to as a "*bamboo type*" (Figure 2.11). [60, 61]

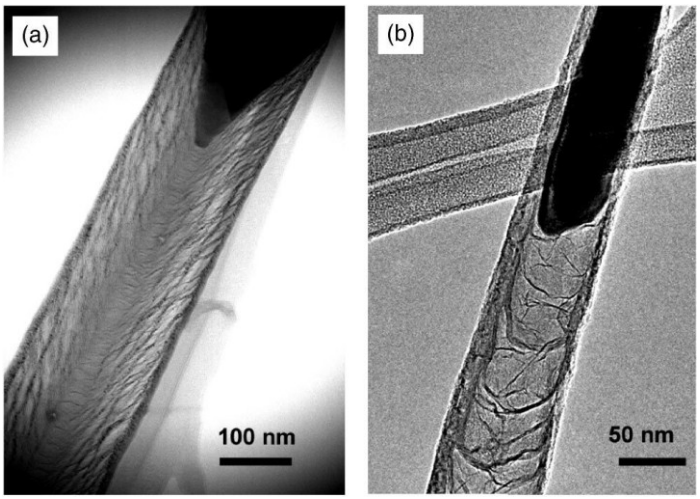

Figure 2.11. a) STEM image of a herringbone carbon nanofibre and b) TEM image of a "*bamboo type*" carbon nanofibre. *Reprinted with permission from [61] Copyright 2005, American Institute of Physics.*

Carbon nanofibres are not often used by themselves in industrial applications. They are typically used to reinforce or add a function to composite materials such as polymers, ceramics or metals. [62] CNFs possess unique physical properties including high specific strength and high specific modulus, and characteristics such as low density, low thermal expansion, heat resistance and chemical stability as well as compatibility with organochemical compounds.

2.2.3. Carbon Nanotubes (CNTs)

Carbon nanotubes (CNTs) are one-dimensional carbon materials with a large aspect ratio (typically ca. 300 - 1000), high surface area, high flexibility and low mass density. CNTs are considered as long cylinders of covalently bonded carbon atoms where the edges of these cylinders can be capped by hemifullerenes. The chemical bonding in CNTs is essentially sp^2 carbon-carbon bonds; however, as the radius of curvature of the cylinders decreases in CNTs the sp^3 character of the carbon atoms increases. [4, 15, 63]

There are two main types of CNTs depending on the process of their production: single-walled carbon nanotubes (SWCNTs) and multi-walled carbon nanotubes (MWCNTs). SWCNTs consist of a single graphene sheet rolled into a seamless cylinder while MWCNTs consist of two or more graphene cylinders coaxially arranged around a central hollow core with an interlayer distance of ~0.34 nm. Consequently, nanotube diameters range from 0.4 to 3 nm in the case of SWCNTs and from 1.4 to 100 nm for MWCNTs. [15]

The different conformations in which graphene are rolled into tubes have been described by the tube chirality or helicity and it determines the atomic structure of the nanotubes. Therefore, the tube chirality is defined by the chiral vector, $\vec{C}$, and the chiral angle, θ, as it is shown in Figure 2.12. The chiral vector is defined as:

$$\vec{C} = n\overrightarrow{a_1} + m\overrightarrow{a_2} \tag{2.3}$$

where $\overrightarrow{a_1}$ and $\overrightarrow{a_2}$ are the unit cell base vectors of the hexagonal lattice and (*n*, *m*) are the number of steps along the zig-zag carbon bonds of the hexagonal lattice. Meanwhile, the chiral angle determines the amount of "*twist*" in the tube. As a result, three different types of orientation of the carbon atoms in terms of roll-up vector (*n*, *m*) can be defined: zig-zag (*n, 0*), armchair (*n,n*) or chiral (all others) (Figure 2.12). [4, 14, 15, 64]

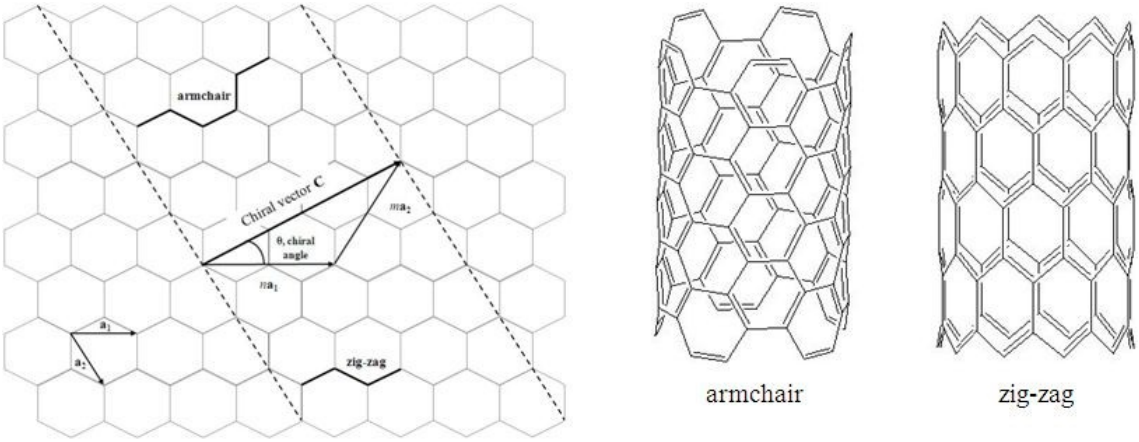

Figure 2.12. Schematic diagram showing how a hexagonal sheet of graphene is rolled to form a carbon nanotube with different chiralities: armchair and zig-zag.
(*adapted with permission from Elsevier [64] Copyright 2001*)

The chirality of CNTs has an important impact on their properties, in particular in the electronic ones, because nanotubes can show metallic or semiconducting behaviour depending on the tube chirality. Hence, armchair SWCNTs are metallic (band gap = 0 eV) or semimetallic (band gap on the order of few meV) or semiconductors (band gap of 0.5 - 1 eV). On the other hand, MWCNTs present a wide variety of tube chiralities and thus, their properties are complicated to predict. [49]

The synthesis method defines the structure and properties of CNTs which can be produced by three different techniques: arc-discharge, laser ablation or catalytic chemical vapour deposition. [15, 64-66]

Arc discharge: this technique involves the use of two high-purity graphite rods as electrodes. These electrodes are placed in a stainless steel vacuum

chamber under an inert He atmosphere. The electrodes are brought together and a voltage (usually 20 V, but it depends on the diameter of the rods) is applied until a stable arc is achieved. Then, the gap between the rods should be maintained at 1 mm or less and the anode is consumed at a rate of some mm per minute while the material is deposited on the cathode. Several factors influence the production of a good yield of high-quality nanotubes: pressure of the He, the current, efficient cooling of the electrodes and the chamber and catalytic metals employed.

Laser ablation: in this method, a laser is used to vaporise a graphite target doped with small amounts of catalyst metal in an inert atmosphere oven at high temperatures (> 3000 °C). Finally, the carbon nanotubes are collected in a water-cooled copper collector. This method produces high-quality SWNTs; however the cost of the laser is very high and the process is not effective for a large scale synthesis.

Chemical vapour deposition (CVD): this method consists on the catalytic decomposition of a hydrocarbon gas source in a furnace at high temperature (500 - 1000 °C) during a period of time. As-grown carbon nanotubes are deposited on a substrate or grown from a substrate and they are collected once the system is cooled at room temperature. Another method that can be included in this group is the CVD in fluidised beds (FBCVD). In this case, the CVD reaction takes place in a fluidised bed of catalyst particles. The FBCVD is used to synthesise freestanding CNTs for applications in composite materials and energy-storage devices. [67]

Arc-discharge and laser ablation techniques have the advantage of producing high crystallinity nanotubes. Nevertheless, both techniques need high temperatures and subsequent purification steps due to the large amounts of byproducts. [14, 66] On the contrary, nanotubes synthesised by the CVD methods possess lower crystallinity but low carbon-based impurities minimising the successive purification processes. In addition, CVD techniques produce aligned arrays of nanotubes and offer the possibility to control the diameter and length of the CNTs, thus allowing a large scale production of the nanotubes.

The interest of carbon nanotubes as nanoscale materials has grown because of their exceptional properties: high electric and thermal conductivity, unusual mechanical properties such as Young's modulus higher than 1 TPa and tensile strength around 200 GPa. [15, 68-71] The most relevant physical properties of SWCNTs and MWCNTs are summarised in Table 2.4.

Table 2.4. Properties of SWCNTs, MWCNTs and graphene.

Property	SWCNTs	MWCNTs	Graphene
Density ($g \cdot cm^{-3}$)	~0.6 - 0.8 [63, 72]	1 ~ 2 [63, 72, 73]	2.28 [7]
Thermal Conductivity $W \cdot (m \cdot K)^{-1}$	~6000 [74-76]	3000 [15, 77, 78]	$4.84 - 5.30 \cdot 10^3$ [79]
Electrical Conductivity ($S \cdot cm^{-1}$)	$\sim 10^4 - 10^6$ [80]	$\sim 10^2 - 10^5$ [81, 82]	6000 [7]
Specific Surface Area ($m^2 \cdot g^{-1}$)	~1300 - 1000 [83, 84]	~800 - 200 [83, 85]	2630 [86]

2.2.4. Graphene

Graphene is a two-dimensional (*2D*), one-atom-thick carbon sheet composed of sp^2 carbon atoms arranged in a honeycomb structure (Figure 2.13). [87, 88] It could be considered as the fundamental building block for graphitic materials of different dimensionalities e.g. fullerenes (*0D*), nanotubes (*1D*) and graphite (*3D*). [21, 89] The outstanding properties of graphenes (Table 2.4), such as high thermal conductivity [79] and high electron mobility [89], large specific surface area [86] and gas impermeability [90], make them promising reinforcing particles for advanced composite systems. Lee *et al*. [91] have reported a Young's modulus of ~1 TPa and an intrinsic strength of 130 GPa, being graphene the strongest material at the moment.

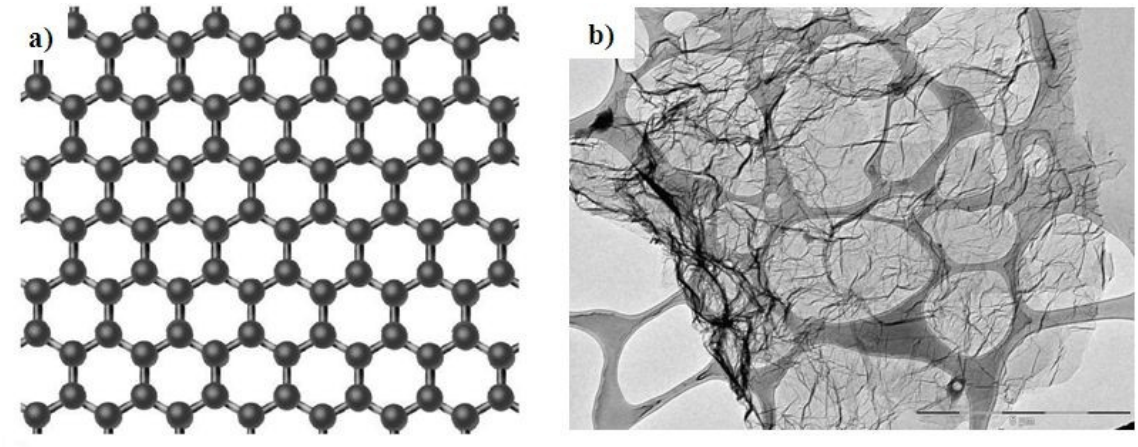

Figure 2.13. a) Schematic illustration of graphene structure and b) TEM image of graphene at 5 μm.

The methods to produce graphene can be classified into different groups:

(i) *Micromechanical cleavage* from bulk graphite using "*scotch tape*": this technique consists on the use of "*scotch tape*" to peel away small quantities of highly oriented pyrolytic graphite. [16, 92] Although, high quality material is obtained by this method it is an arduous process with low probability of finding individual graphene sheets.

(ii) *Chemical vapour deposition* (CVD) techniques: these methods are based on the widely known CVD method to obtain high-quality material with large surface area. Li *et al*. [93] employed a mixture of methane and hydrogen at 1000 °C to grow graphene on copper foils while Kim *et al*. [94] deposited layers of nickel on SiO_2/Si substrates using an electron-beam evaporator at 1000 °C.

(iii) *Epitaxial growth* of graphene films: this method produces ultrathin epitaxial graphite films on SiC(0001) surface by vacuum graphitisation. [95]

(iv) *Longitudinal "unzipping"* of CNTs: this technique is based on the dispersion of pristine nanotubes in a surfactant solution and deposited on a Si substrate. A thin film of PMMA is spin-coated on the top of the nanotubes and the resultant film is peeled off in a basic solution. After that, the polymer film is removed using a solvent and the material is calcinated in order to remove the

polymer traces. [96] The resultant materials are graphene nanoribbons (GNR). Another way to obtain this type of graphene is by suspending CNTs in concentrated sulphuric acid and after that treating them with 500 % of $KMnO_4$ for 1 h at room temperature and 1 h at 55 - 70 °C. The nanotubes are opened along a line, analogous to the "unzipping" of graphite oxide. [97]

Despite of the good quality of the graphene obtained by these methods, they cannot yield bulk amounts of graphene and in some cases require special conditions e.g. high-vacuum in CVD techniques and epitaxial growth. Consequently, chemical exfoliation strategies based on oxidation/reduction of graphite derivatives (graphite oxide (GO) and graphite fluoride [98, 99]) are used to produce functionalised graphene. [100, 101] The production of graphene from GO is the most common process and it can be obtained by two different routes: chemical reduction of GO (CRG) and thermal exfoliation and reduction of GO (TRG). As above said, both of them begin with the oxidation of the GO by the chemical oxidation of graphite via three principal methods developed by Brödie, [18] Hummers [20] and Staundenmeier. [19] Then, the exfoliation is produced by the two methods mentioned below:

Chemical reduction of GO (CRG)

This technique consists on the preparation by sonication of a stable colloidal dispersion of GO in solvents such as water, alcohol or protic solvents. [102, 103] After that, the colloidal dispersion is chemically reduced using hydrazine, [104, 105] dimethylhydrazine, [88] hydroquinone, [106] sodium borohydride [107] and ultraviolet-assisted methods. [108]

Thermal exfoliation and reduction of GO (TRG)

This method is based on the rapid exfoliation of dried GO at high temperatures (1000 °C) and under inert gas atmosphere. [109-111] In this case, a volume expansion of 100 - 300 times is produced due to the exfoliation. The graphenes obtained by this procedure were originally called functionalised graphene sheets (FGS). [109, 110]

2.3. POLYMER NANOCOMPOSITE FOAMS FILLED WITH CNPS

Polymer nanocomposite foams have generated a great deal of interest because they present the combination of high-performance characteristics of polymer nanocomposites together with the foam technology, allowing the generation of multifunctional and lightweight materials that could find a variety of applications at industrial level Nevertheless, literature on polymer nanocomposite foams filled with CNPs is still on its beginnings and the information related to this topic is scarce. This section is focused on carbon-based polymeric nanocomposite foams.

2.3.1. Foaming Process

The main objective in the synthesis of polymer carbon-based nanostructures is to achieve good dispersion of CNPs on the polymer matrix, which strongly influences the properties of the nanocomposites. The synthesis of polymer nanocomposite foams can be divided into two groups: two-step process characteristic of thermoplastic foams and reactive foaming typical of thermoset systems (PU, silicone, polyisocianurate).

The production of thermoplastic nanocomposite foams consists on the preparation of polymer nanocomposites followed by the foaming by means of PBAs or CBAs. The procedures mainly used to prepare polymer nanocomposites can be included into the following groups: i) solution blending, ii) *in-situ* polymerisation, and iii) melt processing. [4, 5, 15, 63] Each method has individual requirements depending on the nature of the filler involved; nonetheless, the basic aspects of how to prepare the nanocomposite are common to all the systems.

Solution blending

The preparation of polymer carbon-based filler composites involves mixing of the carbon-based filler dispersion with a polymer solution and then the controlled evaporation of the solvent with or without vacuum conditions. In general, the most efficient dispersion of CNPs is achieved by bath or tip sonication.

In order to facilitate solubilisation and mixing, the CNPs are often functionalised prior to their addition to the polymer solution. [15, 112]

***In-situ* polymerisation**

This method starts by dispersing CNPs in a monomer followed by its polymerisation. As in the case of solution blending, the functionalisation of CNPs can improve the initial dispersion of the nanotubes in the liquid (monomer, solvent) and as a result in the nanocomposite. Furthermore, *in situ* polymerisation methods facilitate the covalent bonding between functionalised CNPs and the polymer matrix using different condensation reactions. [4, 15, 63]

Melt processing

Due to the fact that many polymers soften when heated above their glass transition temperature (amorphous polymers) or their melting temperature (semi-crystalline polymers), mechanical processing has been a very valuable technique for the fabrication of nanocomposites. This is the most promising method and it has great advantages over both previously described methods, being both compatible with current industrial processes and environmentally friendly, owing to the absence of solvents. In this method, the polymer and filler are mixed by application of intense shear forces. Achieving homogeneous dispersions of CNPs in melts is generally more difficult than in solutions, and high concentrations of filler are hard to achieve, due to the high viscosities of the mixtures. [15, 113]

On the contrary, the method to obtain thermosetting nanocomposite foams consists on the dispersion of the CNPs in one or more of the monomers followed by the foaming due to the addition of the pre-mixture of another monomer. In this process the blowing agents can be CBAs or PBAs and the reaction kinetics characterises the final properties of the material. Hence, appropriate functional groups and their ratios with catalysts and surfactants should be controlled. [8, 22] The surface modification of the CNPs is essential during the first step because they can further react with the monomers creating new cross-links and facilitating the dispersion and processing of the final nanocomposite foams. This method is widely used for reactive PU, silicone and polyisocyanurate foams.

2.3.2. Morphology

The properties of polymer nanocomposite foams depend on the cellular structure obtained during the foaming process. Nanoparticles can act as heterogeneous nucleation agents, affecting the cell size. [114] Theoretically, the inclusion of high concentration of ultra-fine solid particles, i.e. nanoparticles, leads to an increase on the rate of heterogeneous nucleation. However, the processing of nanoparticles-polymer system creates in some cases agglomerates and an increase of the system viscosity. Consequently, the observed cell density is lower than the potential nucleant density, due to both effects: the low nucleation efficiency of the nanoparticle aggregates and their poor dispersion. [8, 114, 115]

Shen *et al*. [116, 117] reported a reduction of the cell size and, hence, an increase on the cell density, for polystyrene (PS) foams filled with CNFs. They obtained a cell density of neat PS foams of 2.29 x 10^8 cells·cm^{-3}, while this density increased to 4.73 x 10^8 cells·cm^{-3} for PS/1wt.-% CNF foams and when the concentration of CNFs was up to 5 wt.-% the cell density was 1.44 x 10^9 cells·cm^{-3}. Other CNPs such as graphene oxide (GO), slightly increased the cell density on PS foams. [118] The presence of the carbonyl group on the surface of the GO sheets and its affinity with the CO_2 facilitated the nucleation. However, it was observed that the increase on the cell density was lower than for PS foams with other nanoparticles, i.e. clay and carbon nanotubes, because of its exfoliated structure and partially hydrophilic surface properties.

The nucleation effect of CNFs has also been observed in polypropylene (PP) foams [119] where the cell density increased from 2.19 x 10^6 cells·cm^{-3} for 5 wt.-% CNFs to 1.16 x 10^7 cells·cm^{-3} for 20 wt.-% CNFs. This study also reported the contribution of CNFs to an isotropic-type of cellular structure and the promotion of finer cellular structures.

The effect of CNTs in a poly(methyl methacrylate) (PMMA) matrix was influenced by the surface functionalisation of the nanofillers, their dispersion on the polymer matrix as well as by the synthesis methods employed for the polymer nanocomposites. Consequently, the cell nucleation mechanism and cell morphology were affected. [120] It was observed an increase on the cell density

for functionalised CNTs (f-CNTs) due to the better dispersion of these nanoparticles in the polymer matrix and the favourable interaction between the CO_2 and the carboxyl group on the surface of the f-CNTs due to a reduction on the wetting angle and nucleation free energy and a higher nucleation efficiency.

The effect of CNPs on the cell size and open-cell/closed-cell ratio is more evident in PU foams and it also depends on the nature of the foams: flexible or rigid. In flexible PU foams it has been reported an increase on the cell size due to the presence of CNPs. [121] The addition of the carbon nanotubes increased the initial viscosity of the mixtures, having a detrimental effect on the foaming and the final cellular structure of the systems. The lower foaming rate observed enabled the diffusion of gas from small to larger cells driven by the free energy of the system. In addition to the viscosity, other factors that could influence the increase of the cell size in flexible PU foams due to the presence of CNPs are: cell coalescence, polymer gelation and the surface functionality of the nanotubes. [121, 122] On the other hand, the inclusion of CNPs in rigid PU foams has similar effects as those observed in thermoplastic foams. You *et al*. [123] observed that the reduction in cell size in rigid PU foams is more effective for low loadings of MWCNTs (up to 0.1 phpp). Similar results were found by Dolomanova *et al*. [124] with the addition of 0.5 to 1 wt.-% of MWCNTs, SWCNTs and CNFs. However, Harikrishnan *et al*. [125] reported that CNFs did not change the cell size in their rigid PU nanocomposite foams and did not induce cell opening due to the antifoaming nature of these nanoparticles.

2.3.3. Properties

In this section, the improvement on the physical properties of polymer carbon-based nanocomposite foams will be discussed.

Mechanical

Shen *et al*. [116] compared the mechanical properties of bulk PS, PS foam and PS/CNF foams. Neat PS foam presented a reduction in weight of 37 % compared to the bulk PS. However, the foaming of PS reduced its tensile modulus

by 40 %, from 1.26 to 0.74 GPa. The presence of up to 5 wt.-% of CNFs on PS foam increased the tensile modulus to 1.07 GPa (45 % enhancement) which was comparable to that of bulk PS. In order to compare the mechanical properties of the samples, the reduced modulus was used and hence the impact of the foam density was taken into account. Due to the lower density of the foam composites, the reduced modulus of PS foam with 5 wt.-% of CNFs is 25 % higher than that of bulk PS. The specific modulus and specific yield strength of PMMA foams with 1 wt.-% graphene sheets also increased by 18 % and 13 %, respectively. [126] Werner *et al*. [127] measured the mechanical properties of CNF/poly(ether ether ketone) (PEEK) foams. They observed an increase of the specific stiffness in bending from 2.7 $GPa \cdot kg^{-1} \cdot m^3$ for the pure solid resin to 4.3 $GPa \cdot kg^{-1} \cdot m^3$ for the 15 wt.-% CNF foam while the specific yield strength increased from 73 to 100 MPa $kg^{-1} \cdot m^3$. Park *et al*. [128] prepared ethylene vinyl acetate copolymer (EVA)/MWCNT nanocomposite foams. They observed a significant improvement of the mechanical properties and compression set with 5 phr (parts per hundred parts of resin) of MWCNTs but not in the elongation at break. Peng *et al*. [129] compared the dispersion state and properties of polyurethane foams filled with up to 8 wt.-% of pristine, un-modified CB and polyol-grafted CB. They reported an increase of the storage modulus and glass transition temperature of the grafted CB compared to both pristine and oxidised CB. Meanwhile, the volume resistivity of the grafted CB/PU foam was lower than that of pristine CB/PU foams, but higher than that of oxidised CB/PU. They suggested that the grafting hindered the formation of a continuous conductive path. Furthermore, Saha *et al*. [130] presented an increase in the compressive modulus and strength of 40 % and 57 %, respectively, in PU foams with 1 wt.-% of CNF.

Thermal stability and flammability

Verdejo *et al*. [131, 132] used as-produced multiwall CNTs in reactive silicone foams and studied the thermal and flammability characteristics of the developed systems. They observed a noticeable increase in the degradation temperature of almost 60 °C, which was attributed to the presence of CNTs, and an enhancement of the thermal dissipation efficiency, which was assigned to both the direct presence of CNTs and their indirect physical effect on the cellular structure.

Vertical fire conditions indicated that the nanocomposite foams may be classified as self-extinguishing, as the limiting oxygen index increased from 20.5 ± 0.5 for the control sample to 30 ± 0.5 oxygen content for the 1 wt.-% CNT sample. These results were attributed to the formation of a CNT network throughout the sample via non-covalent CH-π interactions and to the surface tension of the gas–polymer interface during foaming. They also reported the first study on the use of functionalised graphene sheets in reactive silicone foams with loading fractions up to 0.25 wt.-%. The nanocomposite foams showed a noticeably increase of the decomposition temperature of more than 50 °C, the thermal conductivity by up to 6 % and the normalised modulus of more than 200 %. [132, 133] Zammarano *et al*. [134] studied the use of CNFs as flame retardant fillers for PU foams. They employed a modified cone calorimeter test and observed a decrease of the heat release rate, which represents the point in a fire where heat is likely to spread, and melt dripping. The proposed mechanism for this improvement is the formation of a protective flocculated layer covering the sample surface, which is favoured by an increase in melt viscosity. Harikrishnan *et al*. [125] reported a reduction on the thermal conductivity in 5.4 % with the addition of 1 wt.-% CNFs to PU, increasing the thermal insulating capacity of foam. The inclusion of CNFs has also impact on the thermal expansion coefficient (TEC) of PS foams. The presence of CNFs results in less thermal expansion which means an improvement of the dimensional stability. [116]

Electromagnetic interference (EMI)

Polymer nanocomposite foams filled with CNPs are excellent systems to use as electromagnetic interference (EMI) shielding materials. Recently, it has been developed different polymer foam systems with CNFs, CNTs or graphene sheets since they present the advantage of low density, high conductivity, low dielectric constant (ε') close to that of air, among other properties. The target value of the EMI shielding effectiveness needed for commercial applications is around 20 dB in the X-band region (8-12 GHz) while the target conductivity value required for EMI shielding applications is (1 $S \cdot m^{-1}$). [135] The EMI shielding effectiveness of PS foams filled with CNFs [136] and with CNTs [137] has been compared by Yang *et al*. The target value is achieved with the inclusion of 15 wt.-% of CNFs but

this value is reached with only 7 wt.-% of CNTs. The improvement in both cases is attributed to the formation of conducting interconnected nanotube networks in the insulating PS matrix. The differences observed on the effect of the CNPs are due to the fact that CNTs possess large aspect ratios and small diameters and higher electrical conductivities than CNFs. Zhang *et al*. [126] synthesised graphene/PMMA foams to improve the electrical conductivity and EMI shielding effectiveness of PMMA foams. In this case, the insulator-to-semiconductor transition of graphene/PMMA foams occurred at lower graphene content to that of bulk nanocomposites. The electrical conductivity of PMMA nanocomposite foams at 4 wt.-% of graphene sheets is 3.11 $S \cdot m^{-1}$ which is higher than the aforementioned target value. In addition, the specific EMI shielding effectiveness of the PMMA foam with 1.8 vol.-% was 17 - 25 $dB \cdot cm^3 \cdot g^{-1}$ in the frequency range from 8 - 12 GHz. As for CNTs or CNFs, these results are attributed to the formation of an interconnected network throughout the insulating PMMA matrix. Antunes *et al*. [119] studied the influence of foaming semicrystalline PP reinforced with CNFs on the electrical conductivity. This work demonstrated that the formation of a conductive network was achieved at lower concentrations of CNFs for foams than for solids. By comparing the electrical response from a tunnel conduction point of view, it was demonstrated that the foaming process reduced the CNF aggregation and hence the electrical conductivity of PP/CNF foams was higher than for PP/CNF solids. Furthermore, it was studied the influence of foaming, chemical or physical, on the cell orientation and thus on the electrical conductivity. PP foams with 20 wt.-% CNFs obtained by chemical foaming possessed lower through-plane electrical conductivity (9.4×10^{-8} $S \cdot cm^{-1}$) than the foam obtained by physical foaming (4.1×10^{-5} $S \cdot cm^{-1}$). They suggested that the physical foaming by CO_2 reorientate the nanofibres helping to produce an electrically conductive foam with enhanced isotropic electrical conduction behaviour. Thomassin *et al*. [135] developed foams of polycaprolactone (PCL) filled with MWCNTs for EMI shielding applications. They achieved shielding efficiencies as high as 60 to 80 dB with low reflectivities at a 2 wt.-% of MWCNTs (0.25 vol.-%). Fletcher *et al*. [138] demonstrated that foaming an elastomer fluorocarbon polymer with MWCNTs reduces the weight of the material by 30 % with a minor impact on the EMI properties. Later studies on foam composites comprising functionalised graphene

(FGS) and polyvinylidene fluoride (PVDF) [139] observed a drastic change in the conductivity from 10^{-16} S·m^{-1} for insulating PVDF to 10^{-4} S·m^{-1} for 0.5 wt.-% of FGS composites. The increase in conductivity implies an improvement of the EMI properties and in this case they obtained an EMI shielding effectiveness of ~ 20 dB with 5 wt.-% of functionalised graphene. Xu *et al*. [140] developed electrically conductive CNT/PU foams and studied the density dependent conductor–insulator transition by producing rigid foams with different densities at 2 wt.-% CNT fixed loading fraction. They varied the rigid PU density from 510 to 30 kg·m^{-3} and observed the conductor–insulator transition at 50 kg·m^{-3} with a non-linear abrupt decrease of the conductivity of about eight orders of magnitude from 4.3×10^{-5} S·m^{-1} to 10^{-13} S·m^{-1}. They proposed that at the lower foam density the CNTs concentrated in the cell struts and, hence, non conductive paths were created.

Other properties

Verdejo *et al*. studied the effects of CNTs on the acoustic attenuation activity [121] and the potential application in tissue engineering and biomedical implants [141] of reactive PU foams. They observed that, on addition of CNTs, the acoustic absorption of the system improved over the entire frequency range. [121] They also reported an increase of the acoustic activity, defined as the area under the absorption curve normalised by the frequency range, of 30 % for 0.1 wt.-% CNTs loading fraction. The damping effects were attributed to the large surface area at the polymer-CNT interface, where energy can be dissipated by interfacial sliding and stick-slip behaviour. The second study revealed the CNTs ability to modify the chemical nature and wettability of the pore wall surfaces in a concentration dependent manner. They also studied the biological properties *in vitro* of the scaffolds and revealed that increasing CNTs loading fraction did not cause osteoblast cytotoxicity nor have any detrimental effects on osteoblast differentiation or mineralisation. [141]

2.3.4. Applications

Polymeric foams have been used in many applications because of their excellent strength-to-weight ratio, good thermal insulation and acoustic properties, materials savings, and other factors. By replacing solid plastic with cells, polymeric foams use fewer raw materials and thus reduce the cost and weight for a given volume. However, polymeric foams are rarely used as structural components in the automotive, aerospace, and construction industries (except sandwich composite foams) because of reduced mechanical strength and low dimensional and thermal stability, when compared to bulk polymers. [8]

The inclusion of nanoparticles, in particular, carbon-based nanostructures offer unique advantages for controlling the cellular structure of polymeric foams due to their high nucleation efficiency even at low loading contents. On the other hand, it has widely been demonstrated their ability to reinforce the fine cellular structure of foams. The observed enhancements in mechanical strength, nanoscale surface features, and biocompatibility suggest particular applications in load-bearing tissue engineering applications, acoustically insulating foams, high performance structural panels, sandwich cores, filtration packs, and catalyst supports, to name a few. The development of new products in these areas would be of great benefit to both industry and, of course, to the public who would have access to improved products. However, there are still many fundamental issues to be explored, such as a) the effect of the nanofillers in the cellular development and morphology, b) the interactions between both the nanofillers, and the polymer and the nanofillers and c) the interaction of the nanofillers with liquid-gas interfaces.

3. CARBON NANOPARTICLES

Carbon nanostructures, such as carbon nanotubes and fullerenes, have attracted much attention recently. In particular, this thesis is focused on the inclusion of multi-walled carbon nanotubes (MWCNTs) and functionalised graphene sheets (FGS) on polymeric foam systems. For this reason, these carbon nanoparticles were synthesised in the laboratory. This Chapter describes the synthesis methods used for the production of MWCNTs and FGS, the functionalisation process of MWCNTs and the characterisation techniques used to understand the structure of these graphitic materials, the effect of the functionalisation (type and quantity of oxygen bearing groups on the carbon structures), aspect ratio and thermal stability.

3.1. SYNTHESIS AND CHARACTERISATION OF MULTI-WALLED CARBON NANOTUBES (MWCNTS)

3.1.1. Synthesis of MWCNTs

Carbon nanotubes were grown by the chemical vapour deposition (CVD) injection method in a tubular quartz reactor contained within a heating furnace. [15, 142] This method is based on the injection of a ferrocene (Aldrich 98 %)/hydrocarbon vapour solution (20 mL of 3 wt.-% of ferrocene in hydrocarbon solvent) at a constant rate in a tube furnace, under an inert argon atmosphere (325 $mL \cdot min^{-1}$) and at a temperature of 760 °C in atmospheric pressure. The reaction times were calculated taking into account the injection rate of the solution and adding 1 h and 30 min. Once the reaction finished and the furnace reached room temperature, the MWCNTs were removed from the quartz tube and stored in a sealed container prior to use. Figure 3.1 illustrates the equipment employed for the synthesis of the MWCNTs.

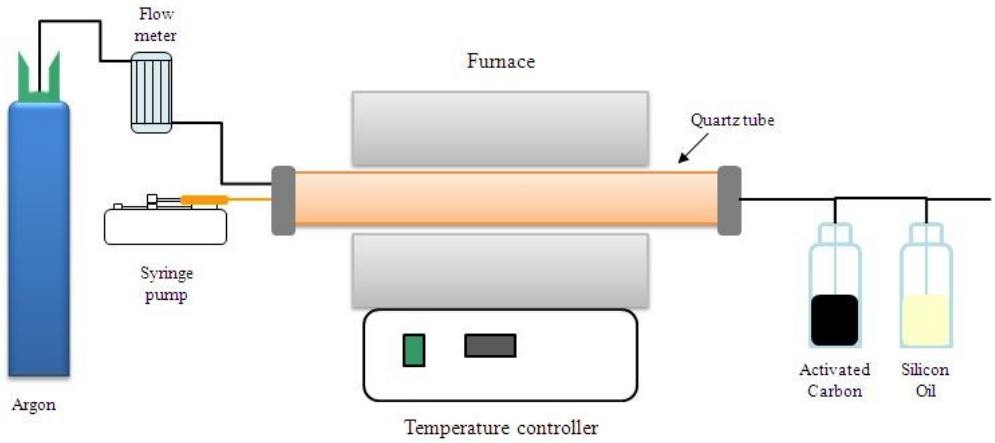

Figure 3.1. Schematic representation of the furnace employed for the synthesis of MWCNTs.

Once established the basic variables of the synthesis process, some parameters were varied in order to see the influence on the morphology and properties of MWCNTs. Four different conditions of synthesis were used, mainly

changing the solvent and the injection rate of the solution of ferrocene. Table 3.1 summarises the different conditions used in each synthesis.

Table 3.1. Conditions of different synthesis processes of MWCNTs.

Synthesis	Hydrocarbon	Injection rate ($mL \cdot h^{-1}$)
MWCNTs-S1	Toluene	10
MWCNTs-S2	Xylene	10
MWCNTs-S3	Toluene	5
MWCNTs-S4	Xylene	5

3.1.2. Characterisation of MWCNTs

In order to evaluate the optimum synthesis process, the morphology and properties of the different MWCNTs were characterised by Raman spectroscopy, scanning electron microscopy and thermogravimetric analysis.

Raman spectroscopy was performed on a Renishaw Invia Raman Microscope. The analyses were done using an argon laser at 514.5 nm excitation wavelength. The CNPs were placed on a glass slide and air-dried before the measurements were taken.

Raman spectroscopy is a straight forward characterisation technique to analyse the structural quality of graphitic materials such as graphite, diamond and carbon nanotubes. The amount of ordering and degree of sp^2 and sp^3 bonding provides a unique Raman "fingerprint" for each carbon nanostructure. [15] A typical Raman spectrum of MWCNTs is shown in Figure 3.2.

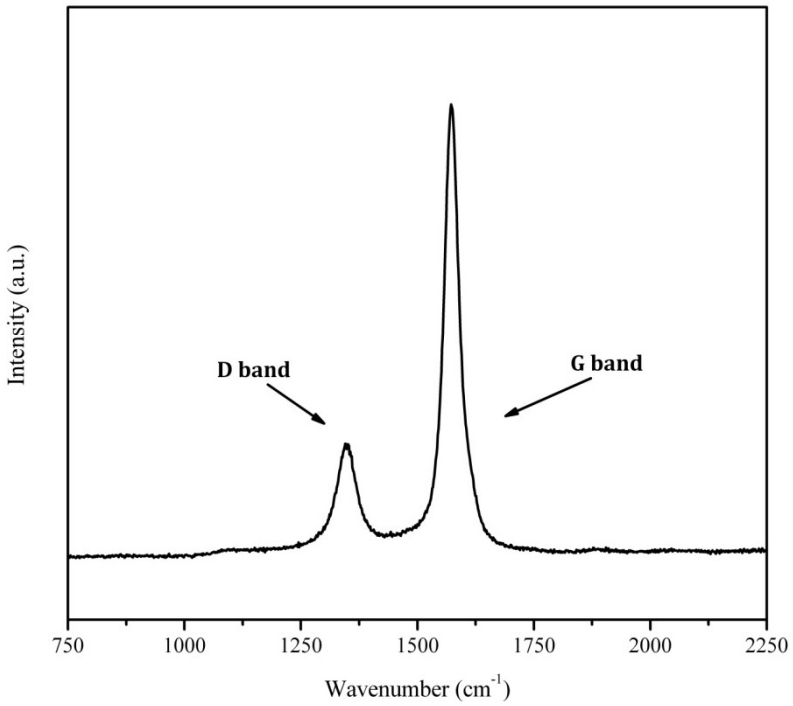

Figure 3.2. Typical Raman spectrum of MWCNTs.

The most distinctive bands of CNPs are the *G* band (in-plane tangential stretching of the carbon-carbon bonds in graphene sheets) at around 1570 cm^{-1}, the *D* band (attributed to the presence of disorder or amorphous carbon in graphitic materials) at ~ 1350 cm^{-1} and the *D'* band at ~ 1610 cm^{-1} (overtone resonance feature induced by disorder and defects). [15, 143-146] Ratios of the relative intensity *D* band and *G* band are widely used as a measure of the amount of disorder within carbon nanotubes. [142] Therefore, large values of the I_D/I_G ratio inform of the presence of a large number of defects within the nanotubes. The I_D/I_G ratios of the different synthesis, calculated from the Lorentzian deconvolution of the *D* and *G* band, are shown in Figure 3.3.

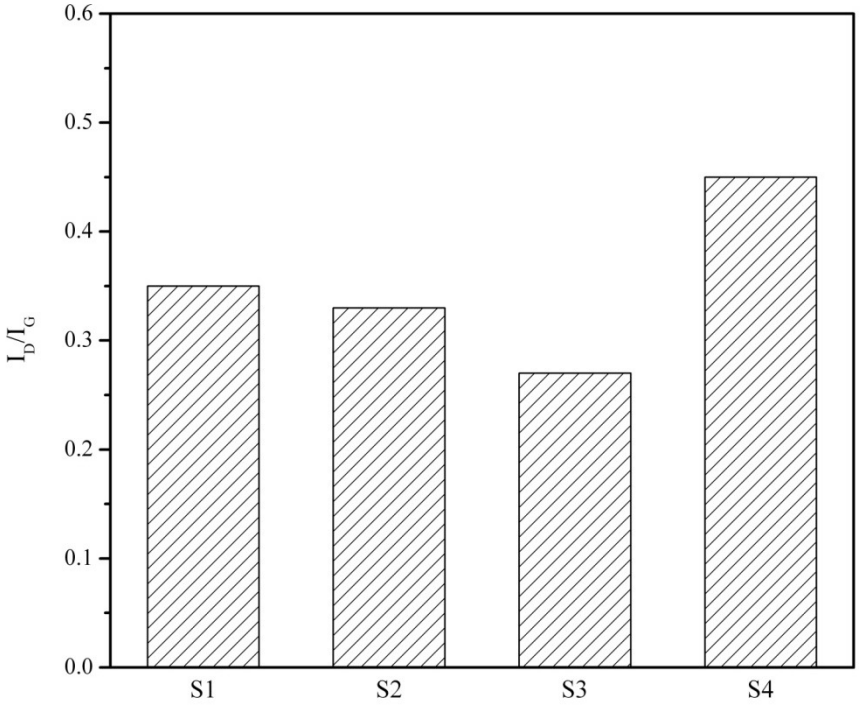

Figure 3.3. I_D/I_G ratio for different synthesis of MWCNTs.

As it is observed in Figure 3.3, MWCNTs prepared from the synthesis method named S3 presents the lowest I_D/I_G ratio with a value of 0.27. MWCNTs obtained from toluene (S1 and S3) as a carbon source show lower I_D/I_G ratio than those prepared from xylene (S2 and S4). The different behaviour of the carbon source (toluene or xylene) at the same reaction temperature could be attributed to the decomposition mechanism of the hydrocarbons. [147-150] Xylene decomposes in toluene, benzene and methane and mainly at the entrance of the furnace, where the temperature is lower due to the non-uniform gradient of temperature inside. This decomposition follows the different gas-phase reactions of the Benson and Shaw mechanism. Thus, a great amount of amorphous carbon is obtained at lower temperatures. However, it can be observed that the feed rate, in the case of synthesis ferrocene/xylene is crucial to obtain MWCNTs with high crystallinity. Higher feed rate, higher values of I_D/I_G ratio, as has previously been observed by Kunadian *et al*. [151]

Thermogravimetric measurements of the samples were carried out on a TGA/SDTA 851ᵉ from Mettler Toledo. Approximately 5 mg of the sample were heated at 10 °C·min^{-1} from 25 °C to 800 °C under an air atmosphere (20 mL·min^{-1}), to determine the oxidative stability of the samples.

Figure 3.4 displays the typical thermogram of MWCNTs. During the thermal oxidation of carbon nanotubes two different stages can be observed: (i) lost weight up to 400 °C corresponding to the amorphous carbon; and (ii) decomposition temperature of MWCNTs, corresponding to the degradation of the carbon backbone.

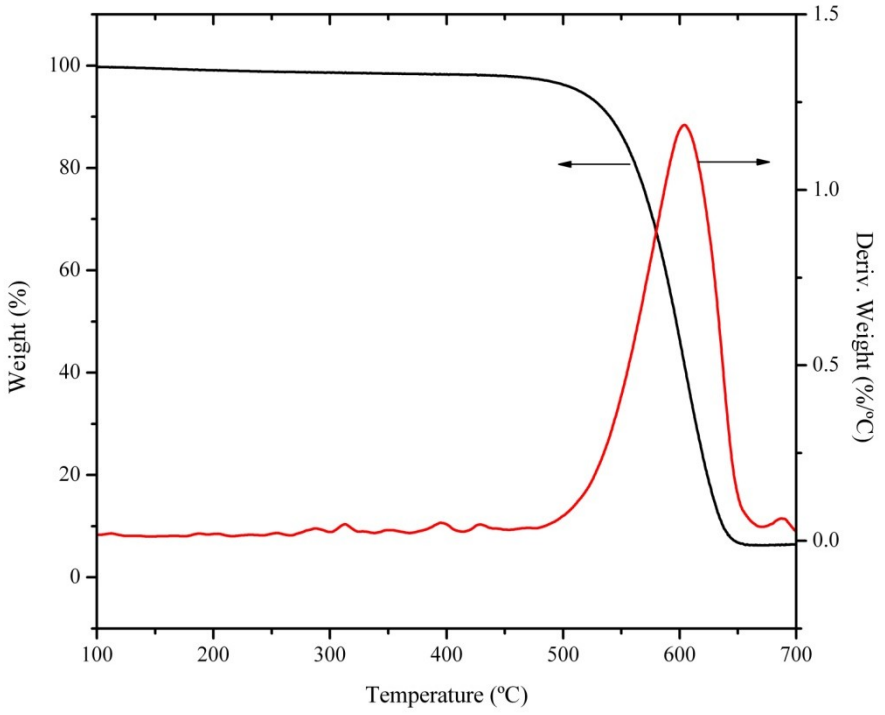

Figure 3.4. Typical TGA of MWCNTs.

Table 3.2 summarises the data obtained from the analysis of the TGA, the temperature at which the decomposition of MWCNTs takes place (T_d) and the weight percent of amorphous carbon from the weight loss at 400 °C. Bom *et al.* [152] and Hunt *et al.* [153] reported in their studies that the decomposition temperature is being reduced for high contents of amorphous carbon due to the thermal oxidative stability of the nanotubes. MWCNTs-S3 displays the higher

decomposition temperature and the lowest weight percent of amorphous carbon which confirms the lower defect sites along the sidewalls of the nanotubes. Recently, Santangelo *et al*. [154] have described a correlation between the Raman I_D/I_G ratio and the thermal oxidative stability of carbon nanotubes. The higher the degree of crystallinity of MWCNTs, the higher the energy needed to oxidise them. Consequently, comparing the results from Raman spectroscopy and TGA, the same correlation is obtained. MWCNTs-S3 is the synthesis with the lowest I_D/I_G ratio and the one with the lowest wt.-% of amorphous carbon and, hence, with the higher thermal stability.

Table 3.2. Decomposition temperature (T_d) and wt.-% of amorphous carbon of the different synthesised MWCNTs.

Synthesis	T_d (°C)	wt.-% amorphous carbon
MWCNTs-S1	597	1.05
MWCNTs-S2	598	0.42
MWCNTs-S3	624	0.30
MWCNTs-S4	592	1.46

The morphology of the MWCNTs was examined using a JEOL J8M 6500f scanning electron microscope (SEM) at 15 kV.

SEM images of MWCNTs-S2 and MWCNTs-S3 are shown in Figure 3.5. It can be observed that MWCNTs synthesised in the laboratory are well-aligned and non-entangled, which would enable easier dispersion protocols of these carbon nanofillers. Nonetheless, carbon nanotubes from toluene (MWCNTs-S3) as carbon source show less impurities and higher degree of alignment than nanotubes from xylene (MWCNTs-S2) corroborating the results obtained from Raman and TGA.

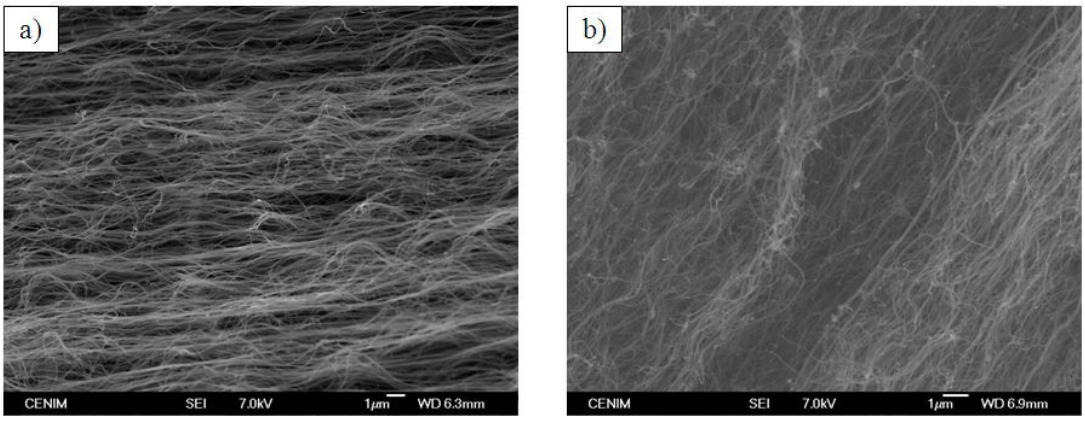

Figure 3.5. Representative SEM image of MWCNTs at a resolution of 1 μm: a) MWCNTs-S3 and b) MWCNTs-S2.

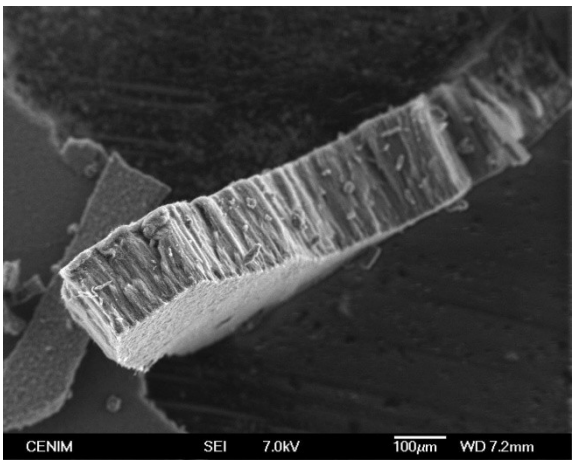

Figure 3.6. Representative SEM image of MWCNTs-S3 at a resolution of 100 μm.

The length of the MWCNTs-S3 measured from the SEM data is ~160 μm (Figure 3.6). On the other hand, the diameter distribution histograms of the MWCNTs (Figure 3.7) are obtained from the analysis of different SEM images using ImageJ software (W.S. Rasband, US. National Institutes of Health, Bethesda). MWCNTs-S1 and MWCNTs-S2 synthesised at higher feed ratios (10 $mL \cdot h^{-1}$) presented narrower diameter distribution than MWCNTs-S3 and MWCNTs-S4. Thereby, increasing the feed injection rate decreases the mean diameter of the nanotubes and narrows their distribution. The effect of high flow rates on the average diameter is related to the number of catalyst particles injected and the

reduction of the growth cycle leading to the pyrolitic overcoating of the nanotubes. [155]

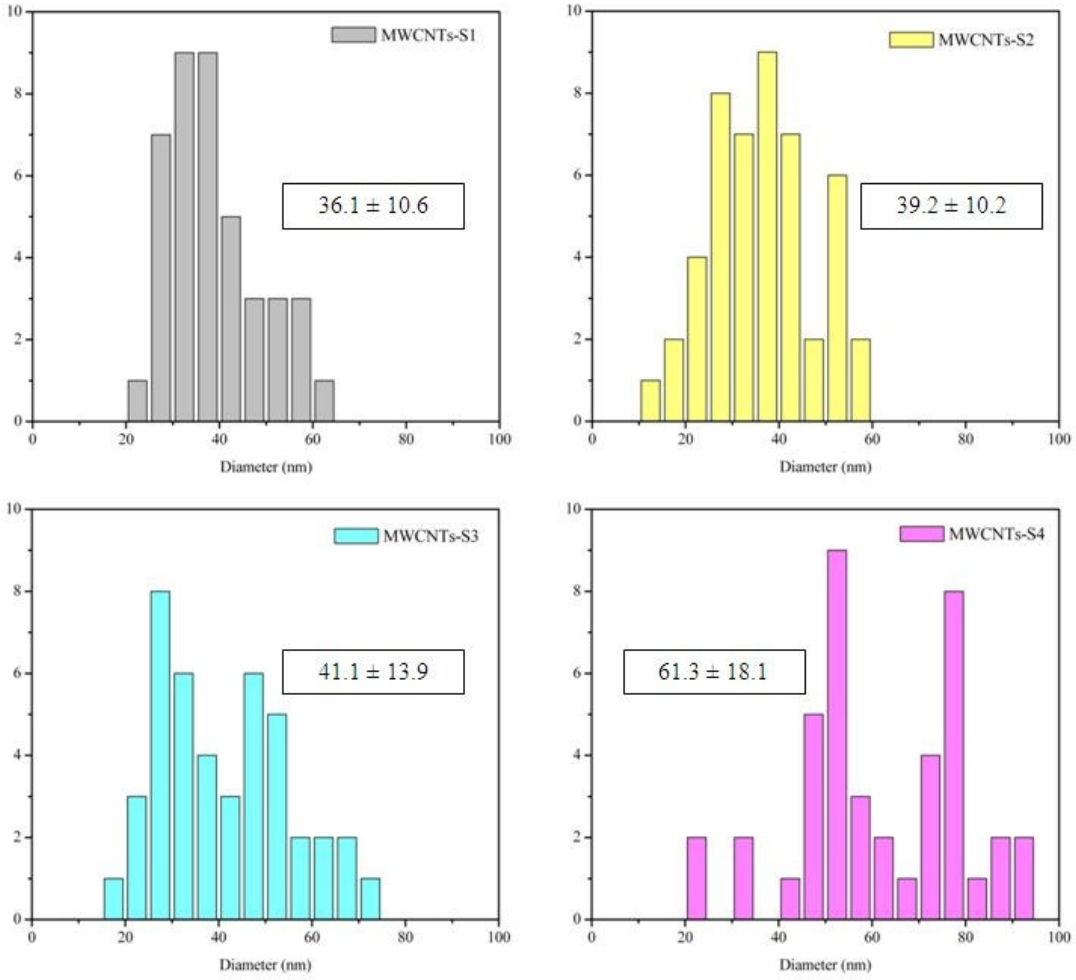

Figure 3.7. Diameter distribution histograms for the different synthesis of MWCNTs.

In summary, after evaluating the results obtained from the analysis of the different synthesis, the MWCNTs grown with toluene as carbon source and at a feed ratio of 5 $mL \cdot h^{-1}$ (MWCNTs-S3) presented the best characteristics in terms of purity and alignment of the grown CNTs and were selected to continue the study.

3.2. FUNCTIONALISATION OF MWCNTS

The chemical functionalisation of CNT surfaces has been a tool widely used to improve the dispersion and the interaction with the polymer matrix at the interface. The functionalisation process reduces the length of carbon nanotubes and introduces functional groups on their surface able to interact with the polymer chains.

The selected MWCNTs (MWCNTs-S3) were chemically treated with a 3:1 concentrated sulphuric/nitric acid mixture and refluxed at 120 °C for 30 min. Then, the mixture was filtered through a glass filter funnel using a PTFE membrane (0.2 μm pore size, Millipore) and washed with distilled water several times until neutral pH. The functionalised MWCNTs (f-MWCNTs) were then dried at 120 °C and stored in a sealed container under vacuum prior to use to avoid possible effects of chemisorbed water due to their hydrophilic nature. [121, 156] A schematic representation of the reaction is given in Figure 3.8.

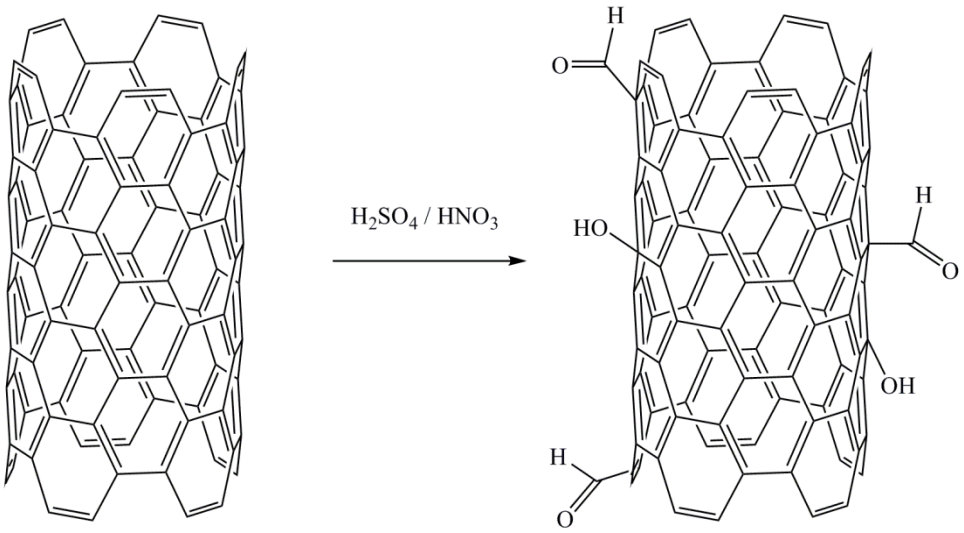

Figure 3.8. Schematic representation of the functionalisation of MWCNTs.

3.2.1. Characterisation of Functionalised MWCNTs

The degree of functionalisation of MWCNTs was evaluated using Raman spectroscopy, X-ray photoelectron spectroscopy (XPS), Fourier transform infrared spectroscopy (FT-IR), transmission electron microscope (TEM) and

thermogravimetric analysis (TGA). The characterisation of f-MWCNTs is compared to pristine MWCNTs in order to corroborate the successful functionalisation of the nanotubes.

The Raman spectra of MWCNTs and f-MWCNTs and the I_D/I_G ratio are shown in Figure 3.9. It is clearly observed an increase on the relative intensity of the *D* band for f-MWCNTs due to the sp^3 carbon which confirms the disruption of the aromatic system of π-electrons because of the functionalisation. [146, 157] Furthermore, it can also be noted that a weak shoulder appears at around 1610 cm^{-1} corresponding to the *D'* band, which confirms the inclusion of defects.

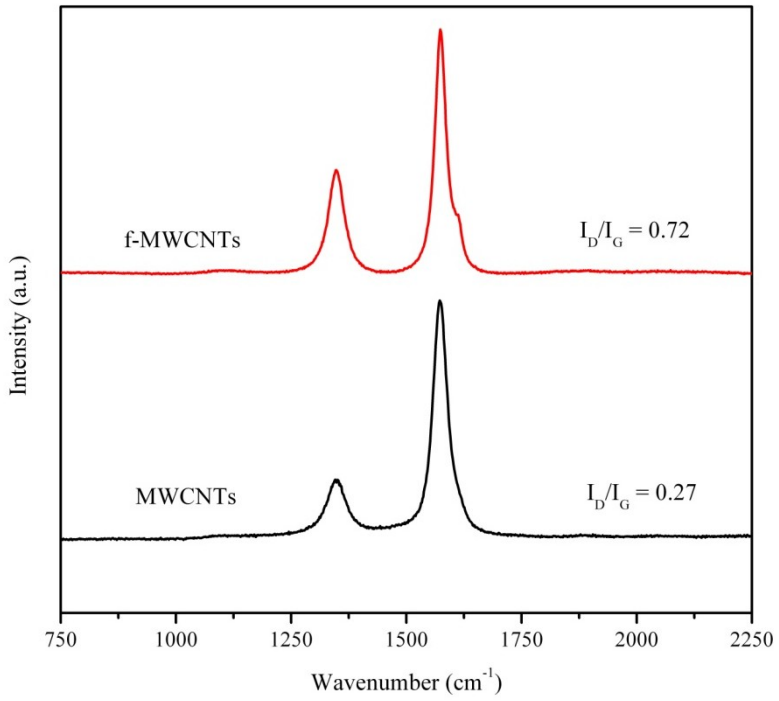

Figure 3.9. Raman spectra of MWCNTs and f-MWCNTs.

XPS studies were performed on a *VG Escalab 200R* spectrometer equipped with a hemispherical electron analyser operated on a constant pass energy mode and non-monochromatised Mg X-ray radiation ($h\upsilon$ = 1253.36 eV) at 10 mA and 12 kV. The samples were first placed in a copper holder mounted on a sample rod in the pre-treatment chamber of the spectrometer and then, degassed at room temperature for 1 h before being transferred to the analysis chamber. Data

analysis was performed with the XPS peak program. The spectra were decomposed by the least-squares fitting routine using a Gauss Lorentz product information after subtracting a Shirley background. The binding energies (BE) were normalised by using the C_{1s} peak (284.8 eV) of carbon as an internal standard.

XPS is used to determine the surface chemical composition and bonding of MWCNTs and f-MWCNTs. The C_{1s} and O_{1s} spectra of carbon nanotubes are shown in Figure 3.10 and the relative amount is reported in Table 3.3. The C_{1s} spectra are dominated by a single peak at 284.8 eV assigned to the sp^2 C-C bonds of graphitic carbon. The deconvolution of the C_{1s} peak into different fitting curves has been assigned to a peak between 285-286 eV of sp^3 C-atoms and the peaks in the region 286.3-290.5 eV assigned to carbon attached to different oxygen groups. It can be observed that C_{1s} spectra show a broad weak component at around 291.5 eV which corresponds to π-π^* transition of carbon atoms in graphene structures. [104, 158-160] The O_{1s} spectrum shows a broad peak indicating that different oxygen-containing groups are present on the surface of the carbon nanofillers (Figure 3.10). The deconvoluted peaks are centred at 532.2 eV and 533.6 eV, corresponding to O=C surface groups and O-C bonds, respectively. [159] The information provided by the C_{1s} spectra is complemented analysing the O_{1s} spectra. The O_{1s} spectra are more surface specific than the C_{1s} because the O_{1s} photoelectron kinetic energies are lower than those of the C_{1s}, and the O_{1s} sampling depth is smaller. [161] As it can be observed in Table 3.3, the functionalisation of MWCNTs introduces new oxygen groups on the surface of the nanofillers and a decrease on the carbon graphitic layer.

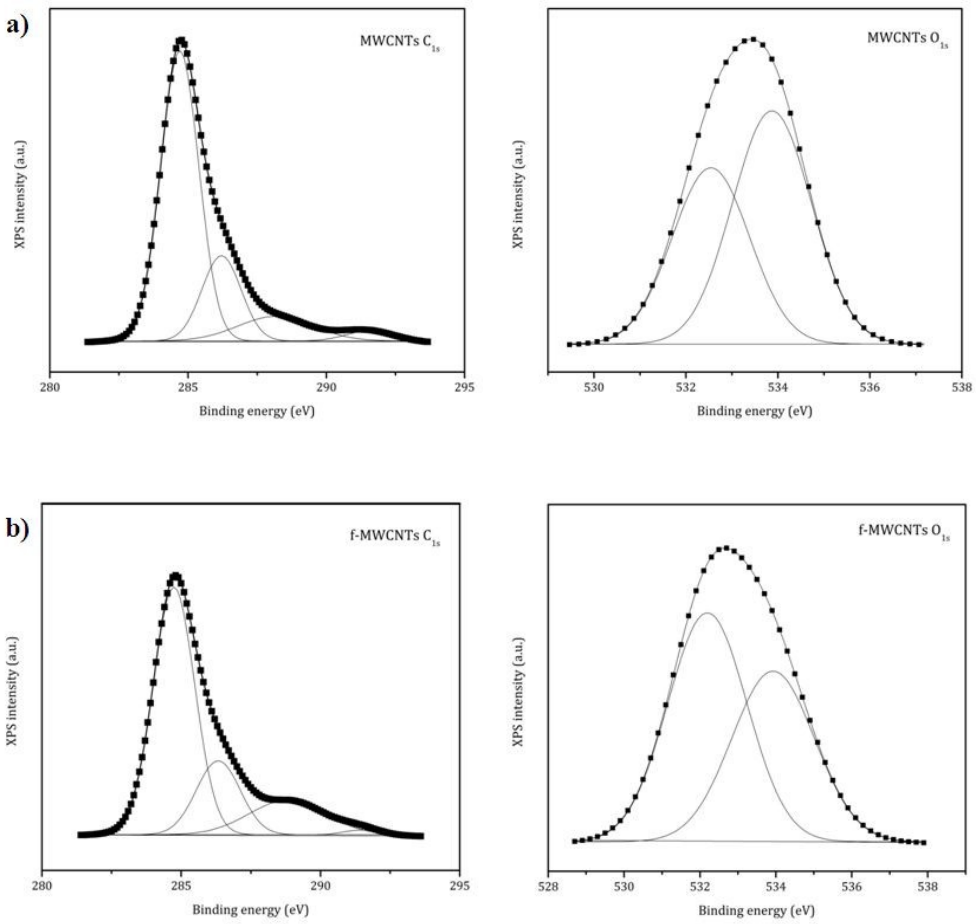

Figure 3.10. High resolution C_{1s} and O_{1s} XPS spectra of: a) MWCNTs and b) f-MWCNTs. Solid lines are fitting curves of the spectra.

Table 3.3. Binding energy (BE), peaks assignment and atomic percentage for MWCNTs, and f-MWCNTs.

Peak	BE (eV)	Assignment	at.-%	
			MWCNTs	f-MWCNTs
C_{1s}	284.6-285.8	C-C sp^2 C-C sp^3	86	63
	286.3-286.5	C-O-C	-	20
	288.0-289.0	-O-C=O	11	16
	291.0-291.5	π-π*	3	1
O_{1s}	532.0-532.5	C=O	43	56
	533.5-533.9	C-O-C	57	44

The surface atomic ratios of oxygen to carbon are calculated from the area of the O_{1s} peak divided by the area of the C_{1s} peak normalised by the atomic sensitivity factors. [162] Hence, the atomic amount of oxygen atoms estimated for MWCNTs and f-MWCNTs are 2.5 % and 17.9 %, respectively. These values confirm the successful functionalisation of f-MWCNTs.

Fourier transform infrared spectra (FT-IR) were obtained on a Perkin-Elmer Spectrum One FT-IR spectrometer accessory and with a resolution of 4 cm^{-1}. The samples for the measurements were prepared mixing the carbon nanofillers with KBr (the concentration of the CNPs in KBr was in the range of 0.2 % to 1 %) and pressing them into pellets at 7 $kp \cdot cm^{-2}$ for 15 min under vacuum conditions. Infrared spectra of MWCNTs and f-MWCNTs are shown in Figure 3.11.

MWCNTs spectrum presents peaks at 2930 and 2850 cm^{-1} due to aliphatic C–H stretches probably associated with debris from amorphous carbon. [163] The band in the region of 3600-3200 cm^{-1}, is assigned to the vibrational modes of the –OH groups, indicating the presence of chemisorbed water in the samples during the preparation of the KBr pellets. [163] The contaminating water is also confirmed due to the appearance of a peak 1630 cm^{-1}. [156]

f-MWCNTs spectrum shows an increase of the 3600-3200 cm^{-1} band due to the functionalisation and the appearance of a shoulder at 1730 cm^{-1} attributed to the C=O stretches. [156] Furthermore, f-MWCNTs present characteristic peaks at 2920 cm^{-1} and 2850 cm^{-1} corresponding to sp^3 CH stretching or asymmetric stretching of sp^3 CH_2 group and to symmetric stretching of sp^3 CH_2 groups, respectively. [164] Meanwhile, peaks in the 1340-1480 cm^{-1} region are assigned to deformation modes of the CH. [165] The high intensity of the bands corresponding to sp^3 further confirms the change from sp^2 to sp^3 hybridisation as a consequence of the oxidation of MWCNTs.

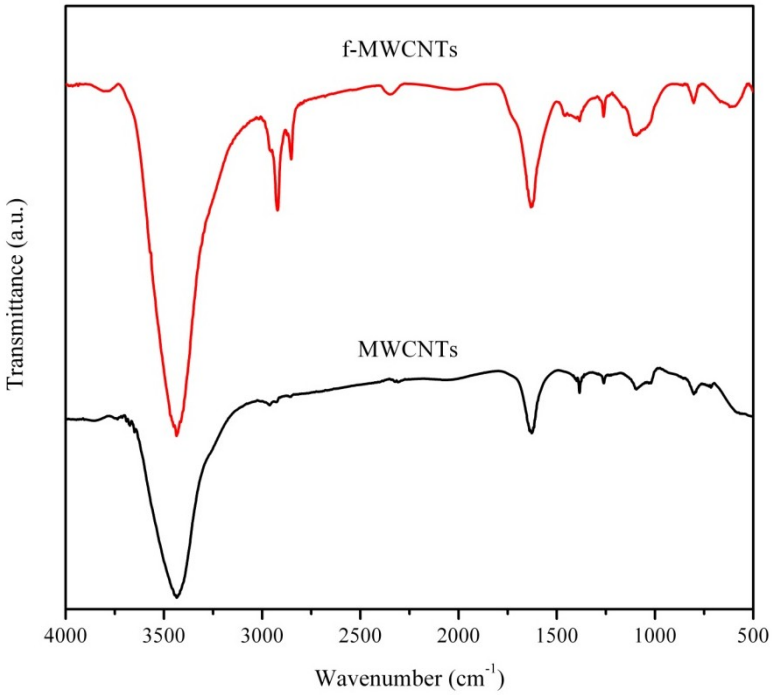

Figure 3.11. Infrared spectra of MWCNTs and f-MWCNTs.

The morphology of CNPs was observed by transmission electron microscopy (TEM). Transmission electron microscope (TEM) images were obtained with a JEOL JEM 2100 TEM apparatus using an accelerating voltage of 200 kV. The samples were prepared by drop-casting a dilute suspension in THF onto a carbon grid and allowing the solvent to evaporate. The images of MWCNTs and f-MWCNTs are shown in Figures 3.12 and 3.13.

Pristine MWCNTs present the characteristic tube-like structure with well-graphitised concentric layers. The diameter of the as-synthesised carbon nanotubes is 41 ± 14 nm and the interlayer distance is 0.34 nm. Low resolution TEM image (Figure 3.12) shows (a), the presence of some catalyst particles can be detected, while high magnification image shows (b) some amorphous carbon on the sidewalls of the carbon nanotubes.

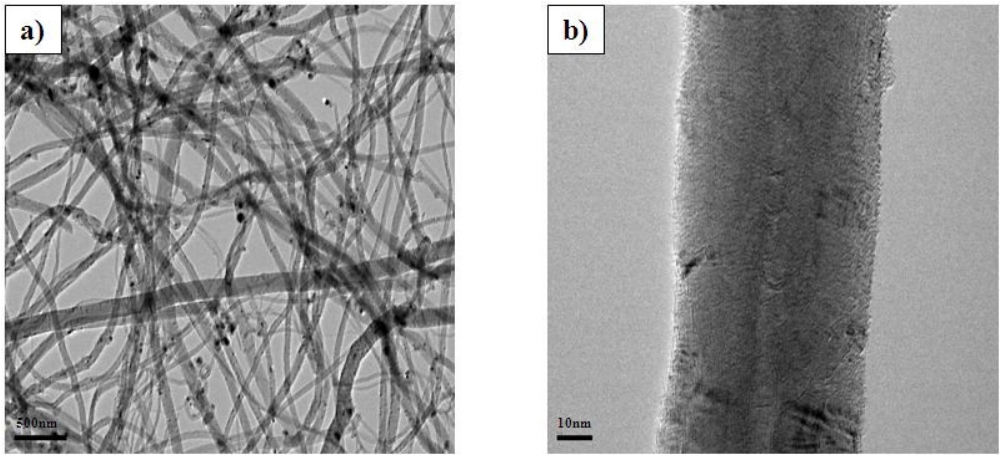

Figure 3.12. TEM image of MWCNTs at a resolution of: a) 500 nm and b) 10 nm.

The effects of the oxidation of carbon nanotubes can clearly be observed in Figure 3.13. The acid treatment of MWCNTs causes severe etching of the graphitic surface and hence the size of the nanofillers is affected. The diameter of f-MWCNTs is 32 ± 11 nm, which is 10 nm smaller than MWCNTs. Furthermore it can be observed an alteration of the structural integrity and the length (~24 μm for f-MWCNTs) of the nanotubes. [166]

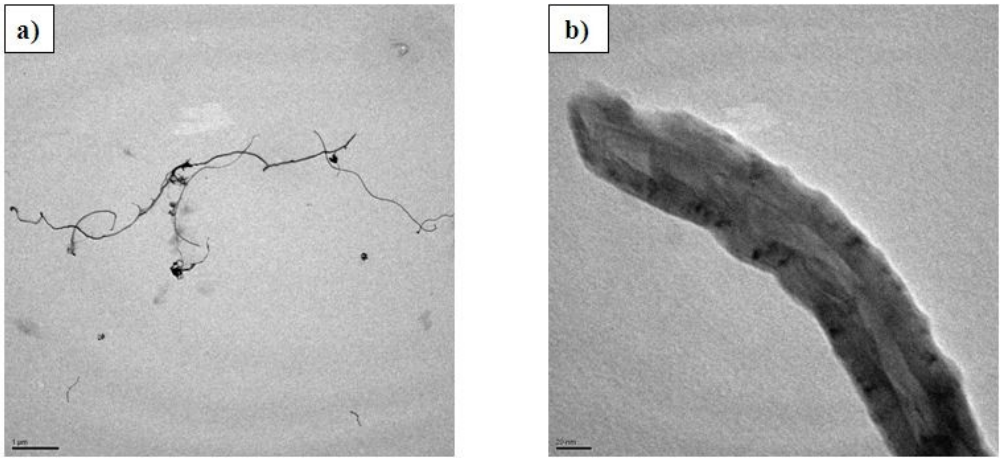

Figure 3.13. TEM image of f-MWCNTs at a resolution of: a) 1 μm and b) 20 nm.

Finally, the thermal stability of the MWCNTs is studied. The thermogravimetric analysis of pristine and functionalised MWCNTs was performed in air atmosphere to study the oxidative stability of these CNPs

(Figure 3.14). The thermogram of f-MWCNTs shows two stages due to the functional moieties attached on the sidewalls of these carbon nanofillers. The first stage is observed at 373 °C and is mainly attributed to the decarboxylation of the COOH groups. [146] However, it can also be observed a weight loss of 5 % between 150 and 300 °C, which corresponds to water and OH groups. The second degradation temperature, corresponding to the thermal oxidation of the carbon backbone occurs at around 595 °C. It can be noticed that the temperature of the f-MWCNTs for the thermal oxidation of the carbon backbone is lower than for pristine MWCNTs (623 °C). The low thermal stability of f-MWCNTs is due to the oxidative process which introduces defects on the structure of the nanotube, reducing its crystallinity.

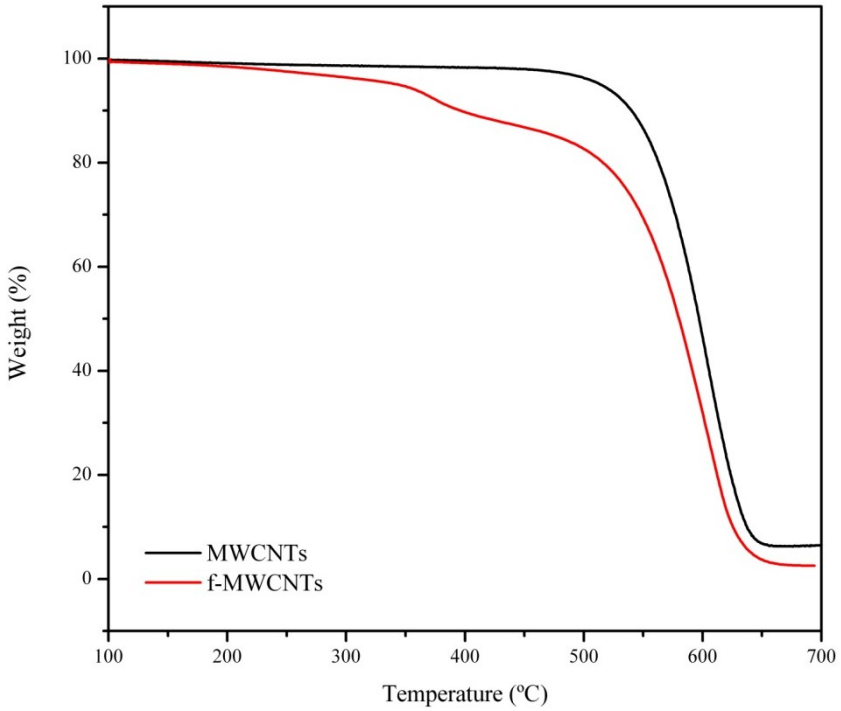

Figure 3.14. TGA analysis of MWCNTs and f-MWCNTs.

3.3. Synthesis and Characterisation of Functionalised Graphene Sheets (FGS)

3.3.1. Synthesis of FGS

The synthesis of functionalised graphene sheets (FGS) was carried out following the steps illustrated in Figure 3.15. First, graphite oxide (GO) was produced using natural graphite (NG) powder (universal grade, 200 mesh, 99.9995 %, Fluka) according to the Brödie method. [18, 167] In a typical preparation procedure, a reaction flask with 20 mL fuming nitric acid was cooled to 0 °C in a cryostat bath for 20 min. Then, the graphite powder (1 g) was carefully added to avoid its agglomeration. After that, $KClO_3$ (8 g) was gradually added over 1 h, in order to avoid sudden increases in temperature due to the exothermic nature of the reaction. The mixture was stirred for 21 h maintaining the reaction temperature at 0 °C. Next, it was diluted in distilled water and filtered using a PTFE membrane until the filtrate reached a neutral pH. The GO obtained was dried and stored in a vacuum oven at 50 °C until use. Then, the GO was thermally exfoliated at 1000 °C and under an inert argon atmosphere for a short time, usually less than 1 min, to produce the FGS. Finally, FGS were stored in a sealed container prior to use.

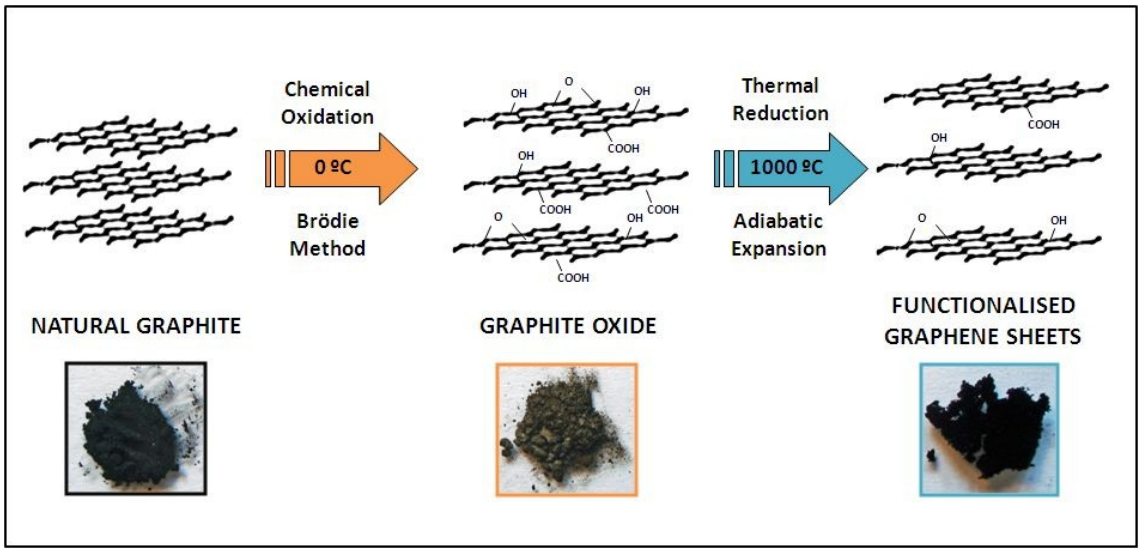

Figure 3.15. Scheme of the synthesis of FGS.

3.3.2. Characterisation of FGS

The morphology and structure of the FGS was successfully characterised by several techniques, X-ray diffraction, Raman spectroscopy, FT-IR spectroscopy, XPS, TEM and TGA.

X-ray diffraction (XRD) data were obtained for natural graphite (NG), graphite oxide (GO) and functionalised graphene sheets (FGS). A diffractometer (*Bruker, D8 Advance*) was employed with a radiation source of CuKα and wave length λ_w= 1.54 Å operated at 40 kV and 40 mA. The incidence angle (2θ) was fixed between 1° and 30° and the scan rate was 0.02 °/s.

The successful exfoliation of FGS is corroborated by the changes on the interlayer distance calculated from the XRD data. X-ray diffraction patterns of the natural graphite (NG), graphite oxide (GO) and functionalised graphene sheets (FGS) are shown in Figure 3.16. Natural graphite presents a peak at 2θ = 26° corresponding to d = 0.34 nm graphite interlayer spacing calculated from the Bragg's law (Equation (3.1)):

$$n\lambda = 2dsin(\theta) \tag{3.1}$$

During the oxidation process of the NG, graphite flakes break down into smaller GO flakes. The value of the 2θ diminishes to 17° (d = 0.52 nm) due to the intercalation by oxygen groups. [109] XRD data of the FGS does not present any diffraction peak indicating the complete exfoliation. [133]

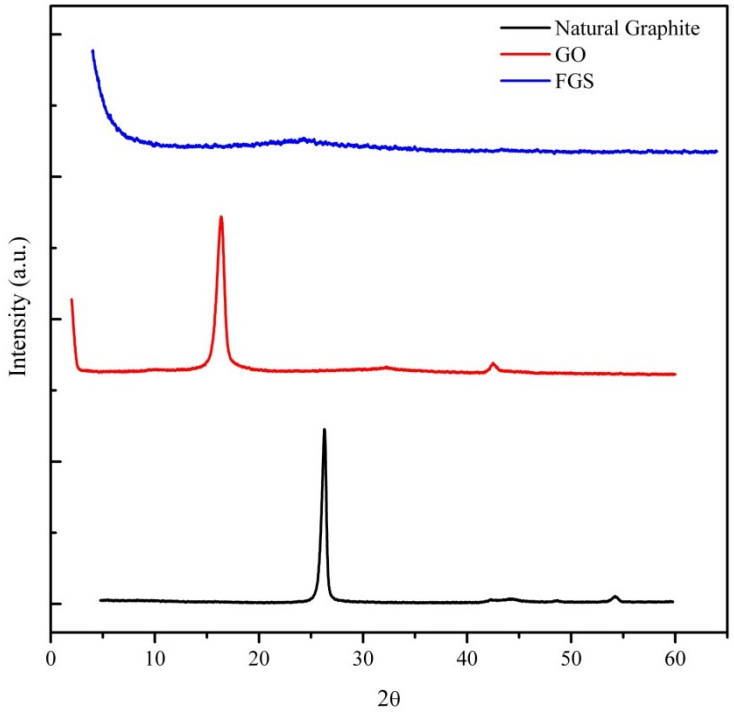

Figure 3.16. X-ray diffraction patterns of NG, GO and FGS.

Raman spectroscopy is a powerful technique in the structural characterisation of graphitic materials. [168] Therefore, the Raman measurements of NG and FGS were performed in order to confirm the changes on the graphite structure of the FGS due to the exfoliation (Figure 3.17). Both Raman spectra present the two well-known relative intensity *D* and *G* bands, previously explained. The Raman spectrum of NG displays the intensity of the *G* band at 1568 cm^{-1} while it upshifts towards 1582 cm^{-1} for FGS which has been attributed to the single-layer graphene sheets. [169, 170] Furthermore, it is worth noting that the *D* and *G* bands broaden for FGS compared to NG thereby increasing the I_D/I_G ratio (Figure 3.17). The changes observed on the *G* and *D* bands for FGS are ascribed to a higher disorder in graphite, confirming that some sp^3 carbon remain in FGS due to the previous functionalisation of NG to GO. [171]

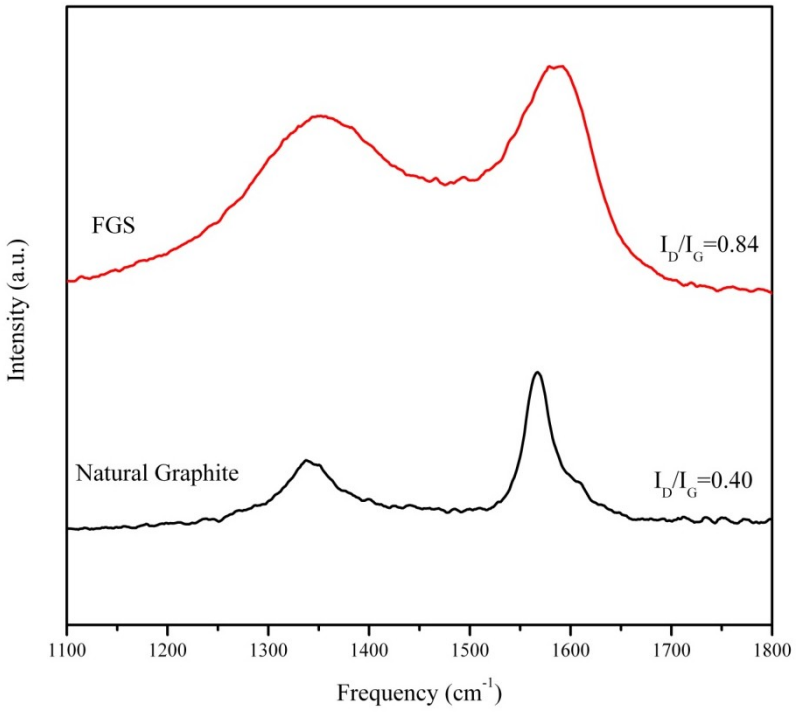

Figure 3.17. Raman spectra of natural graphite and FGS.

XPS was employed to analyse the nature and the relative amount of oxygen-containing functional groups present on the graphene surface.

The C_{1s} and O_{1s} XPS spectra are shown in Figure 3.18 and the relative amount and the corresponding assignment of binding energy are summarised in Table 3.4. All peaks are decomposed into several symmetrical components (four for C_{1s}, two for O_{1s}). The most intense peak between 284.6-285.8 eV in the C_{1s} spectra is assigned to sp^2 and sp^3 carbon atoms. Meanwhile, the peaks on the region 286.3-286.5 eV and 288.0-289.0 eV correspond to C-O-C and –O-C=O functional groups, respectively. [110, 161] It is worth noting that the peak corresponding to the signature of graphitic carbon (291.0-291.5 eV) is still present in the FGS. This peak is known as the shake-up satellite of the 284.5 eV peak and it is characteristic of graphitic systems. [172] This means that the exfoliation process at high temperatures (1000 °C) reduces the GO. [170]

Although the C_{1s} spectrum provides information about the possible functional groups on FGS, some conflicts can be found on the correct assignments

of these groups. Therefore, the O_{1s} spectrum complements the C_{1s} spectrum as has previously been said. Deconvolution of the O_{1s} spectrum resulted into two peaks: (i) at 531.5 eV corresponding to –O-C=O groups and (ii) between 533.5-533.9 eV assigned to C-O-C groups.

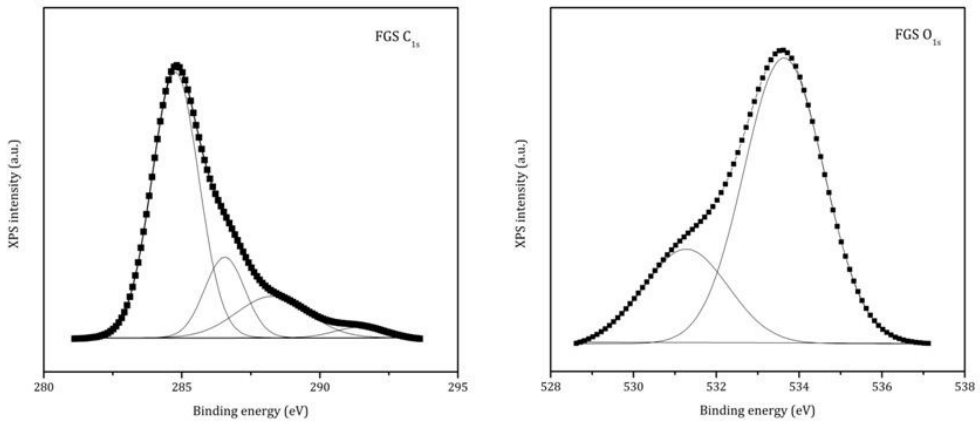

Figure 3.18. High resolution C_{1s} and O_{1s} XPS spectra of FGS. Solid lines are fitting curves of the spectra.

Table 3.4. Binding energy (BE), peaks assignment and atomic percentage for FGS.

Peak	BE (eV)	Assignment	at.-%
C_{1s}	284.6-285.8	C-C sp^2 C-C sp^3	65
	286.3-286.5	C-O-C	17
	288.0-289.0	-O-C=O	16
	291.0-291.5	π-π*	3
O_{1s}	531.5	-O-C=O	26
	533.5-533.9	C-O-C	74

Finally, the surface atomic ratios of oxygen are calculated, as it has been explained before for the XPS of MWCNTs and f-MWCNTs. In the case of FGS, the atomic amount of oxygen atoms estimated is 9.2 %.

The infrared spectrum of FGS is shown in Figure 3.19. It can be clearly observed a broad band absorption in the region 3700-3000 cm^{-1} corresponding to stretching vibration of surface hydroxyls (~3400 cm^{-1}) and water absorption (~3200 cm^{-1}). The features at 2921 cm^{-1} and 2851 cm^{-1} are attributed to asymmetric and symmetric stretching of sp^3 CH_2 groups. [173] There is a shoulder at 1730 cm^{-1} representing C=O stretching and a broad absorption band at ~1630 cm^{-1} corresponding to skeletal vibrations of un-oxidised aromatic domains as well as vibrations of the cyclic ether groups (C-O-C) or water molecules. [174] The band at ~1400 cm^{-1} is assigned to C-OH groups in amorphous defects (sp^3 hybridisation) or particle edges and the significant band at 1261 cm^{-1} represents C-O stretching indicating the presence of the –COOH bonding. [175]

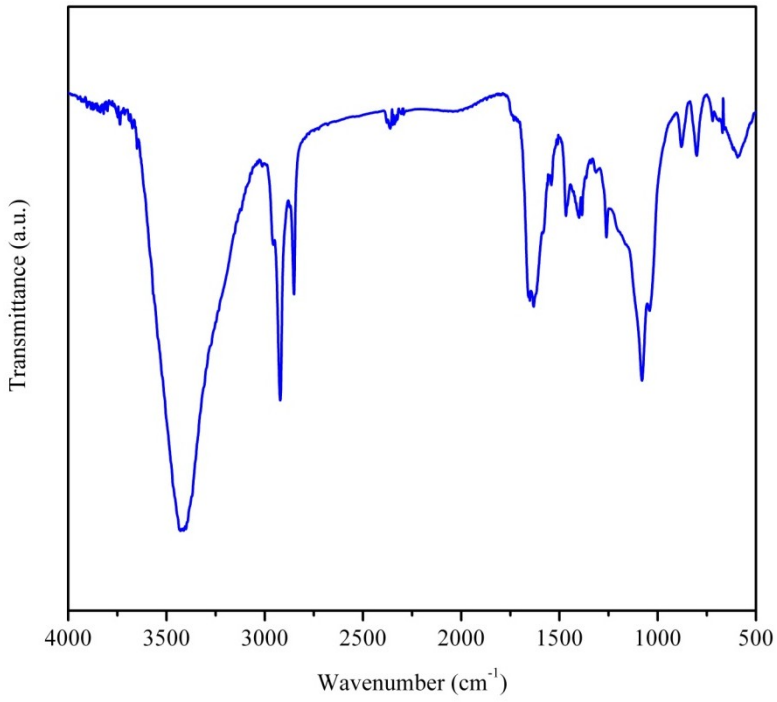

Figure 3.19. Infrared spectra of FGS.

The thermogravimetric analysis of FGS in air atmosphere is presented in Figure 3.20. The FGS sample shows two degradation temperatures at 285 °C and 575 °C. The first degradation temperature corresponds to the functional groups such as hydroxyl, carboxyl and epoxy groups on the surface of the graphene sheets,

as observed by FT-IR and XPS. The second step at 575 °C is due to the degradation of the carbon backbone.

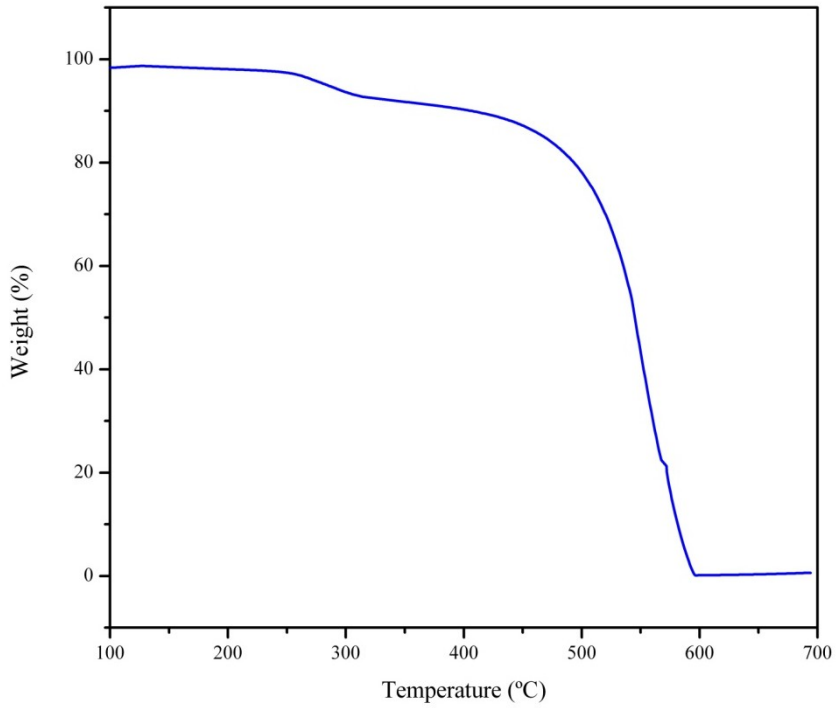

Figure 3.20. TGA analysis of FGS.

HRTEM images (Figure 3.21 a) show the characteristic wrinkled structure of the particle due to the thermal shock to which it has been subjected. Figure 3.21 b) shows the presence of stacks of a small number of graphene sheets, of up to 7 layers, with inter-graphene spacing of 0.6 nm. The selected area electron diffraction (SAED) pattern of those stacks presents only weak and diffuse rings, confirming the loss of long range ordering. This result is in agreement with a recent study where the exfoliation of FGS particles on single sheets was found to be roughly 80 % of the material. [109]

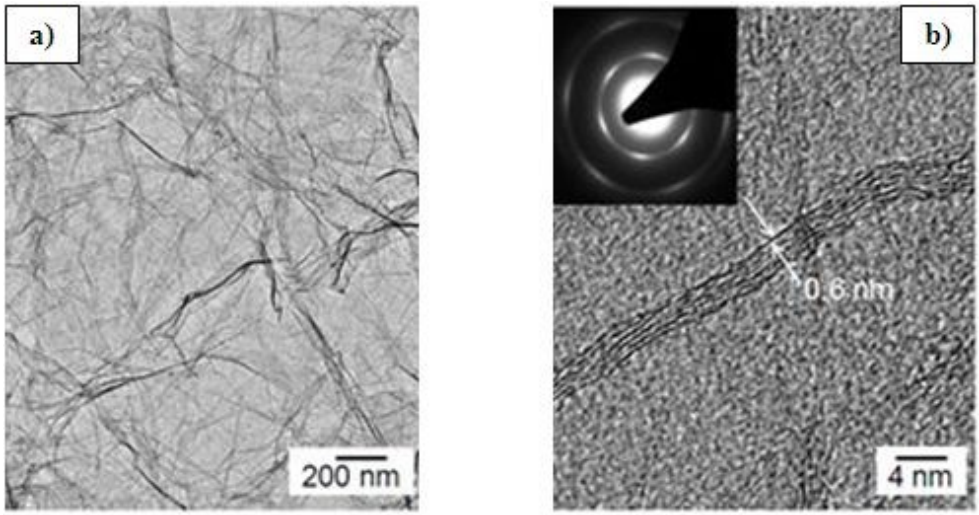

Figure 3.21. TEM image of FGS at a resolution of: a) 200 nm and b) 4 nm.

3.4. CONCLUSIONS

In this chapter, CNPs (MWCNTs, f-MWCNTs and FGS) have been synthesised, functionalised and characterised to be used as reinforcements of the flexible and rigid polyurethane foams.

MWCNTs were synthesised by the CVD method varying the parameters of the growth process, in order to obtain nanotubes with the required characteristics to be introduced in the polymer systems. The amount of defects within the carbon nanotubes was studied by Raman spectroscopy. Less defects means higher degree of purity and thus, better properties. These results were correlated with the data obtained from the thermogravimetric analysis. Samples with a lower defect degree display higher thermal oxidative stability and lower amount of amorphous carbon. The alignment and average diameters of the nanotubes were obtained by SEM. As a result, the sample synthesised at lower reaction rate and using toluene as the carbon source was selected as the most appropriate for the purpose of the study.

The selected MWCNTs were then functionalised in order to favour the compatibility polymer-nanoparticle in the later process. The successful functionalisation of MWCNTs was confirmed by comparing both, MWCNTs and f-MWCNTs, by different techniques. Raman spectrum of f-MWCNTs displayed an

increase on the number of defects due to the disruption of the aromatic structure by the functional groups. In addition, XPS results showed an increase on the atomic amount of oxygen atoms from 2.5 % for MWCNTs to 17.9 % for f-MWCNTs and facilitated the type of functional groups formed during the functionalisation. These results were also corroborated by FT-IR spectroscopy. The thermal oxidative stability of the nanotubes was affected by the oxidation and a reduction on the temperature of decomposition of the carbon backbone was observed. Finally, TEM images showed the effect of the acid treatment on the sidewalls of the nanotubes, reducing the diameter and the length of the nanotube.

FGS was synthesised by the thermal expansion of the GO. The exfoliation of the FGS was confirmed from the XRD data where the peak corresponding to the NG almost disappears. Meanwhile, Raman spectroscopy displayed an increase of the relative intensities for FGS and an upshift of the *G* band attributed to the single-layer graphene sheets. Additionally, XPS spectra confirmed the presence of some functional groups attached on the layers that could also be observed in the FT-IR spectrum. Finally, HRTEM images established the exfoliation of the FGS on single sheets.

4. FLEXIBLE POLYURETHANE NANOCOMPOSITE FOAMS

Flexible PU (FPU) foams are lightweight materials with a characteristic open-cell structure that provides them of interesting properties, which can be improved by the introduction of fillers such as CNPs.

The aim of this chapter is to analyse both the effects of CNPs in the kinetics of polymerisation and foaming evolution and in the final properties of FPU foams with two different phase-separated morphologies. Hence, two FPU systems are developed with different HS/SS ratio and filled with the CNPs previously synthesised. This Thesis establishes a comprehensive knowledge of the matrix morphology and cellular structure of the systems and relates them to the final properties of the foam. The dispersions of MWCNTs show a strong shear-thinning behaviour, with a rheological percolation threshold at 0.1 wt.-%. Meanwhile, the polyol/FGS dispersions present a Newtonian behaviour even at 0.5 wt.-%. All the CNPs slow down the polymerisation reaction and the foaming evolution, leading to an increase on the foam density. A sensible enhancement of the thermal, mechanical and electrical properties are observed by adding the CNPs, being FGS the most effective for FPU. The observed effects of the CNPs in the FPU foams appear to be less pronounced in systems with high content of hard segments due to the rigidity of these materials.

4.1. MATERIALS AND METHODS

4.1.1. Materials

Two sets of FPU nanocomposite foams (25 % and 32.5 % HS) were prepared following the formulation summarised in Table 4.1. The amount of each component was based on parts by hundred parts of polyol (phpp).

Table 4.1. Flexible polyurethane foam formulations.

Material	Description	(25 % HS)	(32.5 % HS)
Voranol 6150	Polyether polyol	100	100
Voranol CP1421	Polyether polyol	4	4
Voranate 2940	Isocyanate	40.4	55.3
DEOA	Cross-link	0.8	0.8
TEDA-L33B	Amine catalyst	0.25	0.25
NIAX E-A-1	Amine catalyst	0.1	0.1
FASCAT	Tin catalyst	0.05	0.05
SH 209	Surfactant	0.4	0.4
Water	Blowing agent	2	3
CNPs	Fillers	0.1 0.5	0.1 0.5

Due to the strong effect of the hard segments on the properties of FPU foams, two contents of HS were considered. The amounts of water and isocyanate were calculated to obtain hard segment contents of 25 % and 32.5 % and keeping constant the isocyanate index at 100. The hard segment (HS) and soft segment (SS) contents were calculated using the equations (4.1), (4.2) and (4.3) and assuming that HS are formed via the reaction of isocyanate with water, DEOA, and OH on polyol. [176]

$$HS = E_{H2O}x_{H2O} + E_{DEOA}x_{DEOA} + E_{iso}(x_{H2O} + x_{DEOA}) \quad (4.1)$$

$$SS = E_{OH}x_{OH} + E_{iso}x_{iso} \quad (4.2)$$

$$HS(\%) = \frac{HS}{HS + SS} \times 100 \quad (4.3)$$

where E is the equivalent molecular weight, x are the equivalents and subscripts H_2O, $DEOA$, iso and OH refer to water, DEOA, isocyanate and polyol, respectively.

The polyol used for the synthesis of FPU foams was a highly reactive polyether based triol, Voranol 6150 (Dow Plastics). The polyether-based triol Voranol CP1421 (Dow Plastics) was used as a cell-opener in the reaction. Both polyols presented an average functionality of 3. The properties of the polyols used are summarised in Table 4.2.

Table 4.2. Properties of polyols used.

Polyol	Voranol 6150	Voranol CP1421
Hydroxyl number (mg KOH·g^{-1})	27	31
Molecular weight (g·mol^{-1})	6000	5000
Viscosity (mPa s^{-1}, 25 °C)	1150	1400
Acid number (mg KOH·g^{-1})	0.050	0.2
Density (g·cm^{-3})	1026	1091

The isocyanate was a methylene diphenyl diisocyanate (MDI), Voranate M2940 from Dow Plastics. It is a low viscosity (49 mPa·s^{-1}, 25 °C) polymeric material with an isocyanate content of 31.4 wt.-%.

The additives used in the formulation were: FASCAT 4202 (dibutyl dilaurate from Arkema Inc.) as tin-based catalyst for the gelling reaction, TEDA L-33B (a solution of 33 % triethylendiamine in 1,4-butanediol) and NIAX E-A-1 (a solution of 70 % bis(2-dimethylaminoethyl) ether in 30 wt.-% dipropylene glycol) as amine derivative catalysts in the water/isocyanate and polyol/isocyanate reactions, balancing the tin catalyst, DEOA (85 % diethanolamine in water) as a cross-linker agent, SH-209 as silicone surfactant and distilled water as blowing agent.

4.1.2. Synthesis

FPU nanocomposite foams were prepared in two steps. First, CNPs (MWCNTs, f-MWCNTs and FGS) were added into the polyol (Voranol 6150), stirred

for 6 hours at 2400 rpm and ultra-sonicated for 20 minutes with a probe, within a water/ice bath to avoid temperature rising. Afterwards, the catalysts, surfactant and water were added to the polyol-carbon nanofiller dispersion and stirred again for 3 min at 2400 rpm. To reduce the reaction rate for *in-situ* experiments, both polyol mixture and isocyanate were maintained at 5 °C until use, when the isocyanate was added to the mixture and stirred for 20 seconds (Figure 4.1).

Two loading fractions in polyol were initially studied (0.1 phpp and 0.5 phpp) by rheology. Due to the low effect of the lower loading fraction on the rhelogical behaviour of the dispersions, the rest of the analysis was performed on the high loading fraction systems. The 0.5 phpp of CNPs (MWCNTs, f-MWCNTs and FGS) correspond to 0.30 wt.-% in the final foam (Figure 4.2).

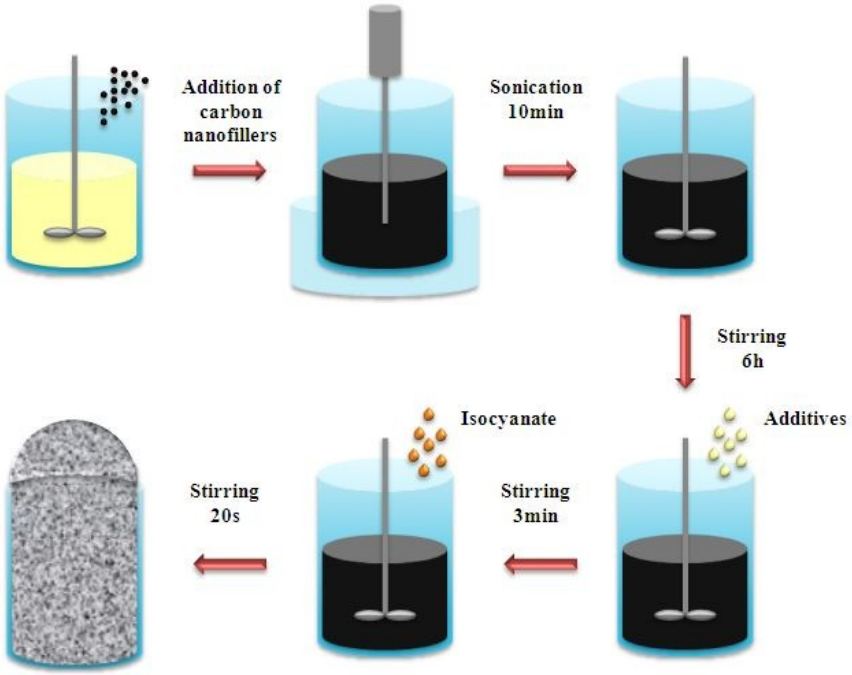

Figure 4.1. Schematic representation of the synthesis of polyurethane nanocomposite foams.

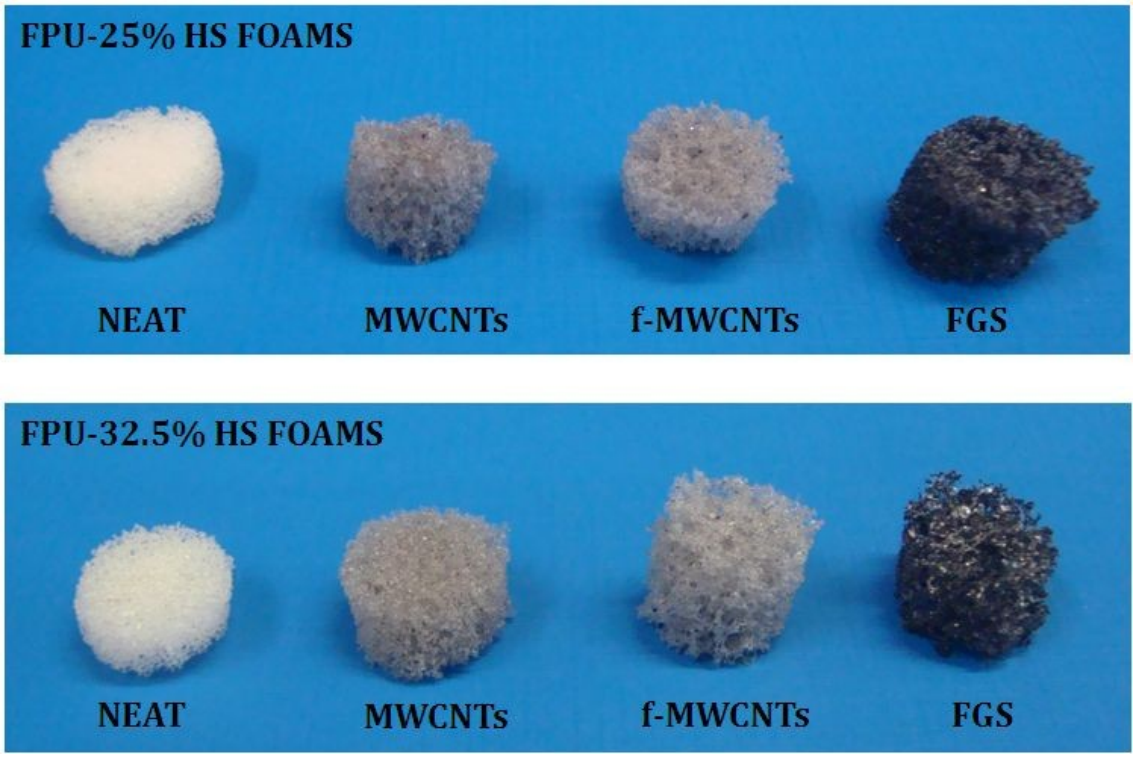

Figure 4.2. FPU nanocomposite samples.

4.1.3. Characterisation

The viscosity of the polyol/CNP dispersions was measured using a TA Instruments Advanced Rheometer AR1000. The geometry used was a stainless-steel corrugated parallel plate with a diameter of 20 mm. The gap was fixed to 0.6 mm and the measurements were recorded in frequency from 0.01 to 10 Hz at 21 °C and at an oscillation stress of 6.4 Pa. The results were averaged over three different samples. The standard error for each set of samples was less than 1 %.

The infrared data were recorded on a Perkin-Elmer Spectrum One FT-IR spectrometer using the attenuated total reflectance (ATR) technique. Data were collected at 8 cm^{-1} resolution co-adding 6 scans per spectrum. The scanning time was about 2 seconds per spectrum and the reaction was followed for 1800 sec. An air background was performed at 4 cm^{-1} resolution and co-adding 256 scans prior to the execution of the reaction. The reactive mixture was placed in direct contact with the diamond crystal of the FT-IR where the foaming process occurred while monitoring the polymerisation kinetics. A background file was recorded prior to

each run at 4 cm^{-1} resolution co-adding 6 scans per spectrum. A total of five spectra per sample were recorded and analysed to obtain statistically-relevant data.

Synchrotron SAXS experiments were carried out at the Spanish operated BM16-CRG beamline of the European Synchrotron Radiation Facility (ESRF) in Grenoble. The X-ray beam energy was fixed to the Se-K to the edge (λ = 0.9795 Å). Data were collected using a MarCCD165 detector (MarResearch) in 1024 x 1024 pixels resolution mode (effective pixel size of 156 µm). The distance of the sample to the detector was set to 3420 mm. The experimental procedure performed was as follows: the isocyanate was added to the polyol dispersions and mixed for 20 sec. Then, the reactive mixture was injected into the SAXS cell by means of a syringe. Samples were loaded in BM16-CRG designed flat cells for which 25 µm thick mica foils were used as windows. Experimental temperature (T = 5 °C) was achieved by circulating a fluid in the cell. Data processing was performed using Fit2D software and BM16-CRG routines. The reactions were recorded for 1500 sec.

Atomic force microscopy images were obtained using a tapping mode AFM (multimode Nanoscope Iva, Digital Instrument/Veeco) under ambient conditions. The oscillation frequency for the tapping mode was set to approximately 320 kHz. FPU nanocomposite foams were compressed into solid sheets at 140 °C and 200 bar in an electrically heated hydraulic press (Gumix TP 300/450/1) for 1 h. The final thicknesses of the samples were ~ 150 µm.

X-ray radioscopy was used to analyse the density changes of FPU nanocomposite foams. Figure 4.3 shows a scheme of the set up developed to perform the X-ray radioscopy experiments. A microfocus X-ray tube from Hamamatsu was used to produce the X-rays (spot size: 5-20 µm, voltage: 20-100 kV, current: 0-200 µA) with a maximum output power of 20 W. A high resolution detector (12 bits, area 120 x 120 mm^2, 2240 x 2344 pixels, pixel size: 50 µm) was placed in front of the X-ray source, acting as a screen. This setup allows magnification of the radiated object. The source-detector (*SD*) distance was fixed at 580 mm and the object-source (*OS*) at 80 mm, yielding a magnification (*M*) of 7.25, applying Equation (4.4). Radiographs of each sample were recorded every 0.8 sec for ~ 500 sec.

$$M = \frac{SD}{OS} \tag{4.4}$$

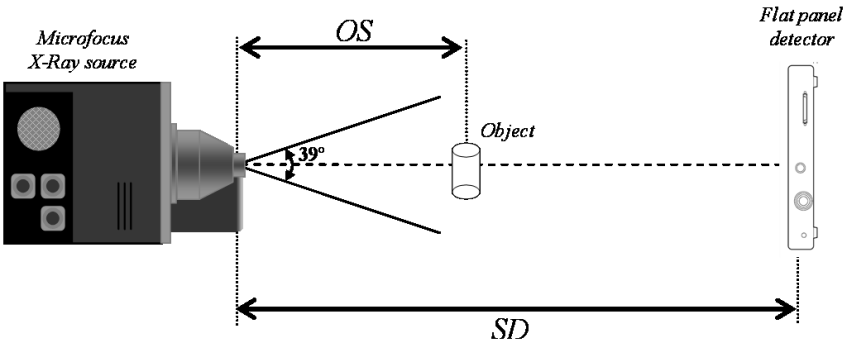

Figure 4.3. Schematic view of the X-ray radioscopy system.

The structure of the FPU nanocomposite foams was qualitatively examined using a Philips XL30 environmental scanning electron microscope (ESEM) at 15 kV. Cross-sections of the samples were cryo-fractured perpendicular to the foaming direction and the fracture surface was sputter-coated with gold/palladium.

The density of a cubic sample was measured as the sample weight divided by its volume according to ASTM D 3574-11. The results are the average of at least three different foam samples.

Thermogravimetric analysis (TGA) of 5 mg of foam samples was performed on a TGA Q500, TA Analysis, under air environment at a heating rate of 20 °C·min^{-1} over a temperature range of 25 - 700 °C.

The glass transition temperature (T_g) of FPU nanocomposite foams was measured by means of differential scanning calorimetry (DSC) of 6 mg of the samples using a Mettler Toledo DSC 822^e connected to a cooling system. Experiments were carried out from -100 °C to 25 °C at 10 °C·min^{-1} under 10 ml·min^{-1} of dry nitrogen atmosphere.

Dynamic mechanical analysis (DMA) was performed on a DMA/SDTA 861[e], Mettler Toledo, in compression mode. The samples were measured at frequencies of 1, 2, 5 and 10 Hz and heated at a rate of 3 °C·min^{-1}. The samples had 10 mm of diameter and 5 mm of thickness.

The electromagnetic interference (EMI) characterisation was reported as a set of scattering parameters. The *S*-parameters (S_{mn}) of foam nanocomposites were measured with a Wiltron 360B vector network analyser (VNA) in a frequency range from 8 to 12 GHz (X-band). The *S* parameter is known as the scattering parameter. For S_{mn}, *m* corresponds to the network analyser port number that receives the scattered energy, while *n* is the network analyser port number that transmits the incident energy. Nanocomposite foams were cut into a rectangle (2.9 x 1.07 cm^2) to fit a steel waveguide sample holder. A full two-port VNA calibration was performed at the beginning of each test sequence to correct systematic measurement errors. The reported results were the average of three tested samples for each foam. The measured scattering parameters are: S_{11}, the forward reflection coefficient; S_{21}, the forward transmission coefficient; S_{22}, the reverse reflection coefficient; and S_{12}, the reverse transmission coefficient. The unit of the *S*-parameters is decibels (dB).

4.2. RESULTS AND DISCUSSION

4.2.1. Rheology of Dispersions

The foaming evolution of polyurethane foams involves the interplay of several physical phenomena such as surface tension and bulk viscosity [23] of the initial reactants which determine the final cellular microstructure of the system. Therefore, the rheological properties of the initial polyol/CNP dispersions determine the flow behaviour of the systems and the later foaming process. The concentration of CNPs as well as their size, shape, presence or lack of functional groups, adsorption affinity of the polymer on the surface of the nanoparticles and the chain bridging between the nanofillers influence the rheological behaviour of the CNP dispersions. [7, 177-181] The dependence of the complex viscosity with

the angular frequency for neat polyol and its filled dispersions at 0.1 and 0.5 phpp of CNPs is shown in Figure 4.4.

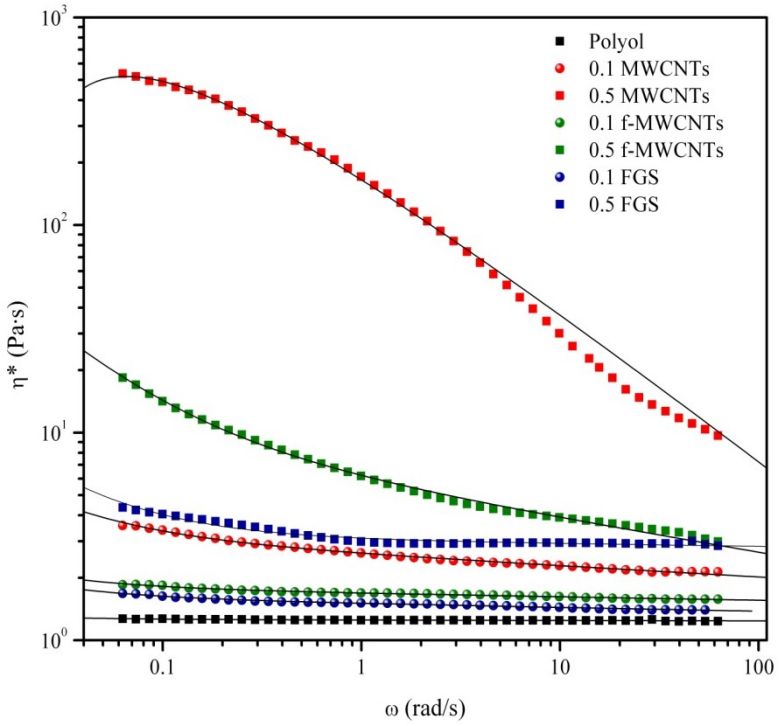

Figure 4.4. Variation of the complex viscosity (η^*) as a function of the angular frequency (ω) for polyol/CNP dispersions. The solid lines are the fit to the Herschel-Bulkley model.

The rheological behaviour of polyol/CNP dispersions is further analysed by the Herschel-Bulkley model (Equation (4.5)). This model describes a non-linear power law fluid with a yield stress and is valid for a wide range of dispersions, emulsions and foams. [182-184] The model has also been applied to carbon nanotube dispersions [183, 185, 186] and, in particular, to polyol/CNT dispersions: [185]

$$\eta^* = \frac{\tau_0}{\omega} + k\omega^{n-1} \tag{4.5}$$

where η^* is the complex viscosity, ω the angular frequency, τ_0 the yield stress, k the consistency index and n is the flow behaviour index. If $n > 1$, the fluid shows a shear-thickening behaviour; for $n = 1$, it behaves as a Newtonian fluid with

a yield stress term added to it (or Bingham fluid); and for $n < 1$, the fluid shows a shear-thinning behaviour. Table 4.3 summarises the parameters obtained from the fitting of the Herschel-Bulkley model to experimental data and the correlation coefficient (r^2).

Table 4.3. Parameters and the correlation coefficient (r^2) of the Herschel-Bulkley model for the polyol/CNP dispersions.

Sample	τ_0 (Pa)	k (Pa·s^n)	n	r^2
Polyol	≈0	1.25	0.99	0.91
0.1 MWCNTs	0.04	2.59	0.95	0.99
0.5 MWCNTs	18.14	162.23	0.51	0.82
0.1 f-MWCNTs	0.01	1.68	0.98	0.99
0.5 f-MWCNTs	0.61	5.62	0.85	0.99
0.1 FGS	0.01	1.50	0.99	0.98
0.5 FGS	0.09	3.01	0.98	0.95

As expected, the addition of CNPs resulted in an increase of the complex viscosity and a dependency of frequency with loading fraction. [187-189] There is a change on the rheology behaviour from a Newtonian fluid to a non-linear power law fluid with yield stress. This change has been associated to the formation of an interconnected structure of CNPs that restrains the motion of the polymer chains hence, indicating the existence of a rheological percolation network. [187]

CNPs show a very different rheological behaviour. The polyol dispersions at 0.5 phpp MWCNTs and f-MWCNTs show a shear-thinning behaviour, in particular as-produced MWCNTs, while the polyol/FGS dispersions exhibit still a quasi-linear behaviour at these concentrations.

The dispersions of carbon nanotubes can be considered as rods in solution and, according to Doi and Edwards theory, [190, 191] the rheology of rods in solution is strongly dependent on rod concentration and aspect ratio. The functionalisation of the MWCNTs produces a less marked change of the complex viscosity compared to as-produced MWCNTs, which is attributed to a shorter nanotube length as a result of the aggressive acid treatment. [178]

The increase of the viscosity on polymer nanocomposites has been related to the formation of a nanoparticle network, via direct contacts or bridging by polymer chains. [179, 192] While high loading fractions of MWCNTs present a shear-thinning behaviour, polyol/FGS dispersions only show a weak increase of the viscosity compared to the neat polyol. This different behaviour is related to their different morphology. MWCNTs are rod-shape nanoparticles that facilitate interchain and entanglement interactions, and lead to a strong network due to the large intertube Van der Waals interactions as described by Knauert *et al*. [179] and Pujari *et al*. [193]. Meanwhile, FGS are considered as platelet-like nanoparticles with high aspect ratio and large interfacial areas, which in addition possess functional groups on their surface. Therefore, a great amount of molecules are adsorbed on the FGS surface through hydrogen-bonding or electrostatic interactions, reducing the interactions of the sheets within the dispersions. [179, 194]

4.2.2. Kinetics of Foaming Evolution

The formation of FPU foams is a complex process that involves many ingredients and several competing reactions. [11] The polymerisation kinetics of the PU foams and the development of the morphology are usually studied by infrared spectroscopy. [33, 41, 42, 195] In the analysis of the infrared spectra of polyurethanes (Figure 4.5), four regions are studied: (1) the NH stretching region between 3500-3200 cm^{-1}, (2) the amide I region known as the carbonyl region between 1800-1600 cm^{-1}, (3) the isocyanate absorbance band approximately at 2270 cm^{-1} and (4) the amide II region below 1600 cm^{-1}. The complex nature of the peaks in the amide II region and the variations in the extinction coefficient with hydrogen bonding in the NH stretching region difficult their analysis and hence the study has been focused on the decrease of the isocyanate band and the evolution of the carbonyl groups in the amide I region. [42, 50]

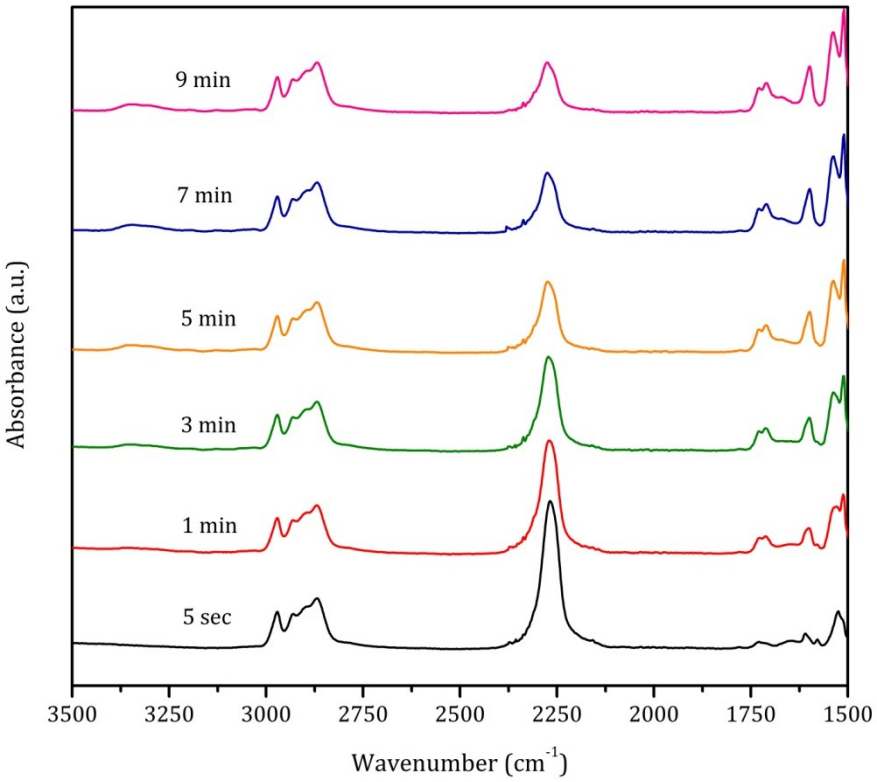

Figure 4.5. Infrared spectra of FPU foams at different reaction times illustrating the evolution of the different regions.

The extent of the reaction in PU foams is determined following the isocyanate conversion during the reaction by FT-IR. [195] The isocyanate absorption band appears at approximately 2270 cm^{-1} and it is normalised to an internal reference band that remains constant during the reaction (CH stretch at 2970 cm^{-1}), to compensate for the density change. Hence, the conversion is defined by:

$$p_{NCO} = 1 - \frac{A_{NCO}}{A_0} \tag{4.6}$$

where A_{NCO} is the integrated intensity of the normalised isocyanate absorbance band, and A_0 is the normalised isocyanate absorbance band at zero reaction time.

The isocyanate conversion for FPU-25% HS and FPU-32.5% HS nanocomposite foams is shown in Figures 4.6 and 4.7, respectively. A common practice in PU foam chemistry is to add an excess of isocyanate in the reaction over that required for chain extension and cross-linking [11] and thus, the isocyanate is not fully converted.

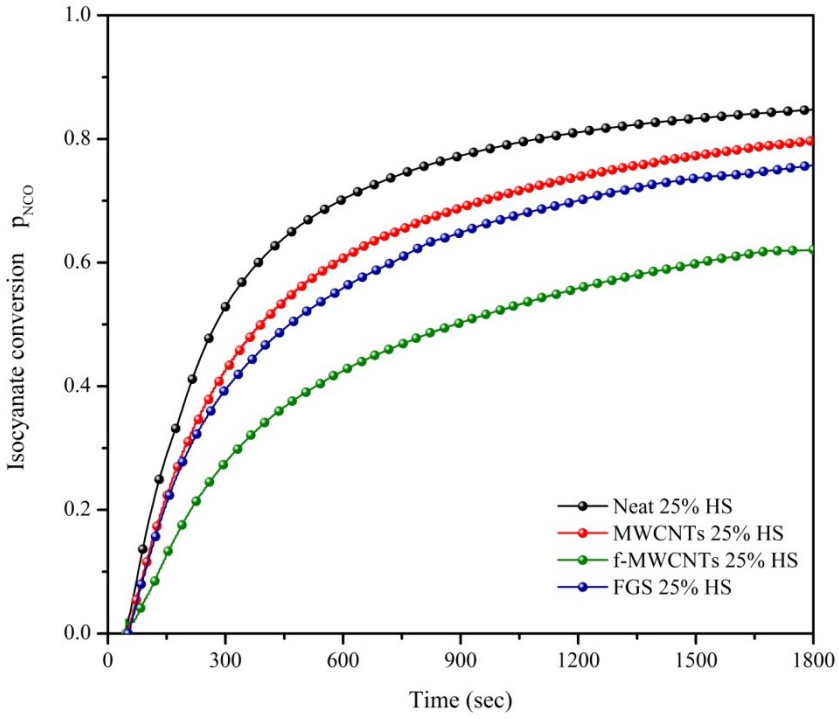

Figure 4.6. Isocyanate conversion, p_{NCO}, as a function of time for FPU-25% HS nanocomposite foams.

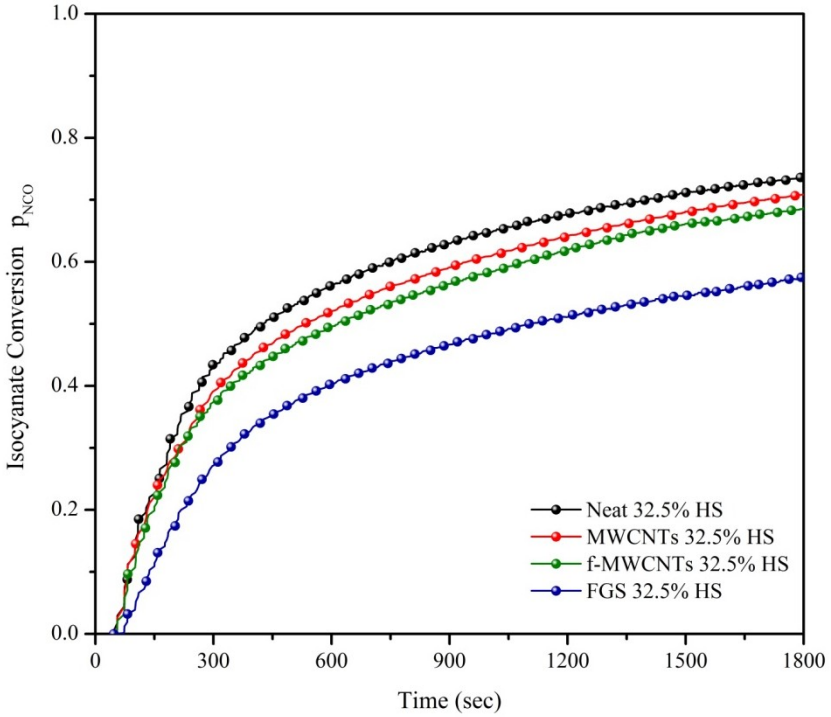

Figure 4.7. Isocyanate conversion, p_{NCO}, as a function of time for FPU-32.5% HS nanocomposite foams.

The morphology and properties of polyurethane foams are determined by the chemical reactions taking place during the curing reaction of the polymer. The degree of cure can be expressed as:

$$p(t) = \int_0^t dp \tag{4.7}$$

Different kinetic models, based on empirical rate laws, can be employed to describe the curing process of PU systems. The rate can be expressed as a function of curing degree and temperature and the basic equation is:

$$\frac{dp}{dt} = k(T)f(p) \tag{4.8}$$

The equations (4.7) and (4.8) and n^{th} order kinetics models are widely used for the modelling of the thermosetting polymers. [196, 197] The kinetic data are determined taking into account the approximation of Li *et al*. [198] to a n^{th} order kinetics approach, widely used for the modelling of PUs. [199-201]

$$\frac{dp}{dt} = k_0(1-p)^n \tag{4.9}$$

The integration of the equation (4.9) for a first, second and third order reaction, respectively, results in:

$$n = 1 \quad ln(1-p) = -k_0 t + C \tag{4.10}$$

$$n = 2 \quad \frac{1}{(1-p)} = k_0 t + C \tag{4.11}$$

$$n = 3 \quad \frac{1}{(1-p)^2} = -k_0 t + C \tag{4.12}$$

where p is the isocyanate conversion, n is related to the order of the reaction, k_0 is the kinetic constant, t is the time value and C is the integration constant. Equations (4.10), (4.11) and (4.12) are applied to the isocyanate conversion data in order to find the appropriate kinetic model. In this study, the reaction of both sets of FPU nanocomposite foams follows a third-order kinetics resulting from the autocatalytic effect of hydrogen bonding between the hydroxyl groups and the formed urethane and urea groups. [202-204] Figures 4.8 and 4.9 illustrate the third order kinetic model applied to FPU nanocomposite foams while the fitting results are summarised in Table 4.4.

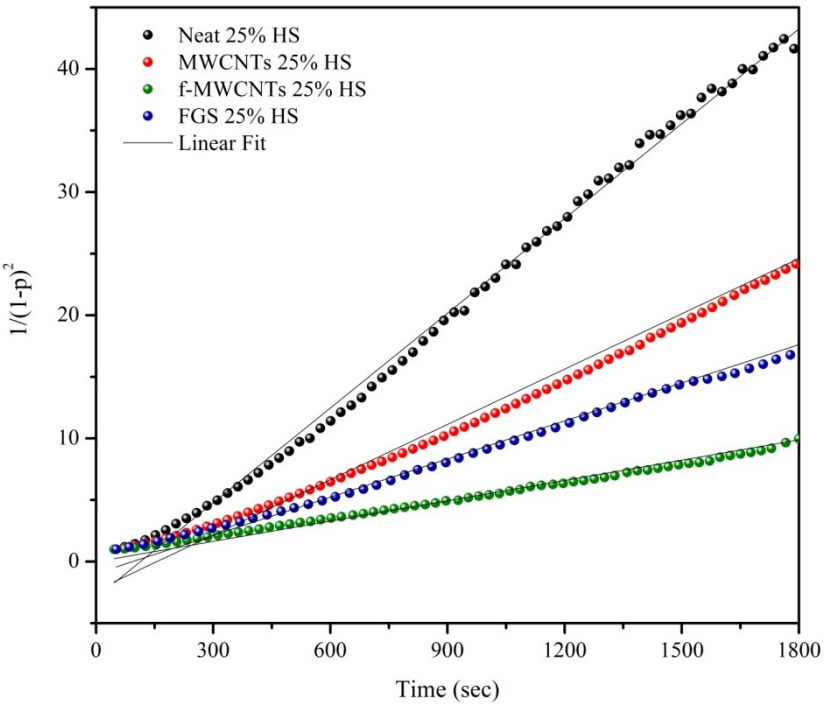

Figure 4.8. Third-order kinetic model for FPU-25% HS nanocomposite foams.

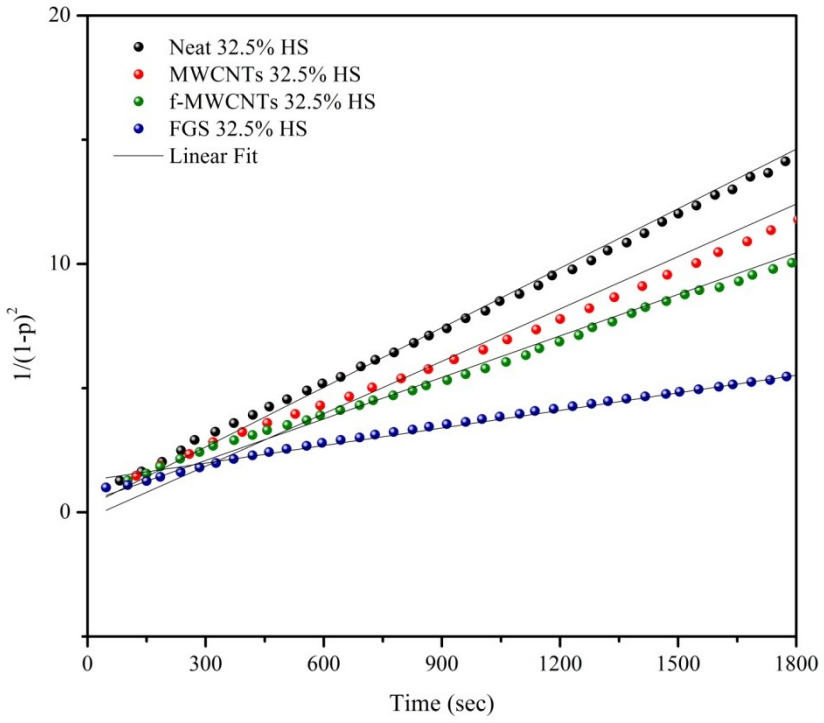

Figure 4.9. Third-order kinetic model for FPU-32.5% HS nanocomposite foams.

Table 4.4. Rate constants k (sec) and fitting results (r^2) for FPU nanocomposite foams.

	Sample	(1st order)		(2nd order)		(3rd order)	
		k	r^2	k	r^2	k	r^2
25 % HS	Neat	$4.1 \cdot 10^{-4}$	0.779	$2.0 \cdot 10^{-3}$	0.935	0.026	0.995
	MWCNTs	$4.2 \cdot 10^{-4}$	0.863	$1.0 \cdot 10^{-3}$	0.976	0.015	0.998
	f-MWCNTs	$3.5 \cdot 10^{-4}$	0.913	$0.9 \cdot 10^{-3}$	0.933	0.006	0.992
	FGS	$3.9 \cdot 10^{-4}$	0.879	$1.0 \cdot 10^{-3}$	0.930	0.010	0.998
32.5% HS	Neat	$3.5 \cdot 10^{-4}$	0.884	$1.0 \cdot 10^{-3}$	0.970	0.008	0.999
	MWCNTs	$3.4 \cdot 10^{-4}$	0.918	$1.0 \cdot 10^{-3}$	0.960	0.007	0.995
	f-MWCNTs	$3.3 \cdot 10^{-4}$	0.912	$0.9 \cdot 10^{-3}$	0.936	0.006	0.998
	FGS	$2.5 \cdot 10^{-4}$	0.904	$0.5 \cdot 10^{-3}$	0.973	0.002	0.998

The evolution of the phase-separated morphology, characteristic of polyurethanes, implies the competition between the kinetics of polymerisation, kinetics of phase separation and vitrification of hard segments. [43] Thus, the rate of reaction depends on the competitive reactions during the process, including the reactions with the functional groups present on the surface of the nanoparticles. Once these reactions have taken place, the mobility of the recently formed urea HS groups, depends on the local constraints. Hence, the reaction kinetics is strongly influenced by the HS content (Figures 4.6 and 4.7). The FPU-25% HS nanocomposite foams reach a maximum isocyanate conversion of about 80 % at 1800 sec, while the isocyanate conversion only reaches 70 % or even lower for the FPU-32.5% HS samples. This decrease on the rate and isocyanate conversion is ascribed to an increase in the viscosity of the system and, hence, a restriction of the chain mobility due to the larger HS content. This result agrees well with previously reported studies of the effect of HS content on the isocyanate conversion. [33, 50, 205]

The inclusion of CNPs also affects the rate of polymerisation as can be observed in Figures 4.6 and 4.7. The mobility of CNP systems is further hindered by both, the rigidity of these nanoparticles and their obstruction to the formation and aggregation of new hydrogen bonds between the HS. In addition, the influence of the CNPs on the rate of reaction varies for the different sets of FPU foams but, in

all cases, there is a decrease on the extent of reaction (Table 4.4). In order to describe the effect of the CNPs, it has to be taken into account two factors: the morphology of the nanofillers and the type and proportion of oxygen-bearing groups on their surface. The morphology of MWCNTs and f-MWCNTs can be considered as rod-like nanoparticles while FGS are platelet-like nanofillers with high surface area. The functional groups attached on the sidewalls of f-MWCNTs are mainly C-OH and COOH, while FGS present C-OH, COOH and C-O groups as determined by XPS (See Chapter 3).

Therefore, pristine MWCNTs slow down the rate of the isocyanate conversion on both sets of FPU foams due to the restriction on the mobility of the systems mentioned above. However, the deceleration is less pronounced for MWCNTs FPU-32.5% HS foams because the increase on HS content already significantly delays the reaction. Besides the rigidity effect observed for pristine MWCNTs, f-MWCNTs present COOH groups on their surface which can deactivate the tin catalyst of the isocyanate-polyol reaction. [206] Thus, the kinetics of polymerisation of the formulations with f-MWCNTs is slower than the one with MWCNTs. Meanwhile, the samples filled with FGS present an even slower polymerisation reaction than f-MWNTs and MWNTs samples for high contents of HS. The explanation to this behaviour would be the result of an additional effect probably related to the presence of C-O groups. It has been reported [207] that adsorbed polar molecules, such as water, on the graphene surface tends to move towards oxidised edges creating in some cases hydrogen bonds with the oxygen of the C-O bonds (H···O-C). A charge transfer between graphene and the hydrogen atoms in water molecules is then created and its efficiency increases with the number of water molecules. Hence, the dramatic deceleration observed on FPU-32.5% HS foams filled with FGS would be attributed to the formation of hydrogen bonds with the C-O groups on the surface of the graphene due to the increase of water content in these foams. Consequently, the water molecules available for the reaction with isocyanate are reduced and the reaction is slower compared to FPU-25% HS foams with the same content of FGS.

On the other hand, synchrotron SAXS measurements are used to analyse the influence of the hard segment content and the presence of the CNPs on the formation of the microphase separated structure. Figure 4.10 shows a representative plot of scattered intensity, *I(q,t)*, against scattering vector, *q*, at different reaction times for FPU-25% HS foam. The scattering vector, *q*, is defined as:

$$q = \left(\frac{2}{\lambda}\right) sin\left(\frac{\theta}{2}\right) \tag{4.13}$$

Where λ is the wavelength of the X-ray beam source and θ is the radial scattering angle.

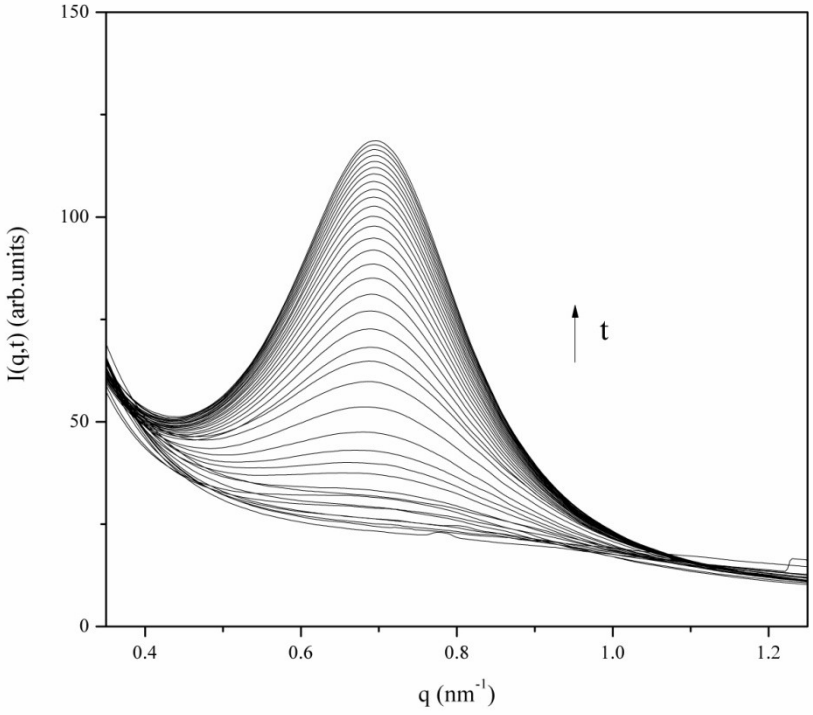

Figure 4.10. Evolution of the scattered intensity, *I(q,t)*, vs the scattering vector, *q*, during the reaction time of FPU-25% HS foam.

It can be observed, in all cases, that at the early stages of the reaction there is a homogeneous liquid present. Then, once the microphase separation transition is achieved, a scattering maximum can be detected and its intensity progressively

increases until a constant value is reached. This constant value can be related to the Berghmans point of the FPU foams where vitrification freezes the morphology. [11]

Therefore, the maximum observed in *I(q)* is indicative of the presence of a periodic structure within the systems. Equation (4.14), derived from Bragg's law, is applied in order to determine the average interdomain spacing *(d)*, which is inversely proportional to the scattering vector q_{max} calculated from the Lorentz corrected plot $I(q)q^2$ vs q.

$$d = \frac{2\pi}{q_{max}} \tag{4.14}$$

The evolution of the interdomain spacing is calculated from the first reliable q_{max} obtained from the $I(q)q^2$ vs q plots to the end of the measurements (1500 sec). Figures 4.11 and 4.12 show the development of d as a function of time for FPU-25% HS and FPU-32.5% HS nanocomposite foams, respectively. It is observed that the interdomain spacing continuously increases until the microphase separation is arrested by vitrification. This increase in the interdomain spacing could be related to the increase of the size of the urea hard segments. [43] It can be noticed that the trend followed by the rate of formation of the interdomain spacing is similar to the rate of isocyanate conversion analysed by FT-IR for both sets of FPU nanocomposite foams. Hence, it appears to be a correlation between the kinetics of polymerisation and the kinetics of phase separation of hard segments. Table 4.5 summarises the values of the interdomain spacing (d) obtained at the final point of the experiments. However, it should be noted that for FPU-32.5% HS nanocomposite foams the development of the HS does not reach the plateau at the end of the measurement (Figures 4.11 and 4.12) and hence it would continue afterwards.

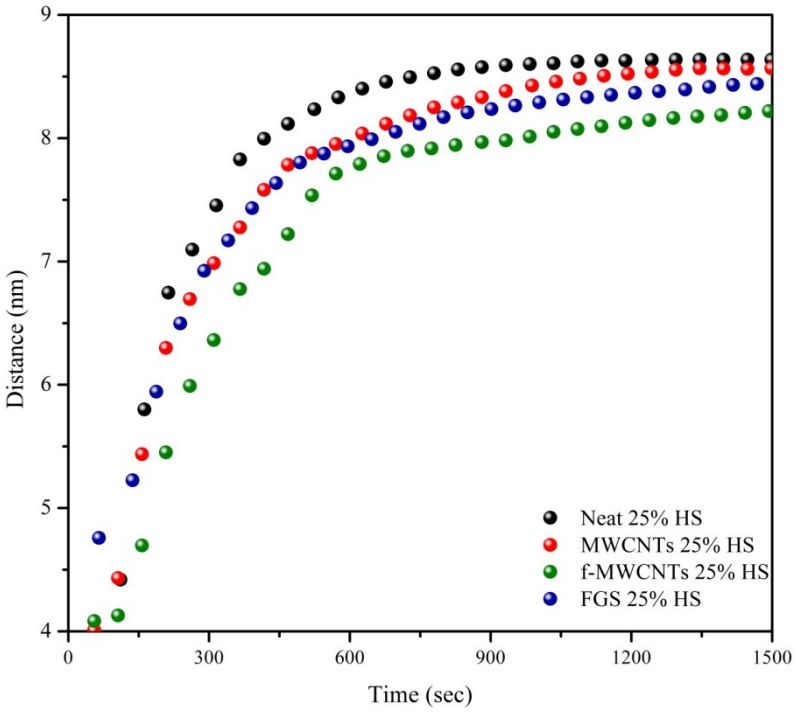

Figure 4.11. Evolution of the interdomain spacing, *d*, with time for FPU-25% HS nanocomposite foams.

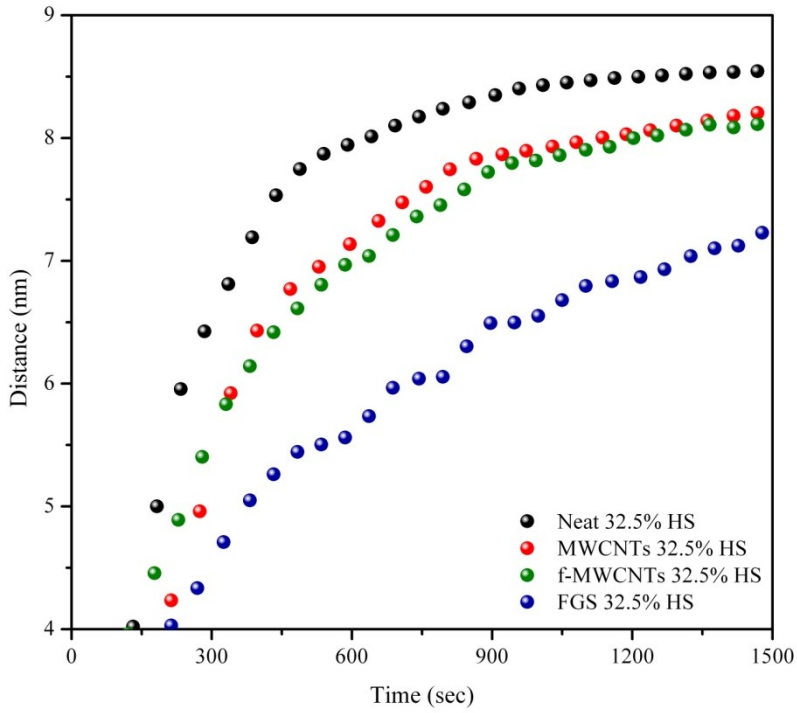

Figure 4.12. Evolution of the interdomain spacing, *d*, with time for FPU-32.5% HS nanocomposite foams.

The interdomain spacing could also be estimated using the one-dimensional correlation function $\gamma(r)$ which is related to the electron density fluctuation within the system and is defined by Equation (4.15):

$$\gamma(r) = \frac{1}{Q}\int_0^\infty I(q)q^2 cos(qr)\, dq \tag{4.15}$$

In Figures 4.13 and 4.14, the correlation functions for the two FPU foam systems at the end of the measurements are plotted. The one-dimensional correlation function shows periodicity for both FPU foam series indicating a two-phase structure in the systems [40, 208-210] and the first maximum observed in the correlation curve is associated with the interdomain spacing or long period (L_p). The values of the long period at 1500 sec of reaction are reported in Table 4.5 and are in good agreement with those estimated using Bragg's law. The increase of the HS content and the presence of carbon nanotubes (MWCNTs and f-MWCNTs) have little influence on the interdomain spacing. [40] However, the inclusion of FGS decreases this value for systems with high contents of HS. As it has been explained in the FT-IR results, the higher water content on FPU-32.5% HS nanocomposite foams enhance the efficiency of the charge transfer between the graphene and the hydrogen atoms of the water molecules which would thus affect the phase-separated structure of the HS.

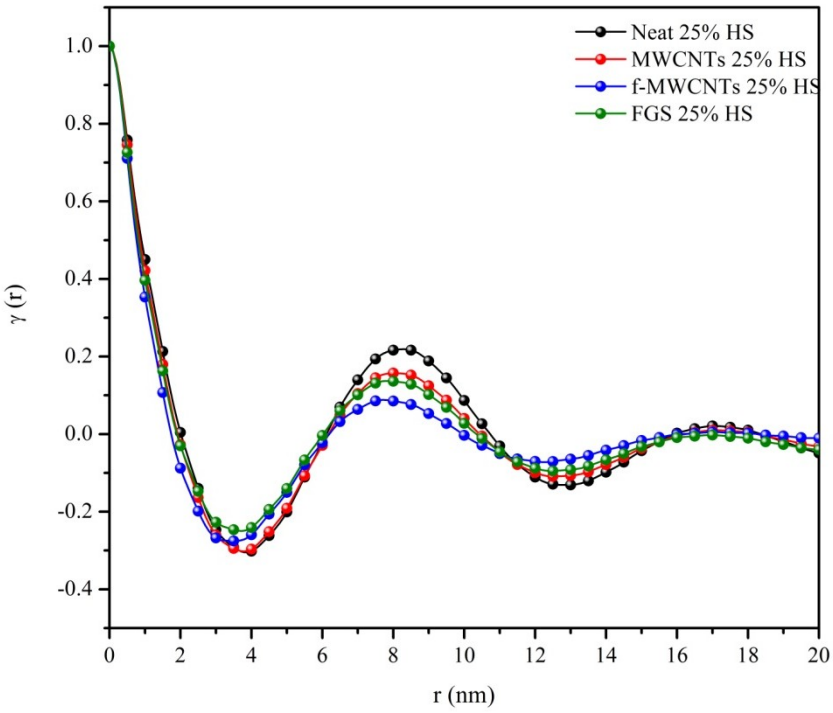

Figure 4.13. One-dimensional correlation function $\gamma(r)$ of the SAXS data for FPU-25% HS nanocomposites foams.

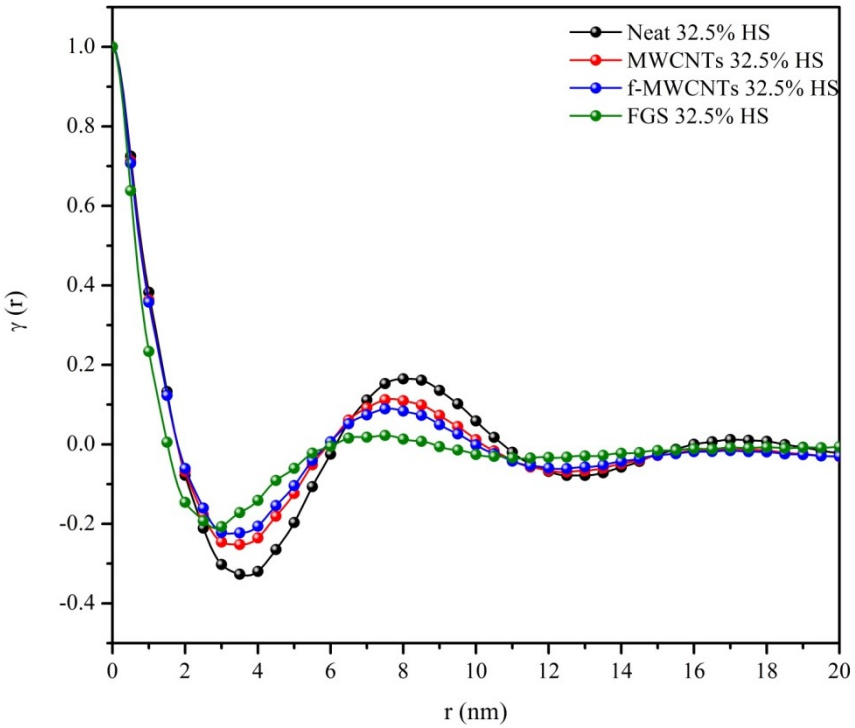

Figure 4.14. One-dimensional correlation function $\gamma(r)$ of the SAXS data for FPU-32.5% HS nanocomposites foams.

Table 4.5. Interdomain spacing (d) calculated from the Lorentz corrected plot and long period (L_p) estimated by the correlation function at 1500 sec.

	Sample	d (nm)	L_p (nm)
25% HS	Neat	8.6	8.3
	MWCNTs	8.5	8.0
	f-MWCNTs	8.2	7.7
	FGS	8.4	7.9
32.5% HS	Neat	8.5	8.1
	MWCNTs	8.2	7.7
	f-MWCNTs	8.1	7.6
	FGS	7.1	7.5

The SAXS data are finally analysed with a clipped random wave (*CRW*) technique that provides a visual representation of the structure of the FPU nanocomposite foams. This model has widely been used to analyse the morphology of other disordered bicontinuous phase materials, such as gels, [211] polymer blends, [212] aerogels, [213] and ionomers. [214] This model-independent approach provides the most likely *3D* structure corresponding to the experimental scattering data. [215]

Cahn proposed, in 1965, a clipped random wave (*CRW*) model to produce *3D* structures formed via spinodal decomposition. [216] These morphologies are produced by "clipping" a Gaussian random field, which is generated by superposing many isotropically directed sinusoidal waves with random phases. The Gaussian random field can be normalised in order to fluctuate continuously between -1 and +1, which provides a bicontinuous two-phase morphology by clipping the random process. Hence, the features of the morphologies obtained by the *CRW* model depends on the spectral density function, *f(k)*, which is the inverse Fourier transform of the two-point correlation function, *g(r)*, of the Gaussian random field. The spectral density function (*SDF*) describes the distribution of the magnitudes of the propagation wave vectors, *k*, of the sinusoidal waves. This first model was further extended mathematically by Berk for the analysis of the scattering data. [217] This contribution was related to a two-point correlation

function and the Debye correlation function ($\Gamma^{\alpha}(r)$) which determines the scattering intensity. Chen *et al.* [218] developed a peaked *SDF* to generate more disordered morphologies which quantitatively reproduce the small-angle neutron scattering (SANS) profiles of the microemulsions.

The generation of the morphology is performed using the SAXSMorph program [160] which follows the next steps:

First, the Debye correlation function ($\Gamma^{\alpha}(r)$) is calculated from the experimental SAXS intensities as:

$$\Gamma^{\alpha}(r) = \int_0^{\infty} 4\pi q^2 I(q) \frac{sin(qr)}{qr} dq \tag{4.16}$$

The two-point correlation function, $g(r)$, is obtained from $\Gamma^{\alpha}(r)$:

$$\Gamma^{\alpha}(r) = \Gamma^{\alpha}(0) - \frac{1}{2\pi} \int_{g(r)}^{\infty} e^{-\frac{\alpha^2}{1+t}} \frac{1}{\sqrt{1-t^2}} dt \tag{4.17}$$

$\Gamma^{\alpha}(0)$ is the "true volume fraction" (1-porosity) and the porosity is taken, in this study, as the volume fraction of the hard segment. The clipping parameter (α) is related to $\Gamma^{\alpha}(0)$ by

$$\Gamma^{\alpha}(0) = \frac{1}{2\pi} \int_{g(r)}^{\infty} e^{-\frac{x^2}{2}} dx \tag{4.18}$$

The spectral function, $f(k)$, is then obtained by the inverse Fourier transform,

$$\mathrm{f}(k) = \int_0^{\infty} 4\pi r^2 \, g(r) \frac{sinkr}{kr} dr \tag{4.19}$$

The Gaussian random field is then generated by summing several (N=10000) cosine waves with random phases where the magnitudes of the wave vectors are obtained from the spectral function (Equation (4.19)).

In order to calculate the morphology, a *3D* array is constructed using the Gaussian random field and *f(k)*. The value obtained at each point of the array is then compared to α and if it is less than this value is designated as "solid".

The specifications that have been introduced in the SAXSMorph program are the box size, 200 Å, and the volume fraction of the hard segment. SAXSMorph generates *2D* images (Figure 4.15) that are then rendered into the *3D* volume using POV-Ray. The volume fraction parameter was selected to generate the best approximation to the average interdomain size determined in Table 4.5, by analysing 50 *2D* images using ImageJ program. This criterion ensured the correct representation of the morphology. Table 4.6 summarises the average size corresponding to the interdomain distance and the connectivity calculated by SAXSMorph from where the *3D* structures are generated.

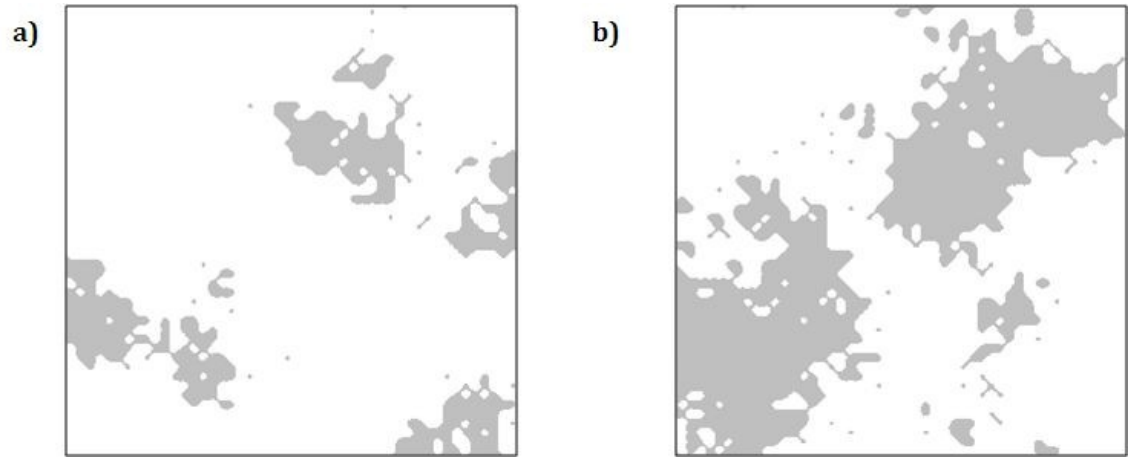

Figure 4.15. Representative *2D* image generated by SAXSMorph at 250 sec and 1500 sec. Box size is 200 Å and the volume fraction 25 %. Grey colour represents the HS.

Table 4.6. Average size and connectivity of the structures from image analysis of the *CRW* morphologies.

	Sample	Average size (nm)	Connectivity (%)
25% HS	Neat	9.1	82.7
	MWCNTs	9.0	85.3
	f-MWCNTs	9.0	80.4
	FGS	8.9	83.1
32.5% HS	Neat	9.0	84.7
	MWCNTs	8.8	87.1
	f-MWCNTs	8.3	89.2
	FGS	8.1	88.1

Figures 4.16 and 4.17 show the *3D* structures of the evolution of the morphology (HS are represented as solid) at 250 sec and 1500 sec for FPU-25% HS and FPU-32.5% HS nanocomposite foams, respectively. The deceleration observed for FPU-32.5% HS foams in the formation of the interdomain spacing compared to the FPU-25% HS foams is clearly observed on the *CRW* results. At the early stages of the reaction (250 sec), the HS domains formed for FPU-32.5% HS foams with carbon nanotubes and especially for FGS foams are lower compared to the FPU-25% HS foam. However, at 1500 sec the neat sample of FPU-32.5% HS foam is more interconnected than the neat FPU-25% HS system, while foams with CNPs still present low concentration of HS domains and less interconnection which confirms the results obtained by other techniques.

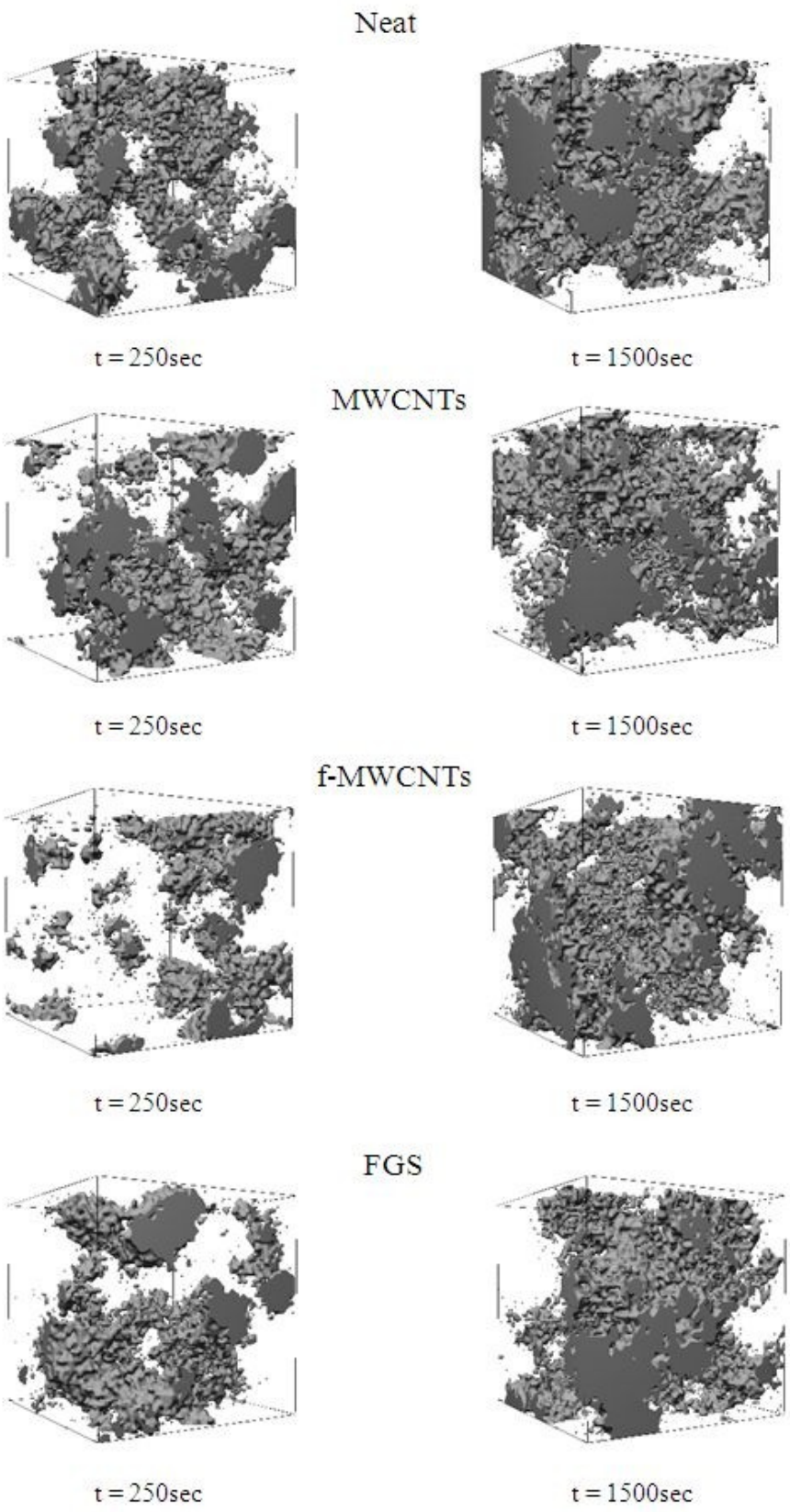

Figure 4.16. *3D* structure of the evolution of the microdomains at 250 sec and 1500 sec for FPU-25% HS nanocomposite foams.

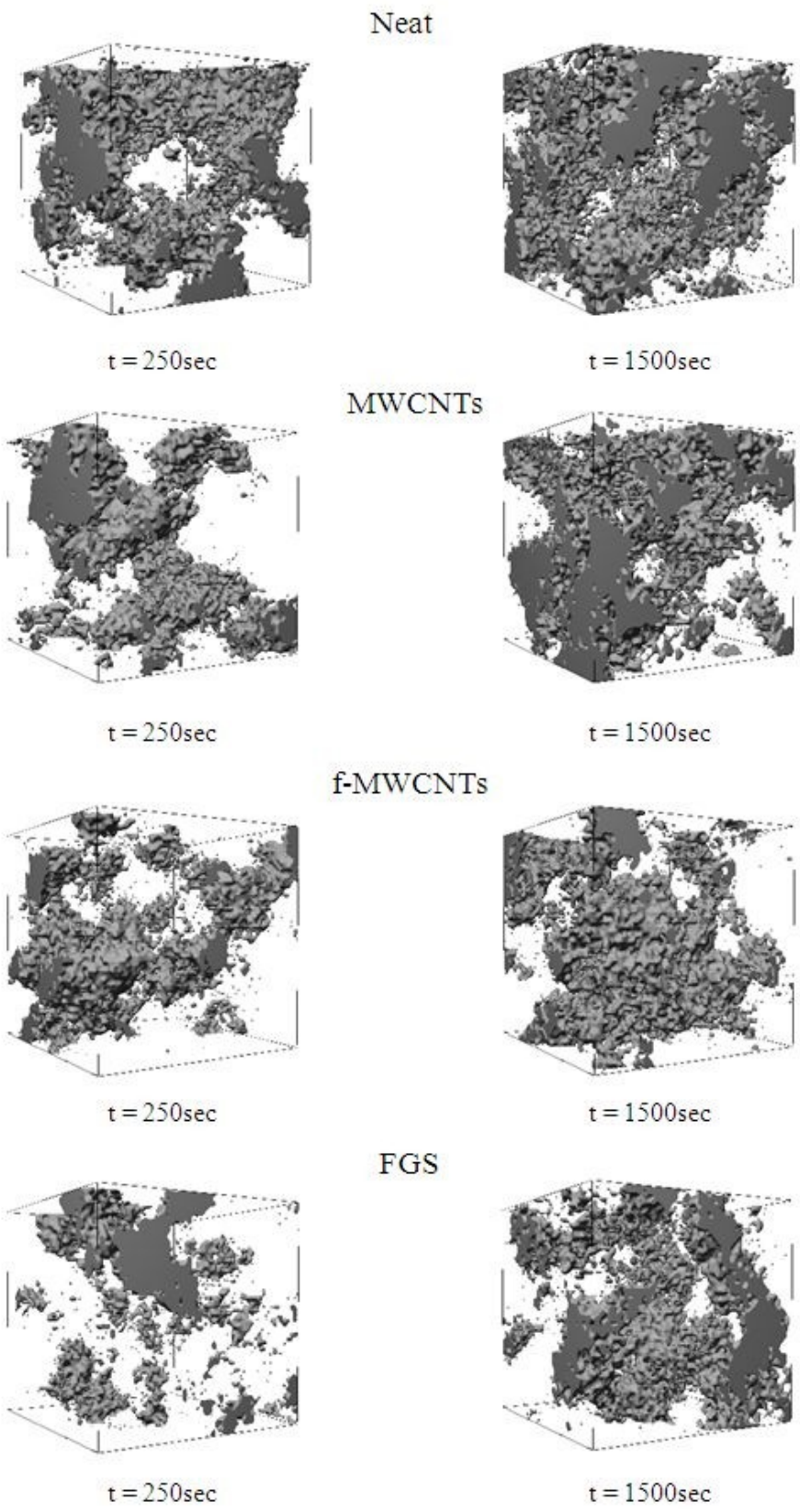

Figure 4.17. *3D* structure of the evolution of the microdomains at 250 sec and 1500 sec for FPU-32.5% HS nanocomposite foams.

Atomic force microscopy (AFM) was used to qualitatively examine the presence of two-phases in the morphology of FPU nanocomposite foams. In the phase images (Figure 4.18), two different coloured areas are observed: light ones for hard segment domains and dark areas for soft segment domains. [44-46] The overall phase scale of the images was adjusted to 25° in order to clarify the foam morphology and facilitate the comparison between samples.

As the hard segment content increases, AFM images reveal an increase on the hard domain connectivity and the formation of large structures. [45, 219, 220] It has previously been reported [45, 221] that larger structures are aggregates of smaller hard domains. The AFM images showed an estimated interdomain spacing of 10 - 12 nm. Since SAXS gives values of the interdomain distances of only periodic structures, [44, 221] the results of both techniques are in good agreement. Nevertheless, it appears that the formation of the urea aggregates on nanocomposite foams is influenced by the presence of CNPs. Song *et al*. [222] suggested that formation of aggregates is related to the reaction kinetics and the presence of fillers in the matrix. Therefore, fast reaction rates form aggregates with smaller average size due to the rapid aggregation behaviour, while the presence of fillers inhibits the aggregation of hard domains which is observed in foams filled with CNPs. On the other hand, it is observed on the AFM images that foams with MWCNTs display a denser urea aggregates and clearer phase contrast compared to foams filled with functionalised CNPs, which indicates a better microphase separation. [223, 224] This observation suggests that the functional groups on the surface of the carbon nanofillers are creating interactions with the hard domains.

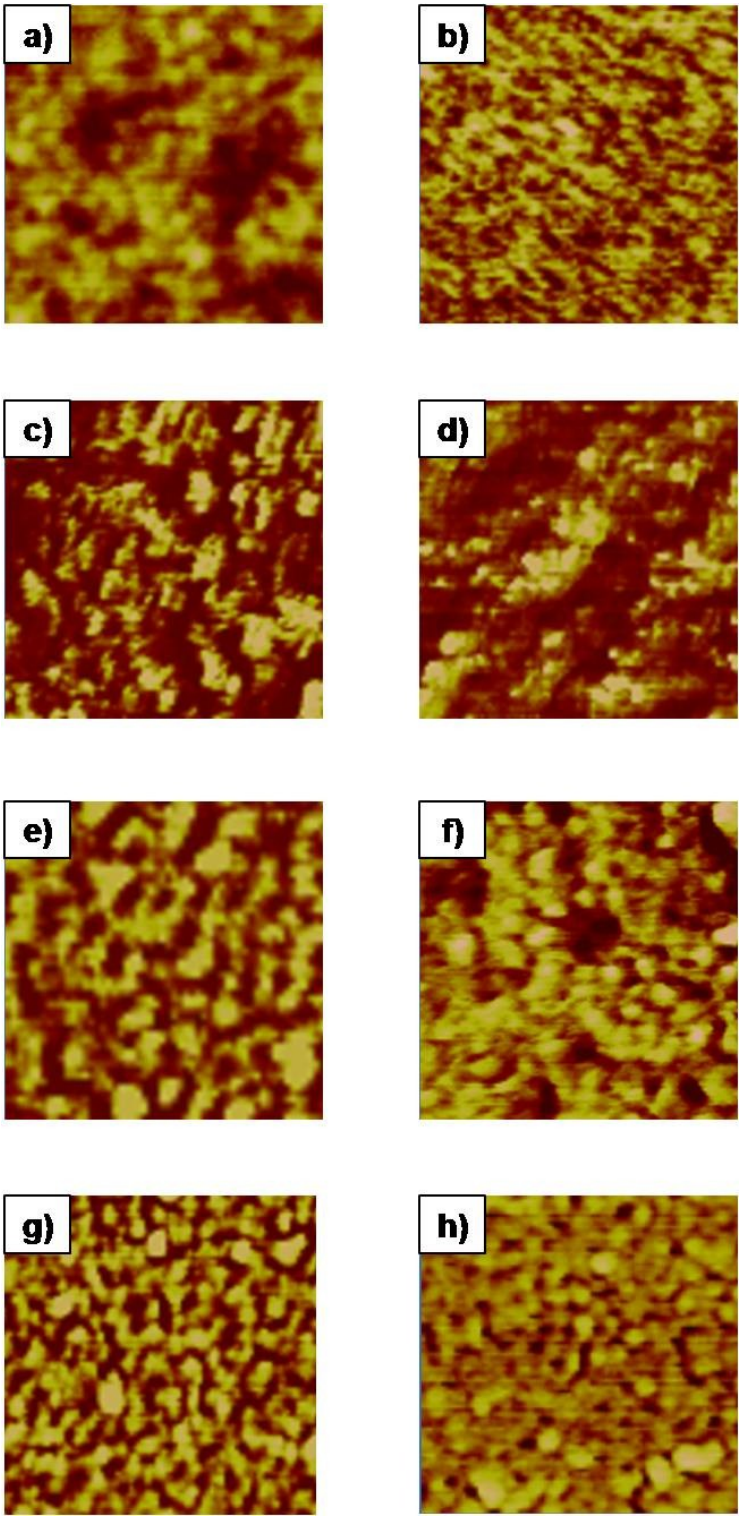

Figure 4.18. Tapping mode AFM phase images. Images are displayed at a total phase scale of 25 ° and the scan width is 500 nm. Images a), c), e) and g) are neat, MWCNTs, f-MWCNTs and FGS FPU-25% HS nanocomposite foams, respectively. Images b), d), f) and h) are neat, MWCNTs, f-MWCNTs and FGS FPU-32.5% HS nanocomposite foams, respectively.

4.2.3. Morphological Analysis

The density evolution during foaming of FPU-25% HS nanocomposite foams is studied by X-ray radioscopy. This technique has previously been used to reveal the temporal evolution of metal foams and to analyse the different phenomena during foaming, such as coalescence or coarsening effects. [225-228] However, there is only one study reported by Verdejo *et al*. [229] on the use of synchrotron X-ray radioscopy on polymer nanocomposite foams, in particular silicone foams filled with CNTs and FGS. Here, initial studies are presented on the use of the X-ray radioscopy to follow the kinetics of density evolution and their relation to the kinetics of polymerisation. Further work is envisioned to fully understand the physical events during foaming and the effect of the increase of HS content.

The density profile is calculated from the radiograph intensities applying the Beer-Lambert law of attenuation (Equation (4.20)):

$$I(x,z) = I_0 exp(-\mu d) \tag{4.20}$$

where d is the sample thickness in the beam direction and is assumed to be constant, μ is the attenuation coefficient and I_0 is the initial beam intensity. Considering that: (i) μ is equal for all particles in the beam and (ii) μ can be assumed as a constant over the sample thickness, then the mass attenuation coefficient μ_m can be defined as:

$$\mu_m = \mu/\rho(x,z,t) \tag{4.21}$$

In these experiments, it is more adequate to use μ_m because its value is invariant for the solid, liquid or gaseous state of a given element. [230] Therefore, rearranging equations (4.21) and (4.22) and taking into account that the density of the initial liquid system ($\rho_0 \approx 1082.1\ kg{\cdot}m^{-3}$) and the density of the final foam (ρ_f) are known values, it is obtained:

$$\rho(x,z,t) = \rho_0 + \frac{ln(I(x,z,t)/I_0)}{ln(I_f/I_0)} \cdot (\rho_f - \rho_0) \tag{4.22}$$

where $\rho(x,z,t)$ is the density of the system at each time, t. Applying this equation to the experimental data from the X-ray images and correcting the initial time (t_0), the density profile of FPU samples during foaming is obtained (Figure 4.19).

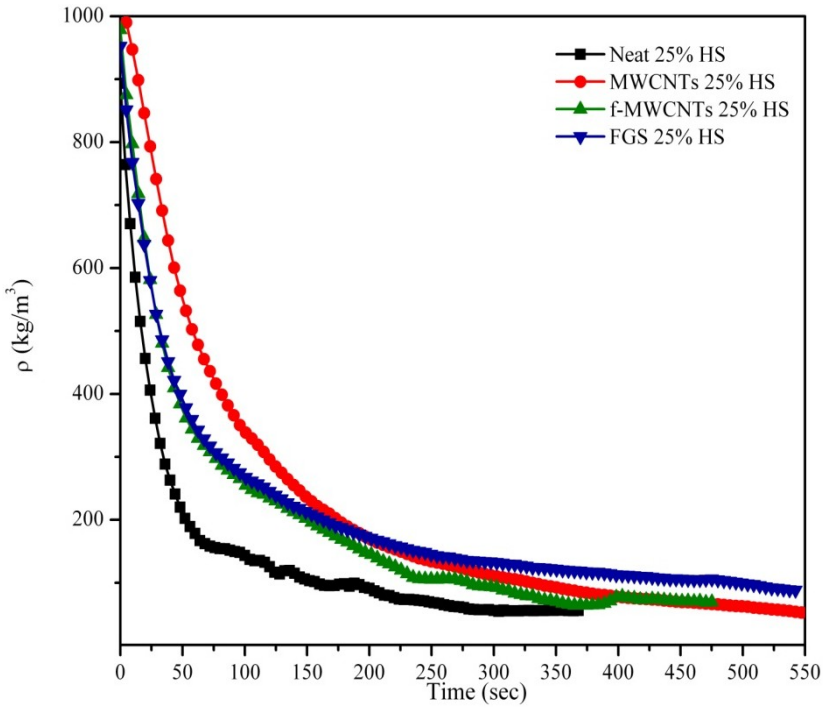

Figure 4.19. Density profile during foaming of FPU-25% HS nanocomposite foams.

The generation of CO_2 gas during the blowing reaction, leads to the expansion of the initial mixture to form the foam structure. This phenomenon is observed by the fast decrease of the density of FPU foams during the initial stages of the foaming (Figure 4.19). Then, the polymerisation reaction is responsible for the consolidation of the foam structure observed as the density plateaus. The CO_2 is produced by the reaction between isocyanate and water; hence FPU systems with the same formulation should expand at the same reaction rate, achieving similar final densities. However, in FPU nanocomposite foams, other parameters such as viscosity of the polyol/CNP dispersions, surface tension or polymerisation reaction should be considered. Therefore, the slope of the first points in each curve (Figure 4.19) was calculated in order to compare the kinetics of foaming

expansion. The slope of neat was 16.2 changing to 10.2 for MWCNTs, 13.1 for f-MWCNTs and 12.1 for FGS samples. As it was observed in section 4.2.1., the 0.5 phpp polyol/MWCNT dispersion showed the highest viscosity, followed by the 0.5 phpp polyol/f-MWCNT, while systems with FGS displayed a Newtonian behaviour similar to that of neat polyol. Hence, the increase on the viscosity of the initial systems correlates well with the deceleration observed in MWCNTs and f-MWCNTs foams. This result agrees with a previous study by Bikard *et al*. [231] showing that the larger the viscosity of the fluid, the slower the expansion in flexible foams. Meanwhile, the delay observed for FPU foams with FGS should be ascribed to the adsorbed water molecules on the surface of these nanoparticles due to the hydrogen bonds created between the water and the C-O groups, [207] as has previously been mentioned. This means that less water molecules are available for the reaction with isocyanate and this would explain the delay on the foaming reaction.

In Figure 4.20 it is observed at t_0 that the diameters of the cells of neat FPU foams are larger compared to the nanocomposite foams, due to the faster rate of expansion. Meanwhile, it is clearly observed that for MWCNTs and FGS the cell size is similar, which can be due to the high viscosity of polyol/MWCNT dispersions and to the lower amount of CO_2 generated in the foaming of FPU with FGS, respectively. On the other hand, foams with f-MWCNTs present an intermediate state, but the decrease on the cell diameter compared to the neat FPU foam can be attributed to the rheological behaviour of the initial reactant system, rather than the presence of functional groups, which do not affect the reaction between water and isocyanate as has been observed in FT-IR analysis.

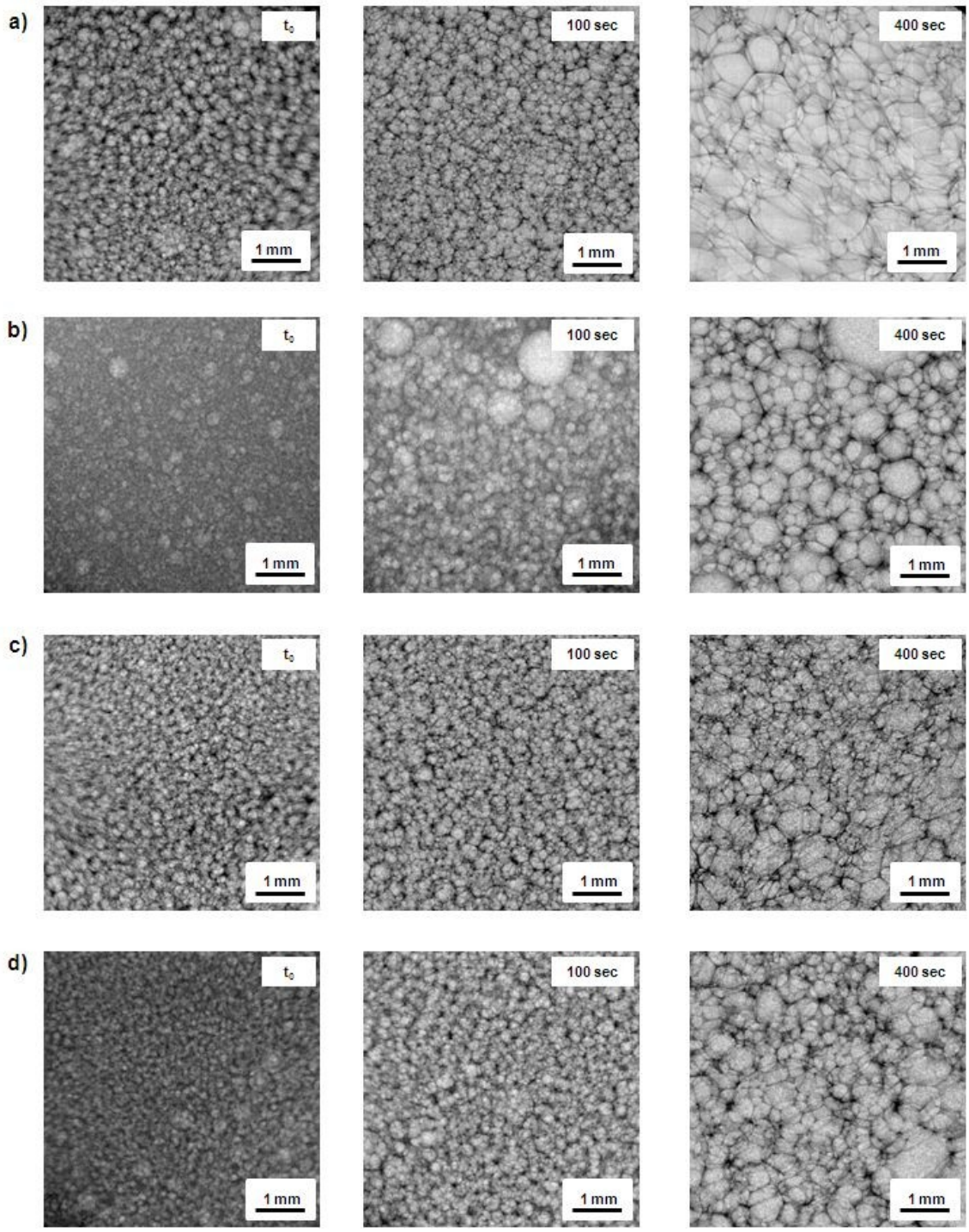

Figure 4.20. X-ray radiographs of expanding FPU-25% HS nanocomposite foams for: a) neat, b) MWCNTs, c) f-MWCNTs and d) FGS.

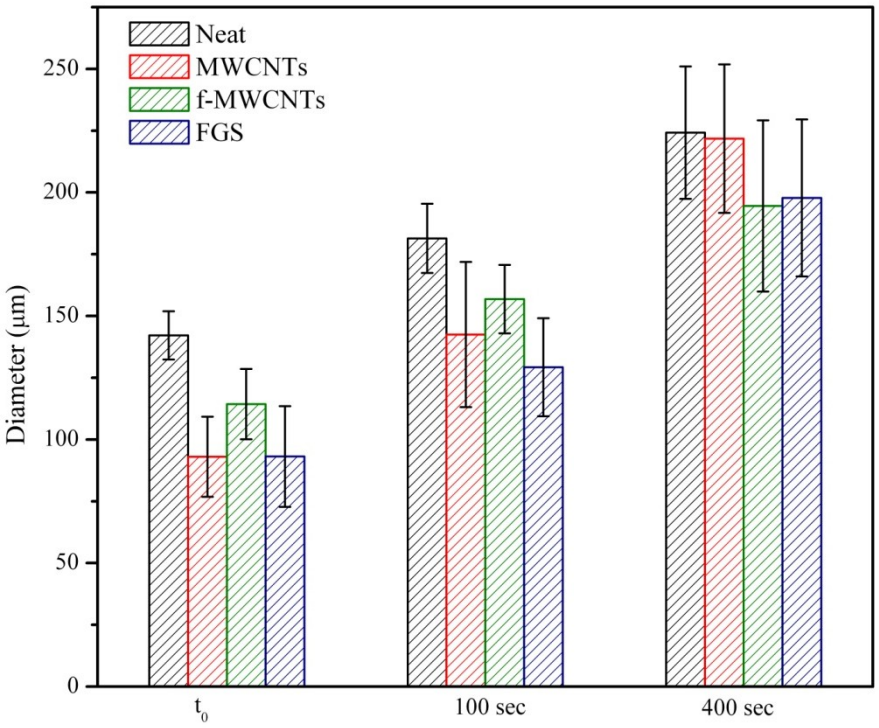

Figure 4.21. Diameter of expanding FPU-25% HS nanocomposite foams at t_0, 100 sec and 400 sec.

After the first seconds and as the reaction progresses, the cell diameter in all the samples increases (Figures 4.20 and 4.21). The foaming evolution with time is controlled by the short-term stability and stability under expansion. [232] The short-term stability depends on film drainage rate and ability to prevent local thinning in liquid films. In general, the liquid film drains to the Plateau borders (Figure 4.22) because of capillary pressure and gravity. The velocity of drainage, derived by Reynolds equation from the flow between two rigid plates, can be expressed as:

$$V = -\frac{dh}{dt} = \frac{2h^3}{3\eta R^2}\Delta P \tag{4.23}$$

where h is the film thickness, R is the film radius, η is the bulk viscosity and ΔP is the difference in pressure between the film centre and border that drives film draining. [232, 233] The rate at which this drainage occurs determines the film

thickness and density of FPU foams. Hence, as the viscosity of the systems increases the drainage rate of a thin liquid film decreases linearly. [234-236] The slower drainage rate of the foam cells will lead to thicker film and lower percentage of rupture cell windows will be observed. [236]

On the other hand, local thinning of films leads to film rupture and bubble coalescence. These effects are controlled by the bulk viscosity of the systems and occur eventually as the foam evolves. [237-240]

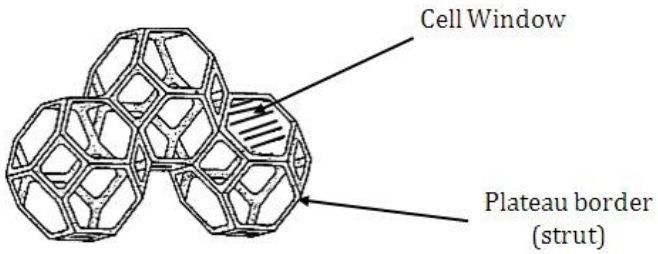

Figure 4.22. Structural characteristics in an open foam cell. [232]

Neat FPU foam shows higher drainage rate due to the lower initial viscosity of the system. However, the polymerisation reaction occurs faster leading to a rapid increase of the viscosity that helps to stabilise the cellular structure. Therefore, due to both effects, thinner cells are formed and fewer coalescence effects can be observed, being more important the film ruptures after ~180 sec from the beginning of the reaction. Meanwhile, it is observed (Figure 4.21) that the cell diameter grows faster during the first stages (up to 100 sec), when the water-isocyanate reaction occurs and slows down after the initial stages, due to the abovementioned increase of the viscosity.

The effect of MWCNTs during foam evolution is quite different compared to neat FPU foam. The high initial viscosity of the systems slows the drainage rate, forming thicker films and smaller cell sizes (Figure 4.20). Hence, this thicker cell walls and bubble size result in a higher density (Table 4.7) compared to neat FPU foam.

FPU foams filled with f-MWCNTs have a similar foaming evolution behaviour as neat FPU foams. However, due to the higher viscosity of the initial system, compared to that of neat polyol, the drainage rate is slowed down, helping to the stabilisation of the nanocomposite foam. Nonetheless, the polymerisation reaction rate is the slowest due to the catalyst deactivation of the polymerisation reaction and hence, the consolidation of the cellular structure is being retarded. Consequently, thinner films are formed, which should result in lower foam density compared to foams with MWCNTs; however, the opposite trend is observed, being the density of foams filled with f-MWCNTs higher than the measured for foams with MWCNTs (Table 4.7). This change on the density behaviour could be attributed to two different factors: (i) the hydrogen bonding between the functional groups of f-MWCNTs and HS and (ii) the rupture of the films observed at ~270 sec which partially collapses the cell structure, preventing the foam expansion, which is observed towards the end of the foaming evolution (Figure 4.20).

The effect of FGS on FPU foams differs from what has been observed for MWCNTs and f-MWCNTs. While the initial viscosity of the systems with FGS is similar to that of neat foams, the polymerisation reaction is slower which should account to the later stabilisation of the cellular structure. Furthermore, FPU foams filled with FGS presented several coalescence effects while the foam is evolving, and the rupture of the films occurs at long times (> 400 sec) compared to neat and f-MWCNT FPU foams. In consequence, the foam collapses locally, producing the partial lost of the structure and increasing the density of the foam (Table 4.7).

SEM images (Figures 4.23 and 4.24) of the nanocomposite foams stored for several days show the effect of CNPs on the final cellular structure of FPU-25% HS and FPU-32.5% HS nanocomposite foams. The cell size appears to increase as the HS content increases in the system and with the presence of CNPs in both sets of FPU foams compared to the neat FPU foams. This increase of the cell size has previously been observed on systems produced by reactive foaming, in particular in PU foams and has been ascribed to an increase of the viscosity of the system. [121] Moreover, it could be attributed to the different mechanisms observed during foaming process. In the case of FPU foams filled with FGS (Figures 4.23 d

and 4.24 d), a large number of broken cells is observed because during the preparation of the samples for the SEM, the frozen matrix becomes too fragile.

Close inspection of the polymeric matrix (Figures 4.25 and 4.26) reveals a good dispersion of CNPs throughout the sample, in both the walls, and particularly the struts of the cellular structure.

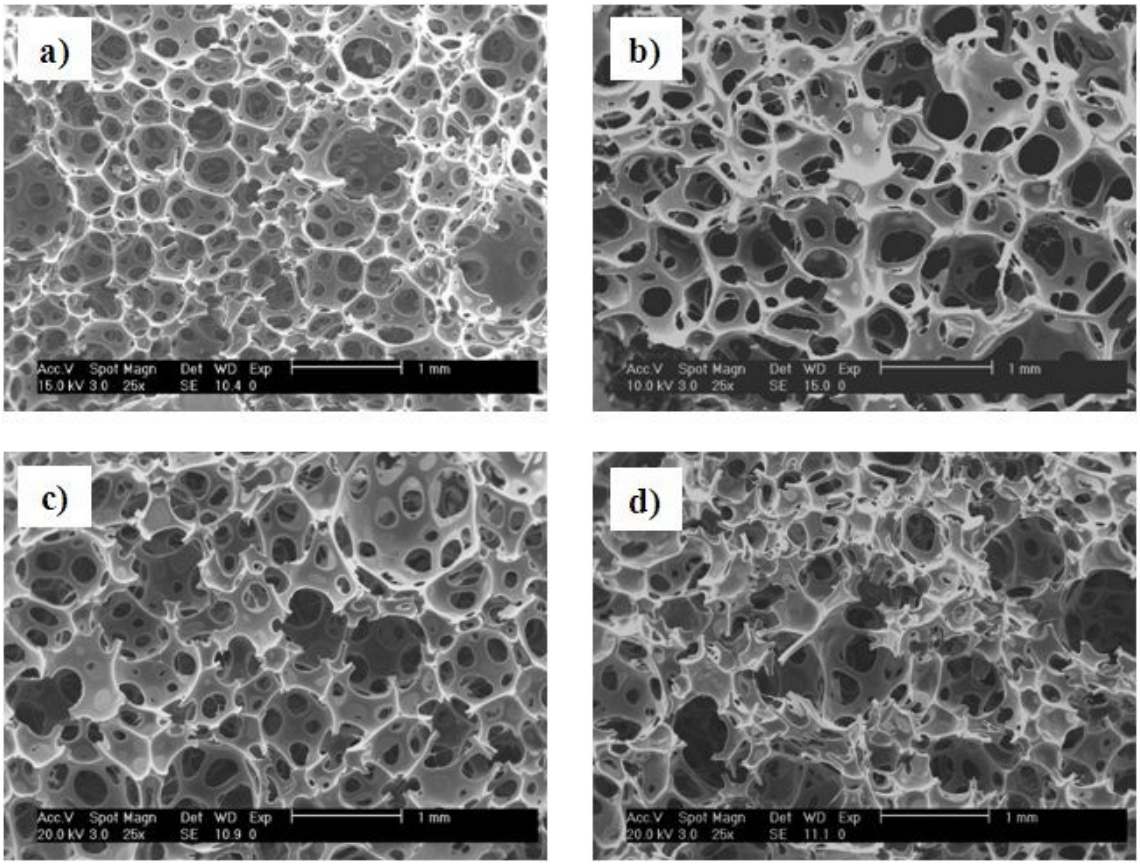

Figure 4.23. Representative SEM images of flexible FPU-25% HS nanocomposite foams: a) neat, b) MWCNTs, c) f-MWCNTs and d) FGS.

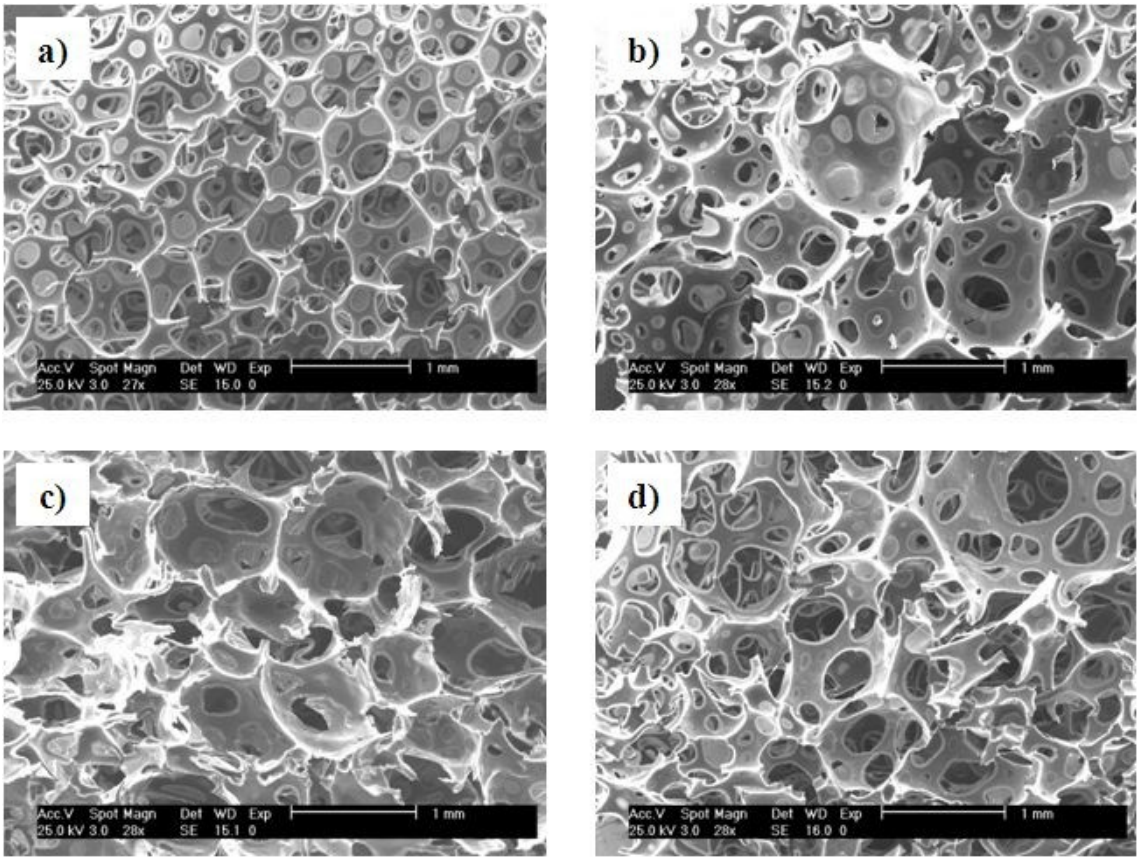

Figure 4.24. Representative SEM images of flexible FPU-32.5% HS nanocomposite foams: a) neat, b) MWCNTs, c) f-MWCNTs and d) FGS.

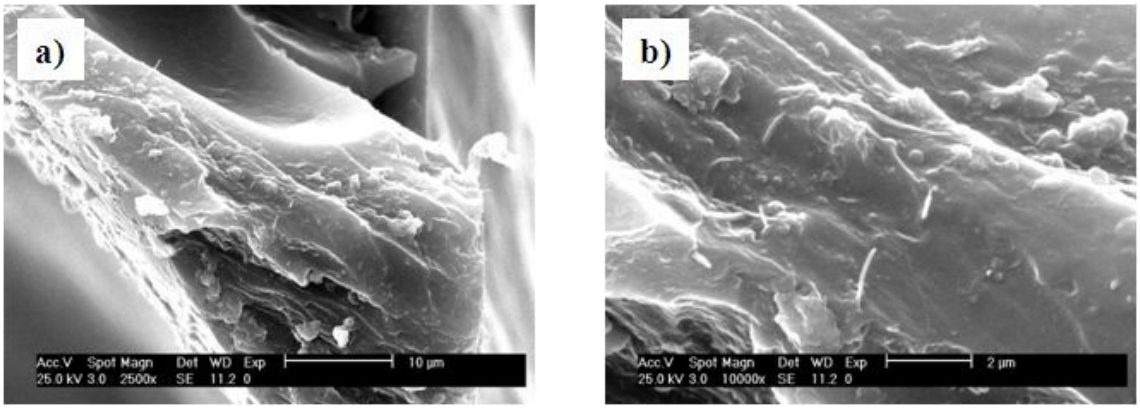

Figure 4.25. Representative SEM image at high magnification of FPU-25% HS foam filled with MWCNTs: a) 10 μm and b) 2 μm.

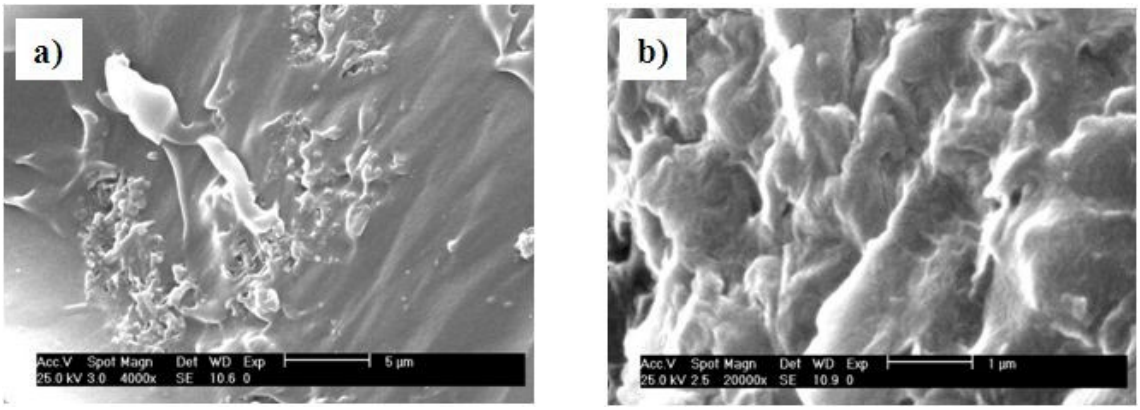

Figure 4.26. Representative SEM image at high magnification of FPU-25% HS foam filled with FGS: a) 5 µm and b) 1 µm.

The densities of FPU nanocomposite foams for 25% HS and 32.5% HS are shown in Table 4.7. It is observed an increase of the foam density for neat foams with high content of HS compared to the respective one with lower HS content, due to both higher amount of HS and thicker cell walls. [241] Additionally, the presence of CNPs increased the density of the system with respect to their neat PU foam. The effect of the CNPs in the foaming process leads to an extended rising time and reduced volume. [38] Hence, it would be expected the same behaviour on the filled samples, that is, higher foam densities for FPU-32.5% HS nanocomposite foams filled with CNPs than for the FPU-25% HS nanocomposite foams; however, the values obtained are lower. This low density could be attributed to the delayed polymerisation reaction, that extended the evolution of the foam and, hence, the final volume of the sample. This would explain the lower densities obtained for nanocomposite foams with 32.5 % HS compared to nanocomposite foams with 25 % HS. In order to confirm these statements, studies on the foaming evolution by radioscopy should be performed.

Table 4.7. Density (kg·m^{-3}) of FPU nanocomposite foams.

	Sample	Density (kg·m^{-3})
25% HS	Neat	52.0 ± 0.8
	MWCNTs	65.3 ± 0.6
	f-MWCNTs	70.7 ± 0.4
	FGS	90.1 ± 1.0
32.5% HS	Neat	57.3 ± 0.1
	MWCNTs	55.8 ± 0.3
	f-MWCNTs	64.6 ± 0.2
	FGS	74.3 ± 0.5

4.2.4. Differential Scanning Calorimetry (DSC)

Differential scanning calorimetry (DSC) is applied to examine the thermal properties of FPU foams. Figures 4.27 and 4.28 show the DSC thermograms corresponding to FPU-25% HS and FPU-32.5% HS nanocomposite foams, respectively. As can be noticed, the temperature range of the DSC heating profiles is between -75 to 15 °C and hence, only the glass transition temperature (T_g) of the SS is observed. Although several attempts were made, the glass transition of the HS was not detected in the DSC heating profiles due to its small heat capacity change. The difficulty to observe the T_g of the HS phase has been reported in other polyurethane systems. [242, 243] Hence, Table 4.8 illustrates the T_g of the SS of FPU nanocomposite foams.

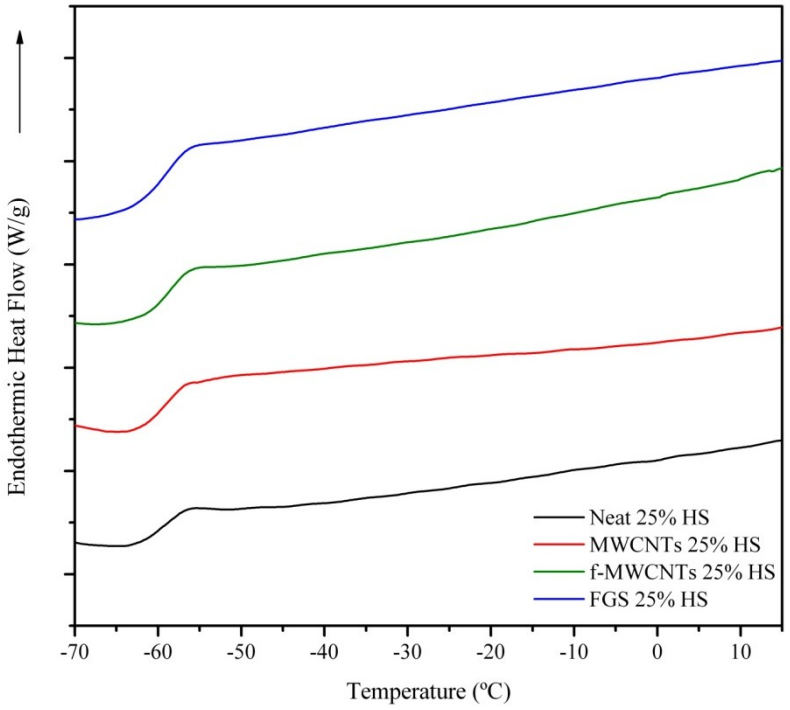

Figure 4.27. DSC heating profiles of FPU-25% HS nanocomposite foams.

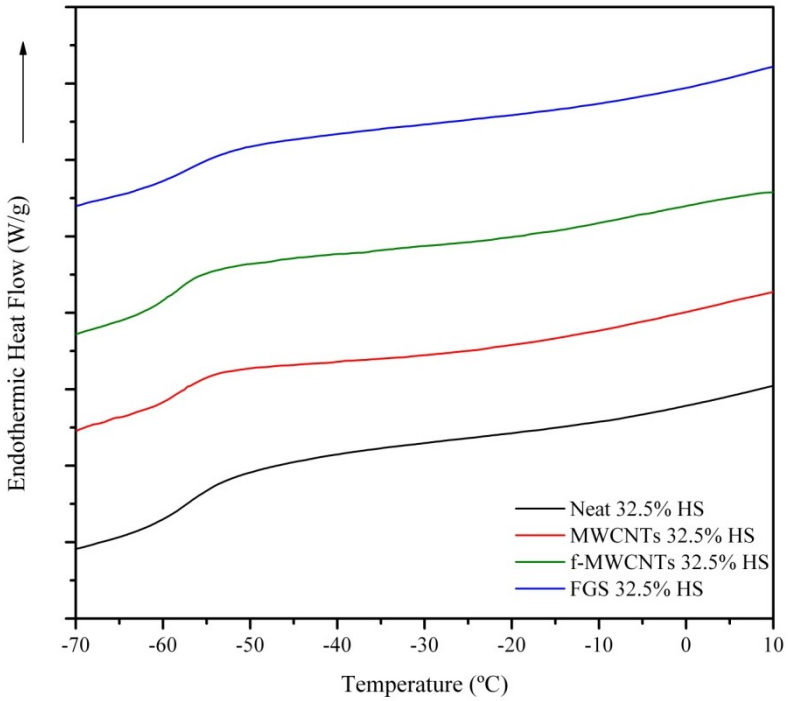

Figure 4.28. DSC heating profiles of FPU-32.5% HS nanocomposite foams.

Comparing the DSC heat profiles of FPU-25% HS and FPU-32.5% HS nanocomposite foams, it can be noted that as the HS content increases, the breadth of the glass transition region increases while the ΔC_p at the glass transition decreases. However, the T_g increases for higher contents of HS on the system (Table 4.8) as has previously been observed on segmented polyurethanes. [241, 244-246]

The increase of the T_g could be ascribed to different factors: (i) the increase of the HS content, (ii) the presence of HS in the SS phase and (iii) the restricted movement introduced by the HS junctions and at a phase boundaries where the hard domains act as filler particles. [208, 245] In this study, and taking into account the standard deviations on the T_g, the effect of the content of HS is significant but not the presence of carbon nanofillers. Tien *et al*. [247] also reported no change in the glass transition temperature of the SS for segmented polyurethanes filled with nanosize silicate layers. This invariability on the T_g is because DSC cannot probe the glass transition temperature of polymer chains close to the nanofillers and hence the T_g measured is the same as that of the neat FPU foam for both sets of foams. Nevertheless, DMA provides a more sensitive measure of the T_g of SS and the results will be presented later.

In Figures 4.27 and 4.28, it can be observed that ΔC_p slightly decreases as the HS content increases. This parameter, ΔC_p, can be described as the magnitude of the transition at the T_g and is related to the amount of the SS chains. Hence, the decrease of the ΔC_p with HS content is related to the strong steric hindrance induced by the HS. [248, 249] However, the effect of the CNPs does not seem significative, as can be observed in the heating profiles.

Table 4.8. Glass transition temperature (T_g) of the soft segments of FPU nanocomposite foams obtained by DSC.

	Sample	T_g (°C)
25% HS	Neat	-60.1 ± 0.3
	MWCNTs	-59.9 ± 0.1
	f-MWCNTs	-59.3 ± 0.1
	FGS	-59.7 ± 0.4
32.5% HS	Neat	-57.0 ± 0.2
	MWCNTs	-57.5 ± 0.3
	f-MWCNTs	-57.2 ± 0.1
	FGS	-56.7 ± 0.3

4.2.5. Thermogravimetric Analysis (TGA)

The thermal degradation mechanism of FPU nanocomposite foams is very complex because of the byproducts produced during the process. [250] In general, polyurethanes degrade following a two-step process: the first step is associated with the degradation of the HS, which depolymerises into the main monomers, and the second step with the decomposition of the soft segments [8, 29, 30]. In this study, the thermal stability of FPU foams is reported and the TGA profile is shown in Figure 4.29. As can be observed, the first degradation step occurs in a temperature range between 250-450 °C while the second step takes place between 500-650 °C.

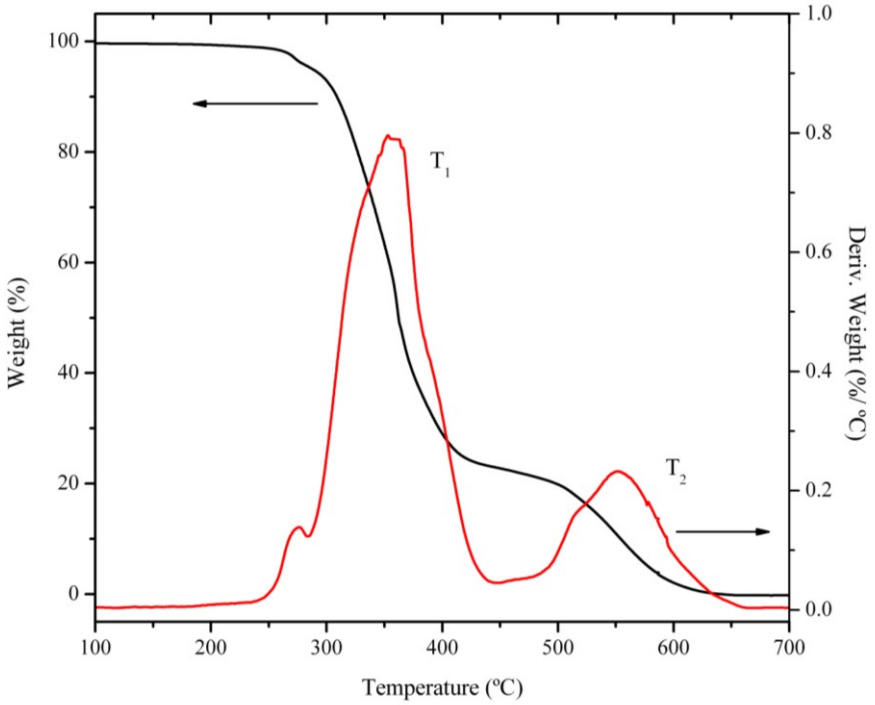

Figure 4.29. Representative TGA thermogram of neat FPU-25%HS foam under air.

The maximum degradation temperatures at each step, as well as the temperature at 50 % of weight loss and the char yield at 700 °C are summarised in Table 4.9. Ferguson *et al.* [251] reported that the thermal stability of the first step increases for higher contents of SS, while the opposite effect is observed on the later step where the HS have a stabilising effect on the degradation of the SS. Indeed, this behaviour is clearly observed on the FPU-25% HS and FPU-32.5% HS nanocomposite foams. The first degradation step takes place at similar temperature in both sets of FPU foams, being higher for FPU-25% HS foams, while the second degradation temperature occurs at higher temperatures for FPU-32.5 % HS foams.

On the other hand, the introduction of the CNPs strongly influences the two degradation temperatures of the FPU-25% HS foams, while hardly affects the thermal stability of FPU-32.5% HS (Table 4.9). The lower effect of CNPs on foams with high HS content could be attributed to the confinement of the CNPs into the

larger aggregates of hard segment domains for FPU-32.5 % HS, decreasing the enhancement of the thermal stability by the CNPs.

In addition to the effect of the HS, the two steps appear to be influenced not only by the functional groups present on the surface of the CNPs but also by the nanoparticle morphology. While MWCNTs increase both temperatures, f-MWCNTs only improve the first degradation temperature because of the interaction of the functional groups with the HS. f-MWCNTs ought to have improved heat dissipation and thermal stability compared to MWCNT, due to the direct covalent bonding with the matrix; but that is not the case. One hypothesis is that the hydroxyl and carboxyl groups of the modified nanoparticles disrupt the formation of large urea HS decreasing the thermal stability in relation to the pristine MWCNTs, as has been observed by AFM. Nonetheless, the inclusion of FGS shows a significant improvement of the thermal decomposition of the system, even considering the existence of the same functional groups as on f-MWCNTs. Therefore, the FGS effect should be related to both the lower functionalisation degree of FGS and their wrinkled morphology, which could result in a nanoscale surface roughness likely to product an enhanced mechanical interlocking and adhesion with the polymer chains. [180, 252] This morphology probably hinders the diffusion of volatile compounds and hence an enhancement of the thermal stability. [253]

Table 4.9. TGA results of FPU nanocomposite foams.

	Sample	T_1 (°C)	T_2 (°C)	Residue % (700 °C)
25% HS	Neat	355	552	0.13
	MWCNTs	374	577	0.37
	f-MWCNTs	364	553	0.28
	FGS	395	585	1.30
32.5% HS	Neat	347	573	0.73
	MWCNTs	356	580	0.88
	f-MWCNTs	351	575	0.84
	FGS	360	577	1.72

4.2.6. Dynamic Mechanical Analysis (DMA)

The dynamic mechanical analysis provides information about the viscoelastic properties of FPU foams. In Figures 4.30 and 4.31 the damping factor (*tan δ*) as function of the temperature is represented for FPU-25% HS and FPU-32.5% HS nanocomposite foams at a frequency of 1 Hz. The measurements were carried out at 1, 2, 5 and 10 Hz showing a non-frequency dependency. The peak observed in *tan δ* at low temperatures is related to the glass transition temperature (T_g) of the polyol SS. Generally, the increase of the T_g is attributed to a greater fraction of the HS dissolved in the SS. However, for FPU-32.5% HS foams, the T_g became broader and a maximum is difficult to define which could be ascribed to an increase in the interphase between hard and soft segments. [29] Therefore, the information related to the T_g value is not conclusive for foams containing high contents of HS. However, it is observed that the magnitude of the peak in *tan δ* decreases as the HS content increases corroborating the differences in the relative amount of the constituent phases and hence in the character of the polymer. Furthermore, the *tan δ* peak broadens for high contents of hard segment, which has been attributed to the increase in size and interconnectivity of the HS domains. [244, 254]

In FPU nanocomposite systems, the T_g is being affected by two effects: [185] well-dispersed CNPs would restrict the molecular motion, increasing the T_g, while the effect of CNPs on the degree of phase separation would lead to a reduction of the T_g. The values of the T_g for FPU-25% HS foams are -55.6, -53.3, -57.7 and -59.8 °C for neat, MWCNTs, f-MWCNTs and FGS, respectively. The decrease of the T_g values of both f-MWCNT and FGS samples could be attributed to the interactions between the functional nanoparticles and the hard segments resulting in an enhancement of the soft segment mobility and thus a decrease of the T_g. [255] In contrast, the T_g value of the sample filled with raw MWCNTs shows a modest increase suggesting a reduction of the molecular chain mobility of the soft segments. Nevertheless, as above mentioned, the glass transition of FPU-32.5% HS occurs in the same range of temperatures as for FPU-25% HS, but the peak corresponding to the T_g is not well defined and hence, the effect of the CNPs on the T_g of FPU-32.5% HS cannot be explained.

It is worth noting that, FPU-25% HS and FPU-32.5% HS foams with FGS show lower values of the *tan δ* compared to the other samples in both sets of foams, as can be observed in Figures 4.30 and 4.31. The magnitude of the *tan δ* is related to the freedom of motion of the soft segment chains and hence low values means higher mobility of the SS. [255, 256] This observation confirms the interactions between FGS and HS above mentioned.

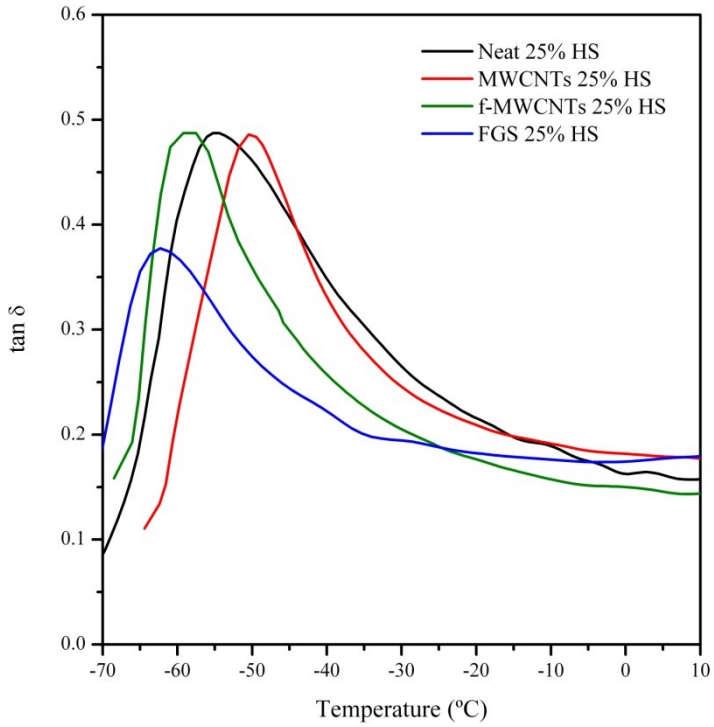

Figure 4.30. Damping factor (*tan δ*) of FPU-25% HS nanocomposite foams as a function of temperature.

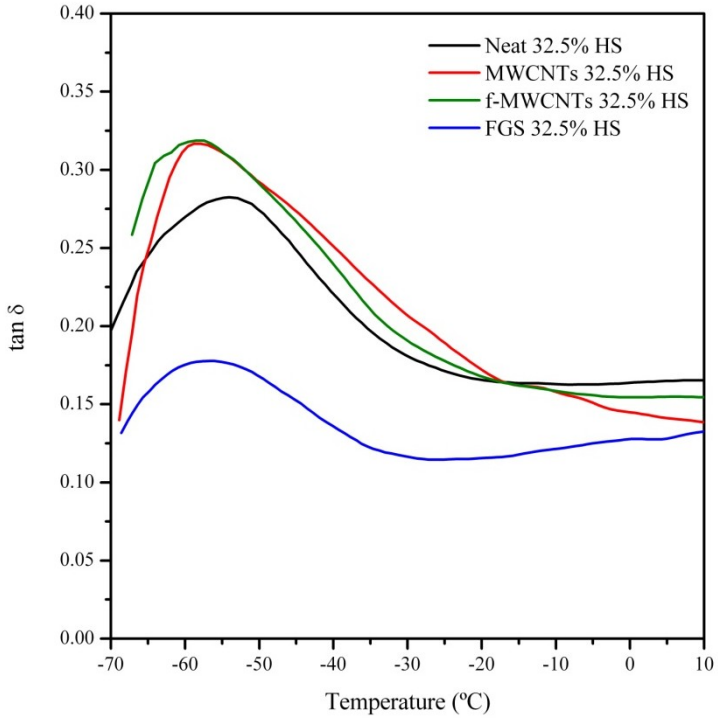

Figure 4.31. Damping factor (*tan δ*) of FPU-32.5% HS nanocomposite foams as a function of temperature.

The mechanical properties of FPU foams, in particular, the specific storage moduli (*E'*) measured by DMA at 25 °C for FPU-25% HS and FPU-32.5% HS are summarised in Table 4.10. The storage modulus increases for FPU foams with higher hard segment content above the glass transition temperature (T_g). This effect is observed on the *E'* at 25 °C for neat FPU foams with 25% HS and 32.5% HS. However, it has been reported [29] that the influence of the two-phase morphology depends on the structure of the HS and its organisation on the system, which can be observed for the filled FPU foams. Although CNPs act as reinforcing fillers for FPU-25% HS foams, these nanoparticles have a detrimental effect on the mechanical properties of FPU-32.5% HS foams. As previously suggested, CNPs are less effective in systems with high HS content due to their higher rigidity, diminishing the storage modulus.

For FPU-25% HS foams, the greater improvements of the functionalised nanofillers are attributed to the favourable interactions between functional

nanoparticles and the hard segments. The best reinforcing behaviour was obtained with FGS due to their characteristic morphology, as explained in section 4.2.5. [180]

Table 4.10. Specific Storage Modulus (E') at 25 °C for FPU foams.

Sample	E' (kPa·(kg·m^{-3})$^{-1}$) FPU-25% HS	E' (kPa·(kg·m^{-3})$^{-1}$) FPU-32.5% HS
Neat	0.8	2.7
MWCNTs	2.3	2.1
f-MWCNTs	3.9	1.9
FGS	10.5	2.2

4.2.7. Electromagnetic Interference (EMI) Shielding

Electromagnetic interferences (EMI) have been defined as electromagnetic radiations emitted by electrical circuits under current operation that disturb the operation of surrounding electrical equipment. Therefore, the function of a shield is to prevent the emissions of the electric and magnetic waves from propagation from one region to another by using conducting or magnetic materials. [257, 258]

The EMI shielding effectiveness (SE) of FPU nanocomposite foams is directly related to their conductivity in the X-band frequency region (8 - 12 GHz) and defined as:

$$SE = 10log\left(\frac{P_{in}}{P_{out}}\right) \quad (4.24)$$

where P_{in} is the incident power and P_{out} is the power transmitted through a shielding material. In order to compare the different systems, the specific EMI shielding effectiveness that is, the EMI SE corrected by the density of the material is plotted for FPU-25% HS and FPU-32.5% HS nanocomposite foams (Figure 4.32).

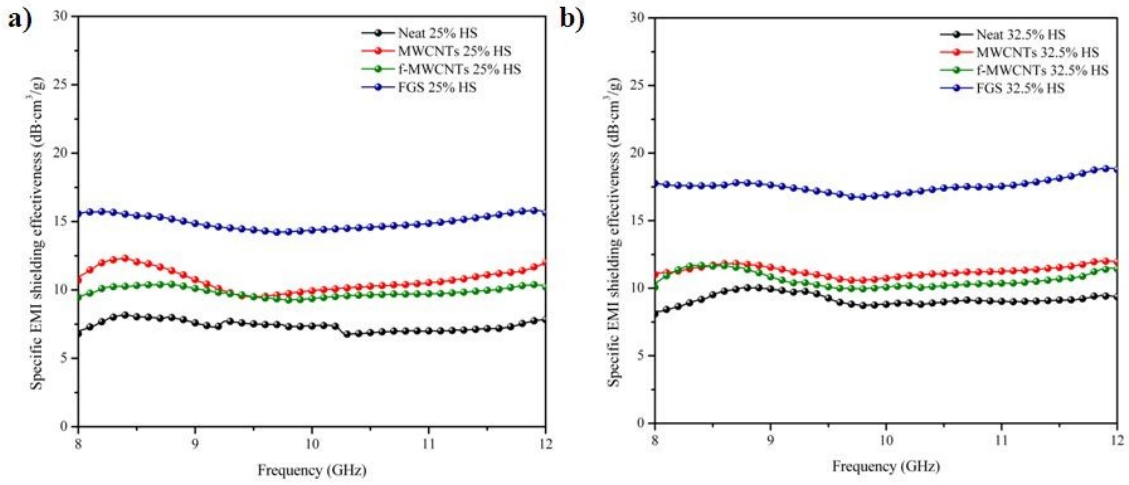

Figure 4.32. Specific EMI shielding effectiveness of: a) FPU-25% HS and b) FPU-32.5% HS nanocomposite foams as a function of frequency.

In the high frequency range, the shielding effectiveness of the systems is independent of the frequency and enhanced by the inclusion of the CNPs in both sets of FPU nanocomposite foams. However, it can be observed that the difference between MWCNTs and f-MWCNTs is not significant while FGS greatly enhances the specific EMI SE of the FPU foams. The maximum values obtained are 15.2 dB·cm^3/g and 18.2 dB·cm^3/g for FPU-25% HS and FPU-32.5% HS FGS foams, respectively. These results confirm that graphene sheets form a better conductive network in FPU foams than carbon nanotubes. Nonetheless, this enhancement is due to the effects on the foaming evolution of foams with FGS, which limits their expansion compared to the other nanocomposite foams and thus, facilitates the interaction between the nanoparticles within the system. It is worth noting that similar EMI SE values were achieved in a closed-cell polystyrene nanocomposite foam with a loading fraction ten times higher than the loading fraction of CNPs used here. [137]

In order to obtain a good microwave absorber material the dielectric constant (ε') should be close to that of air ($\varepsilon'=1$) while the conductivity must be as high as possible. Figures 4.33 and 4.34 show the electrical conductivity and the dielectric constant of FPU nanocomposites foams. As it is widely known, there is a relationship between the electrical conductivity, the dielectric constant and the EMI properties of the systems [259] and hence the results in Figures 4.33 and 4.34 follow the same trend as the ones in Figure 4.32. However, the minor increase in

both, conductivity and EMI shielding effectiveness in these systems is attributed to the open-cell structure of FPU foams that difficult the formation of a good conductive network. On the other hand, this open-cell structure favours low dielectric constant values ($\varepsilon' \approx 1$), even with the inclusion of CNPs, due to the high relative volume of air in the foams.

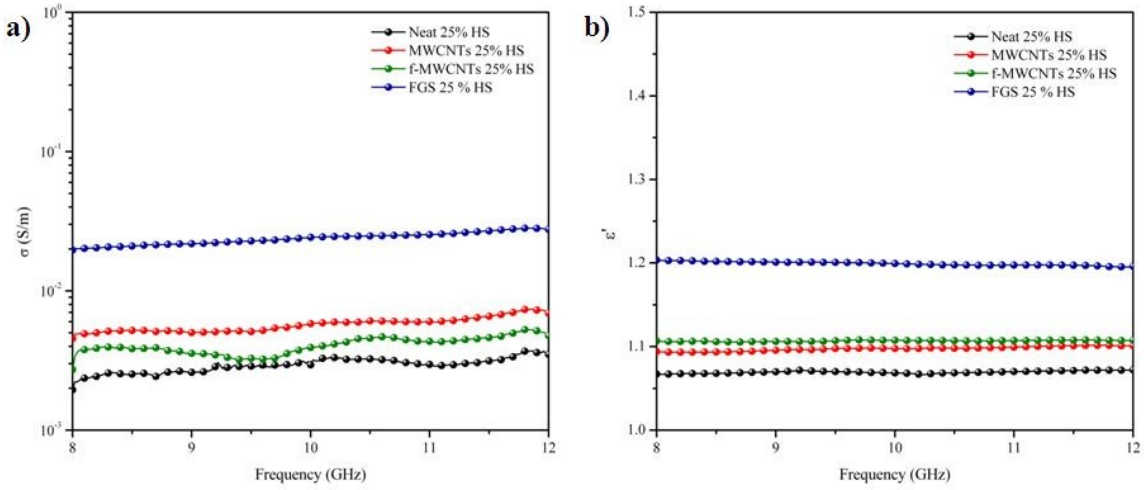

Figure 4.33. Electrical conductivity (σ) and dielectric constant (ε') as a function of frequency for FPU-25% HS nanocomposite foams.

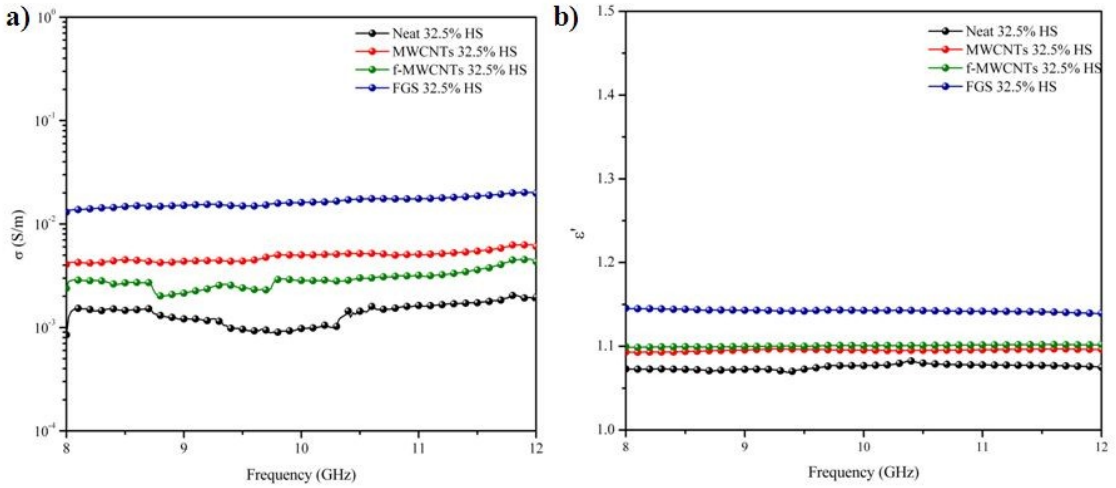

Figure 4.34. Electrical conductivity (σ) and dielectric constant (ε') as a function of frequency for FPU-32.5% HS nanocomposite foams.

Finally, the shielding phenomena of a material can be divided into three mechanisms: reflection, transmission and absorption (Figure 4.35). In the vector network analyser (VNA), the *S*-parameters of the two-port network system represent the reflection and transmission coefficients. From the analysis of the *S*-parameters, the transmissivity (*T*), reflectivity (*R*) and absorptivity (*A*) can be calculated as:

$$\mathrm{T} = \left|{S_{12}}^2\right| = \left|{S_{21}}^2\right| \tag{4.25}$$

$$\mathrm{R} = \left|{S_{11}}^2\right| = \left|{S_{22}}^2\right| \tag{4.26}$$

$$\mathrm{A} = 1 - S - T \tag{4.27}$$

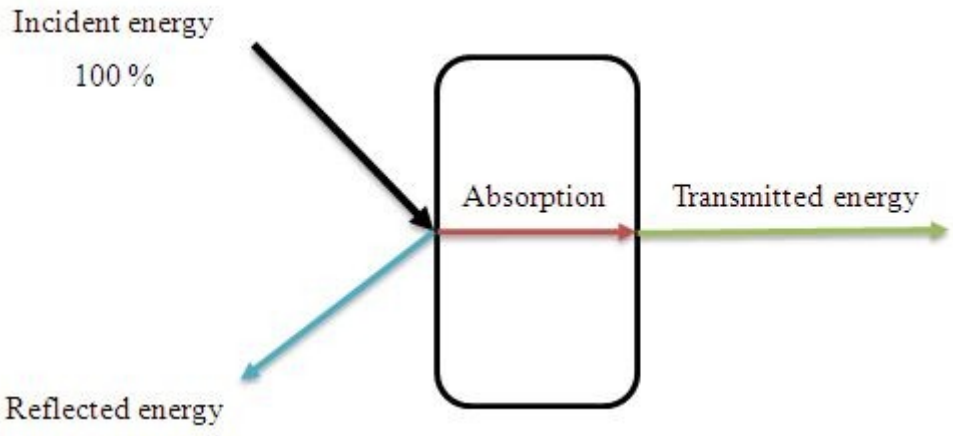

Figure 4.35. Schematic representation of the phenomena observed due to the incident energy on a shielding material.

Table 4.11 summarises the percentage values of *T*, *R* and *A* obtained for both sets of FPU nanocomposite foams. It can be observed that FPU nanocomposite foams transmitted almost 90 % of the incident energy. Hence, the primary EMI shielding mechanism of FPU foams is transmission in the X-band frequency region. However, FPU nanocomposite foams show a slight increase on the absorptivity due to a decrease on the transmissivity (Table 4.11), which means that CNPs produce a change on the behaviour of the materials, making them more absorbers.

Table 4.11. Percentage values of transmissivity (*T*), reflectivity (*R*) and absorptivity (*A*) for FPU nanocomposite foams.

	Sample	*T* (%)	*R* (%)	*A* (%)
25% HS	Neat	91.7	0.1	7.2
	MWCNTs	88.4	1.5	10.1
	f-MWCNTs	86.7	1.4	11.9
	FGS	69.8	3.5	26.7
32.5% HS	Neat	92.5	0.7	6.8
	MWCNTs	90.8	1.5	7.7
	f-MWCNTs	88.5	1.4	10.1
	FGS	75.8	2.0	22.2

4.3. CONCLUSIONS

In this Chapter, two sets of flexible nanocomposite foams were studied with two different contents of HS (25 % and 32.5 %) and filled with three different CNPs: MWCNTs, f-MWCNTs and FGS. Initially, the rheological behaviour of the polyol/CNP dispersions was studied in order to understand the effect of the different CNPs on the viscosity, which will influence the later kinetics of polymerisation and foaming evolution of the systems. MWCNTs conferred a strong shear-thinning behaviour due to their aspect ratio and the ability to form a network within the polyol while the effect of f-MWCNTs was less pronounced because of the presence of functional groups and low aspect ratio. However, polyol/FGS dispersions showed a Newtonian behaviour ascribed to a reduction on the number of interactions between sheets within the dispersions.

Next, the kinetics of polymerisation of both sets of FPU nanocomposite foams were analysed by means of *in-situ* FT-IR spectroscopy and synchrotron SAXS. The polymerisation reaction and the development of the phase-separated structure of FPU foams are strongly influenced by both, HS content and presence of CNPs with different morphologies and surface bearing groups. FT-IR analysis confirmed a deceleration on the kinetics of polymerisation due to the increase of the hard segment content. Meanwhile, synchrotron SAXS analysis showed a delay

of the morphology development being the rate of evolution of the interdomain spacing slower for FPU-32.5% HS nanocomposite foams. Thus, the kinetics of polymerisation and the kinetics of phase separation of hard segments follow a parallel trend. The effect of the nanoparticles on the polymerisation and microphase structure depended on their rigidity, type of functional groups on their surface and the water/isocyanate ratio. The visualisations of the CRW model images clarify the results obtained by FT-IR spectroscopy and SAXS. Meanwhile, AFM images showed the influence of the nanoparticles on the two-phase morphology of FPU nanocomposite foams. The foaming expansion and density evolution of FPU-25% HS were analysed by X-ray radioscopy in order to understand the physical phenomena occurred during the development of these systems. The rheological behaviour of the polyol/CNP dispersions and the increase of viscosity during polymerisation, which depend on the morphology and surface functionalisation of CNPs, strongly influence the mechanisms of cellular structure evolution. Consequently, the effect of the CNPs on the micro- and macrostructure of FPU foams was significant.

On the other hand, the effects of HS content and CNPs on the characteristics of the resultant FPU nanocomposite foams were analysed. The influence of the hard segment content was observed on the glass transition temperature (T_g) of the soft segments. FPU foams with higher HS contents showed an increase of the T_g due to the restrictions on the movement of the polyol chains imposed by the HS, while the influence of the CNPs can also be detected for low contents of HS. In addition the mechanical properties were enhanced by the presence of CNPs for foams with low contents of HS, while they have a detrimental effect for higher contents of HS. Similar results were observed on the thermal properties where FPU nanocomposite foams with less HS presented greater improvements compared to the FPU-32.5% HS. Hence, CNPs appear to be less effective in foams with high content of hard segments due to the higher rigidity of this system. Finally, an enhancement of the EMI shielding effectiveness is observed due to the inclusion of the CNPs. In particular, the highest values in conductivity and EMI SE were obtained for foams filled with FGS due to the formation of a better conductive network in these systems. Nonetheless, the delay on the reaction kinetics affected

the final expansion and final density of FPU foams filled with FGS, which strongly influenced the physical properties of these nanocomposite foams.

5. RIGID POLYURETHANE NANOCOMPOSITE FOAMS

Rigid polyurethane (RPU) foams are employed in a wide range of industrial products and processes. Their characteristic closed-cell structure and rigidity provide these materials of good properties such as thermal insulation, high mechanical strength and strong adhesive properties.

This Chapter reports the effect of CNPs on the kinetics of foaming evolution and the resultant properties of RPU nanocomposite foams. The rheological behaviour of the polyol/CNP dispersions showed a strong shear-thinning behaviour MWCNTs at 0.8 wt.-%, being Newtonian for FGS at the same loading content. Due to the characteristics of the RPU foams, the kinetics of foaming was measured by adiabatic temperature rise observing an acceleration for systems filled with CNPs. Meanwhile, the density of the final nanocomposites decreased compared to the neat RPU foam mainly due to the nucleation and blowing effects. Nonetheless, the thermal stability has been improved in the RPU nanocomposite foams, in particular for FGS and a notable enhancement of the EMI shielding effectiveness it is observed for MWCNTs.

5.1. MATERIALS AND METHODS

5.1.1. Materials

RPU foams were prepared following the formulation summarised in Table 5.1. First, the polyol and the additives (catalysts, surfactants and water) were stirred for 3 minutes until a homogeneous mixture was obtained. Then, the required amount of isocyanate was added and mixed again for 20 seconds. The amount of each component was based on parts by hundred parts of polyol (phpp) and the isocyanate index was adjusted to 130. In this case, the HS/SS ratio was not considered because RPU foams are highly cross-linked and the phase-separated structure observed on FPU foams is hard to define.

Table 5.1. Rigid polyurethane foam formulation.

Trade name	Description	phpp
Alcupol R-4520	Polyether polyol	100.00
Isocianato H	Isocyanate	138.38
PC CAT NP60	Amine-catalyst	0.74
DABCO 2097	Catalyst	0.16
SILSTAB 2100	Surfactant	1.58
PC TOPA	Flow improver	3.16
Water	Blowing agent	1.47
CNPs	Nanofiller	0.4 0.8

The polyol used for the synthesis was a polyether polyol with high functionality, Alcupol R-4520 (Repsol Química). The molecular weight was 536 $g \cdot mol^{-1}$ with a hydroxyl number of 450 mg $KOH \cdot g^{-1}$. Hence, the average functionality of the polyol was 4. The isocyanate was a 4,4'-diphenilmethane diisocyanate (MDI), Isocianato H from SynthesiaEspañola S.A. with a viscosity of 300 $mPa \cdot s^{-1}$ at 20 °C and an isocyanate content of 31 wt.-%. DABCO 2097 (potassium acetate in diethylene glycol, AirProducts) and PC CAT NP 60 (N,N-dimethylbenzylamine, Performance Chemicals Handels GmbH) were used as catalysts in the reaction. SILSTAB 2100 (block copolymer of dimethylsiloxane and

a polyoxyalkylene, Siltech Corp.) was used as a surfactant, PC TOPA (N-[3-(dimethylamino) propyl] tall-oil amide, Performance Chemicals Handels GmbH) was used as a flow improving agent and distilled water was the blowing agent in the reaction.

5.1.2. Synthesis

RPU nanocomposite foams were prepared in two steps and following the same formulation as for unfilled RPU foams (Table 5.1). First, a fixed amount of CNPs (MWCNTs, f-MWCNTs and FGS) was added into the polyol. The mixture was initially sonicated for 10 min with an ultrasonication probe (Sonics VibraCell) in a water/ice bath, and was then stirred under high shear at 2400 rpm for 6 h. Subsequently, the surfactant, catalysts and distilled water were added to the polyol/CNP mixture and stirred at 2400 rpm for 3 min. Finally, the isocyanate was added and mixed for 20 s before foaming occurred in an open cylindrical mould. Images of the resultant samples can be observed in Figure 5.1.

The final loading fractions of CNPs (MWCNTs, f-MWCNTs and FGS) introduced in RPU foams were 0.17 and 0.35 wt.-% of the resulting composite foam.

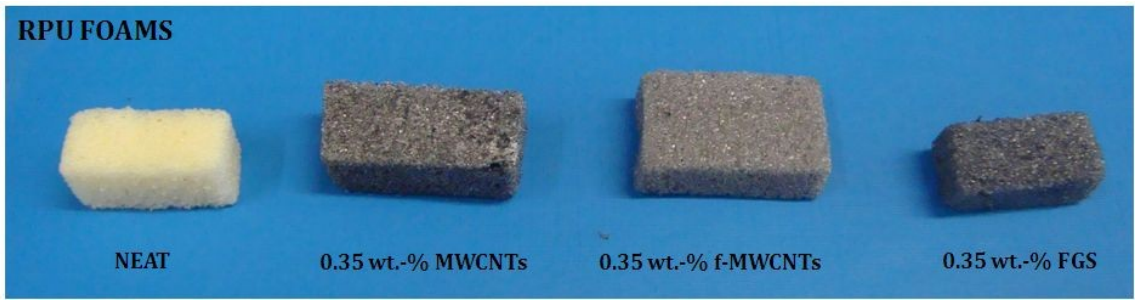

Figure 5.1. RPU nanocomposite foams.

5.1.3. Characterisation

The rheological behaviour of the polyol/CNP dispersions was measured using an Anton Paar P-PTD200/ERD Rheological Device. The geometry used was a

stainless-steel corrugated parallel plate with a diameter of 20 mm. The gap was fixed to 0.3 mm and a dynamic frequency sweep from 0.01 to 100 rad·s^{-1} at 21 °C was employed. The results were averaged over three different samples. The standard error for each set of samples was less than 1 %.

The thermal conductivity of the polyol/CNP dispersions was measured with a KD2 probe (Decagon Devices Inc.), based on the hot wire technique, and consisting of a needle located inside the sample (Figure 5.2). The needle had a waiting time of 30 seconds until the sample temperature was stable and then it was heated up for 30 seconds, being used to monitor the cooling rate and calculate the thermal conductivity with an accuracy of 5 %. The measurements were carried out at room temperature where no convection was present in the polyol/CNP dispersions. The results were the average of at least six measurements for each sample.

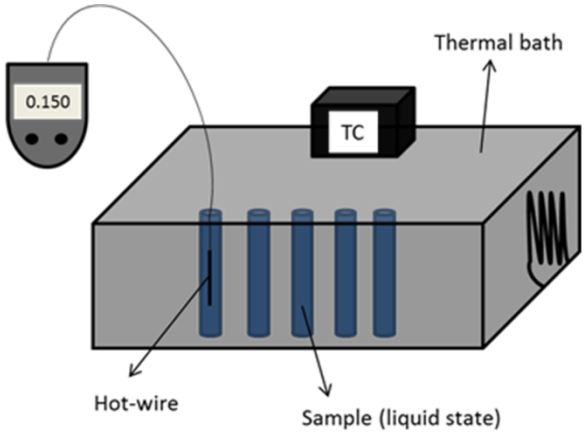

Figure 5.2. Experimental setup employed to measure the thermal conductivity.

The adiabatic temperature rise was used to follow the reaction kinetics of RPU nanocomposite foams. The exotherms were determined using a Scanning Vibrating Needle Curemeter (Rapra Technology Ltd.) which measured the temperature of the rising foam. The experimental measurements were carried out by centring a stainless steel type K thermocouple in the middle of the mould where the components were pre-mixed for 20 seconds. The thermocouple was connected to a computer where the data were registered. The results were the average of at

least three different foam samples. The experimental error for each set of samples was around 10 % ascribed to small-scale laboratory sample preparation and vibrating needle positioning.

The structure of the foams was qualitatively examined using a Phillips XL30 environmental scanning electron microscope (ESEM) at 15 kV. Cross-sections of the samples were cryo-fractured perpendicular to the foaming direction and the fracture surface was sputter-coated with gold/palladium.

The density of a cubic sample was measured as the sample weight divided by its volume according to ASTM D 1622-03. The results were the average of at least three different foam samples.

Thermogravimetric analysis (TGA) of 5 mg of foam samples was performed on a TGA Q500, TA Analysis, under air environment at a heating rate of 20 °C/min over the temperature range of 25-700 °C.

Uniaxial compression tests were performed according to ASTM D1621 using an INSTRON universal testing instrument (Model 3366). All measurements were carried out at a crosshead speed of 5 mm/min. The samples were loaded to a maximum compressive strain of 75 %. The experiments were performed on rectangular samples of 15 x 15 mm^2 cross-section and 9 mm height.

The EMI characterisation is reported as a set of scattering parameters. The *S*-parameters (S_{mn}) of foam nanocomposites were measured with a Wiltron 360B vector network analyser (VNA) in a frequency range from 8 to 12 GHz (X-band). The S parameter is known as the scattering parameter. For S_{mn}, m corresponds to the network analyser port number that receives the scattered energy, while n is the network analyser port number that transmits the incident energy. Nanocomposite foams were cut into a rectangle (2.9 cm x 1.07 cm) to fit a steel waveguide sample holder. A full two-port VNA calibration was performed at the beginning of each test sequence to correct systematic measurement errors. The reported results were the average of three tested samples for each foam. The measured scattering parameters are: S_{11}, the forward reflection coefficient; S_{21}, the

forward transmission coefficient; S_{22}, the reverse reflection coefficient; and S_{12}, the reverse transmission coefficient. The unit of the *S*-parameters is decibels (dB).

5.2. RESULTS AND DISCUSSION

5.2.1. Rheology of Dispersions

The study of the rheological behaviour of polyol/CNP systems is essential to understand the later foaming process. Additionally, it provides an effective tool for understanding the dispersion degree in filled polymer systems. The dependence of the complex viscosity with the angular frequency for neat polyol and its filled dispersions at 0.4 phpp and 0.8 phpp of CNPs is shown in Figure 5.3.

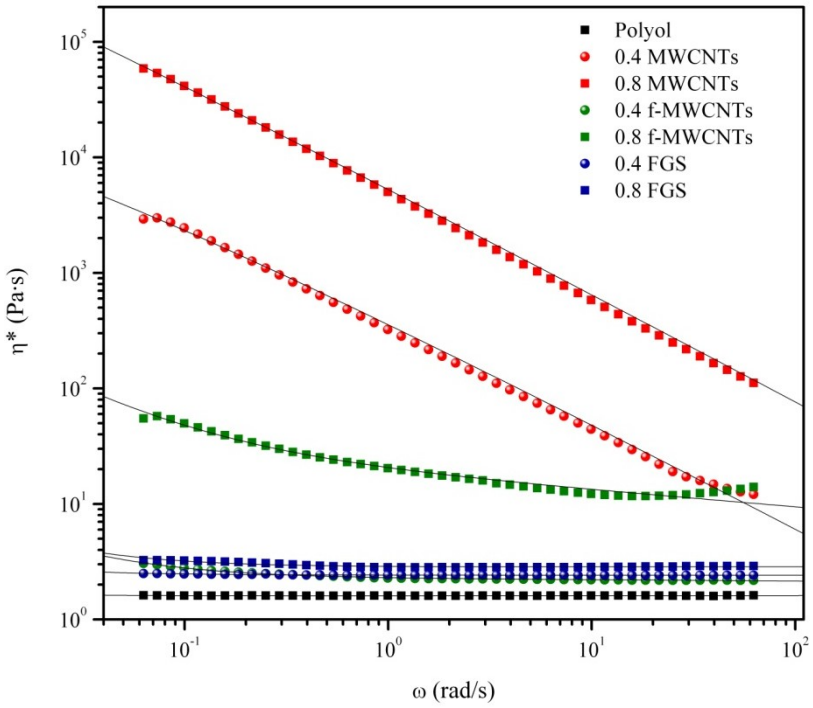

Figure 5.3. Variation of the complex viscosity (η^*) as a function of the angular frequency (ω) for polyol/CNP dispersions. The solid lines are the fit to the Herschel-Bulkley model.

The rheological behaviour of polyol/CNP dispersions can be quantitatively described by the Herschel-Bulkley model (Equation (5.1)):

$$\eta^* = \frac{\tau_0}{\omega} + k\omega^{n-1} \quad (5.1)$$

where η^* is the complex viscosity, ω is the angular frequency, τ_0 is the yield stress below which there is no flow, k is the consistency index and n is the flow index which describes the rheological behaviour (for $n<1$ shear-thinning, for $n>1$ shear thickening and for $n=1$ Newtonian fluid). Table 5.2 summarises the parameters obtained from the fitting of the Herschel-Bulkley model. This model has widely been applied in emulsions, suspensions of solid particles, gels and foams. [182-184] In the case of polyol dispersions, it has previously been used for clays [260] and for carbon nanotubes, [185] observing a decrease of the shear thinning exponent as the concentration of nanoparticles increased in the systems.

Table 5.2. Parameters and the correlation coefficient (r^2) of the Herschel-Bulkley model for the polyol/CNP dispersions.

Sample	**τ_0 (Pa)**	**k (Pa·s^n)**	**n**	**r^2**
Polyol	≈0	1.61	1.00	0.99
0.4 MWCNTs	192.87	181.41	0.57	0.98
0.8 MWCNTs	3740.79	1730.58	0.42	0.98
0.4 f-MWCNTs	0.05	2.25	0.98	0.99
0.8 f-MWCNTs	2.23	18.44	0.83	0.98
0.4 FGS	0.01	2.41	1.00	0.93
0.8 FGS	0.03	2.85	0.99	0.88

The results show a distinctive rheological behaviour of the dispersions as a function of the loading amount of CNPs. Neat polyol exhibits the typical behaviour of a Newtonian fluid, in which, the viscosity is independent of the frequency. The addition of FGS and low f-MWCNTs loading fractions do not vary the rheological properties of the polyol, showing a flow index value close to 1. However, the dispersions with high loading fractions of f-MWCNTs and in particular, those containing MWCNTs behave as shear-thinning fluids, where the viscosity decreases with increasing frequency. For polyol/MWCNTs dispersions, the complex viscosity η^* increases up to five orders of magnitude compared to the

Newtonian fluids. In agreement with previous studies, [185, 260] the shear thinning exponent of both MWCNTs and f-MWCNTs decrease with increasing loading fractions.

The shear-thinning behaviour has widely been observed in polymer nanocomposites [261, 262] and has been ascribed to the development of network structures either through direct interaction of CNPs or polymeric chain bridging between at least two different nanoparticles. The different behaviour of the CNPs is related to their different morphology and aspect ratio. Knauert *et al.* [179] showed that rod-shaped nanoparticles presented the largest complex viscosity and shear-thinning behaviour, at any given shear rate, than spherical or sheet-like nanoparticles. They explain this result in terms of the presence of chains that bridge the nanoparticles: MWCNTs readily interact with the polymer chains forming a network of particles interconnected with the matrix; while FGS interact by surface adsorption with the polymer chains and correspondingly have the smallest fraction of bridging chains. Recently, Guimont *et al.* [263] reported the occurrence of shear-thinning in graphite oxide-PDMS suspensions at concentrations above 2 wt.-% compared to 0.5 wt.-% MWCNTs of a previous study. [264] Finally, although both MWCNTs and f-MWCNTs presented a shear-thinning behaviour it occurs at different percolation threshold due to the lower aspect ratio of the functionalised nanotubes, reported in Chapter 3.

5.2.2. Kinetics of Foaming Evolution

The reaction kinetics of the PU, such as rates of polymerisation, phase separation, solidification as well as the inherent connectivity between the phases, have a profound effect on the final properties of the system. In this study, three factors have to be considered to establish the effect of CNPs on the reaction kinetics: i) chain mobility, ii) CNP functionalisation and surface area, and iii) reaction temperatures. Chain mobility, linked to the system viscosity, has already been reported to control the phase segregation of segmented PU. [40, 242] Hence, large viscosities could result in a slowdown of the reaction kinetics. Meanwhile, large surface area or the presence of OH-bearing groups on the CNPs, able of

reacting with the isocyanate, could lead to high conversion rates. Finally, due to the highly exothermic nature of the PU reaction, the urethane reaction could be favoured by increasing heat transfer. [265] Hence, higher values of the thermal conductivities of the initial reactants could enhance the heat transfer in the reaction, and then the reaction rates would be faster.

The thermal conductivities (K) of the polyol dispersions are carried out at room temperature and the results are shown in Table 5.3. The thermal conductance in polymer/MWCNT systems is normally assumed to be controlled by a phonon conduction mechanism. [266, 267] The thermal conductivity of CNTs depends on different factors, such as morphology, chirality, diameter and length of the tubes, number of structural defects, specific surface area, as well as on the presence of impurities. [268-270] All CNPs increase the thermal conductivity of the polyol, being this effect more evident for polyol/MWCNT dispersion, which presents an increase of 50 % compared to the neat polyol value. Therefore, MWCNTs facilitate an efficient phonon transfer through the inner layers increasing the thermal conductivity of nanofluids. [77, 271] In the case of polyol/f-MWCNTs, the enhancement in K is lower due to the presence of functional groups that disrupt the π-conjugation, decreasing the phonon conduction mechanism and hence lowering the K value. Dispersions of FGS showed even lower values than f-MWCNTs (Table 5.3). The thermal conductivity of graphene strongly depends on the synthesis method, size of graphene, edge roughness, concentration of defects and the dispersant molecules adsorbed on the surface. [272] Hence, the presence of defects and the capacity of adsorption of molecules on their surface, as well as their high specific surface area, reduce the thermal conductivity of polyol/FGS with respect to the dispersions of polyol/MWCNTs. Similar results have been reported by Martin-Gallego *et al*. [271] in liquid epoxy resins.

Table 5.3. Thermal Conductivity (*K*) of polyol/CNP dispersions at room temperature.

Sample	*K* (W·m^{-1}·K^{-1})
Polyol	0.160 ± 0.001
0.8 MWCNTs	0.237 ± 0.004
0.8 f-MWCNT	0.188 ± 0.004
0.8 FGS	0.170 ± 0.001

At this point it is worth noting that, the closed-cell structure of RPU foams hinders the *in-situ* measurement of the kinetics of polymerisation and foaming. Therefore, parallel studies as those done in FPU nanocomposite foams failed due to the overlap of both (i) the enclosing CO_2 gas on the isocyanate band in FT-IR and (ii) the maximum peak in the scattering vector, q, on the instrument beam stop peak in SAXS.

Hence, the extent of conversion in RPU nanocomposite foams was followed by adiabatic temperature rise, [3, 4, 273, 274] which monitors the temperature profile during the foaming reaction. Although this technique provides little information on the reaction chemistry sequence, morphological changes or macroscopic properties as a function of the extent of reaction, [275] it enables the evaluation of the extent of the monomer conversions. Therefore, the kinetic data on fast bulk polymerising systems can be calculated as follows.

The energy balance per unit polymer mass can be expressed as:

$$c_p \frac{dT_{exp}}{dt} = (-\Delta H_r)\frac{dx}{dt} - U(T - T_0) \tag{5.2}$$

where c_p = 1.788 J·(g °K)$^{-1}$ is the average value of the specific heat taking into account the values given by Modern Plastics Encyclopedia [276] for cast polyurethane materials, $(-\Delta H_r)$ is the heat evolved per unit polymer mass, U is the global heat transfer coefficient per polymer unit mass, x and T are the conversion and the experimental temperature at a measured time t and T_0 is the temperature

at $t = 0$. The adiabatic temperature, T_{ad}, can be obtained from the energy balance for adiabatic conditions and verifies:

$$c_p \frac{dT_{ad}}{dt} = (-\Delta H_r) \frac{dx}{dt} \tag{5.3}$$

The adiabatic temperature profile with time of the experimental data is calculated combining Equations (5.2) and (5.3) and using the limits $T = T_0$ for $t = 0$ and $T = T_{ad}$ for the measured time t:

$$T_{ad} = T_{exp} + \int_0^t U'\left(T_{exp} - T_0\right) dt \tag{5.4}$$

where $U'=U/c_p$ is the heat transfer coefficient, obtained by integrating equation (5.2) for long times when $dx/dt \rightarrow 0$. Consequently, the conversion of the reaction, x, is given by:

$$x = r \cdot \left(\frac{T - T_0}{\Delta T_{ad}}\right) \tag{5.5}$$

where r is the stoichiometric ratio of the functional groups, calculated taking into account the formulation data in Section 5.1.1. (0.774 in all the experiments) and ΔT_{ad} is the maximum temperature rise. Figure 5.4 shows the variation of the conversion x with time for neat and RPU nanocomposite foams with 0.35 wt.-% of CNPs loading fractions. All samples show a similar conversion profile and final degree conversion. However, RPU nanocomposite foams have faster conversion rates during the initial stages of the reaction compared to the neat foam (Figure 5.4 inset), but no substantial differences are observed among the different CNPs. This similar behaviour should be ascribed to a combination of the factors mentioned above as follows:

MWCNTs: the large increase in the thermal conductivity of this system compared to the other two should have accelerated the reaction [265, 277]. However, its high viscosity appears to counteract such effect.

f-MWCNTs and FGS: although the thermal conductivity of these systems is smaller compared to the MWCNTs system, the low viscosities and surface functionalities seem to favour the extent of conversion. Similar effects have been observed using the adiabatic temperature rise method for PU foams with montmorillonite (MMT), [278] and the acceleration was attributed to the surface catalytic effect and the high surface area of the MMT.

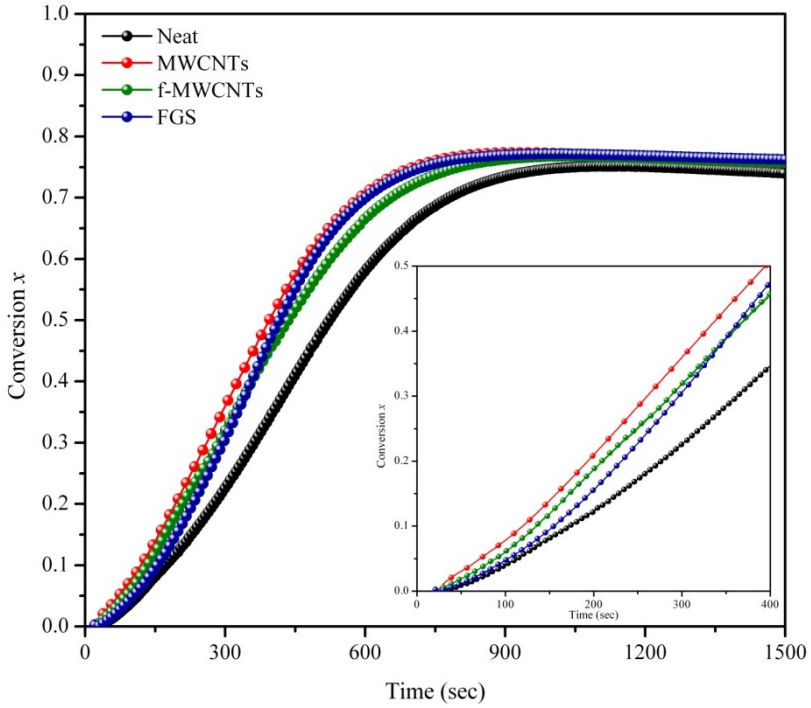

Figure 5.4. Variation of the conversion *x* with time for RPU nanocomposite foams.

5.2.3. Morphological Analysis

The final morphology of foams is determined by the reaction rate which controls the production of gas and the evolution of the fluid rheology. [279] Furthermore, it should be considered that in reactive foams two phases govern the foaming dynamics and hence the morphological development: the continuously polymerising liquid matrix and the disperse gas phase. [280] Both phases are strongly influenced by several parameters (e.g. rate of gas production, diffusivity) being surface tension, temperature and viscosity important on the bubble growth, formation and stability. Hence, if temperature increases, both viscosity and surface

tension decrease, and then membranes become thinner and in some cases rupture because they cannot support the polymer stresses. [11, 121, 279, 280]

Besides these parameters, in polymer nanocomposite foams, two other competing effects influence the cell diameter and should be taken into account: the blowing effect, which increases the cell diameter and the nucleation effect which decreases the cell diameter. The blowing effect is produced by the presence of water on the surface of the nanoparticles. Meanwhile, the nucleation effect depends on the degree of dispersion of nanofillers on the polymer matrix. [281]

The final structure of the RPU nanocomposite foams is observed by scanning electron microscopy (SEM). Figure 5.5 shows the closed-cell structure of these nanocomposite foams and the average cell size is summarised in Table 5.4.

It is widely known that hydrophobic particles can cause instability, producing the rupture of the cells. However, if the particles are well-dispersed in the system, they increase the bulk viscosity and thus can cause an increase of the stability. [22, 282] In addition, the effective stabilisation mechanism is higher as the particle size is smaller. [283] This effect is observed in RPU foams filled with MWCNTs, where a good dispersion of the nanotubes is achieved in the initial system increasing the bulk viscosity. The higher values of the viscosity slow down the drainage rate, preventing the rupture of the cells. Furthermore, due to the strong shear-thinning behaviour of the polyol/MWCNT dispersions, even if there is an important increase on the temperature of the reaction during the foaming, the high viscosity is enough to withstand the polymer stresses on the cell walls maintaining the cell structure. [121, 284] Therefore, the clear reduction of the cell diameter, as the content of nanoparticles increases, confirms the nucleation effect of MWCNTs on RPU foams.

On the other hand, RPU foams filled with 0.17 wt.-% of f-MWCNTs show similar cell diameters as 0.17 wt.-% of MWCNTs. However, they also present a wide cell diameter distribution compared to MWCNTs, as observed in Figure 5.5 d). In the case of high contents (0.35 wt.-%) of f-MWCNTs, the cell diameter is similar to that of neat RPU foam. This increase in the cell size as a function of loading fraction suggests that the blowing effect is dominant for these foams due to

the hydrophilic nature of f-MWCNTs. In the case of FGS, the effect of low loading contents in the cell size of RPU foams is similar to that of f-MWCNTs. However, larger loading fractions of FGS (0.35 wt.-%) result in an increase of the cell diameter although less pronounced than in RPU foams with f-MWCNTs, because the content of the hydrophilic groups on the surface of the graphene sheets is lower, as has been analysed by XPS in Chapter 3. In addition, for RPU foams filled with high contents of FGS and f-MWCNTs, it can be observed (Figure 5.5) a broad distribution of the cell size, which is related to coalescence effects. The lower viscosity of the initial dispersions of f-MWCNTs and FGS causes instability because of the stresses generated in the cell walls by the polymer and the nanoparticles, collapsing the cell structure.

Figures 5.6 and 5.7 show representative SEM images of RPU foams filled with f-MWCNTs at high magnification. It is observed a good dispersion of the CNPs in the system, being located in the struts and walls of the cellular structure.

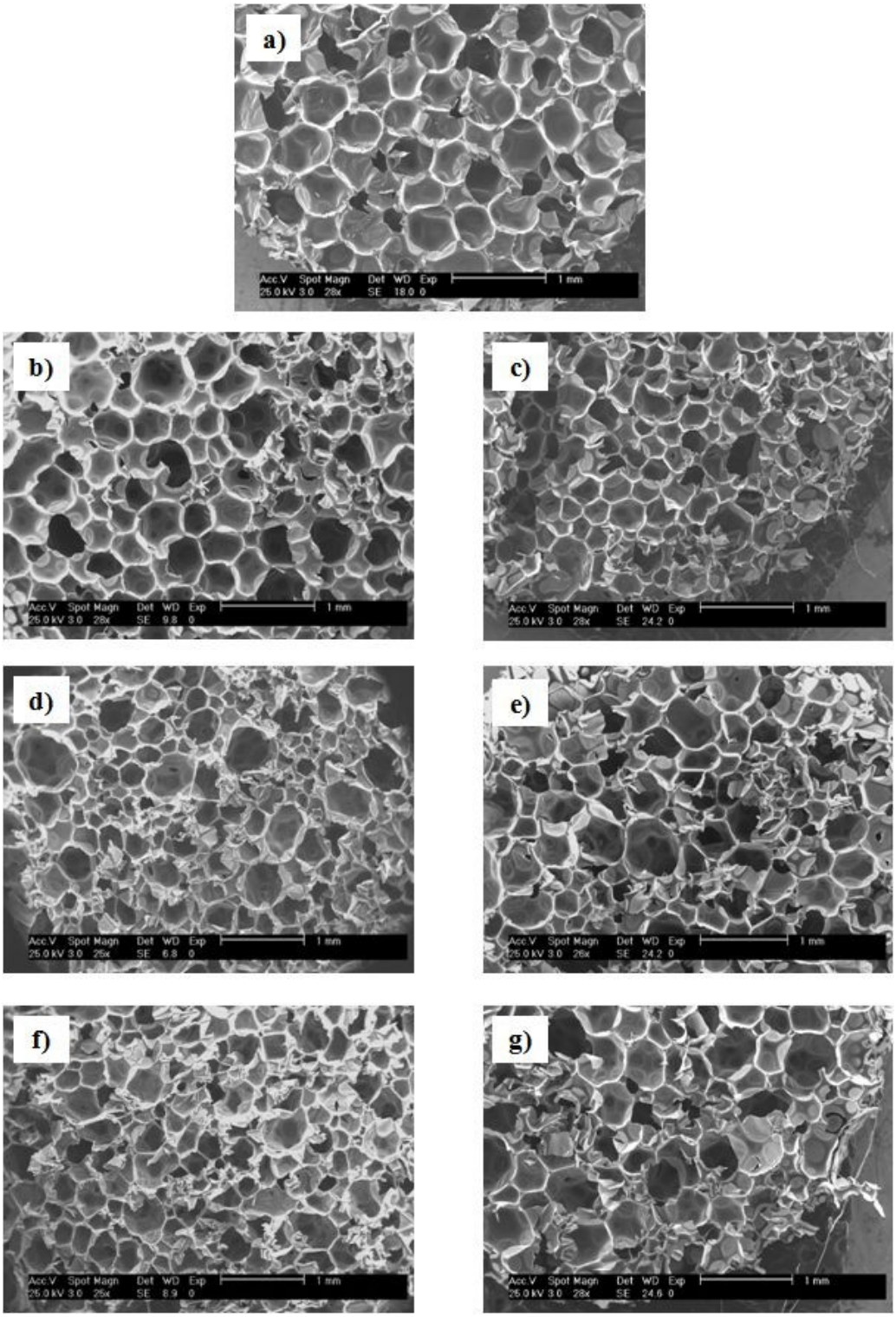

Figure 5.5. Representative SEM images of RPU nanocomposite foams: a) neat; (Left) 0.17 wt.-% CNPs b) MWCNTs, d) f-MWCNTs, and f) FGS; (Right) 0.35 wt.-% CNPs c) MWCNTs, e) f-MWCNTs, and g) FGS.

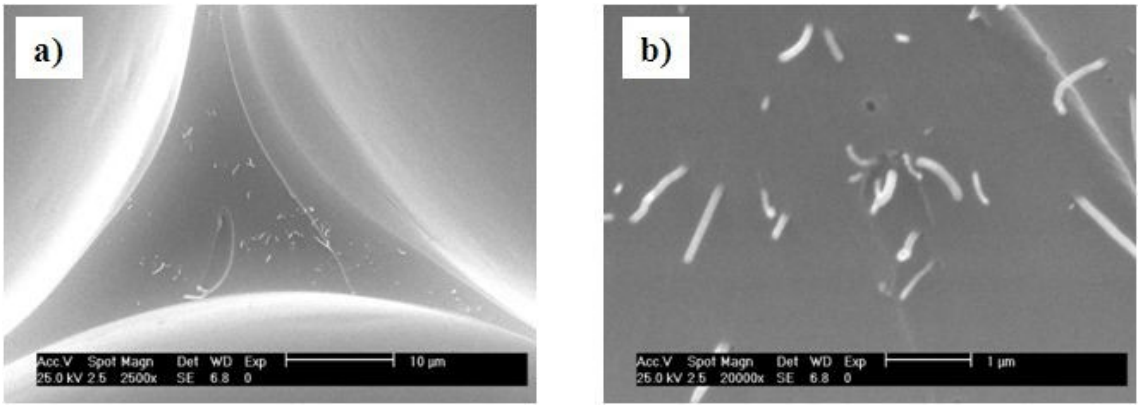

Figure 5.6. Representative SEM image at high magnification of RPU foam filled with f-MWCNTs: a) 10 μm and b) 1 μm.

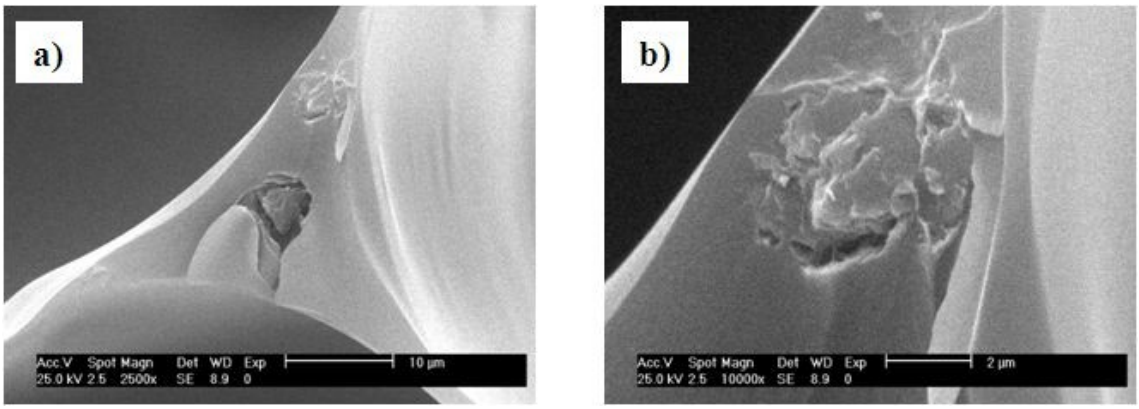

Figure 5.7. Representative SEM image at high magnification of RPU foam filled with FGS: a) 10 μm and b) 2 μm.

Foam density is an important physical property which influences the mechanical properties and hence the final applications of these materials. The densities of RPU nanocomposite foams are given in Table 5.4. It can be observed that as the content of the CNPs increase, the foam density decreases. The SEM images show thinner cell walls for RPU nanocomposite foams, decreasing the foam density. This effect is also observed on the shape of the cell (Figure 5.8), which can be approximated to regular spheres for unfilled RPU foam while in the case of RPU nanocomposite foams become polyhedrons. [140] The low densities for RPU foams filled with high contents (0.35 wt.-%) of f-MWCNTs and FGS are probably caused by the aforementioned instability of the cell structure.

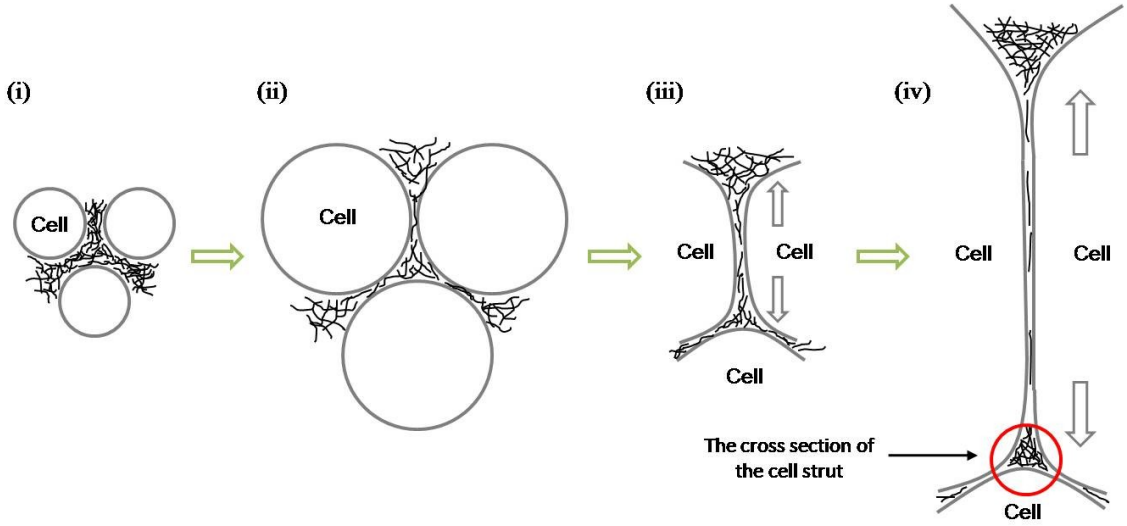

Figure 5.8. Schematic diagram of the changes on the cell structure in RPU nanocomposite foams with the decrease of density during foaming from (i) to (iv). (*Reprinted with permission from Wiley [140] Copyright 2007*).

Table 5.4. Cell size (μm) and density (kg·m^{-3}) of RPU nanocomposite foams.

Sample	Cell size (μm)	Density (kg·m^{-3})
Neat	545 ± 12	82.4 ± 0.4
MWCNTs-0.17 %	442 ± 19	75.3 ± 0.6
MWCNTs-0.35 %	359 ± 10	70.9 ± 3.5
f-MWCNTs-0.17 %	424 ± 48	71.9 ± 2.6
f-MWCNTs-0.35 %	533 ± 55	58.2 ± 1.5
FGS-0.17 %	427 ± 17	65.1 ± 2.3
FGS-0.35 %	476 ± 43	58.2 ± 0.9

5.2.4. Thermogravimetric Analysis (TGA)

The thermo-oxidative degradation of RPU foam and its nanocomposites takes place in a two-step process as can be observed in Figure 5.9. The first degradation in the range between 250-380 °C is related to the depolymerisation of urea bonds, or hard segments (HS), while the second stage at around 470-620 °C

proceeds from the depolycondensation and polyol degradation and is related to the soft segment (SS) content. [250]

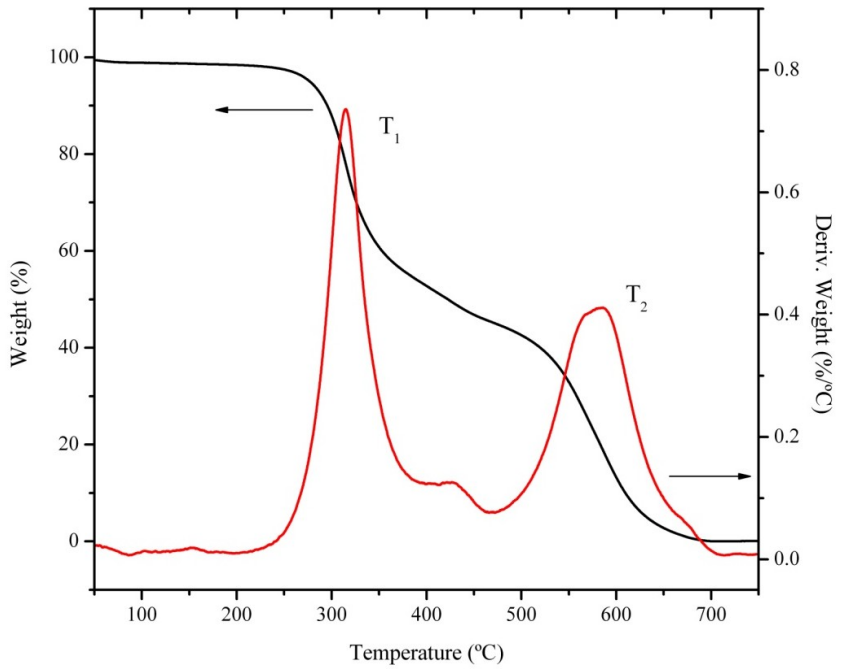

Figure 5.9. Representative TGA thermogram of neat RPU foam under air.

Table 5.5 summarises the results obtained from the degradation temperature at the two main steps and the residue (wt.-%) at 700 °C for RPU nanocomposite foams at 0.17 and 0.35 wt.-% of CNPs. The incorporation of CNPs does not modify the first decomposition step but improves the second one, in particular for FGS, suggesting that CNPs preferably interact with the soft segments. Similar results have been observed by Xia *et al.* [185] in PU-CNT composites. They ascribed the improvement of the thermal stability to: (i) homogeneous dispersion of CNPs, increasing the thermo-oxidative stability of the polymer matrix close to the nanofiller surfaces; (ii) the presence of CNPs enhances the thermal conductivity of the nanocomposite facilitating the heat transport and increasing the thermal stability; (iii) possible formation and stabilisation of CNP-bonded macroradicals.

The best behaviour of the FGS can be attributed to its wrinkled structure which acts as a barrier in polymer systems delaying the escape of volatile degradation products. [252] Furthermore, it is observed in Table 5.5 an increase of

the total residue at 700 °C because of the inclusion of nanofillers. This value is higher for FGS nanocomposite foams due to their morphology and fine dispersion which improves the interfacial adhesion between the nanofillers and the matrix. This evidence means that there is a restriction on the thermal motion of the PU chains improving the thermal stability. [285]

MWCNTs have a less effect on the thermal stability of PU foams. The differences observed on T_2 for carbon nanotubes can be attributed to the lower thermal conductivity of f-MWCNTs, reducing the thermal-oxidative stability of RPU foams filled with f-MWCNTs compared to MWCNTs. As it has been explained in the kinetics section, the functionalisation of carbon nanotubes decreases the phonon conduction mechanism lowering the thermal conductivity of nanotubes. [77]

Table 5.5. TGA results of RPU nanocomposite foams.

Sample	T_1 (°C)	T_2 (°C)	Residue %(700°C)
Neat	316	576	2.8
MWCNTs-0.17 %	316	583	3.2
MWCNTs-0.35 %	319	588	3.4
f-MWCNTs-0.17 %	312	580	3.0
f-MWCNTs-0.35 %	316	581	3.1
FGS-0.17 %	314	586	4.9
FGS-0.35 %	318	600	5.2

5.2.5. Mechanical Properties

The mechanical properties of RPU nanocomposite foams were studied to understand the effect of the CNPs. Figure 5.10 shows typical compressive stress-strain curves of neat RPU foams and with MWCNTs, f-MWCNTs and FGS. All curves show three stages of deformation described by Gibson and Ashby [56]: 1) the initial linear behaviour (until ~ 15 % deformation), resulting from cell wall bending and cell wall stretching, defines the compressive modulus; 2) the broad plateau region resulting from the collapse or cell wall buckling of the foam and 3) the densification region, which occurs at larger strains, where the foam begins to

densify because the cells have almost completely collapsed and hence the compressive stress increases. [286, 287]

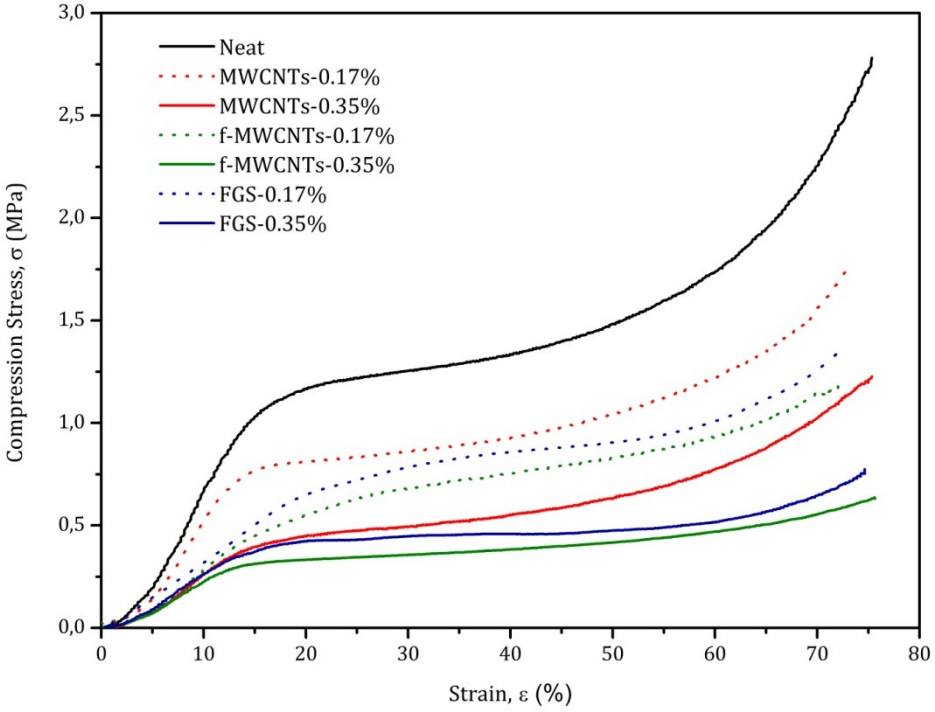

Figure 5.10. Compression stress (σ)-strain (ε) behaviour of the RPU nanocomposite foams.

Figure 5.11 shows the compressive and the specific compressive modulus for the studied foams. In order to exclude the density difference between foams, the specific compressive modulus (i.e. the compressive modulus divided by the density of the foam sample) was used to compare the mechanical properties of RPU foams with different CNPs. It was observed an important reduction on the mechanical properties for nanocomposite foams compared to the neat RPU foam. Hence, samples with 0.35 wt.-% MWCNTs, f-MWCNTs and FGS present a decrease on the specific compressive modulus more than 40 %. Similar results were obtained by Cao *et al*. [288] in polyurethane/clay nanocomposite foams.

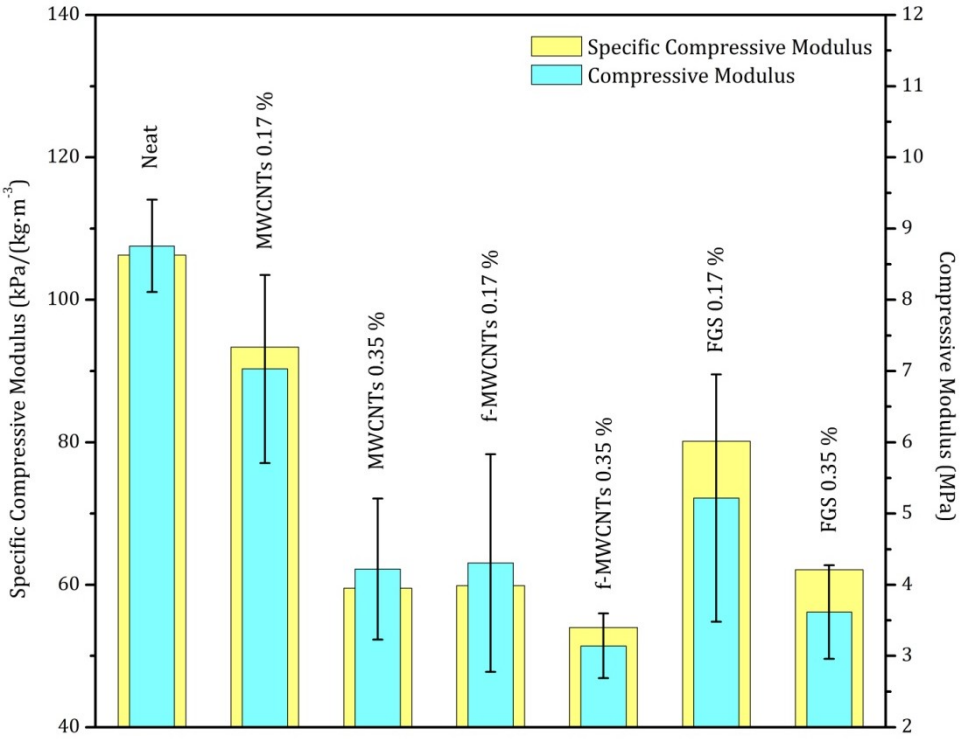

Figure 5.11. Compressive modulus and specific compressive modulus of RPU nanocomposite foams (error bars represent the standard deviation for compressive modulus).

Mechanical properties in foams depend mainly on the structure, size, shape and thickness of the cell walls. [56, 289, 290] The differences on the mechanical behaviour of foams in both linear and densification regions (Figure 5.10) are influenced by the difference on the cell structure of the foams. In SEM images, it was observed that neat RPU foams presented thicker cell walls than RPU nanocomposite foams, which contribute to higher strength and density. However, RPU nanocomposite foams present relatively thinner cell walls and edges, leading to lower mechanical properties. [291] In addition RPU foams filled with 0.35 wt.-% f-MWCNTs and FGS show more collapsed cell structures, which are unable to impart any reinforcement when the network is under load. [290] Hence, the thinner cell walls and proportion of collapsed cells of RPU foams with CNPs contribute to the lower compressive modulus observed for these samples.

Another parameter that greatly contributes to the strength and modulus of polyurethanes is the formation of H-bonding among urethane groups. CNPs may interfere during the polymerisation reaction with the H-bond formation causing a negative effect on the network structure of PU and hence on the mechanical properties. [288, 292] It is observed that in the case of f-MWCNTs this effect is more meaningful than for raw MWCNTs due to the reaction between the functional groups on their surface with the –NCO groups of the isocyanate. [293] However, for foams with FGS the specific compressive modulus improves with respect to foams with MWCNTs, despite of the presence of functional groups on their surface. This suggests that FGS accommodate better on the fine structure of RPU foams than MWCNTs.

5.2.6. Electromagnetic Interference (EMI) Shielding

The EMI shielding effectiveness of RPU nanocomposite foams was measured in the X-band frequency region (8 - 12 GHz) as it was explain in Chapter 4. The measured shielding effectiveness is defined as:

$$SE = 10log\left(\frac{P_{in}}{P_{out}}\right) \tag{5.6}$$

where P_{in} is the incident power and P_{out} is the power transmitted through a shielding material. Figure 5.12 shows the specific EMI shielding effectiveness (SE) of RPU nanocomposite foams while Figure 5.13 shows the comparison of the specific EMI SE for high loading contents of CNPs calculated using Eq. (5.6) and normalised by the density of the nanocomposite foams.

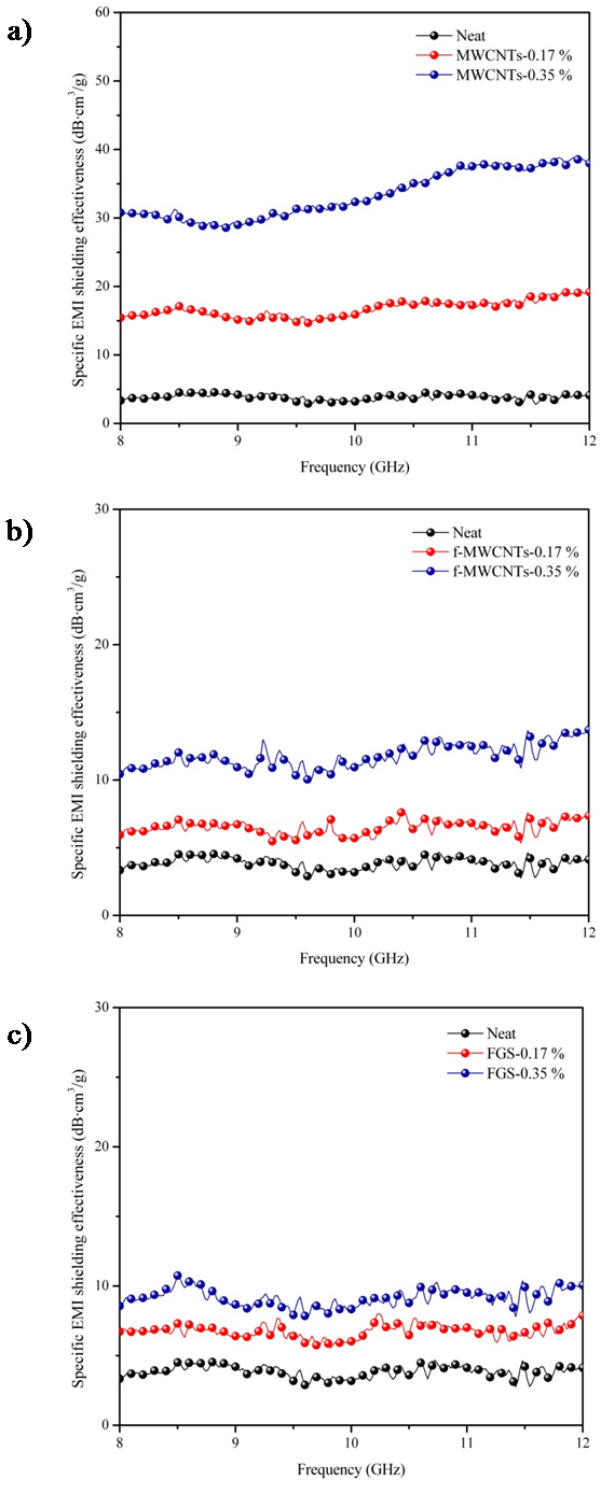

Figure 5.12. Specific EMI shielding effectiveness of RPU nanocomposite foams as a function of frequency for: a) MWCNTs, b) f-MWCNTs and c) FGS.

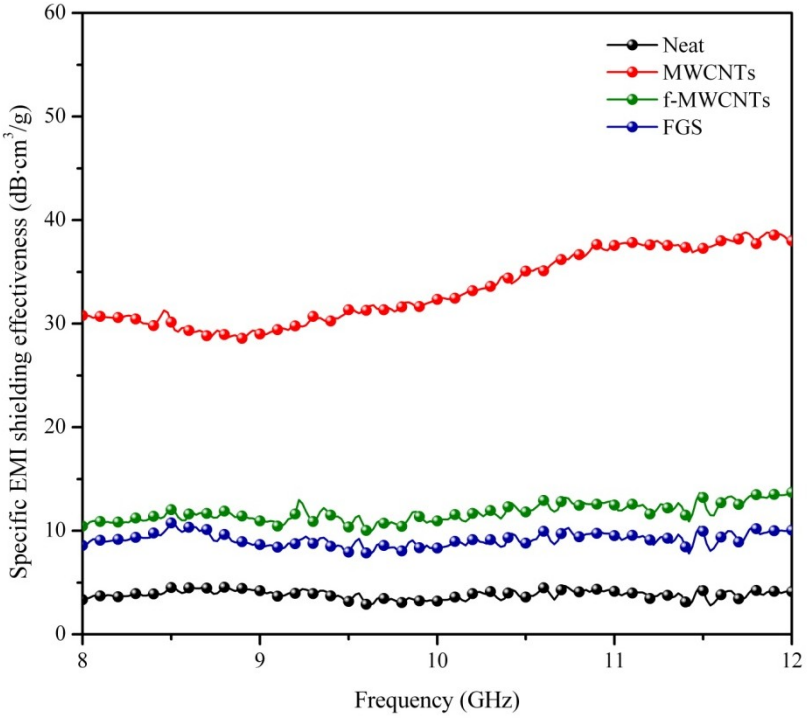

Figure 5.13. Specific EMI shielding effectiveness of RPU nanocomposite foams at 0.35 wt.-% CNPs as a function of frequency.

The presence of CNPs increases the values of the specific EMI shielding effectiveness. While the average value for neat RPU foam was approximately 4 $dB \cdot cm^3 \cdot g^{-1}$, the inclusion of 0.35 wt.-% of f-MWCNTs and FGS enhances this value to around 12.5 and 9.8 $dB \cdot cm^3 \cdot g^{-1}$, respectively (Figure 5.12 b and c). On the other hand, for MWCNT sample the specific EMI shielding effectiveness was more frequency dependent and the maximum value achieved for 0.35 wt.-% at 12 GHz was around 38.7 $dB \cdot cm^3 \cdot g^{-1}$.

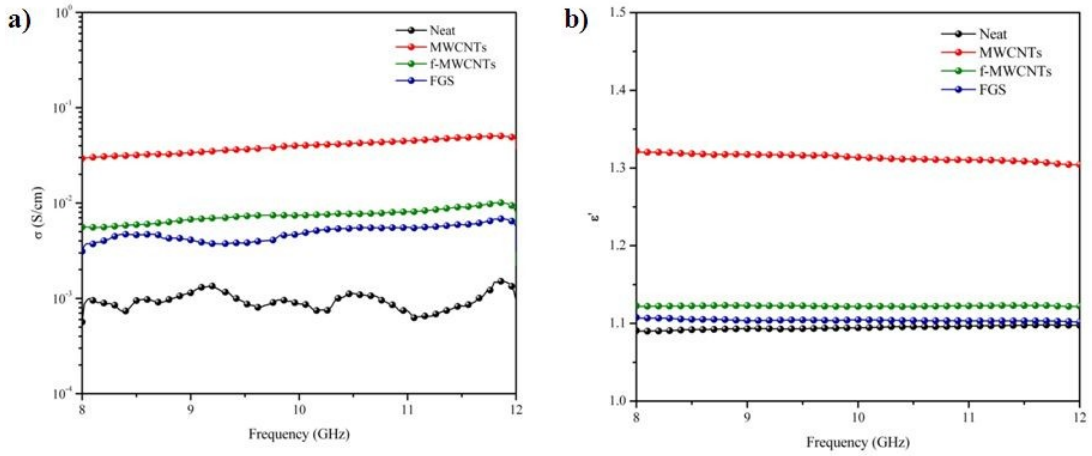

Figure 5.14. a) Electrical conductivity (σ) and b) dielectric constant (ε'), as a function of frequency for RPU nanocomposite foams with 0.35 wt.-% of CNPs.

The increase in EMI shielding effectiveness is attributed to an increase in conductivity of the nanocomposite foams (Figure 5.14 a). The conductivity increases by two orders of magnitude for foams with 0.35 wt.-% of MWCNTs and by one order for f-MWCNTs and FGS compared to the neat foam. Hence, raw MWCNTs form a better conductive network than f-MWCNTs and FGS in RPU nanocomposite foams. This favourable effect of the MWCNTs on RPU foams can be ascribed to the higher density and less collapsed structure, helping to the formation of a better conductive pathway. On the other hand, the increase on the electrical conductivity is related to an increase on the dielectric constant. However, we could notice (Figure 5.14 b) that the ε' value is still close to 1 even for MWCNTs foams which is favoured by the foamed structure of these materials and the high content of air volume.

As it has been explained in Chapter 4, when electromagnetic radiation is incident on a shielding material, phenomena such as reflection, transmission and absorption are observed. The corresponding percentage values of absorptivity (A), transmissivity (T) and reflectivity (R) of RPU nanocomposite foams are reported in Table 5.6.

Table 5.6. Percentage values of transmissivity (*T*), reflectivity (*R*) and absorptivity (*A*) for RPU nanocomposite foams.

Sample	*T* (%)	*R* (%)	*A* (%)
Neat	93.8	1.3	4.9
MWCNTs-0.17 %	76.5	2.5	21.0
MWCNTs-0.35 %	59.2	7.4	33.4
f-MWCNTs-0.17 %	90.6	1.9	7.5
f-MWCNTs-0.35 %	87.0	1.5	11.5
FGS-0.17 %	91.0	1.7	7.3
FGS-0.35 %	89.1	1.4	9.5

The inclusion of low contents of f-MWCNTs and FGS (0.17 wt.-%) has little influence on the average values of *T*, *R* and *A*. However, the effect of MWCNTs is significant even at low loading contents. Theoretically, the higher the decibel level of EMI SE, the less energy is transmitted through the shielding material. [139] This is confirmed by the values of EMI SE and the average data of the transmissivity obtained. Although the main mechanism on all samples is the transmission of the incident radiation, the inclusion of MWCNTs, greatly increases the absorption mechanism of the EMI shielding in the X-band region.

5.3. CONCLUSIONS

Rigid polyurethane nanocomposite foams filled with MWCNTs, f-MWCNTs and FGS were studied in this Chapter. First, the rheological behaviour of polyol/CNP dispersions was analysed in order to understand the effect of the viscosity on the later foaming process. It was observed that the viscosities of the polyol/CNP dispersions depend strongly on the shape, surface functionalisation and concentration of the CNP on the system. Therefore, functionalised CNPs showed, at low concentrations, similar Newtonian behaviour as neat polyol. Nevertheless, MWCNT dispersions behave as shear-thinning fluids even at lower loading fractions.

Once the dispersions were analysed, the extent of conversion of RPU nanocomposite foams was followed using the adiabatic temperature rise technique. Further efforts were tried to follow the reaction by spectroscopy techniques, however, the characteristics of RPU foams did not allow these measurements. Therefore, it was observed that RPU foams filled with CNPs showed faster reaction rates due to the combination of factors such as thermal conductivity and viscosity of the initial dispersions which were influenced by the type of nanoparticles and their surface functionalisation. In addition, it was analysed the effect of the reaction and addition of CNPs on the final cellular structure of RPU nanocomposite foams. Systems filled with MWCNTs had smaller cell size than neat RPU foam but lower density, because their cell walls were thinner. On the other hand, the functionalised nanoparticles also showed collapsed cells because of the instability of these systems during foaming and thus the foam density of these systems was even lower than for neat RPU foam.

The effect CNPs on the characteristics of the resultant RPU nanocomposite foams was studied. The thermal stability of RPU foams was improved for the nanocomposites, in particular for foams filled with FGS due to the wrinkled structure of these nanofillers. Nevertheless, it was observed a detrimental effect on the mechanical properties of RPU foams due to the inclusion of the CNPs, which can be attributed to the thinner cell walls and proportion of collapsed cells. On the other hand, the EMI properties of RPU nanocomposite foams were improved in the X-band region. In particular, the presence of MWCNTs enhanced the conductivity of the foam systems because they formed a better conductive network due to the higher density and cellular structure of these nanocomposite foams.

6. CONCLUDING REMARKS

Polymer nanocomposite foams are novel composite materials with interest at the industrial and academic level. As a result, the number of studies on the potential benefits of nanofillers on the foaming process, cellular structure and properties of the final nanocomposite foams is increasing over the years. In particular, the attention is focused on the introduction of carbon-based nanoparticles, due to their remarkable properties and the capacity to reinforce fine structures in which conventional fillers cannot be readily accommodated. One class of polymeric foams with high versatility and large market, because of the ease production and wide variety of products depending on their formulation, are polyurethane foams. Therefore, the combination of PU foams and carbon-based nanoparticles generate lightweight and multifunctional materials.

This Thesis deals with the study of PU nanocomposite foams and their effect on the kinetics of polymerisation, foaming and physical properties of the resultant materials. The different chemical formulations and resultant cellular structures, depending on the type of foam, flexible or rigid, and the different CNPs introduced strongly affect the polymerisation and foaming evolution as well as the final morphology and cellular structure and thus the final properties. From the results of the study the next conclusions can be extracted:

- Several carbon nanoparticles (CNPs), multi-walled carbon nanotubes (MWCNTs), functionalised MWCNTs (f-MWCNTs) and functionalised graphene sheets (FGS), have been successfully in-house synthesised with desired characteristics of morphology, aspect ratio, purity and functional groups to be

compatible with the polymer media and transfer efficiently their properties to the polyurethane foams.

- The dispersion of the CNPs was carried out in the corresponding polyol, depending on the type of PU foam, flexible or rigid. The rheological behaviour of the dispersions was confirmed to be strongly dependent of the aspect ratio, morphology, surface functionalisation of the CNPs and the ability to create a nanoparticles network within the dispersion. MWCNTs have shown to be the most effective filler, attaining a rheological percolation threshold at 0.1 wt.-%.
- Water-blown FPU nanocomposite foams and RPU nanocomposite foams were successfully developed. Furthermore, the variation of the HS/SS ratio in FPU nanocomposite foams was studied due to the strong influence on the phase-separation and final characteristics of this type of PU foams. However, CNPs appear to be less effective in FPU foams with high content of hard segments due to the higher rigidity of this system.
- The kinetics of polymerisation and foaming evolution were analysed by spectroscopy and radioscopy techniques for FPU foams and by adiabatic temperature rise in the case of RPU foams. The spectroscopy techniques showed that the polymerisation reaction and the development of the phase-separated structure of FPU foams are delayed because of the increase of HS content and the presence of CNPs with different morphologies and surface bearing groups. Meanwhile, the temperature profiles obtained for RPU foams displayed an acceleration of the extent of conversion due to the addition of CNPs in the system. The opposite behaviour is ascribed to both the deactivation of the catalyst observed in FPU and the techniques employed to carry out the measurements, being different in FPU and RPU foams due to the particular characteristics of each type of system. While spectroscopy techniques provide information on the reaction chemistry sequence and morphological changes as a function of the extent of reaction the adiabatic temperature rise technique just enables the evaluation of the extent of the monomer conversions.
- SEM images showed an open-cell structure for FPU nanocomposite foams, being closed-cell for RPU foams. The CNPs increase the cell size in FPU nanocomposite foams due to the viscosity effects while decrease this parameter in RPU systems due to the competition between nucleation and blowing effects.

- In FPU foams it was observed an increase of the T_g due to the increase of the HS content, while CNPs had little influence on the glass transition. However, the detrimental effect of the storage modulus observed for FPU foams with higher HS contents and presence of CNPs may be ascribed to the hindering effect on the formation of a nanoparticles network within the system.
- The mechanical properties of RPU foams decreased by the presence of CNPs, because of the lower density and thinner cells walls developed during the formation of the nanocomposites.
- The thermal stability improved in both, FPU and RPU nanocomposite foams because of the addition of CNP. In particular, the presence of FGS greater enhanced the thermo-oxidative degradation of PU foams due to the morphology of these CNPs.
- The EMI shielding effectiveness properties were improved in the X-band region for FPU and RPU foams. However, greater values were obtained for RPU than for FPU nanocomposite foams influenced by the cellular structure (close or open-cell) which facilitated, in the case of RPU systems, the formation of a better conductive network. Furthermore it was observed that for FPU foams, FGS are better fillers, while for RPU foams greater improvements were obtained with MWCNTs. It is worth noting that FGS strongly affects the structure and expansion of FPU foams, leading to lower height and high density and thus facilitating the formation of a conductive network.
- Considering the desired final application of the developed foams, graphene appear to be more effective modifying the overall properties of flexible foams while the properties of rigid PU foams are more influenced by MWCNTs.

This Thesis makes a profound insight on the development of PU nanocomposite foams filled with CNPs. In particular, the kinetics of foaming and polymerisation have been exhaustively analysed in FPU foams by different techniques to understand the effects of both the variation of the chemical composition and the presence of the nanoparticles. However the studies on X-ray radioscopy should be continued in order to fully identify the physical events taking place during the foaming reaction. Furthermore, radioscopy could be used for RPU

nanocomposite foams to compare the results with FPU foams due to the different cellular structure obtained in each case.

Other recommendations to continue this work will be the functionalisation of the CNPs with isocyanate or polyethylene glycol (PEG). The aim will be to enhance the interaction between HS and SS with CNPs to better distribute the nanofillers on one of the phases. In this way, a comparison between the properties would better clarify the effect of the CNPs on the different segments.

6. CONCLUSIONES

Los nanocompuestos poliméricos son nuevos materiales de gran interés a nivel industrial y académico. Debido a esto, el número de estudios donde se exponen los beneficios potenciales de las nanocargas en el proceso de espumado, estructura celular y propiedades de las espumas de nanocompuestos se ha incrementado a lo largo de los años. En particular, la atención se centra en la incorporación de nanopartículas de carbono debido a sus excepcionales propiedades y a su capacidad para reforzar estructuras delicadas en las cuales las fibras convencionales no se pueden acomodar físicamente. Uno de los tipos de espumas poliméricas de gran versatilidad y extenso mercado, debido a su facilidad de producción y amplia variedad de productos en función de la formulación empleada, son las espumas de poliuretano. Por tanto, la combinación de estas espumas de PU con las nanopartículas de carbono genera materiales ligeros y multifuncionales.

Esta tesis aborda el estudio de las espumas de nanocompuestos de poliuretano, analizando el efecto de las nanocargas en las cinéticas de polimerización y espumado y en las propiedades físicas de los materiales obtenidos. Las diferentes formulaciones químicas y la estructura celular, dependiendo del tipo de espuma, flexible o rígida, y las diferentes CNPs afectan considerablemente a la polimerización y a la evolución del espumado, así como a su morfología y estructura celular y por tanto, a las propiedades finales. De los resultados obtenidos durante el estudio se han extraído las siguientes conclusiones:

- Diferentes nanopartículas de carbono (CNPs), nanotubos de carbono de múltiple capa (MWCNTs), MWCNTs funcionalizados (f-MWCNTs) y láminas de grafeno funcionalizadas (FGS) se sintetizaron con éxito en el laboratorio, obteniéndose las características requeridas de morfología, dimensiones, pureza y grupos funcionales para que fueran más compatibles con el polímero y poder transferir eficientemente sus propiedades a las espumas de poliuretano.
- La dispersión de las CNPs se llevó a cabo en el poliol correspondiente, dependiendo del tipo de espuma de PU, flexible o rígida. El comportamiento reológico de las dispersiones resultó ser fuertemente dependiente de la relación de aspecto, morfología y funcionalización de las CNPs así como de la habilidad de éstas para formar una red de nanopartículas dentro de la dispersión. Los MWCNTs fueron las cargas más efectivas, alcanzando un umbral de percolación reológico con un contenido de 0.1 % en peso.
- Se sintetizaron las espumas de nanocompuestos de FPU y RPU. Además, en el caso de las espumas flexibles se estudió la variación de contenido de segmentos debido a que tiene una gran influencia en la separación de fases del sistema y en las características finales de este tipo de espumas de PU. Sin embargo, se observó como las CNPs parecen ser menos efectivas en las espumas FPU con mayor contenido de segmento duro debido a la alta rigidez de estos sistemas.
- Las cinéticas de polimerización y la evolución del espumado se analizaron por técnicas de espectroscopia y radioscopia, en el caso de las espumas FPU, y mediante variación de la temperatura adiabática en las espumas RPU. Las técnicas de espectroscopia mostraron que tanto la reacción de polimerización como el desarrollo de la estructura de fases separadas de las espumas FPU sufre una desaceleración debido al aumento en el contenido de segmento duro y a la presencia de CNPs con diferentes morfologías y grupos funcionales. Sin embargo, las curvas de variación de temperatura obtenidas para las espumas RPU mostraron una aceleración en el grado de conversión debido a la adición de CNPs en el sistema. Este comportamiento distinto se debe tanto a la desactivación del catalizador en las espumas FPU como a las técnicas empleadas para llevar a cabo las medidas, siendo diferentes para las espumas FPU y las RPU debido a las características particulares de cada sistema. Mientras que las técnicas de espectroscopia dan información de la secuencia de la reacción química y los

cambios en la morfología en función del grado de reacción, la técnica de variación de la temperatura adiabática únicamente permite la evaluación del grado de conversión de los monómeros.

- Las imágenes de SEM mostraron la estructura de celda abierta de las espumas de nanocompuestos de FPU y la de celda cerrada de los RPU. Las CNPs incrementan el tamaño de celda en los nanocompuestos de FPU debido a una mayor viscosidad mientras que disminuyen este parámetro en los sistemas RPU debido a la competencia entre los efectos de nucleación y espumado.

- En las espumas FPU se observó un aumento de la T_g debido al incremento en el contenido de segmento duro, mientras que las CNPs apenas afectan a la transición vítrea. Sin embargo, la disminución en el módulo de almacenamiento de las espumas FPU con altos contenidos de segmento duro y en presencia de CNPs es debido la imposibilidad de formar una red de nanopartículas en el sistema.

- Las propiedades mecánicas de las espumas RPU disminuyen en las que contienen CNPs, ya que durante el desarrollo de los nanocopuestos se formaron paredes celulares más delgadas y por tanto de menor densidad.

- La estabilidad térmica mejoró tanto en las espumas de nanocompuestos de FPU como en los RPU por la adición de cargas. En concreto, la presencia de FGS mejoró significativamente la termo-oxidación de las espumas de PU debido a la morfología de estas CNPs.

- Las propiedades EMI mejoraron para ambos tipos de espumas de nanocompuestos de PU. Sin embargo, los valores obtenidos para los RPU fueron más satisfactorios que para los FPU, debido fundamentalmente a su estructura celular (celda cerrada o abierta) lo que facilitó, en el caso de los sistemas RPU, la formación de una mejor red conductora. Además, se observó que para las espumas FPU, los FGS se comportan como mejores agentes reforzantes mientras que en el caso de las RPU se obtuvieron mejores resultados con MWCNTs. Cabe destacar que los FGS afectan enormemente a la estructura y la expansión de las espumas FPU, lo que da lugar a menores dimensiones y elevadas densidades del material y por tanto se facilita la formación de la red conductora.

- Considerando las aplicaciones requeridas para las espumas preparadas, el grafeno parece ser más efectivo en la modificación de las

propiedades de las espumas de PU flexibles mientras que las características de las espumas de PU rígidas se ven más afectadas por los MWCNTs.

En esta tesis se ha realizado un profundo estudio en el desarrollo de espumas de nanocompuestos de PU cargados con CNPs. En concreto, las cinéticas de espumado y polimerización han sido exhaustivamente analizadas en las espumas FPU mediante el uso de distintas técnicas con el objetivo de entender el efecto en la variación de la composición química y la presencia de las nanopartículas. Sin embargo, se deberían continuar los estudios de radioscopia para poder identificar completamente los eventos físicos que están teniendo lugar durante la reacción de espumado. Además, la radioscopia podría emplearse en los espumas de nanocompuestos de RPU para comparar los resultados con las espumas FPU debido a las diferentes estructuras celulares obtenidas en cada caso.

Otras recomendaciones para continuar con este trabajo estarían relacionadas con la funcionalización de las CNPs con isocianato o polietilenglicol (PEG). El objetivo sería mejorar la interacción de las CNPS con los segmentos duros o blandos, para conseguir una mejor distribución de las nanocargas en una de las fases. Así, mediante la comparación de las propiedades se podría entender mejor el efecto de las CNPs en los diferentes segmentos.

7. REFERENCES

1. Bhattacharya, S.N.;Kamal, M.R. and Gupta, R.K., *Polymeric nanocomposites: theory and practice*. 2008: Hanser.
2. Bhushan, B., *Handbook of nanotechnology*. 2010: Springer.
3. Jordan, J.;Jacob, K.I.;Tannenbaum, R.;Sharaf, M.A. and Jasiuk, I., *Experimental trends in polymer nanocomposites—a review.* Materials Science and Engineering: A, 2005. **393**(1-2): 1-11.
4. Moniruzzaman, M. and Winey, K.I., *Polymer nanocomposites containing carbon nanotubes.* Macromolecules, 2006. **39**(16): 5194-5205.
5. Advani, S.G., *Processing & properties of nanocomposites*. 2007: World Scientific Publishing.
6. Paul, D.R. and Robeson, L.M., *Polymer nanotechnology: nanocomposites.* Polymer, 2008. **49**(15): 3187-3204.
7. Kim, H.;Abdala, A.A. and Macosko, C.W., *Graphene/Polymer nanocomposites.* Macromolecules, 2010. **43**(16): 6515-6530.
8. Lee, L.J.;Zeng, C.;Cao, X.;Han, X.;Shen, J.*, et al.*, *Polymer nanocomposite foams.* Composites Science and Technology, 2005. **65**(15-16): 2344-2363.
9. Ibeh, C.C. and Bubacz, M., *Current trends in nanocomposite foams.* Journal of Cellular Plastics, 2008. **44**(6): 493-515.
10. Verdejo, R.;Bernal, M.M.;Romasanta, L.J.;Tapiador, F.J. and Lopez-Manchado, M.A., *Reactive nanocomposite foams.* Cellular Polymers, 2011. **30**(2): 45-61.
11. Klempner, D. and Sendijarevic, V., *Handbook of polymeric foams and foam technology*. 2004, Munich: Hanser Publishers.

12. Neff, R.A. and Macosko, C.W., *Simultaneous measurement of viscoelastic changes and cell opening during processing of flexible polyurethane foam.* Rheologica Acta, 1996. **35**: 656-666.
13. Xie, X.-L.;Mai, Y.-W. and Zhou, X.-P., *Dispersion and alignment of carbon nanotubes in polymer matrix: A review.* Materials Science and Engineering: R: Reports, 2005. **49**(4): 89-112.
14. Popov, V.N., *Carbon nanotubes: properties and application.* Materials Science and Engineering: R: Reports, 2004. **43**(3): 61-102.
15. Harris, P.J.F., *Carbon nanotube science. Synthesis, properties and applications*. 2009: Cambridge University Press.
16. Novoselov, K.S.;Geim, A.K.;Morozov, S.V.;Jiang, D.;Zhang, Y.*, et al.*, *Electric field effect in atomically thin carbon films.* Science, 2004. **306**(5696): 666-669.
17. Kotov, N.A., *Materials science: carbon sheet solutions.* Nature, 2006. **442**(7100): 254-255.
18. Brödie, B.C., *On the atomic weight of graphite.* Philosophical Transactions of the Royal Society of London, 1859. **149**: 249-259.
19. Staudenmaier, L., *Verfahren zur darstellung der graphitsäure.* Berichte der Deutschen Chemischen Gesellschaft, 1898. **31**(2): 1481-1487.
20. Hummers, W.S. and Offeman, R.E., *Preparation of graphitic oxide.* Journal of the American Chemical Society, 1958. **80**(6): 1339-1339.
21. Terrones, M.;Martin, O.;Gonzalez, M.;Pozuelo, J.;Serrano, B.*, et al.*, *Interphases in graphene polymer-based nanocomposites: achievements and challenges.* Advanced Materials, 2011. **23**(44): 5302-5310.
22. Lee, S.T. and Ramesh, N.S., *Polymeric foams: mechanisms and materials*. 2004, Boca Raton, Florida, USA: CRC Press LLC.
23. Prud'homme, R.K. and Khan, S.A., eds. *Foams: Theory, Measurements and Applications*. 1996, CRC Press: New York.
24. Singh, S.N., *Blowing Agents*, in *Handbook of Polymer Foams*, Eaves, D., Editor. 2004, Rapra Technology Limited: Shropshire.
25. vandeWitte, P.;Dijkstra, P.J.;vandenBerg, J.W.A. and Feijen, J., *Phase separation processes in polymer solutions in relation to membrane formation.* Journal of Membrane Science, 1996. **117**(1-2): 1-31.

26. Zhang, R. and Ma, P.X., *Processing of Polymer Scaffolds: Phase Separation*, in *Methods of tissue engineering*, Atala, A. and Lanza, R.P., Editors. 2002, Gulf Professional Publishing.
27. Saunders, J.H. and Hansen, R.H., *The Mechanism of Foam Formation*, in *Plastics Foams*, Frisch, K.C. and Saunders, J.H., Editors. 1972, Marcel Dekker: New York.
28. Oërtel, G., *Polyurethane handbook*. 2nd ed ed. 1993, Munich Carl Hanser, GmbH & Co.
29. Randall, D. and Lee, S., *The polyurethanes book*. 2002: J.Wiley.
30. Forrest, M.J., *Chemical characterisation of polyurethanes*, in *Rapra Review Reports*. 1999, iSmithers Rapra Publishing.
31. Woods, G., *Flexible Polyurethane Foams. Chemistry and Technology*. 1982, London: Applied Science Publishers LTD.
32. Bicerano, J.;Daussin, R.D.;Elwell, M.J.A.;Wal, H.R.v.d.;Berthevas, P.*, et al.*, *Flexible polyurethane foams*, in *Polymeric Foams. Mechanisms and Materials*, Lee, S.T. and Ramesh, N.S., Editors. 2004, CRC Press: Boca Raton, Florida, USA.
33. Elwell, M.J.;Ryan, A.J.;Grünbauer, H.J.M. and Van Lieshout, H.C., *An FT ir study of reaction kinetics and structure development in model flexible polyurethane foam systems.* Polymer, 1996. **37**(8): 1353-1361.
34. Herrington, R.;Broos, R. and Knaub, P., *Flexible polyurethane foams*, in *Polymeric Foams and Foam Technology*. 2004, Hanser Publishers: Munich.
35. Tan, S., *Polyurethane rigid foam from soybean oil-based polyol*, in *Faculty of the Graduate School*. 2010, University of Minnesota: Minessota.
36. Artavia, L. and Macosko, C.W., *Polyurethane flexible foam formation*, in *Low Density Cellular Plastics, Physical Basis of Behavior*, Hilyard, N.C. and Cunningham, A., Editors. 1994, Chapman and Hall: London.
37. Eaves, D., *Rigid polyurethane foams*, in *Handbook of Polymer Foams*, Eaves, D., Editor. 2004, Rapra Technology Limted: Shropshire.
38. Housel, T., *Flexible polyurethane foam*, in *Handbook of Polymer Foams*, Eaves, D., Editor. 2004, Rapra Technology Limted: Shropshire.

39. Elwell, M.J.;Mortimer, S. and Ryan, A.J., *A synchrotron SAXS study of structure development kinetics during the reactive processing of flexible polyurethane foam.* Macromolecules, 1994. **27**(19): 5428-5439.

40. Li, Y.;Ren, Z.;Zhao, M.;Yang, H. and Chu, B., *Multiphase structure of segmented polyurethanes: effects of hard-segment flexibility.* Macromolecules, 1993. **26**(4): 612-622.

41. Elwell, M.J.;Ryan, A.J.;Grünbauer, H.J.M. and Van Lieshout, H.C., *In-situ studies of structure development during the reactive processing of model flexible polyurethane foam systems using FT-IR spectroscopy, synchrotron SAXS and rheology.* Macromolecules, 1996. **29**(8): 2960-2968.

42. Li, W.;Ryan, A.J. and Meier, I.K., *Effect of chain extenders on the morphology development in flexible polyurethane foam.* Macromolecules, 2002. **35**(16): 6306-6312.

43. Li, W.;Ryan, A.J. and Meier, I.K., *Morphology development via reaction-induced phase separation in flexible polyurethane foam.* Macromolecules, 2002. **35**(13): 5034-5042.

44. McLean, R.S. and Sauer, B.B., *Tapping-mode AFM studies using phase detection for resolution of nanophases in segmented polyurethanes and other block copolymers.* Macromolecules, 1997. **30**(26): 8314-8317.

45. Garrett, J.T.;Runt, J. and Lin, J.S., *Microphase separation of segmented poly(urethane urea) block copolymers.* Macromolecules, 2000. **33**(17): 6353-6359.

46. Zhang, L.;Jeon, H.K.;Malsam, J.;Herrington, R. and Macosko, C.W., *Substituting soybean oil-based polyol into polyurethane flexible foams.* Polymer, 2007. **48**(22): 6656-6667.

47. Neff, R.;Adedeji, A.;Macosko, C.W. and Ryan, A.J., *Urea hard segment morphology in flexible polyurethane foam.* Journal of Polymer Science Part B: Polymer Physics, 1998. **36**(4): 573-581.

48. Kaushiva, B.D.;McCartney, S.R.;Rossmy, G.R. and Wilkes, G.L., *Surfactant level influences on structure and properties of flexible slabstock polyurethane foams.* Polymer, 2000. **41**(1): 285-310.

49. Aneja, A. and Wilkes, G.L., *On the issue of urea phase connectivity in formulations based on molded flexible polyurethane foams.* Journal of Applied Polymer Science, 2002. **85**(14): 2956-2967.
50. Artavia, L.D. and Macosko, C.W., *Foam kinetics.* Journal of Cellular Plastics, 1990. **26**(6): 490-511.
51. Mora, E.;Artavia, L.D. and Macosko, C.W., *Modulus development during reactive urethane foaming.* Journal of Rheology, 1991. **35**(5): 921-940.
52. Park, H. and Youn, J.R., *Study on reaction injection molding of polyurethane microcellular foam.* Polymer Engineering and Science, 1995. **35**(23): 1899-1906.
53. Niyogi, D.;Kumar, R. and Gandhi, K.S., *Water blown free rise polyurethane foams.* Polymer Engineering and Science, 1999. **39**(1): 199-209.
54. Youn, J.R. and Park, H., *Bubble growth in reaction injection molded parts foamed by ultrasonic excitation.* Polymer Engineering and Science, 1999. **39**(3): 457-468.
55. Hyliard, N., *Mechanics of cellular plastics*. 1982, NY: MacMillan.
56. Gibson, L.J. and Ashby, M.F., *Cellular solids: structure and properties*. 2nd ed. 1997, Cambridge: Cambridge University Press.
57. Modesti, M.;Lorenzetti, A. and Besco, S., *Influence of nanofillers on thermal insulating properties of polyurethane nanocomposites foams.* Polymer Engineering and Science, 2007. **47**(9): 1351-1358.
58. Koo, J.H., *Polymer nanocomposites: processing, characterization, and applications*. 2006: McGraw-Hill.
59. Boehm, H.P., *Some aspects of the surface chemistry of carbon blacks and other carbons.* Carbon, 1994. **32**(5): 759-769.
60. Klein, K.L.;Melechko, A.V.;McKnight, T.E.;Retterer, S.T.;Rack, P.D.*, et al.*, *Surface characterization and functionalization of carbon nanofibers.* Journal of Applied Physics, 2008. **103**(6).
61. Melechko, A.V.;Merkulov, V.I.;McKnight, T.E.;Guillorn, M.A.;Klein, K.L.*, et al.*, *Vertically aligned carbon nanofibers and related structures: Controlled synthesis and directed assembly.* Journal of Applied Physics, 2005. **97**(4).
62. Saito, N.;Aoki, K.;Usui, Y.;Shimizu, M.;Hara, K.*, et al.*, *Application of carbon fibers to biomaterials: A new era of nano-level control of carbon fibers after*

30-years of development. Chemical Society Reviews, 2011. **40**(7): 3824-3834.

63. Ma, P.-C.;Siddiqui, N.A.;Marom, G. and Kim, J.-K., *Dispersion and functionalization of carbon nanotubes for polymer-based nanocomposites: A review.* Composites Part A: Applied Science and Manufacturing, 2010. **41**(10): 1345-1367.
64. Thostenson, E.T.;Ren, Z. and Chou, T.-W., *Advances in the science and technology of carbon nanotubes and their composites: a review.* Composites Science and Technology, 2001. **61**(13): 1899-1912.
65. M. S. Dresselhaus, G.D., Phaedon Avouris, *Carbon nanotubes: synthesis, structure, properties, and applications*. 2001: Springer.
66. Dai, H., *Carbon nanotubes: synthesis, integration, and properties.* Accounts of Chemical Research, 2002. **35**(12): 1035-1044.
67. See, C.H. and Harris, A.T., *A review of carbon nanotube synthesis via fluidized-bed chemical vapor deposition.* Industrial & Engineering Chemistry Research, 2007. **46**(4): 997-1012.
68. Treacy, M.M.J.;Ebbesen, T.W. and Gibson, J.M., *Exceptionally high Young's modulus observed for individual carbon nanotubes.* Nature, 1996. **381**(6584): 678-680.
69. Qian, D.;Wagner, G.J.;Liu, W.K.;Yu, M.-F. and Ruoff, R.S., *Mechanics of carbon nanotubes.* Applied Mechanics Reviews, 2002. **55**(6): 495-533.
70. Li, F.;Cheng, H.M.;Bai, S.;Su, G. and Dresselhaus, M.S., *Tensile strength of single-walled carbon nanotubes directly measured from their macroscopic ropes.* Applied Physics Letters, 2000. **77**(20): 3161-3163.
71. Tombler, T.W.;Zhou, C.W.;Alexseyev, L.;Kong, J.;Dai, H.J.*, et al.*, *Reversible electromechanical characteristics of carbon nanotubes under local-probe manipulation.* Nature, 2000. **405**(6788): 769-772.
72. Ajayan, P.M., *Nanotubes from carbon.* Chemical Reviews, 1999. **99**(7): 1787-1800.

73. Coleman, J.N.;Khan, U. and Gun'ko, Y.K., *Mechanical reinforcement of polymers using carbon nanotubes.* Advanced Materials, 2006. **18**(6): 689-706.

74. Berber, S.;Kwon, Y.-K. and Tománek, D., *Unusually high thermal conductivity of carbon nanotubes.* Physical Review Letters, 2000. **84**(20): 4613-4616.

75. Zhang, G. and Li, B., *Thermal conductivity of nanotubes revisited: effects of chirality, isotope impurity, tube length, and temperature.* The Journal of Chemical Physics, 2005. **123**(11): 114714-4.

76. Che, J.;Çagin, T. and Goddard, W., *Thermal conductivity of carbon nanotubes.* Nanotechnology, 2000. **11**(2): 65-69.

77. Han, Z.D. and Fina, A., *Thermal conductivity of carbon nanotubes and their polymer nanocomposites: A review.* Progress in Polymer Science, 2011. **36**(7): 914-944.

78. Kim, P.;Shi, L.;Majumdar, A. and McEuen, P.L., *Thermal transport measurements of individual multiwalled nanotubes.* Physical Review Letters, 2001. **87**(21).

79. Balandin, A.A.;Ghosh, S.;Bao, W.Z.;Calizo, I.;Teweldebrhan, D.*, et al.*, *Superior thermal conductivity of single-layer graphene.* Nano Letters, 2008. **8**(3): 902-907.

80. Ramasubramaniam, R.;Chen, J. and Liu, H.Y., *Homogeneous carbon nanotube/polymer composites for electrical applications.* Applied Physics Letters, 2003. **83**(14): 2928-2930.

81. Grimes, C.A.;Dickey, E.C.;Mungle, C.;Ong, K.G. and Qian, D., *Effect of purification of the electrical conductivity and complex permittivity of multiwall carbon nanotubes.* Journal of Applied Physics, 2001. **90**(8): 4134-4137.

82. Kim, Y.J.;Shin, T.S.;Choi, H.D.;Kwon, J.H.;Chung, Y.C.*, et al.*, *Electrical conductivity of chemically modified multiwalled carbon nanotube/epoxy composites.* Carbon, 2005. **43**(1): 23-30.

83. Peigney, A.;Laurent, C.;Flahaut, E.;Bacsa, R.R. and Rousset, A., *Specific surface area of carbon nanotubes and bundles of carbon nanotubes.* Carbon, 2001. **39**(4): 507-514.

84. Panella, B.;Hirscher, M. and Roth, S., *Hydrogen adsorption in different carbon nanostructures.* Carbon, 2005. **43**(10): 2209-2214.

85. Bacsa, R.R.;Laurent, C.;Peigney, A.;Bacsa, W.S.;Vaugien, T.*, et al.*, *High specific surface area carbon nanotubes from catalytic chemical vapor deposition process.* Chemical Physics Letters, 2000. **323**(5–6): 566-571.

86. Stoller, M.D.;Park, S.J.;Zhu, Y.W.;An, J.H. and Ruoff, R.S., *Graphene-based ultracapacitors.* Nano Letters, 2008. **8**(10): 3498-3502.

87. Novoselov, K.S.;Geim, A.K.;Morozov, S.V.;Jiang, D.;Katsnelson, M.I.*, et al.*, *Two-dimensional gas of massless Dirac fermions in graphene.* Nature, 2005. **438**(7065): 197-200.

88. Stankovich, S.;Dikin, D.A.;Dommett, G.H.B.;Kohlhaas, K.M.;Zimney, E.J.*, et al.*, *Graphene-based composite materials.* Nature, 2006. **442**(7100): 282-286.

89. Geim, A.K. and Novoselov, K.S., *The rise of graphene.* Nature Materials, 2007. **6**(3): 183-191.

90. Bunch, J.S.;Verbridge, S.S.;Alden, J.S.;van der Zande, A.M.;Parpia, J.M.*, et al.*, *Impermeable atomic membranes from graphene sheets.* Nano Letters, 2008. **8**(8): 2458-2462.

91. Lee, C.;Wei, X.D.;Kysar, J.W. and Hone, J., *Measurement of the elastic properties and intrinsic strength of monolayer graphene.* Science, 2008. **321**(5887): 385-388.

92. Novoselov, K.S.;Jiang, D.;Schedin, F.;Booth, T.J.;Khotkevich, V.V.*, et al.*, *Two-dimensional atomic crystals.* Proceedings of the National Academy of Sciences of the United States of America, 2005. **102**(30): 10451-10453.

93. Li, X.S.;Cai, W.W.;An, J.H.;Kim, S.;Nah, J.*, et al.*, *Large-area synthesis of high-quality and uniform graphene films on copper foils.* Science, 2009. **324**(5932): 1312-1314.

94. Kim, K.S.;Zhao, Y.;Jang, H.;Lee, S.Y.;Kim, J.M.*, et al.*, *Large-scale pattern growth of graphene films for stretchable transparent electrodes.* Nature, 2009. **457**(7230): 706-710.

95. Berger, C.;Song, Z.M.;Li, X.B.;Wu, X.S.;Brown, N.*, et al.*, *Electronic confinement and coherence in patterned epitaxial graphene.* Science, 2006. **312**(5777): 1191-1196.

96. Jiao, L.Y.;Zhang, L.;Wang, X.R.;Diankov, G. and Dai, H.J., *Narrow graphene nanoribbons from carbon nanotubes.* Nature, 2009. **458**(7240): 877-880.

97. Kosynkin, D.V.;Higginbotham, A.L.;Sinitskii, A.;Lomeda, J.R.;Dimiev, A.*, et al.*, *Longitudinal unzipping of carbon nanotubes to form graphene nanoribbons.* Nature, 2009. **458**(7240): 872-876.

98. Worsley, K.A.;Ramesh, P.;Mandal, S.K.;Niyogi, S.;Itkis, M.E.*, et al.*, *Soluble graphene derived from graphite fluoride.* Chemical Physics Letters, 2007. **445**(1-3): 51-56.

99. Cheng, S.H.;Zou, K.;Okino, F.;Gutierrez, H.R.;Gupta, A.*, et al.*, *Reversible fluorination of graphene: Evidence of a two-dimensional wide bandgap semiconductor.* Physical Review B, 2010. **81**(20): 205435.

100. Compton, O.C. and Nguyen, S.T., *Graphene oxide, highly reduced graphene oxide, and graphene: versatile building blocks for carbon-based materials.* Small, 2010. **6**(6): 711-723.

101. Verdejo, R.;Bernal, M.M.;Romasanta, L.J. and Lopez-Manchado, M.A., *Graphene filled polymer nanocomposites.* Journal of Materials Chemistry, 2011. **21**(10): 3301-3310.

102. Titelman, G.I.;Gelman, V.;Bron, S.;Khalfin, R.L.;Cohen, Y.*, et al.*, *Characteristics and microstructure of aqueous colloidal dispersions of graphite oxide.* Carbon, 2005. **43**(3): 641-649.

103. Dubin, S.;Gilje, S.;Wang, K.;Tung, V.C.;Cha, K.*, et al.*, *A one-step, solvothermal reduction method for producing reduced graphene oxide dispersions in organic solvents.* Acs Nano, 2010. **4**(7): 3845-3852.

104. Stankovich, S.;Dikin, D.A.;Piner, R.D.;Kohlhaas, K.A.;Kleinhammes, A.*, et al.*, *Synthesis of graphene-based nanosheets via chemical reduction of exfoliated graphite oxide.* Carbon, 2007. **45**(7): 1558-1565.

105. Lomeda, J.R.;Doyle, C.D.;Kosynkin, D.V.;Hwang, W.F. and Tour, J.M., *Diazonium functionalization of surfactant-wrapped chemically converted graphene sheets.* Journal of the American Chemical Society, 2008. **130**(48): 16201-16206.

106. Wang, G.;Shen, X.;Wang, B.;Yao, J. and Park, J., *Synthesis and characterisation of hydrophilic and organophilic graphene nanosheets.* Carbon, 2009. **47**(5): 1359-1364.

107. Bourlinos, A.B.;Gournis, D.;Petridis, D.;Szabó, T.;Szeri, A.*, et al.*, *Graphite oxide: chemical reduction to graphite and surface modification with primary aliphatic amines and amino acids.* Langmuir, 2003. **19**(15): 6050-6055.

108. Williams, G.;Seger, B. and Kamat, P.V., *TiO(2)-graphene nanocomposites. UV-assisted photocatalytic reduction of graphene oxide.* Acs Nano, 2008. **2**(7): 1487-1491.

109. McAllister, M.J.;Li, J.-L.;Adamson, D.H.;Schniepp, H.C.;Abdala, A.A.*, et al.*, *Single sheet functionalized graphene by oxidation and thermal expansion of graphite.* Chemistry of Materials, 2007. **19**(18): 4396-4404.

110. Schniepp, H.C.;Li, J.L.;McAllister, M.J.;Sai, H.;Herrera-Alonso, M.*, et al.*, *Functionalized single graphene sheets derived from splitting graphite oxide.* Journal of Physical Chemistry B, 2006. **110**(17): 8535-8539.

111. Wang, X.;Zhi, L.J. and Mullen, K., *Transparent, conductive graphene electrodes for dye-sensitized solar cells.* Nano Letters, 2008. **8**(1): 323-327.

112. Gogotsi, Y., *Nanomaterials Handbook*. 2006, Boca Raton, Florida, USA: CRC Press.

113. Spitalsky, Z.;Tasis, D.;Papagelis, K. and Galiotis, C., *Carbon nanotube–polymer composites: chemistry, processing, mechanical and electrical properties.* Progress in Polymer Science, 2010. **35**(3): 357-401.

114. Colton, J.S. and Suh, N.P., *The nucleation of microcellular thermoplastic foam with additives: Part I: Theoretical considerations.* Polymer Engineering & Science, 1987. **27**(7): 485-492.

115. Spitael, P.;Macosko, C.W. and McClurg, R.B., *Block copolymer micelles for nucleation of microcellular thermoplastic foams.* Macromolecules, 2004. **37**(18): 6874-6882.

116. Shen, J.;Han, X. and Lee, L.J., *Nanoscaled reinforcement of polystyrene foams using carbon nanofibers.* Journal of Cellular Plastics, 2006. **42**(2): 105-126.

117. Shen, J.;Zeng, C. and Lee, L.J., *Synthesis of polystyrene–carbon nanofibers nanocomposite foams.* Polymer, 2005. **46**(14): 5218-5224.

118. Yang, J.;Wu, M.;Chen, F.;Fei, Z. and Zhong, M., *Preparation, characterization, and supercritical carbon dioxide foaming of polystyrene/graphene oxide composites.* The Journal of Supercritical Fluids, 2011. **56**(2): 201-207.

119. Antunes, M.;Mudarra, M. and Velasco, J.I., *Broad-band electrical conductivity of carbon nanofibre-reinforced polypropylene foams.* Carbon, 2011. **49**(2): 708-717.

120. Zeng, C.;Hossieny, N.;Zhang, C. and Wang, B., *Synthesis and processing of PMMA carbon nanotube nanocomposite foams.* Polymer, 2010. **51**(3): 655-664.

121. Verdejo, R.;Stampfli, R.;Alvarez-Lainez, M.;Mourad, S.;Rodriguez-Perez, M.A.*, et al.*, *Enhanced acoustic damping in flexible polyurethane foams filled with carbon nanotubes.* Composites Science and Technology, 2009. **69**(10): 1564-1569.

122. Bandarian, M.;Shojaei, A. and Rashidi, A.M., *Thermal, mechanical and acoustic damping properties of flexible open-cell polyurethane/multi-walled carbon nanotube foams: effect of surface functionality of nanotubes.* Polymer International, 2011. **60**(3): 475-482.

123. You, K.;Park, S.;Lee, C.;Kim, J.;Park, G.*, et al.*, *Preparation and characterization of conductive carbon nanotube-polyurethane foam composites.* Journal of Materials Science, 2011. **46**(21): 6850-6855.

124. Dolomanova, V.;Rauhe, J.C.M.;Jensen, L.R.;Pyrz, R. and Timmons, A.B., *Mechanical properties and morphology of nano-reinforced rigid PU foam.* Journal of Cellular Plastics, 2011. **47**(1): 81-93.

125. Harikrishnan, G.;Singh, S.N.;Kiesel, E. and Macosko, C.W., *Nanodispersions of carbon nanofiber for polyurethane foaming.* Polymer, 2010. **51**(15): 3349-3353.

126. Zhang, H.-B.;Yan, Q.;Zheng, W.-G.;He, Z. and Yu, Z.-Z., *Tough graphene–polymer microcellular foams for electromagnetic interference shielding.* ACS Applied Materials & Interfaces, 2011. **3**(3): 918-924.

127. Werner, P.;Verdejo, R.;Wöllecke, F.;Altstädt, V.;Sandler, J.K.W.*, et al.*, *Carbon nanofibers allow foaming of semicrystalline poly(ether ether ketone).* Advanced Materials, 2005. **17**(23): 2864-2869.

128. Park, K.-W. and Kim, G.-H., *Ethylene vinyl acetate copolymer (EVA)/multiwalled carbon nanotube (MWCNT) nanocomposite foams.* Journal of Applied Polymer Science, 2009. **112**(3): 1845-1849.

129. Peng, M.;Zhou, M.X.;Jin, Z.J.;Kong, W.W.;Xu, Z.B.*, et al.*, *Effect of surface modifications of carbon black (CB) on the properties of CB/polyurethane foams.* Journal of Materials Science, 2010. **45**(4): 1065-1073.

130. Saha, M.C.;Kabir, M.E. and Jeelani, S., *Enhancement in thermal and mechanical properties of polyurethane foam infused with nanoparticles.* Materials Science and Engineering: A, 2008. **479**(1-2): 213-222.

131. Verdejo, R.;Barroso-Bujans, F.;Rodriguez-Perez, M.A.;Antonio de Saja, J.;Arroyo, M.*, et al.*, *Carbon nanotubes provide self-extinguishing grade to silicone-based foams.* Journal of Materials Chemistry, 2008. **18**(33): 3933-3939.

132. Verdejo, R.;Saiz-Arroyo, C.;Carretero-Gonzalez, J.;Barroso-Bujans, F.;Rodriguez-Perez, M.A.*, et al.*, *Physical properties of silicone foams filled with carbon nanotubes and functionalized graphene sheets.* European Polymer Journal, 2008. **44**(9): 2790-2797.

133. Verdejo, R.;Barroso-Bujans, F.;Rodriguez-Perez, M.A.;de Saja, J.A. and Lopez-Manchado, M.A., *Functionalized graphene sheet filled silicone foam nanocomposites.* Journal of Materials Chemistry, 2008. **18**(19): 2221-2226.

134. Zammarano, M.;Kramer, R.H.;Harris, R.;Ohlemiller, T.J.;Shields, J.R.*, et al.*, *Flammability reduction of flexible polyurethane foams via carbon nanofiber network formation.* Polymers for Advanced Technologies, 2008. **19**(6): 588-595.

135. Thomassin, J.-M.;Pagnoulle, C.;Bednarz, L.;Huynen, I.;Jerome, R.*, et al.*, *Foams of polycaprolactone/MWNT nanocomposites for efficient EMI reduction.* Journal of Materials Chemistry, 2008. **18**(7): 792-796.

136. Yang, Y.;Gupta, M.C.;Dudley, K.L. and Lawrence, R.W., *Conductive carbon nanofiber–polymer foam structures.* Advanced Materials, 2005. **17**(16): 1999-2003.

137. Yang, Y.;Gupta, M.C.;Dudley, K.L. and Lawrence, R.W., *Novel carbon nanotube–polystyrene foam composites for electromagnetic interference shielding.* Nano Letters, 2005. **5**(11): 2131-2134.

138. Fletcher, A.;Gupta, M.C.;Dudley, K.L. and Vedeler, E., *Elastomer foam nanocomposites for electromagnetic dissipation and shielding applications.* Composites Science and Technology, 2010. **70**(6): 953-958.

139. Eswaraiah, V.;Sankaranarayanan, V. and Ramaprabhu, S., *Functionalized Graphene–PVDF Foam Composites for EMI Shielding.* Macromolecular Materials and Engineering, 2011. **296**(10): 894-898.

140. Xu, X.-B.;Li, Z.-M.;Shi, L.;Bian, X.-C. and Xiang, Z.-D., *Ultralight conductive carbon-nanotube–polymer composite.* Small, 2007. **3**(3): 408-411.

141. Verdejo, R.;Jell, G.;Safinia, L.;Bismarck, A.;Stevens, M.M.*, et al.*, *Reactive polyurethane carbon nanotube foams and their interactions with osteoblasts.* Journal of Biomedical Materials Research Part A, 2009. **88A**(1): 65-73.

142. Singh, C.;Shaffer, M.S. and Windle, A.H., *Production of controlled architectures of aligned carbon nanotubes by an injection chemical vapour deposition method.* Carbon, 2003. **41**(2): 359-368.

143. Dresselhaus, M.S.;Dresselhaus, G.;Saito, R. and Jorio, A., *Raman spectroscopy of carbon nanotubes.* Physics Reports-Review Section of Physics Letters, 2005. **409**(2): 47-99.

144. Eklund, P.C.;Holden, J.M. and Jishi, R.A., *Vibrational modes of carbon nanotubes; Spectroscopy and theory.* Carbon, 1995. **33**(7): 959-972.

145. Ferrari, A.C., *Raman spectroscopy of graphene and graphite: Disorder, electron-phonon coupling, doping and nonadiabatic effects.* Solid State Communications, 2007. **143**(1-2): 47-57.

146. Datsyuk, V.;Kalyva, M.;Papagelis, K.;Parthenios, J.;Tasis, D.*, et al.*, *Chemical oxidation of multiwalled carbon nanotubes.* Carbon, 2008. **46**(6): 833-840.

147. Benson, S.W. and Shaw, R., *Kinetics and mechanism of hydrogenolyses. Addition of hydrogen atoms to propylene toluene and xylene* Journal of Chemical Physics, 1967. **47**(10): 4052-4056.

148. Li, Q.;Yan, H.;Zhang, J. and Liu, Z., *Effect of hydrocarbons precursors on the formation of carbon nanotubes in chemical vapor deposition.* Carbon, 2004. **42**(4): 829-835.

149. Wasel, W.;Kuwana, K. and Saito, K., *Chemical and thermal structures of a xylene-based CVD reactor to synthesize carbon nanotubes.* Chemical Physics Letters, 2006. **422**(4–6): 470-474.

150. Kuwana, K.;Li, T.X. and Saito, K., *Gas-phase reactions during CVD synthesis of carbon nanotubes: Insights via numerical experiments.* Chemical Engineering Science, 2006. **61**(20): 6718-6726.

151. Kunadian, I.;Andrews, R.;Menguc, M.P. and Qian, D., *Multiwalled carbon nanotube deposition profiles within a CVD reactor: An experimental study.* Chemical Engineering Science, 2009. **64**(7): 1503-1510.

152. Bom, D.;Andrews, R.;Jacques, D.;Anthony, J.;Chen, B.*, et al.*, *Thermogravimetric analysis of the oxidation of multiwalled carbon nanotubes: evidence for the role of defect sites in carbon nanotube chemistry.* Nano Letters, 2002. **2**(6): 615-619.

153. Hunt, M.R.C.;Montalti, M.;Chao, Y.;Krishnamurthy, S.;Dhanak, V.R.*, et al.*, *Thermally induced decomposition of single-wall carbon nanotubes adsorbed on H/Si(111).* Applied Physics Letters, 2002. **81**(25): 4847-4849.

154. Santangelo, S.;Messina, G.;Faggio, G.;Lanza, M. and Milone, C., *Evaluation of crystalline perfection degree of multi-walled carbon nanotubes: correlations between thermal kinetic analysis and micro-Raman spectroscopy.* Journal of Raman Spectroscopy, 2011. **42**(4): 593-602.

155. Tapasztó, L.;Kertész, K.;Vértesy, Z.;Horváth, Z.E.;Koós, A.A.*, et al.*, *Diameter and morphology dependence on experimental conditions of carbon nanotube arrays grown by spray pyrolysis.* Carbon, 2005. **43**(5): 970-977.

156. Verdejo, R.;Lamoriniere, S.;Cottam, B.;Bismarck, A. and Shaffer, M., *Removal of oxidation debris from multi-walled carbon nanotubes.* Chemical Communications, 2007(5): 513-515.

157. Peng, H.;Alemany, L.B.;Margrave, J.L. and Khabashesku, V.N., *Sidewall carboxylic acid functionalization of single-walled carbon nanotubes.* Journal of the American Chemical Society, 2003. **125**(49): 15174-15182.

158. Ago, H.;Kugler, T.;Cacialli, F.;Salaneck, W.R.;Shaffer, M.S.P.*, et al.*, *Work functions and surface functional groups of multiwall carbon nanotubes.* The Journal of Physical Chemistry B, 1999. **103**(38): 8116-8121.

159. Okpalugo, T.I.T.;Papakonstantinou, P.;Murphy, H.;McLaughlin, J. and Brown, N.M.D., *High resolution XPS characterization of chemical functionalised MWCNTs and SWCNTs.* Carbon, 2005. **43**(1): 153-161.

160. Webb, M.J.;Palmgren, P.;Pal, P.;Karis, O. and Grennberg, H., *A simple method to produce almost perfect graphene on highly oriented pyrolytic graphite.* Carbon, 2011. **49**(10): 3242-3249.

161. Yang, D.;Velamakanni, A.;Bozoklu, G.;Park, S.;Stoller, M.*, et al.*, *Chemical analysis of graphene oxide films after heat and chemical treatments by X-ray photoelectron and Micro-Raman spectroscopy.* Carbon, 2009. **47**(1): 145-152.

162. Wagner, C.D.;Davis, L.E.;Zeller, M.V.;Taylor, J.A.;Raymond, R.H.*, et al.*, *Empirical atomic sensitivity factors for quantitative analysis by electron spectroscopy for chemical analysis.* Surface and Interface Analysis, 1981. **3**(5): 211-225.

163. Fogden, S.;Verdejo, R.;Cottam, B. and Shaffer, M., *Purification of single walled carbon nanotubes: The problem with oxidation debris.* Chemical Physics Letters, 2008. **460**(1-3): 162-167.

164. Zhang, G.Y.;Qi, P.F.;Wang, X.R.;Lu, Y.R.;Mann, D.*, et al.*, *Hydrogenation and hydrocarbonation and etching of single-walled carbon nanotubes.* Journal of the American Chemical Society, 2006. **128**(18): 6026-6027.

165. Zhang, L.;Kiny, V.U.;Peng, H.;Zhu, J.;Lobo, R.F.M.*, et al.*, *Sidewall functionalization of single-walled carbon nanotubes with hydroxyl group-terminated moieties.* Chemistry of Materials, 2004. **16**(11): 2055-2061.

166. Liu, J.;Rinzler, A.G.;Dai, H.J.;Hafner, J.H.;Bradley, R.K.*, et al.*, *Fullerene pipes.* Science, 1998. **280**(5367): 1253-1256.

167. Dreyer, D.R.;Park, S.;Bielawski, C.W. and Ruoff, R.S., *The chemistry of graphene oxide.* Chemical Society Reviews, 2010. **39**(1): 228-240.

168. Malard, L.M.;Pimenta, M.A.;Dresselhaus, G. and Dresselhaus, M.S., *Raman spectroscopy in graphene.* Physics Reports, 2009. **473**(5–6): 51-87.

169. Rao, C.N.R.;Biswas, K.;Subrahmanyam, K.S. and Govindaraj, A., *Graphene, the new nanocarbon.* Journal of Materials Chemistry, 2009. **19**(17): 2457-2469.

170. Akhavan, O., *The effect of heat treatment on formation of graphene thin films from graphene oxide nanosheets.* Carbon, 2010. **48**(2): 509-519.

171. Shen, J.;Hu, Y.;Shi, M.;Lu, X.;Qin, C.*, et al.*, *Fast and facile preparation of graphene oxide and reduced graphene oxide nanoplatelets.* Chemistry of Materials, 2009. **21**(15): 3514-3520.

172. Biedermann, L.B.;Bolen, M.L.;Capano, M.A.;Zemlyanov, D. and Reifenberger, R.G., *Insights into few-layer epitaxial graphene growth on 4H-SiC(000(1)over-bar substrates from STM studies.* Physical Review B, 2009. **79**(12).

173. Misra, A.;Tyagi, P.K.;Singh, M.K. and Misra, D.S., *FTIR studies of nitrogen doped carbon nanotubes.* Diamond and Related Materials, 2006. **15**(2-3): 385-388.

174. Stankovich, S.;Piner, R.D.;Nguyen, S.T. and Ruoff, R.S., *Synthesis and exfoliation of isocyanate-treated graphene oxide nanoplatelets.* Carbon, 2006. **44**(15): 3342-3347.

175. Lin, Y.;Jin, J. and Song, M., *Preparation and characterisation of covalent polymer functionalized graphene oxide.* Journal of Materials Chemistry, 2011. **21**(10): 3455-3461.

176. Macosko, C.W., *RIM: fundamentals of reaction injection molding*. 1989, Munich: Hanser Publishers.

177. Potschke, P.;Fornes, T.D. and Paul, D.R., *Rheological behavior of multiwalled carbon nanotube/polycarbonate composites.* Polymer, 2002. **43**(11): 3247-3255.

178. Xu, J.H.;Chatterjee, S.;Koelling, K.W.;Wang, Y.R. and Bechtel, S.E., *Shear and extensional rheology of carbon nanofiber suspensions.* Rheologica Acta, 2005. **44**(6): 537-562.

179. Knauert, S.T.;Douglas, J.F. and Starr, F.W., *The effect of nanoparticle shape on polymer-nanocomposite rheology and tensile strength.* Journal of Polymer Science Part B-Polymer Physics, 2007. **45**(14): 1882-1897.

180. Ramanathan, T.;Abdala, A.A.;Stankovich, S.;Dikin, D.A.;Herrera-Alonso, M.*, et al.*, *Functionalized graphene sheets for polymer nanocomposites.* Nature Nanotechnology, 2008. **3**(6): 327-331.

181. Heine, D.R.;Petersen, M.K. and Grest, G.S., *Effect of particle shape and charge on bulk rheology of nanoparticle suspensions.* Journal of Chemical Physics, 2010. **132**(18).

182. Gupta, R.K., *Polymer and Composite Rheology*. 2000, Boca Raton, Florida, USA: CRC Press.

183. Kinloch, I.A.;Roberts, S.A. and Windle, A.H., *A rheological study of concentrated aqueous nanotube dispersions.* Polymer, 2002. **43**(26): 7483-7491.

184. Mueller, S.;Llewellin, E.W. and Mader, H.M., *The rheology of suspensions of solid particles.* Proceedings of the Royal Society a-Mathematical Physical and Engineering Sciences, 2009. **466**(2116): 1201-1228.

185. Xia, H.S. and Song, M., *Preparation and characterization of polyurethane-carbon nanotube composites.* Soft Matter, 2005. **1**(5): 386-394.

186. Tiwari, M.K.;Bazilevsky, A.V.;Yarin, A.L. and Megaridis, C.M., *Elongational and shear rheology of carbon nanotube suspensions.* Rheologica Acta, 2009. **48**(6): 597-609.

187. Bose, S.;Bhattacharyya, A.R.;Kulkarni, A.R. and Pötschke, P., *Electrical, rheological and morphological studies in co-continuous blends of polyamide 6 and acrylonitrile–butadiene–styrene with multiwall carbon nanotubes prepared by melt blending.* Composites Science and Technology, 2009. **69**: 365-372.

188. Huang, Y.Y.;Ahir, S.V. and Terentjev, E.M., *Dispersion rheology of carbon nanotubes in a polymer matrix.* Physical Review B, 2006. **73**(12).

189. Zhang, Q.;Rastogi, S.;Chen, D.;Lippits, D. and Lemstra, P.J., *Low percolation threshold in single-walled carbon nanotube/high density polyethylene composites prepared by melt processing technique.* Carbon, 2006. **44**(4): 778-785.

190. Doi, M. and Edwards, S.F., *The Theory of Polymer Dynamics*. 1986, London: Oxford Press.

191. Marceau, S.;Dubois, P.;Fulchiron, R. and Cassagnau, P., *Viscoelasticity of brownian carbon nanotubes in PDMS semidilute regime.* Macromolecules, 2009. **42**(5): 1433-1438.

192. Kim, H. and Macosko, C.W., *Processing-property relationships of polycarbonate/graphene composites.* Polymer, 2009. **50**(15): 3797-3809.

193. Pujari, S.;Rahatekar, S.;Gilman, J.W.;Koziol, K.K.;Windle, A.H.*, et al.*, *Shear-induced anisotropy of concentrated multiwalled carbon nanotube suspensions using x-ray scattering.* Journal of Rheology, 2011. **55**(5): 1033-1058.

194. Wan, C. and Chen, B., *Reinforcement and interphase of polymer/graphene oxide nanocomposites.* Journal of Materials Chemistry, 2012. **22**(8): 3637-3646.

195. Heintz, A.M.;Duffy, D.J.;Nelson, C.M.;Hua, Y.;Hsu, S.L., *et al.*, *A spectroscopic analysis of the phase evolution in polyurethane foams.* Macromolecules, 2005. **38**(22): 9192-9199.

196. Chen, J.W. and Chen, L.W., *The kinetics of diethylene glycol formation from bis-hydroxyethyl terephthalate with antimony catalyst in the preparation of PET.* Journal of Polymer Science Part a-Polymer Chemistry, 1999. **37**(12): 1797-1803.

197. Macan, J.;Ivanković, H.;Ivanković, M. and Mencer, H.J., *Study of cure kinetics of epoxy-silica organic–inorganic hybrid materials.* Thermochimica Acta, 2004. **414**(2): 219-225.

198. Li, S.;Vatanparast, R. and Lemmetyinen, H., *Cross-linking kinetics and swelling behaviour of aliphatic polyurethane.* Polymer, 2000. **41**(15): 5571-5576.

199. Chattopadhyay, D.K.;Prasad, P.S.R.;Sreedhar, B. and Raju, K., *The phase mixing of moisture cured polyurethane-urea during cure.* Progress in Organic Coatings, 2005. **54**(4): 296-304.

200. Maji, P.K. and Bhowmick, A.K., *Influence of number of functional groups of hyperbranched polyol on cure kinetics and physical properties of polyurethanes.* Journal of Polymer Science Part a-Polymer Chemistry, 2009. **47**(3): 731-745.

201. de Lima, V.;Pelissoli, N.D.;Dullius, J.;Ligabue, R. and Einloft, S., *Kinetic study of polyurethane synthesis using different catalytic systems of Fe, Cu, Sn, and Cr.* Journal of Applied Polymer Science, 2010. **115**(3): 1797-1802.

202. Cunliffe, A.V.;Davis, A.;Farey, M. and Wright, J., *The kinetics of the reaction of isophorone di-isocyanate with mono-alcohols.* Polymer, 1985. **26**(2): 301-306.

203. Eceiza, A.;de la Caba, K.;Gascon, V.;Corcuera, M.A. and Mondragon, I., *The influence of molecular weight and chemical structure of soft segment in reaction kinetics with tolyl isocyanate.* European Polymer Journal, 2001. **37**(8): 1685-1693.

204. Han, J.L.;Yu, C.H.;Lin, Y.H. and Hsieh, K.H., *Kinetic study of the urethane and urea reactions of isophorone diisocyanate.* Journal of Applied Polymer Science, 2008. **107**(6): 3891-3902.

205. Ryan, A.J., *Spinodal decomposition during bulk copolymerization. Reaction injection molding* Polymer, 1990. **31**(4): 707-712.

206. Draye, A.C. and Tondeur, J.J., *Kinetic study of organotin-catalyzed alcohol-isocyanate reactions Part 1. Inhibition by carboxylic acids in toluene.* Journal of Molecular Catalysis a-Chemical, 1999. **138**(2-3): 135-144.

207. Berashevich, J. and Chakraborty, T., *Doping graphene by adsorption of polar molecules at the oxidized zigzag edges.* Physical Review B, 2010. **81**(20).

208. Chang, S.L.;Yu, T.L.;Huang, C.C.;Chen, W.C.;Linliu, K.*, et al.*, *Effect of polyester side-chains on the phase segregation of polyurethanes using small-angle X-ray scattering.* Polymer, 1998. **39**(15): 3479-3489.

209. Strobl, G.R. and Schneider, M., *Direct evaluation of the electron-density correlation-function of partially crystalline polymers.* Journal of Polymer Science Part B-Polymer Physics, 1980. **18**(6): 1343-1359.

210. Roe, R.-J., *Methods of X-ray and neutron scattering in polymer science*. 2000: Oxford University Press: New York.

211. Gommes, C.J. and Roberts, A.P., *Structure development of resorcinol-formaldehyde gels: Microphase separation or colloid aggregation.* Physical Review E, 2008. **77**(4).

212. Jinnai, H.;Hashimoto, T.;Lee, D. and Chen, S.H., *Morphological characterization of bicontinuous phase-separated polymer blends and one-phase microemulsions.* Macromolecules, 1997. **30**(1): 130-136.

213. Quintanilla, J.;Reidy, R.F.;Gorman, B.P. and Mueller, D.W., *Gaussian random field models of aerogels.* Journal of Applied Physics, 2003. **93**(8): 4584-4589.

214. Aieta, N.V.;Stanis, R.J.;Horan, J.L.;Yandrasits, M.A.;Cookson, D.J.*, et al.*, *Clipped random wave morphologies and the analysis of the SAXS of an ionomer formed by copolymerization of tetrafluoroethylene and CF(2)=CFO(CF(2))(4)SO(3)H.* Macromolecules, 2009. **42**(15): 5774-5780.

215. Ingham, B.;Li, H.;Allen, E.L. and Toney, M.F., *SAXSMorph: a program for generating representative morphologies for two-phase materials from small-*

angle X-ray and neutron scattering data. Journal of Applied Crystallography, 2011. **44**(1): 221-224.

216. Cahn, J.W., *Phase separation by spinodal decomposition in isotropic systems.* Journal of Chemical Physics, 1965. **42**(1): 93-99.
217. Berk, N.F., *Scattering properties of a model bicontinuos structure with a well defined length scale.* Physical Review Letters, 1987. **58**(25): 2718-2721.
218. Chen, S.H.;Chang, S.L. and Strey, R., *Simulation of bicontinuos microemulsions - Comparison of simulated real-space microstructures with scattering experiments.* Journal of Applied Crystallography, 1991. **24**: 721-731.
219. O'Sickey, M.J.;Lawrey, B.D. and Wilkes, G.L., *Structure-property relationships of poly(urethane urea)s with ultra-low monol content poly(propylene glycol) soft segments. I. Influence of soft segment molecular weight and hard segment content.* Journal of Applied Polymer Science, 2002. **84**(2): 229-243.
220. Aneja, A. and Wilkes, G.L., *A systematic series of 'model' PTMO based segmented polyurethanes reinvestigated using atomic force microscopy.* Polymer, 2003. **44**(23): 7221-7228.
221. Kaushiva, B.D. and Wilkes, G.L., *Uniaxial orientation behavior and consideration of the geometric anisotropy of polyurea hard domain structure in flexible polyurethane foams.* Polymer, 2000. **41**(18): 6987-6991.
222. Song, M.;Xia, H.S.;Yao, K.J. and Hourston, D.J., *A study on phase morphology and surface properties of polyurethane/organoclay nanocomposite.* European Polymer Journal, 2005. **41**(2): 259-266.
223. Zhang, S.;RenLiu;Jiang, J.;Yang, C.;Chen, M.*, et al.*, *Facile synthesis of waterborne UV-curable polyurethane/silica nanocomposites and morphology, physical properties of its nanostructured films.* Progress in Organic Coatings, 2011. **70**(1): 1-8.
224. Xia, H.;Song, M.;Zhang, Z. and Richardson, M., *Microphase separation, stress relaxation, and creep behavior of polyurethane nanocomposites.* Journal of Applied Polymer Science, 2007. **103**(5): 2992-3002.
225. Stanzick, H.;Wichmann, M.;Weise, J.;Helfen, L.;Baumbach, T.*, et al.*, *Process control in aluminum foam production using real-time x-ray radioscopy.* Advanced Engineering Materials, 2002. **4**(10): 814-823.

226. Garcia-Moreno, F.;Fromme, M. and Banhart, J., *Real-time X-ray radioscopy on metallic foams using a compact micro-focus source.* Advanced Engineering Materials, 2004. **6**(6): 416-420.

227. Kumar, G.S.V.;Garcia-Moreno, F.;Babcsan, N.;Brothers, A.H.;Murty, B.S.*, et al.*, *Study on aluminium-based single films.* Physical Chemistry Chemical Physics, 2007. **9**(48): 6415-6425.

228. Garcia-Moreno, F.;Solorzano, E. and Banhart, J., *Kinetics of coalescence in liquid aluminium foams.* Soft Matter, 2011. **7**(19): 9216-9223.

229. Verdejo, R.;Tapiador, F.J.;Helfen, L.;Bernal, M.M.;Bitinis, N.*, et al.*, *Fluid dynamics of evolving foams.* Physical Chemistry Chemical Physics, 2009. **11**(46): 10860-10866.

230. Banhart, J., *Advanced tomographic methods in materials research and engineering* 2008, New York: Oxford University Press.

231. Bikard, J.;Bruchon, J.;Coupez, T. and Vergnes, B., *Numerical prediction of the foam structure of polymeric materials by direct 3D simulation of their expansion by chemical reaction based on a multidomain method.* Journal of Materials Science, 2005. **40**(22): 5875-5881.

232. Zhang, X.D.;Neff, R.A. and Macosko, C.W., *Foam stability in flexible polyurethane foams systems*, in *Polymeric Foams. Mechanisms and Materials*, Lee, S.T. and Ramesh, N.S., Editors. 2004, CRC Press: Boca Raton, Florida, USA.

233. Langevin, D., *Influence of interfacial rheology on foam and emulsion properties.* Advances in Colloid and Interface Science, 2000. **88**(1–2): 209-222.

234. Yasunaga, K.;Neff, R.A.;Zhang, X.D. and Macosko, C.W., *Study of cell opening in flexible polyurethane foam.* Journal of Cellular Plastics, 1996. **32**(5): 427-448.

235. Zhang, X.D.;Davis, H.T. and Macosko, C.W., *A new cell opening mechanism in flexible polyurethane foam.* Journal of Cellular Plastics, 1999. **35**(5): 458-476.

236. Zhang, X.D.;Macosko, C.W.;Davis, H.T.;Nikolov, A.D. and Wasan, D.T., *Role of silicone surfactant in flexible polyurethane foam.* Journal of Colloid and Interface Science, 1999. **215**(2): 270-279.

237. Zhang, X.D.;Neff, R.A. and Macosko, C.W., *Foam Stability in Flexible Polyurethane Foam Systems*, in *Polymeric foams: mechanisms and materials*, Lee, S.T. and Ramesh, N.S., Editors. 2004, CRC Press: Boca Raton, Florida, USA.

238. Cervantes Martinez, A.;Rio, E.;Delon, G.;Saint-Jalmes, A.;Langevin, D.*, et al.*, *On the origin of the remarkable stability of aqueous foams stabilised by nanoparticles: link with microscopic surface properties.* Soft Matter, 2008. **4**(7): 1531-1535.

239. Stocco, A.;Garcia-Moreno, F.;Manke, I.;Banhart, J. and Langevin, D., *Particle-stabilised foams: structure and aging.* Soft Matter, 2011. **7**(2): 631-637.

240. Weaire, D. and Hutzler, S., *The physics of foams*. 2001, Oxford: Oxford University Press.

241. Koberstein, J.T. and Leung, L.M., *Compression-molded polyurethane block copolymers. 2. Evaluation of microphase compositions.* Macromolecules, 1992. **25**(23): 6205-6213.

242. Camberlin, Y. and Pascault, J.P., *Phase segregation kinetics in segmented linear polyurethanes: relations between equilibrium time and chain mobility and between equilibrium degree of segregation and interacction parameter.* Journal of Polymer Science, Part B: Polymer Physics, 1984. **22**: 1835-1844.

243. Sheth, J.P.;Aneja, A. and Wilkes, G.L., *Exploring long-range connectivity of the hard segment phase in model tri-segment oligomeric polyurethanes via lithium chloride.* Polymer, 2004. **45**(17): 5979-5984.

244. Brunette, C.M.;Hsu, S.L.;Rossman, M.;Macknight, W.J. and Schneider, N.S., *Thermal and mechanical-properties of lineaer segmented polyurethanes with butadiene soft segments.* Polymer Engineering and Science, 1981. **21**(11): 668-674.

245. Li, Y.;Kang, W.;Stoffer, J.O. and Chu, B., *Effect of hard-segment flexibility on phase separation of segmented polyurethanes.* Macromolecules, 1994. **27**(2): 612-614.

246. Chen, T.K.;Chui, J.Y. and Shieh, T.S., *Glass transition behaviors of a polyurethane hard segment based on 4,4'-diisocyanatodiphenylmethane and*

1,4-butanediol and the calculation of microdomain composition. Macromolecules, 1997. **30**(17): 5068-5074.

247. Tien, Y.I. and Wei, K.H., *The effect of nano-sized silicate layers from montmorillonite on glass transition, dynamic mechanical, and thermal degradation properties of segmented polyurethane.* Journal of Applied Polymer Science, 2002. **86**(7): 1741-1748.
248. Bogoslovov, R.B.;Roland, C.M.;Ellis, A.R.;Randall, A.M. and Robertson, C.G., *Effect of silica nanoparticles on the local segmental dynamics in poly(vinyl acetate).* Macromolecules, 2008. **41**(4): 1289-1296.
249. Fragiadakis, D.;Gamache, R.;Bogoslovov, R.B. and Roland, C.M., *Segmental dynamics of polyurea: effect of stoichiometry.* Polymer, 2010. **51**(1): 178-184.
250. Chattopadhyay, D.K. and Webster, D.C., *Thermal stability and flame retardancy of polyurethanes.* Progress in Polymer Science, 2009. **34**(10): 1068-1133.
251. Ferguson, J. and Petrovic, Z., *Thermal stability of segmented polyurethanes.* European Polymer Journal, 1976. **12**(3): 177-181.
252. Wang, X.;Hu, Y.;Song, L.;Yang, H.;Xing, W.*, et al.*, *In situ polymerization of graphene nanosheets and polyurethane with enhanced mechanical and thermal properties.* Journal of Materials Chemistry, 2011. **21**(12): 4222-4227.
253. Yu, J.;Jiang, P.;Wu, C.;Wang, L. and Wu, X., *Graphene nanocomposites based on poly(vinylidene fluoride): Structure and properties.* Polymer Composites, 2011. **32**(10): 1483-1491.
254. Miller, J.A.;Lin, S.B.;Hwang, K.K.S.;Wu, K.S.;Gibson, P.E.*, et al.*, *Properties of polyether-polyurethane block copolymers: effects of hard segment length distribution.* Macromolecules, 1985. **18**(1): 32-44.
255. Pei, A.H.;Malho, J.M.;Ruokolainen, J.;Zhou, Q. and Berglund, L.A., *Strong nanocomposite reinforcement effects in polyurethane elastomer with low volume fraction of cellulose nanocrystals.* Macromolecules, 2011. **44**(11): 4422-4427.
256. Tsagaropoulos, G. and Eisenberg, A., *Dynamic-mechanical study of the factors affecting the 2 glass-transition behavior of filled polymers. Similarities*

and differences with random ionomers Macromolecules, 1995. **28**(18): 6067-6077.

257. Lee, H.-C.;Kim, J.-Y.;Noh, C.-H.;Song, K.Y. and Cho, S.-H., *Selective metal pattern formation and its EMI shielding efficiency.* Applied Surface Science, 2006. **252**(8): 2665-2672.

258. Thomassin, J.-M.;Jérôme, R.;Detrembleur, C.;Molenberg, I. and Huynen, I., *Polymer/carbon nanotube composites for electromagnetic interference reduction*, in *Physical properties and applications of polymer nanocomposites*. 2010, Woodhead Publishing Limited.

259. Thomassin, J.M.;Huynen, I.;Jerome, R. and Detrembleur, C., *Functionalized polypropylenes as efficient dispersing agents for carbon nanotubes in a polypropylene matrix; application to electromagnetic interference (EMI) absorber materials.* Polymer, 2010. **51**(1): 115-121.

260. Xia, H.S. and Song, M., *Intercalation and exfoliation behaviour of clay layers in branched polyol and polyurethane/clay nanocomposites.* Polymer International, 2006. **55**(2): 229-235.

261. Litchfield, D.W. and Baird, D.G., *The rheology of high aspect ratio nano-particle filled liquids*, in *Rheology Reviews 2006*. 2006, The British Society of Rheology. 1-60.

262. Bhattacharya, S.;Gupta, R.K. and Bhattacharya, S., *The Rheology of Polymeric Nanocomposites*, in *Polymer Nanocomposites Handbook*, Gupta, R.K., Kim, K.-J. and Kennel, E., Editors. 2009, CRC Press: Boca Raton, Florida, USA. 151-204.

263. Guimont, A.;Beyou, E.;Martin, G.g.;Sonntag, P. and Cassagnau, P., *Viscoelasticity of graphite oxide-based suspensions in PDMS.* Macromolecules, 2011. **44**(10): 3893-3900.

264. Beigbeder, A.;Linares, M.;Devalckenaere, M.;Degee, P.;Claes, M.*, et al.*, *CH-π interactions as the driving force for silicone-based nanocomposites with exceptional properties.* Advanced Materials, 2008. **20**(5): 1003-1007.

265. Viola, G.G. and Schmeal, W.R., *Isocyanate trimerization kinetics and heat transfer in structural reaction injection molding.* Polymer Engineering & Science, 1994. **34**(15): 1173-1186.

266. Hone, J.;Whitney, M.;Piskoti, C. and Zettl, A., *Thermal conductivity of single-walled carbon nanotubes.* Physical Review B, 1999. **59**(4): R2514-R2516.

267. Yamamoto, T.;Watanabe, S. and Watanabe, K., *Universal features of quantized thermal conductance of carbon nanotubes.* Physical Review Letters, 2004. **92**(7).

268. Maeda, T. and Horie, C., *Phonon modes in single-wall nanotubes with a small diameter.* Physica B, 1999. **263**: 479-481.

269. Kasuya, A.;Saito, Y.;Sasaki, Y.;Fukushima, M.;Maeda, T.*, et al.*, *Size dependent characteristics of single wall carbon nanotubes.* Materials Science and Engineering a-Structural Materials Properties Microstructure and Processing, 1996. **217**: 46-47.

270. Popov, V.N., *Theoretical evidence for T-1/2 specific heat behavior in carbon nanotube systems.* Carbon, 2004. **42**(5-6): 991-995.

271. Martin-Gallego, M.;Verdejo, R.;Khayet, M.;Ortiz de Zarate, J.M.;Essalhi, M.*, et al.*, *Thermal conductivity of carbon nanotubes and graphene in epoxy nanofluids and nanocomposites.* Nanoscale Research Letters, 2011. **6**.

272. Yu, W.;Xie, H.;Wang, X. and Wang, X., *Significant thermal conductivity enhancement for nanofluids containing graphene nanosheets.* Physics Letters A, 2011. **375**(10): 1323-1328.

273. Modesti, M.;Adriani, V. and Simioni, F., *Chemical and physical blowing agents in structural polyurethane foams: Simulation and characterization.* Polymer Engineering & Science, 2000. **40**(9): 2046-2057.

274. Tan, S.;Abraham, T.;Ference, D. and Macosko, C.W., *Rigid polyurethane foams from a soybean oil-based Polyol.* Polymer, 2011. **52**(13): 2840-2846.

275. Elwell, M.J., *Forced-adiabatic sampling environments: Useful tools for the study of structure development during polymerization.* Thermochimica Acta, 1995. **269**: 145-157.

276. Agranoff, J., *Modern plastics encyclopedia, 1985-1986*. Vol. 52. 1985: McGraw-Hill.

277. Broyer, E.;Macosko, C.W.;Critchfield, F.E. and Lawler, L.F., *Curing and heat-transfer in polyurethane reaction molding.* Polymer Engineering and Science, 1978. **18**(5): 382-387.

278. Wilkinson, A.N.;Fithriyah, N.H.;Stanford, J.L. and Suckley, D., *Structure development in flexible polyurethane foam-layered silicate nanocomposites.* Macromolecular Symposia, 2007. **256**: 65-72.

279. Everitt, S.L.;Harlen, O.G.;Wilson, H.J. and Read, D.J., *Bubble dynamics in viscoelastic fluids with application to reacting and non-reacting polymer foams.* Journal of Non-Newtonian Fluid Mechanics, 2003. **114**(2-3): 83-107.

280. Harikrishnan, G.;Patro, T.U.;Unni, A.R. and Khakhar, D.V., *Clay nanoplatelet induced morphological evolutions during polymeric foaming.* Soft Matter, 2011. **7**(15): 6801-6804.

281. Istrate, O.M. and Chen, B., *Relative modulus-relative density relationships in low density polymer-clay nanocomposite foams.* Soft Matter, 2011. **7**(5): 1840-1848.

282. Pugh, R.J., *Foaming, foam films, antifoaming and defoaming.* Advances in Colloid and Interface Science, 1996. **64**(0): 67-142.

283. Tang, F.-Q.;Xiao, Z.;Tang, J.-A. and Jiang, L., *The effect of SiO2 particles upon stabilization of foam.* Journal of Colloid and Interface Science, 1989. **131**(2): 498-502.

284. Kostakis, T.;Ettelaie, R. and Murray, B.S., *Effect of high salt concentrations on the stabilization of bubbles by silica particles.* Langmuir, 2006. **22**(3): 1273-1280.

285. Yan, D.-X.;Dai, K.;Xiang, Z.-D.;Li, Z.-M.;Ji, X.*, et al.*, *Electrical conductivity and major mechanical and thermal properties of carbon nanotube-filled polyurethane foams.* Journal of Applied Polymer Science, 2011. **120**(5): 3014-3019.

286. Li, Y.;Ren, H.F. and Ragauskas, A.J., *Rigid polyurethane foam/cellulose whisker nanocomposites: preparation, characterization, and properties.* Journal of Nanoscience and Nanotechnology, 2011. **11**(8): 6904-6911.

287. Goods, S.H.;Neuschwanger, C.L.;Whinnery, L.L. and Nix, W.D., *Mechanical properties of a particle-strengthened polyurethane foam.* Journal of Applied Polymer Science, 1999. **74**(11): 2724-2736.

288. Cao, X.;Lee, L.J.;Widya, T. and Macosko, C., *Polyurethane/clay nanocomposites foams: processing, structure and properties.* Polymer, 2005. **46**(3): 775-783.

289. Svagan, A.J.;Samir, M. and Berglund, L.A., *Biomimetic foams of high mechanical performance based on nanostructured cell walls reinforced by native cellulose nanofibrils.* Advanced Materials, 2008. **20**(7): 1263-1269.

290. Narine, S.S.;Kong, X.H.;Bouzidi, L. and Sporns, P., *Physical properties of polyurethanes produced from polyols from seed oils: II. Foams.* Journal of the American Oil Chemists Society, 2007. **84**(1): 65-72.

291. Mahfuz, H.;Rangari, V.K.;Islam, M.S. and Jeelani, S., *Fabrication, synthesis and mechanical characterization of nanoparticles infused polyurethane foams.* Composites Part A: Applied Science and Manufacturing, 2004. **35**(4): 453-460.

292. Zhang, X.-G.;Ge, L.-L.;Zhang, W.-Q.;Tang, J.-H.;Ye, L.*, et al.*, *Expandable graphite-methyl methacrylate-acrylic acid copolymer composite particles as a flame retardant of rigid polyurethane foam.* Journal of Applied Polymer Science, 2011. **122**(2): 932-941.

293. Oprea, S.;Vlad, S.;Stanciu, A.;Ciobanu, C. and Macoveanu, M., *Synthesis and characterization of poly(urethane-urea-acrylate)s.* European Polymer Journal, 1999. **35**(7): 1269-1277.

8. LIST OF PUBLICATIONS

The publications obtained from the thesis are:

- Bernal M.M., Molenberg I., Estravis S., Rodriguez-Perez M.A., Huynen I., Lopez-Manchado M.A., Verdejo R. Comparing the effect of carbon-based nanofillers on the physical properties of flexible polyurethane foams. *Journal of Materials Science*. 2012. DOI 10.1007/s10853-012-6331-4.
- Bernal M.M., Lopez-Manchado M.A., Verdejo R. In situ foaming evolution of polyurethane foam nanocomposites. *Macromolecular Chemistry and Physics*. 2011. **212** (9): 971-979
- Verdejo R., Bernal M.M., Romasanta L.J., Tapiador F.J., Lopez-Manchado M.A. Reactive Nanocomposite Foams. *Cellular Polymers*. 2011. **30** (2): 45-61
- Bernal M.M., Martin-Gallego M., Romasanta L.J., Mortamet AC., Lopez-Manchado M.A., Ryan A.J., Verdejo R. Effect of hard segment content and carbon-based nanostructures on the kinetics of flexible polyurethane nanocomposite foams. *Submitted.*

Other publications:

- Bernal M.M., Liras M., Verdejo R., Lopez-Manchado M.A., Quijada-Garrido I., Paris R. Modification of carbon nanotubes with well-controlled fluorescent styrene-based polymers using the Diels-Alder reaction. *Polymer*. 2011. **52** (25): 5739-5745
- Verdejo R., Bernal M.M., Romasanta L.J., Lopez-Manchado M.A. Graphene filled polymer nanocomposites. *Journal of Materials Chemistry*. 2011. **21** (10): 3301-3310
- Verdejo R., Tapiador F.J., Helfen L., Bernal M.M., Bitinis N., Lopez-Manchado M.A. Fluid dynamics of evolving foams. *Physical Chemistry Chemical Physics*. 2009. 11 (46): 10860-10866

J Mater Sci
DOI 10.1007/s10853-012-6331-4

SYNTACTIC & COMPOSITE FOAMS

Comparing the effect of carbon-based nanofillers on the physical properties of flexible polyurethane foams

M. Mar Bernal · Isabel Molenberg · Sergio Estravis · Miguel Angel Rodriguez-Perez · Isabelle Huynen · Miguel Angel Lopez-Manchado · Raquel Verdejo

Received: 4 November 2011 / Accepted: 9 February 2012

Abstract Flexible polyurethane foams filled with a fixed amount of carbon-based nanofillers, in particular multiwall nanotubes and graphenes, have been studied to clarify the influence of the morphology and functional groups on the physical properties of these polymeric foams. The effect of the carbon nanoparticles on the microphase separation has been analyzed by FT-IR spectroscopy revealing a decrease in the degree of phase separation of the segments. Variations of the glass transition temperature and an improved thermal stability were observed due to the presence of the nanoparticles. The EMI shielding effectiveness of flexible PU foams has also been enhanced, in particular for FGS nanocomposite foams.

Introduction

The rapid increase of electronic devices in our daily life has resulted in electromagnetic interference (EMI) problems that disrupt the device signals and reduce their performances. Thus, there is a real need to design and develop EMI shields that suppress or minimize undesired signals. Furthermore, the requirements imposed by the continuous design of ultraportable electronic devices and transport sectors have pushed the development of lightweight shielding materials. Polymer foams have shown a potential due to their lightweight characteristics but they require the inclusion of conductive particles to render them effective EMI shields. Therefore, carbon black, metal flakes, or metal fibers have been used as fillers in foams at loading fractions of up to 50 wt% [1]. The use of high aspect ratio conductive fillers, such as carbon nanotubes, can therefore be an attractive alternative. The introduction of carbon nanoparticles in polymer foams has received increasing attention because they can enhance not only the electrical conductivity [2] but also the mechanical strength, thermal stability, and surface quality [3–6]. In general, nanofillers can be easily incorporated in the cellular structure of foams reinforcing these polymeric materials with a minor effect on their structural characteristics (open-cell content, cell size distribution, rupture of cell walls, …) [4, 7–11].

Polyurethane (PU) foams are one of the most versatile polymer foams with the largest market due to their wide range of applications [12–14]. Flexible PU foams are formed during the simultaneous reactions between an isocyanate with a polyol and water. The result of these exothermic reactions is a block copoly(urethane-urea) which forms the cellular structure due to the cogeneration of carbon dioxide [15, 16]. Hence, the properties of PU foams depend not only on their final cellular structure but also on the phase-separated microstructure [15, 17]. Recently, carbon nanofillers have been incorporated in PU foams showing that they did not only improve the physical properties [2, 7, 10, 14, 18] but also affected the kinetics of foaming polymerization [10, 14, 19].

In this study, we have introduced multiwalled carbon nanotubes (MWCNTs), functionalized MWCNTs and

M. M. Bernal · M. A. Lopez-Manchado · R. Verdejo (✉)
Instituto de Ciencia y Tecnología de Polímeros (ICTP-CSIC), C/Juan de la Cierva 3, 28006 Madrid, Spain
e-mail: rverdejo@ictp.csic.es

I. Molenberg · I. Huynen
Information and Communications Technologies, Electronics and Applied Mathematics (ICTEAM), Microwave Laboratory, Université Catholique de Louvain, 1348 Louvain-la-Neuve, Belgium

S. Estravis · M. A. Rodriguez-Perez
Cellular Materials Laboratory (CellMat), Condensed Matter Physics Department, University of Valladolid, 47011 Valladolid, Spain

Published online: 06 March 2012

Full Paper

Macromolecular Journals

Macromolecular Chemistry and Physics

In situ Foaming Evolution of Flexible Polyurethane Foam Nanocomposites

M. Mar Bernal, Miguel Angel Lopez-Manchado, Raquel Verdejo*

The effect of both as-produced and functionalised CNTs on the polymerisation evolution of water-blown PU foams containing up to 0.3 wt.-% CNTs was studied by in situ FT-IR spectroscopy. FT-IR revealed a decrease on the rate of isocyanate conversion as a function of loading fraction for both as-grown and oxidised CNTs. This dependency suggested that the isocyanate conversion at the early stages of the reaction was governed by the kinetic effects imposed by the presence of the CNTs. The onset of microphase separation was accelerated by the addition of functionalised CNTs (f-CNTs) but not by as-produced CNTs due to the different surface functionalities. Measurements of the foaming viscoelastic properties showed an increase on the storage modulus with the CNT content, which indicated the reinforcement of the foam.

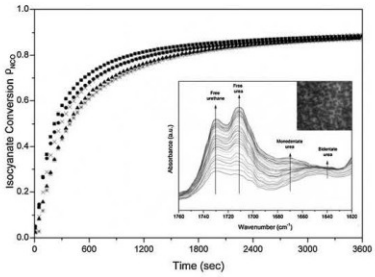

Introduction

Reactive foams are produced as a result of two simultaneous reactions: foaming and polymerisation, water-blown polyurethane foam being one of the largest and most versatile families of these foams. The process presents a liquid/solid phase transition where a liquid mixture, of relatively low-molecular-weight components, is transformed into the supramolecular architecture of solid foams in under 5 min.[1] Hence, the reaction kinetics of this process has to be well understood in order to control the rates of both the evolution of the gas and the increase in viscosity, since the polymer structure must build up rapidly to support the fragile foam, i.e., to form a stable cellular structure, but not so fast as to stop bubble growth.[2]

The versatility of water-blown polyurethane (PU) foams arises not only from the nature and variety of the reaction mixture, but also from the ease of production that enables the development of tailor-made materials over wide range of applications.[3] PU foams are used for their outstanding strength-to-weight ratio, their resilience and their electrical, thermal and acoustic insulating properties, amongst other characteristics.[3] PU foam chemistry is based on the reactions of isocyanates with active hydrogen-containing compounds, in particular polyfunctional hydroxyl compounds (or polyols) and water. The reaction of isocyanate with polyol, often termed the *gelling reaction* (Scheme 1a), forms urethane linkages, leading to the increase in the molecular weight. Meanwhile, the reaction of isocyanate with water, known as the *blowing reaction* (Scheme 1b), forms urea hard segments and carbon dioxide gas from the decomposition of an unstable carbamic acid.[4] As a result of these concurrent reactions a cross-linked network of a segmented *block*-copoly(ether/urethane urea) is blown into a cellular structure by the evolved CO_2 and entrapped air. This reactive processing provides PU foams with a structured morphology stretching over several length scales, from the macroscopic cellular structure to the microdomains of the segregated urea hard segments and the poly(ether-urethane) soft segments joined by urethane covalent bonds (Scheme 1c). Thus, the final properties of PU

M. M. Bernal, M. A. Lopez-Manchado, R. Verdejo
Institute of Polymer Science and Technology (CSIC), C/ Juan de la Cierva 3, 28006 Madrid, Spain
E-mail: rverdejo@ictp.csic.es

Macromol. Chem. Phys. **2011**, *212*, 971–979

DOI: 10.1002/macp.201000748

Reactive Nanocomposite Foams

Raquel Verdejo[1], M. Mar Bernal[1], Laura J. Romasanta[1], Francisco J. Tapiador[2], and Miguel A. Lopez-Manchado[1]*

[1]*Institute of Polymer Science and Technology (CSIC), Juan de la Cierva 3, 28003-Madrid, Spain*

[2] *University of Castilla-La Mancha (UCLM), Avda. Carlos III s/n, 45071-Toledo, Spain*

Received: 17 December 2010, Accepted: 28 January 2011

SUMMARY

One of the most interesting and most accessible opportunities of nanofillers is the reinforcement of fine structures in which conventional fillers cannot be readily accommodated, such as polymer foams. This paper reviews the progress to date towards the development of reactive foam nanocomposites, in particular polyurethane and silicone foams. The discussed systems are summarized based on the types of nanofillers used, i.e. nanoparticles, rod-like, and plate-like systems. The effect of nanofillers on the foaming process, cellular structure and properties is critically reported along with a summary of the measured improvements in the mechanical, electrical and thermal properties of the resulting nanocomposites.

1. INTRODUCTION

Polymer composites have been used for centuries and are the result of blending various polymers or adding fillers, such as minerals, ceramics, and metals. Over the past decade, the use of nanofillers, defined as fillers where at least one of their dimensions is on the nanometer scale, has been recognized as a suitable strategy to enhance polymer performance [1]. Due to the low loading fractions (1-10 vol%) required to provide property enhancements comparable to those achieved by conventional micrometer-scale fillers (with loading fractions up to 40 vol%), polymer nanocomposites have aroused widespread interest. Additionally, nanofillers have demonstrated their ability to act as functional materials capable of imparting value-added properties and property combinations which are not normally possible with traditional fillers.

* Corresponding author. Email: rverdejo@ictp.csic.es, Tel: +34 91 258 7424; Fax: +34 91 564 4853

Effect of hard segment content and carbon-based nanostructures on the kinetics of flexible polyurethane nanocomposite foams

Authors: M. Mar Bernal[1], Mario Martin-Gallego[1], Laura J. Romasanta[1], Anne-Cecile Mortamet[2], Miguel A. Lopez-Manchado[1], Anthony J. Ryan[2], Raquel Verdejo[1]*

[1] Instituto de Ciencia y Tecnología de Polímeros (ICTP-CSIC), C/Juan de la Cierva 3, 28006, Madrid, Spain

[2] Department of Chemistry, University of Sheffield, Sheffield, S3 7HF, United Kingdom

Submitted

Abstract: Reactive flexible polyurethane (PU) foams were synthesized with two contents of hard segments (HS) and filled with multi-walled carbon nanotubes (MWCNTs), functionalized MWCNTs (f-MWCNTs) and functionalized graphene sheets (FGS). The effect of the HS content and the carbon nanofillers on the kinetics of polymerization and the kinetics of phase-separation have been studied by Fourier transform infrared spectroscopy (FT-IR) and synchrotron small-angle X-ray scattering (SAXS). A slow down on the rate of polymerization and on the development of the polymer structure due to the increase of the HS content and the inclusion of the nanoparticles was observed. Therefore, this work demonstrates that there is a relationship between the kinetics of polymerization and the kinetics of phase separation in flexible PU nanocomposite foams. SAXS data was used to generate 3D microstructures of PU nanocomposite foams and the phase separated morphology was observed by AFM.

Polymer 52 (2011) 5739–5745

Contents lists available at SciVerse ScienceDirect

Polymer

journal homepage: www.elsevier.com/locate/polymer

Modification of carbon nanotubes with well-controlled fluorescent styrene-based polymers using the Diels–Alder reaction

M. Mar Bernal, Marta Liras, Raquel Verdejo, Miguel A. López-Manchado, Isabel Quijada-Garrido, Rodrigo París*

Instituto de Ciencia y Tecnología de Polímeros, ICTP-CSIC, Consejo Superior de Investigaciones Científicas, Juan de la Cierva 3, E-28006 Madrid, Spain

ARTICLE INFO

Article history:
Received 24 August 2011
Received in revised form
11 October 2011
Accepted 15 October 2011
Available online 21 October 2011

Keywords:
Atom transfer radical polymerization (ATRP)
Functionalized polymers
Multi-wall carbon nanotubes

ABSTRACT

A simple and single-step "grafting to" approach based on the Diels–Alder (DA) reaction is described to functionalize multi-wall carbon nanotubes (MWCNTs) with polystyrene (PSt). Thus, several fluorescent and furfuryl functionalized PSts, synthesized by the atom transfer radical polymerization (ATRP) of styrene, furfuryl methacrylate and low proportion of a fluorescent monomer, were covalently attached onto the pristine nanotubes. Furfuryl (diene) groups allowed the chemical attachment of the PSt polymer onto the as-synthesized MWCNTs by a DA reaction. On the other hand, the incorporation of fluorescent groups in the polymer has two main advantages. It permits to determine the attachment of the polymer onto the nanotubes and, in further applications, it will allow to follow the dispersion of these modified MWCNTs in a matrix. The efficiency of the functionalization was verified by FTIR, Raman spectroscopy, TEM, AFM and fluorescence techniques.

1. Introduction

The covalent functionalization of carbon nanotubes has attracted much attention over the past years because it introduces new physical and chemical properties useful for a myriad of applications, such as sensors, electronic devices and many others [1–4]. Besides, there is a high technological interest in to manage composites materials based on CNTs and polymers, such as poly(-vinyl alcohol) (PVA) [5], thermoplastic polyurethane (TPU) [6] or polyethyleneimine (PEI) [7].

Covalent functionalization has been widely employed to improve the solubility and the compatibility of these nanomaterials in composite materials as it allows an easier processing of the composites. Thus, several functionalization methodologies have been explored, which include oxidation at defect sites [8], addition reactions of azomethine ylides [9], bromomalonates [10], diazonium salts [11,12], nucleophilic carbenes [13], nitrenes [14] and free radicals [15]. They all have one thing in common, a highly reactive intermediate is necessary to attack the carbon nanotubes. However, this approach is hindered by the loss of the optical, electrical and thermal properties of the nanotube due to the damage produced in the sp^2-hybridized carbon atoms, which could even result in the attachment of carbonaceous debris on the nanotubes surface [16].

An alternative approach to overcome that shortcoming is to use the Diels–Alder (DA) reaction [17–24]. It is a (4 + 2)-cycloaddition reaction between a conjugated diene and a dienophile (alkene or alkyne) that involves the four π-electrons of the diene and two π-electrons of the dienophile to form new C–C σ-bonds. The main advantages of this technique are: i) the reversibility of the reaction, ii) the non-generation of by-products and iii) the use of mild conditions of temperature and pressure for the preparation. Thus, Chang *et al.* [23] demonstrated that MWCNTs can serve as either a dienophile or a diene in DA reactions. These authors verified the successful functionalization of MWCNTs through DA reaction using furfuryl alcohol as a functionalization agent under mild reaction conditions and without the addition of catalysts. These furan compounds are highly reactive agents in DA reactions as these compounds possess electron-withdrawing substitutes. Under these premises, Munirasu *et al.* [24] prepared polystyrene-coated MWCNTs. They used a furfuryl-based initiator of atom transfer radical polymerization (ATRP) for the surface initiated "grafting from" polymerization of styrene onto MWCNT.

Here, we report a simple and scalable "grafting to" approach to attach furfuryl functionalized PSt-based polymers onto pristine MWCNTs through the DA reaction. Therefore, the structural integrity of the nanotube framework is retained and a higher control of the molecular weight of the polymers is attained. Thus, several

* Corresponding author. Tel.: +34 91 258 74 30, +34 91 562 29 00; fax: +34 91 564 48 53.
E-mail address: rparis@ictp.csic.es (R. París).

0032-3861/$ – see front matter © 2011 Elsevier Ltd. All rights reserved.
doi:10.1016/j.polymer.2011.10.031

FEATURE ARTICLE www.rsc.org/materials | Journal of Materials Chemistry

Graphene filled polymer nanocomposites†

Raquel Verdejo,* M. Mar Bernal, Laura J. Romasanta and Miguel A. Lopez-Manchado

Received 17th August 2010, Accepted 27th September 2010
DOI: 10.1039/c0jm02708a

Graphene has attracted the attention of a growing number of scientists from several disciplines due to its remarkable physical properties and chemical functionalisation capabilities. This review presents an overview of graphene/polymer nanocomposites discussing preparation, properties and potential applications. The challenges and outlook of these emerging polymer nanocomposites are also discussed.

1. Introduction

Industrial and academic research on polymer nanocomposites was pursued to provide added value properties to the neat polymer, without sacrificing its processability or adding excessive weight.[1] In this context, carbon-based nanoparticles, in particular carbon nanotubes (CNTs), offered the potential to combine several properties, such as mechanical strength, electrical conductivity and thermal stability, among others. This potential arises from the remarkable properties of the nanotubes, which are based on the building block of all graphitic allotropes: graphene. Although significant advances have been made in the use of carbon nanotubes as reinforcements of polymer matrices, there are still unresolved issues such as the tendency of nanotubes to agglomerate during processing, the limited availability of high-quality nanotubes in large quantities and the high cost of their production. Hence, graphene sheets provide an alternative option to produce functional nanocomposites due to their excellent properties and the natural abundance of their precursor, graphite.[2]

Graphene is a two-dimensional, one-atom-thick carbon sheet with a planar honeycomb lattice. Defect-free graphene presents outstanding physical properties, such as high intrinsic mobility and ballistic transport, high thermal conductivity and Young's modulus, an optical transmittance of almost 98% and large specific surface area.[3–5] The most widely used methods to synthesise these high quality, defect-free graphene sheets have been micromechanical cleavage of graphite ("Scotch tape" or peel off method),[6] and chemical vapour deposition (CVD)[7,8] (Fig. 1, a–e). However, their production yield is relatively small and, in the case of the micromechanical cleavage, time consuming which hinders the effective and full-exploitation of these materials.

An alternative route to produce graphene and chemically modified graphene (CMG) is by the exfoliation of graphite or its derivatives, mainly graphite oxide (GO). The advantage of this approach is that it enables high yield production and, hence, it is a cost-effective and scalable process.[9] These materials are, therefore, suitable for the production of polymer nanocomposites.

Several methods have been reported for the exfoliation of graphite into graphene and CMG. They can be grouped

Institute of Polymer Science and Technology, (CSIC), ClJuan de la Cierva, 3, 28006 Madrid, Spain. E-mail: rverdejo@ictp.csic.es; Fax: +34 91 5644853; Tel: +34 91 258 7424

† This paper is part of a *Journal of Materials Chemistry* themed issue on Chemically Modified Graphenes. Guest editor: Rod Ruoff.

Raquel Verdejo

Raquel Verdejo holds a Ramon y Cajal *senior scientist position at the Institute of Polymer Science and Technology, CSIC (Spain). She obtained her MSc in Physics from the University of Valladolid (Spain) and her PhD in Metallurgy and Materials from the University of Birmingham (UK). She then joined the group led by Prof. Milo Shaffer as a Research Associate at Imperial College London, working in nanocomposite polymer foams. Her current research interests include carbon nanotube and graphene synthesis, and the design, development and characterisation of polymer nanocomposites, for both structural and functional applications.*

M. Mar Bernal

M. Mar Bernal received her M.Sc. in Chemical Engineering from Polytechnic University of Valencia in 2007 and is currently a PhD candidate at the Institute of Polymer Science and Technology, CSIC in Madrid. Her research interests include synthesis and functionalisation of carbon nanotubes and graphene for the preparation of elastomeric nanocomposite foams.

PAPER www.rsc.org/pccp | Physical Chemistry Chemical Physics

Fluid dynamics of evolving foams†

Raquel Verdejo,*[a] Francisco J. Tapiador,[b] Lukas Helfen,[c] M. Mar Bernal,[a] Natacha Bitinis[a] and Miguel A. Lopez-Manchado[a]

Received 3rd July 2009, Accepted 15th September 2009
First published as an Advance Article on the web 2nd October 2009
DOI: 10.1039/b913262g

The physical properties of many multiphase systems are determined by coarsening phenomena. From raindrops to polycrystal grains and foams, the formation and stability of these systems continuously evolve towards lower-energy configurations through events such as coalescence, Ostwald ripening and drainage. Here we propose a procedure to identify and characterise key topological transformations of coarsening phenomena using a physically-based fluid dynamic framework. *In situ*, real-time foaming processes of a polymeric matrix reinforced with two morphologically different nanofillers, carbon nanotubes and graphene sheets were observed by synchrotron X-ray radioscopy. We obtained detailed information on the evolution of the growth patterns and coarsening events. Filled samples showed differences in both trend and speed compared with the unfilled sample. Furthermore, we found different dominating coarsening phenomena due to the wetting nature of carbon nanoparticles. Our procedure can be extended to sequences of any type of 2D projection or 3D images and to other multiphase systems.

Introduction

Foaming is a complex process which involves the formation of gas bubbles in a fluid or the nucleation and evolution of both liquid and gas until stabilization occurs. This spatial and temporal evolution involves the interplay of several physical phenomena, such as surface tension, diffusion and viscosity,[1] which is reflected in the dynamics of the liquid and gaseous phases and determines the final cellular microstructure of the system.

Despite the important influence that this cellular topology has on the properties of foams,[2] the physics of the foaming phenomena, such as drainage and foam flow, are still unclear, even in the simplest case of the aqueous foams.[3] The majority of current studies focusing on foam formation have been carried out on aqueous foams by light scattering techniques[4–6] or AC conductivity.[7] Ideally, the same basic theories should apply to aqueous and non-aqueous foams.[8] However, recent studies of the foaming of metal foams involving synchrotron analyses have shown clear differences between aqueous and non-aqueous foams.[9] Banhart *et al.*[9] showed that drainage due to gravity had only a weak effect on the coarsening phenomena affecting metal foams, while interdependence was observed between drainage and coarsening in aqueous foams.[3,10,11]

Here, we report a procedure based on a fluid dynamic framework to identify and characterise key topological transformations in reactive polymer foams. We studied a polymer foam produced by a reactive foaming process.[12] This process involves the simultaneous foaming and polymerization of liquid reactants, presenting a liquid–solid phase transition (see ESI, video S1†). The foaming is driven by a gas generated as a by-product of the polymerization reaction. This reaction has to be well controlled in order to balance the rates of both the evolution of the gas and the increase in viscosity;[13] if not, the foam will collapse. One practical way in which to improve the stability of reactive foams is to increase the bulk viscosity of the reactants or the surface viscosity of the gas–liquid interface through a colloidal suspension of solid particles.[8] These dispersed particles can also act as nucleation sites for bubbles in the early stages of the process and as functional fillers for the final foam.

We have recently studied the use of nanofillers as reinforcements, as they can be physically introduced into cell walls without disrupting the foam cellular microstructure.[14,15] Electron microscopy of the foams confirmed that the nanofillers were completely embedded and homogeneously dispersed within the polymer matrix, but also showed a drastic change in the cellular microstructure: from isotropic interconnected open pores to highly anisotropic closed pores.

To better understand the foaming evolution and its dynamics, we carried out *in situ* foaming experiments using synchrotron radiation, because conventional X-ray sources do not provide the appropriate spatial and temporal resolutions. Synchrotron radiography (SR) has previously been used to study a broad range of physical and technological phenomena: from fuel injection in a running engine[16] to formation of granular jets[17] and foaming of metal systems.[9] For foaming studies and appropriate spatial sampling distances in the order of several μm, SR allows temporal sampling to be adjusted

[a] *Institute of Polymer Science and Technology, (CSIC), Juan de la Cierva, 3, 28006 Madrid, Spain. E-mail: rverdejo@ictp.csic.es; Fax: +34 91 564 4853; Tel: +34 91 258 7424*
[b] *Institute of Environmental Sciences (ICAM), Department of Environmental Sciences, University of Castilla-La Mancha (UCLM), Toledo, Spain. E-mail: francisco.tapiador@uclm.es*
[c] *ANKA/Institute for Synchrotron Radiation, Forschungszentrum Karlsruhe, Germany*

† Electronic supplementary information (ESI) available: Movies: (S1) foaming recorded by standard video camera; (S2) foaming recorded by high resolution radiography. See DOI: 10.1039/b913262g

